Clustering of Defects and Impurities in Hydrogenated Single-Crystal Silicon

Kh. A. Abdulin, Yu. V. Gorelkinskiĭ, B. N. Mukashev, and S. Zh. Tokmoldin

Physicotechnical Institute, the Ministry of Education and Science of the Republic of Kazakhstan,
Almaty, 480082 Kazakhstan
e-mail: abdullin@sci.kz
Submitted April 4, 2001; accepted for publication August 29, 2001

Abstract—Data obtained to date on specific features of defect formation for hydrogenated single-crystal Si are analyzed. It was demonstrated that, in addition to other effects, interaction of H atoms with radiation defects and impurities leads to the formation of large clusters of three main types, namely, vacancy, interstitial, and impurity clusters. The main condition for formation of these clusters is the simultaneous presence of supersaturated solutions of H and defects in the sample. The interaction of H atoms with impurities and defects initiates the decomposition of the supersaturated solid solution of defects and impurities with the formation of precipitates. This leads to the formation of clusters, which are not observed in the absence of H. The mechanisms of formation and structure of clusters are discussed. © 2002 MAIK "Nauka/Interperiodica".

1. INTRODUCTION

The H impurity exhibits high mobility and chemical activity in the Si lattice. This leads to numerous phenomena associated with the interaction of H atoms with defects and impurities [1–3]. As a result of this interaction, the defect complexes containing H atoms are formed. The following complexes of H atoms have been detected and identified. These are the complexes with Group V donors and Group III acceptors [1, 2], certain metals [4, 5], O atoms [6–8], chalcogens [9] and other impurities, as well as with radiation defects [2, 10–14]. In many cases, the interaction of an H atom with an impurity or defect leads to the suppression of their electrical activity. The passivation of the donor and acceptor impurities is associated with the amphoteric behavior of atomic H. This latter can be either in the positive charge state when it resides at the center of the Si–Si bond or in the negative charge state when it occupies the tetrahedral interstice [14, 15]. The passivation of defects is conditioned by the ability of H atoms to saturate dangling bonds of Si atoms.

In addition, H atoms can to a large extent control all processes associated with the generation and diffusion of defects without being directly incorporated into the defect structure. The characteristic example is the effect of H on the O diffusion in Si. It has been demonstrated in a number of studies [16–18] that the presence of H promotes O precipitation and leads to the formation of O quenched-in donors. This may occur due to the formation of metastable configurations with the participation of O and H atoms. These configurations are favorable for a substantial decrease in the activation energy for the migration of O atoms [19, 20]. For this reason, the presence of H atoms may profoundly affect the decomposition of supersaturated solid solutions of impurities or defects and the structure of their precipitates.

In this paper, the data on the specific features of defect formation in hydrogenated Si are summarized. We consider the published data and our latest experimental results indicative of the formation of clusters of a vacancy, interstitial, or impurity nature, which are initiated by the presence of H atoms.

2. EXPERIMENTAL

We used single-crystal Si samples of three main types. These were Czochralski-grown Si:B samples (Cz-Si), i.e., pulled from the melt, with a resistivity of 1–2 Ω cm; Si:Al samples obtained by floating-zone melting (FZ-Si), with a resistivity of 0.2 Ω cm; and high-purity FZ-Si crystals with a resistivity of 2 kΩ cm.

In order to incorporate H atoms into the sample, several methods were used. First, irradiation with protons with an energy of 30 MeV through an Al absorber ~4 mm thick was used. As a result, the width of H spatial distribution in the sample bulk was ~100 μm at the half-maximum. Thin additional Al foils were used in order to distribute H atoms more uniformly. The implantation dose corresponded to the bulk content of ~$(0.1–1) \times 10^{17}$ cm^{-3}. The implantation was carried out at the sample temperature of ~80 K or close to 295 K. Second, in order to incorporate H atoms, thermal treatment of the samples at ~1250°C for 0.5–1 h in sealed quartz cells, which contained ~1 mg of distilled water, was carried out. Such treatment leads to approximately uniform H distribution over the sample thickness with a concentration of ~10^{16} cm^{-3} [18]. The incorporation
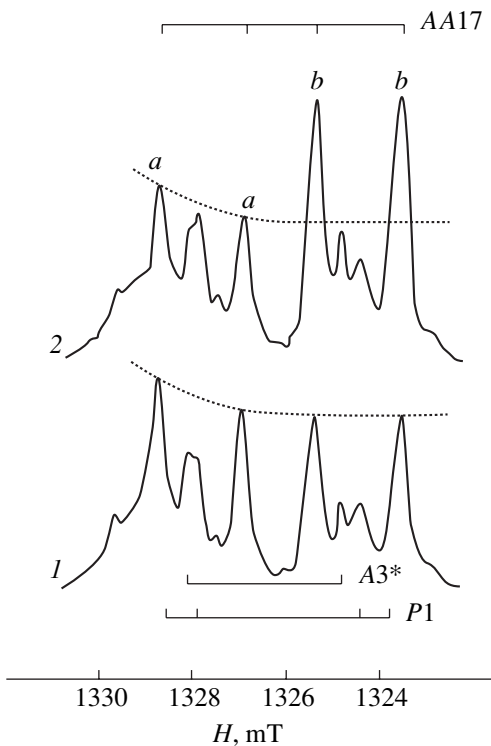
Fig. 1. ESR spectra of the high-purity H-implanted FZ-Si sample. The dose corresponds to the bulk H concentration of $\sim 1 \times 10^{17}$ cm^{-3}. (*1*) After annealing the sample at T_{ann} = 300°C for 20 min. (*2*) After additional annealing at T_{ann} = 200°C for 1 h at a pressure of 150 MPa along the <011> axis of the crystal with subsequent cooling of the sample to room temperature under pressure. The spectra are recorded with the sample illumination, with photon energy being close to the band gap ($h\nu \approx E_g$), at T = 77 K in the dispersion mode. ν_0 = 37.2 GHz, the magnetic field **H** || <011>.

of H atoms into the surface region of the samples by treatment in H plasma at 100–250°C was also used.

Radiation defects were introduced by irradiation with α particles with an energy of 50 MeV or with protons with an energy of 30 MeV up to a dose of 1×10^{17} cm^{-2}. The irradiation was carried out without an absorber. For this reason, no implantation of He or H atoms into the sample occurred.

The electron spin resonance (ESR) was measured at 77 K in the *K*-band (frequency $\nu_0 \approx 37$ GHz) in the absorption or dispersion mode. Experiments with the uniaxial compression of the samples to a pressure as high as 200 MPa were carried out. The infrared (IR) absorption in the frequency range of 300–4000 cm^{-1} was measured using a SPECORD-80 spectrometer in the temperature range T = 80–300 K. The Schottky barriers for deep-level transient spectroscopy (DLTS) measurements were formed by the deposition of Al or Au on the samples of *p*- or *n*-type conduction, respectively. The DLTS measurements were carried out in the temperature range T = 77–300 K using a spectrometer

with an operating frequency of 10 MHz. In order to increase the resolution, the third-order filter was used.

3. VACANCY CLUSTERS

3.1. Si-AA17 Center

FZ-Si samples implanted with protons at room temperature were investigated. In addition to the known ESR spectra (Si-*P*1, Si-*P*3, Si-*P*6, Si-*A*3, and Si-*A*5) [21–23], the new spectrum denoted as Si–*AA*17 was observed (Fig. 1). This spectrum is observed at 77 K subsequent to the short-time illumination of the sample. The *AA*17 ESR spectrum can be attributed to a defect of trigonal symmetry with the spin S = 1. It is found that the presence of both radiation defects and H atoms in Si is necessary for the formation of the *AA*17 defect. Actually, on the irradiation of initial samples with α particles or protons with an energy of 30 MeV (without implantation of protons), the *AA*17 center was not observed. However, for similarly irradiated samples, into which H atoms were introduced (10^{16} cm^{-3}) by preliminary annealing in water vapor at 1250°C for 30 min with subsequent quenching down to 300 K, the ESR signal corresponding to an *AA*17 center becomes noticeable. The best conditions, in which the density of *AA*17 defects was highest, are H implantation to a concentration of 10^{17} cm^{-3} with subsequent through irradiation with protons to a dose of $\sim 10^{17}$ cm^{-2}. For such samples, along with known centers, a weak signal of the *AA*17 spectrum is observed immediately after the irradiation. The density of *AA*17 centers increases considerably with annealing and peaks at the annealing temperature $T_{ann} \approx 250$°C. In these conditions, the *AA*17 spectrum dominates over the other ones (Fig. 1). For the samples H-implanted to a higher bulk concentration of $\sim 10^{18}$ cm^{-3}, the intensity of the *AA*17 signal decreases.

We note that the *AA*17 centers were observed in high-purity FZ-Si samples subjected to multiple zone purification. For Cz-Si samples under similar conditions of implantation and irradiation, the *AA*17 centers are absent or their concentration is low, which indicates that the center formation is suppressed in the presence of O impurities.

The properties of the *AA*17 defect indicate that it is the vacancy complex.

(1) The symmetry of fine and hyperfine splitting is trigonal (Fig. 2). The amplitude (~5%) of observed hyperfine satellites for the *AA*17 spectrum from the ^{29}Si nucleus (I_n = 1/2, abundance ~4.7%) corresponds to the interaction of the paramagnetic electron with two equivalent Si atoms along the interaction axis <111>. For this reason, the symmetry of the defect is D_{3d}. The analysis of hyperfine splitting from the ^{29}Si isotope for the *AA*17 center was carried out similarly to that for other defects in Si [22–24]. It was found that the experimental values of constants of hyperfine interaction $A_\perp$ = 89.0 MHz and $A_\parallel$ = 175.0 ($\pm$1.0) MHz correspond to the degree of localization of the electron wave func-

tion of ~31% at one Si atom. Accordingly, the overall localization at two equivalent Si atoms is ~62%. The contribution of a $3p$ state is 91%, and the contribution of a $3s$ state is 9%. The degree of localization and the degree of hybridization of the wave function for the $AA17$ center are typical of an Si dangling bond in the vicinity of a vacancy defect [23–26].

(2) A small magnitude of zero-field splitting ($D = 16.8$ MHz is the smallest splitting among the known triplet centers in Si) indicates that this splitting is caused by the magnetic dipole–dipole interaction. For this reason, the distance R between the pair of interacting electrons can be determined from the magnitude of fine splitting. We carried out a comparative analysis of the parameter D (in the approximation $D \propto R^{-3}$) of the $AA17$ defect with the data for known spin-triplet centers in Si, for which models have been reliably established. The distance between the pair of interacting spins for the $AA17$ defect was estimated at $R_{17} \approx R_n(D_n/D_{17})^{1/3}$, where R_n and D_n are the parameters of the known center. A comparison with the data for defects whose R and D values substantially differed from those for the $AA17$ defect was carried out. These defects are V_1O ($SL1$), V_2O ($A14$), V_3O ($P4$), and V_4 ($P3$) [24, 27]. The comparison gives the distance between the pair of spins forming the state $S = 1$ in the $AA17$ defect as $R_{17} = (11.0 \pm 1.0)$ Å.

(3) The experiments involving the uniaxial compression of the $AA17$ defect were carried out at a pressure as high as 200 MPa along the $\langle 001 \rangle$ axis of the crystal at ~200°C. The experiments demonstrated that the applied pressure caused preferential alignment of $AA17$ defects and led to considerable polarization P. Here, $P = (b - a)/(b + a)$; b and a are the amplitudes of corresponding lines of the $AA17$ spectrum in Fig. 1. The process of recovery in time t of the equilibrium distribution of the centers over equivalent sites follows the simple exponential law $P = P_0\exp(-t/\tau)$, where τ^{-1} [s^{-1}] $= 1.8 \times 10^{14}\exp(-1.61$ eV$/kT)$. The activation energy of the misorientation noticeably exceeds the values for known vacancy-type defects. This is presumably caused by the complex structure of the $AA17$ defect, which includes Si–H bonds. From the ratio b/a, it is possible to calculate the only (in the case of trigonal symmetry) independent component of the piezospectroscopic B tensor [28, 29]. For $b/a = 1.89$, $T = 463$ K, and a pressure of 150 MPa, we obtained B $= +(13.2 \pm 0.5)$ eV/(unit strain). The positive sign means that the energy of the defect decreases if the pressure is applied along its trigonal axis; i.e., the structure whose lattice is less dense compared to the normal lattice is located on the axis between interacting spins. Thus, the experimental data provide narrow limits for devising the model of the $AA17$ defect. The only possible sites at which dangling bonds forming the spin $S = 1$ can be localized are the A and B atoms arranged on the [111] axis at a distance $R \approx 12$ Å. In this case, dangling bonds at nearest neighboring atoms should be neutralized
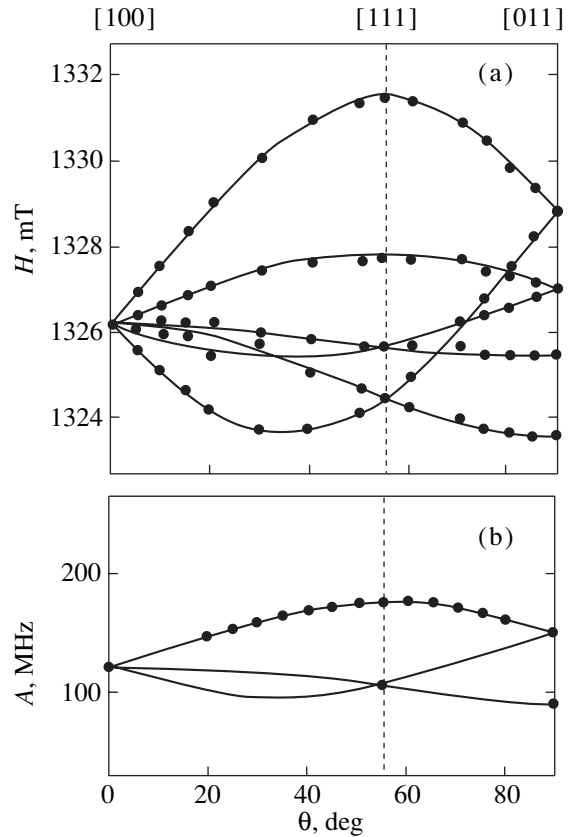

Fig. 2. Angular dependences of (a) Si-$AA17$ spectrum and (b) hyperfine structure. The points correspond to the experiment; the lines represent the results of calculation with the use of constants of g and D tensors. The measurement temperature $T = 77$ K, $\nu_0 = 37.2$ GHz, magnetic field in the plane (011), $g_\parallel$[111] = 2.0028, $g_\perp$ = 2.0106 ($\pm$0.003), $D_\parallel = \pm33.6$ MHz, $D_\perp = \mp16.8$ ($\pm$0.5) MHz, $A_\parallel = 175.0$ ($\pm$1.0) MHz, and $A_\perp = 89.0$ MHz.
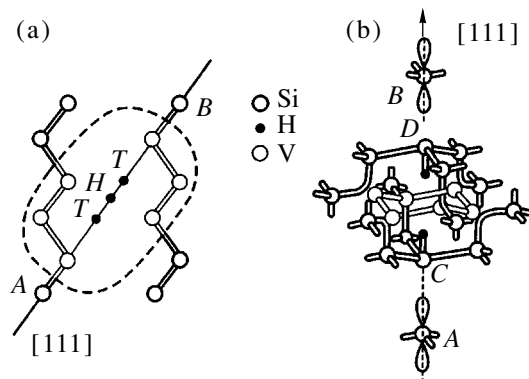

Fig. 3. (a) Arrangement of the pair of dangling bonds at A and B atoms in the $AA17$ defect obtained from the experimental data. The dashed line delineates the region containing the vacancy-type defect, T is the tetrahedral interstice, and H is the hexagonal interstice. (b) Model suggested for the $AA17$ center, which includes two dangling bonds and a hexavacancy centered between them.

(Fig. 3a). Neighboring sites, which are located symmetrically on the $\langle 111 \rangle$ axis, are at distances ~16.5 or ~7.5 Å. It follows from the parameters of the hyperfine interaction with the ^{29}Si nuclei and data on the uniaxial compression of the sample that the internal structure of the defect should be of the vacancy type with the symmetry no lower than D_{3d}. It can be easily seen that the smallest vacancy cluster, which corresponds to the D_{3d} symmetry and given location of dangling bonds (~12 Å along the $\langle 111 \rangle$ axis), is the planar (111) hexavacancy centered between C and D atoms (Fig. 3b).

The question arises as to how the hexavacancy initiates the emergence of dangling bonds on A and B atoms. According to theoretical calculations [30], the hexavacancy introduces no deep levels into the band gap, and no defect, which can be identified as the hexavacancy, has been found to date by the ESR method. The necessary presence of H atoms in the samples in order to form the AA17 defect and the necessity of neutralizing dangling bonds neighboring with A and B atoms may indicate that a pair of H atoms is introduced into the defect. These atoms are arranged along the $\langle 111 \rangle$ axis symmetrically about the center of the defect. As a result, the pair of dangling bonds, which can be detected experimentally, is formed at A and B atoms. In this case, the symmetry D_{3d} of the entire complex is retained in the neutral charge state (Fig. 3b). If this is the case, the absence of the hyperfine structure from ^{1}H nuclei in the AA17 spectrum is indicative of a large distance between dangling bonds and protons. Therefore, it is unlikely that H atoms occupy the sites between $A(B)$ and $C(D)$ atoms. The reason for this is that in this case noticeable hyperfine splitting from protons can be expected, similar to the H atom in the BC position [14]. It is our opinion that the sites on the antibond to C and D atoms are best suited for H atoms (Fig. 3b). Let us make allowance for the relaxation of A and B atoms from the center of the defect as well as the relaxation of C and D atoms to the center of the defect. The large (~91%) contribution of the $3p$ state to the wave function of paramagnetic electrons is indicative of the relaxation of A and B atoms, and the relaxation of C and D atoms is caused by the relaxation of atoms surrounding the hexavacancy. As a result, the distance from the dangling bond to the H atom may be large enough to bring about only a weak dipole interaction of electron spins with the spins of ^{1}H nuclei. With an increase in the H content, the AA17 defect vanishes. This can be explained by the saturation of dangling bonds of the hexavacancy by H atoms, a decrease in the relaxation of C and D atoms, and the disappearance of prerequisites for the formation of dangling bonds on A and B atoms.

It should be noted that the conditions for the formation and the temperature range of thermal stability of the ESR center AA17 are closely similar to the parameters of the luminescence center B_{41} (1.1509 eV) [31]. The luminescence center B_{41} emerges in hydrogenated Si irradiated with electrons or neutrons and is related to the defect with the D_{3d} symmetry, which contains two equivalent H (^{2}H) atoms [32]. Recently, based on experimental data and theoretical cluster calculations *ab initio*, the model of the B_{41} (V_6H_2) defect with the D_{3d} symmetry was suggested [33]. The distinction between the models of the ESR center AA17 (Fig. 3b) and B_{41} center solely consists in the sites of H atoms. In the model of the B_{41} center [33], dangling bonds at A and B atoms are saturated by H atoms, whereas dangling bonds at C and D atoms form a long covalent bond along the [111] axis. Theoretical calculations demonstrate that this configuration has the lowest energy and, for this reason, it is preferential for the luminescence center B_{41} [33]. However, dangling bonds at A and B atoms ($R \approx 12$ Å) should be free for the formation of the spin-triplet state ($S = 1$) of the AA17 defect. On the one hand, H atoms can be located on antibonds at C and D atoms (Fig. 3b). The results of the theoretical calculations [34] demonstrate that the antibonding configuration is unstable and relaxes with the formation of the H_2 molecule, which resides along the [111] axis at the inversion center of the defect. On the other hand, the H_2 molecule itself, which occupies this site, is metastable with a dissociation barrier of 0.23 eV [34]. For this reason, we do not exclude the fact that the model suggested for the ESR center AA17 corresponds to the metastable but frozen state of the defect. This state emerges due to the dissociation of the H_2 molecule residing along the [111] axis at the inversion center of the defect. It is clear that further theoretical and experimental investigations are required for establishing the exact models of the AA17 and B_{41} centers. It is highly probable that their spectra emerge from the same defect.

Thus, the interaction of H atoms with radiation defects leads to the formation of the ESR vacancy complex AA17. It is most probable that the complex consists of a planar {111} hexavacancy and two H atoms.

3.2. Infrared Absorption Bands of the Vacancy Cluster

In the IR absorption spectra of H-implanted Si samples, a large number of absorption bands are observed in the frequency range of stretching Si–H vibrations at 1800–2250 cm^{-1} [10, 12, 35]. It was previously demonstrated that the bands with a frequency <2000 cm^{-1} and >2000 cm^{-1} are related to the Si–H vibrations in the interstitial and vacancy complexes, respectively [36]. Here, we consider the bands at 2107 and 2122 cm^{-1}. The properties of these bands allow one to assume [37] that they are related to the vibrations of the V_6H_{12} complex.

(1) The bands 2107 and 2122 cm^{-1} are located in the frequency range of Si–H vibrations for vacancy clusters.

(2) The thermal behavior of the bands in the temperature range of annealing T_{ann} = 300–600°C is com-

pletely correlated; as a consequence, they belong to the same defect.

(3) The frequencies 2107 and 2122 cm^{-1} are close to the frequencies 2121 and 2145 cm^{-1} of vibrations of the VH$_2$ defect [38]. This should be observed in the case of V_6H$_{12}$, since this complex consists of six defects VH$_2$, whose valence modes interact weakly with each other.

(4) For the same reason, the doublet structure reflects the local symmetry C_{2v} of the defects VH$_2$, which constitute the complex, and corresponds to one symmetric and one asymmetric vibration mode.

(5) The annealing temperature for the bands, 2107 and 2122 cm^{-1} ($T_{ann} > 600°C$), is rather high compared to the annealing temperature for the overwhelming majority of other absorption bands observed. This is in agreement with the theoretically predicted stability of a hexavacancy [30].

(6) Finally, the band intensity depends strongly and anomalously on temperature. Thus, with decreasing the measurement temperature from 300 to 80 K, an increase in absorption for band peaks of Si–H vibrations by a factor of 1.5–2 and a corresponding decrease in the line width are usually observed. In contrast with this, in the case of bands 2107 and 2122 cm^{-1}, the inverse effect is observed, namely, broadening of the bands and a decrease in their intensity. It seems likely that this occurs due to the delocalization of Si–H vibrations because of the scattering of the free carriers by the defect. Scattering by the neutral center increases with increasing mobility of carriers and defect size. For this reason, the vibration delocalization at 2107 and 2122 cm^{-1} with decreasing temperature is indicative of the considerable size of the corresponding complex.

Thus, the data on IR absorption indicate that the H-implanted samples contain extended defects, whose structure involves SiH$_2$ defects. Based on the stability of a hexavacancy and the properties of the bands 2107 and 2122 cm^{-1}, it is possible to relate these bands to vibrations of the Si$_6$H$_{12}$ complex.

3.3. Centers of Selective Capture of Self-Interstitials

Earlier, when investigating the radiation defects in the Si samples treated in the H plasma, it was found that the incorporation of H atoms leads to a variety of effects. These are the suppression of the electrical activity of defects, an increase in the radiation stability of the material, the accelerated thermal annealing of the defects, and others [1–3]. We found one more interesting effect of H atoms, which are incorporated from the plasma, on the behavior of radiation defects, namely, the formation of electrically inactive complexes, which cause the selective capture of self-interstitials.

The spectra of radiation defects in hydrogenated Si samples were investigated by the DLTS technique. It was found that H treatment in the RF plasma at ~150°C leads to an increase in the radiation resistance, which
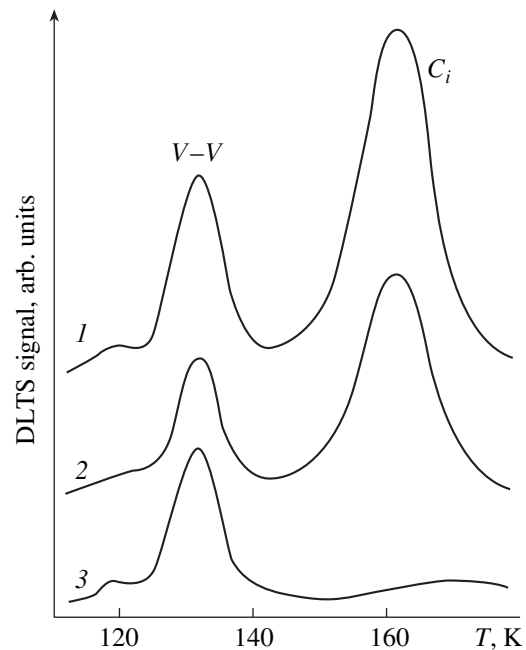

Fig. 4. DLTS spectra for p-type Cz-Si:B samples. (*1*) Reference sample; (*2, 3*) the sample treated in the H plasma (*2*) at 150°C for 2 h and (*3*) at 230°C for 1 h, and then irradiated with α particles at 0°C at a dose of ~5 × 10^9 cm^{-2}.

coincides with the published data [1, 2]. The DLTS spectra of p-Si samples, both reference ones and those preliminarily treated in the plasma and then irradiated with α particles at ~0°C to the dose of ~(0.5–1) × 10^{10} cm^{-2}, are shown in Fig. 4. Two main peaks $H1 = E_v + 0.20$ eV and $H2 = E_v + 0.29$ eV, which correspond to the V–V divacancy and carbon center C$_i$, are shown [39–41]. It can be seen from Fig. 4 that the rate of incorporation of both divacancies and C$_i$ decreases subsequent to H treatment at 150°C, which is explained by the radiation-induced decomposition of complexes (shallow-level acceptor)–H and the passivation of defects by released H atoms. However, an increase in the temperature, at which the preliminary H treatment is carried out to 230°C leads to the sharp distinction of DLTS spectra from reference ones (Fig. 4, curve *3*). Since the B–H complexes are stable to 150–170°C [1, 2], treatment at 230°C does not lead to the passivation of shallow-level acceptors and, as a consequence, the subsequent irradiation is not accompanied by radiation-induced passivation. For this reason, in this case, the rate of incorporation of divacancies is the same as for reference samples. At the same time, the generation of interstitial C$_i$ complexes is sharply suppressed. The subsequent annealing of the samples at room temperature does not lead to the emergence of (C–O)$_i$ centers [39, 42], i.e., the DLTS peak, which corresponds to the level $E_v + 0.38$ eV. The C$_i$ centers are formed due to irradiation according to the Watkins substitution reaction [43] C$_s$ + Si$_i$ ⇒ C$_i$ + Si$_s$. Here, *s* and *i* subscripts are related to the site and interstice residences of the atom.

Thus, this reaction is the pushing of the site of the C_s atom into the interstice by self-interstitial Si_i atoms. A decrease in the reaction yield after treatment in the H plasma is the consequence of a decrease in the content of either C_s or Si_ii. A decrease in the C_s content due to bonding of C atoms by H atoms can be excluded, since the C–H centers are unstable at room temperature [44]. For this reason, a decrease in the content of C_i and $(C–O)_i$ centers for the samples, which are hydrogenated at 230°C, can be associated only with the capture of Si_i atoms by traps formed from H treatment. Thus, the C atoms are the main sinks for self-interstitial atoms at a given temperature for the reference sample. An intense peak in the DLTS spectra, which corresponds to the C_i centers, is observed subsequent to irradiation. In contrast with this, for samples which underwent preliminary plasma treatment at 230°C, most of the self-interstitial atoms are captured by the traps created by plasma treatment. It seems likely that the traps should be of the vacancy type. Since the concentration of charged centers, which is determined from the capacitance of diodes, does not vary during H treatment at 230°C, the traps should be neutral. For point defects, the capture cross section of Si_i atoms by these traps should be comparable to the cross section of capture by C_s atoms. For this reason, the efficiency of the capture means that the trap concentration is at least an order of magnitude higher than the concentration of C_s atoms, i.e., $>10^{17}$ cm^{-3}. In our opinion, it is unlikely that such a high concentration of neutral defects is introduced to the depth of ~1 μm by low-energy plasma treatment. In this case, we must assume that the traps have a large capture cross section of Si_i atoms; i.e., the traps are the extended defects.

The question arises as to the nature of such effective traps of self-interstitial atoms. The defects, similar to extended planar defects formed during H treatment, would act as such traps. The structure of these defects has been inadequately established. However, the experimental data [45–47] and theoretical calculations [48, 49] indicate that, most probably, they are vacancy conglomerates. The vacancies completely occupy two nearest {111} planes, whereas dangling bonds are passivated by H atoms in the H_2^* configuration. Specifically, one H atom occupies the *BC* site at the Si–Si bond, and the second one resides at the *AB* antibond. Due to the vacancy nature, these defects should be the effective traps of interstitial atoms. Although the rate of incorporation of such defects depends on the Fermi level location and is low for *p*-Si, the sensitivity of the DLTS method permits the detecting of their presence. Unfortunately, it is impossible for now to solve the question as to the relation of vacancy defects, which are indirectly observed by DLTS, with structural defects. The latter are detected, as was demonstrated above, by ESR and IR absorption methods as well as by electron microscopy [45, 46].

4. CLUSTERS OF SELF-INTERSTITIAL ATOMS

It is known that the Si samples grown by pulling from the melt (the Czochralski method) contain O atoms in a high concentration. This concentration is approximately equal to the solubility limit of O at the melting point of Si, while the solubility of the impurity decreases with decreasing temperature. For this reason, under typical conditions, the solid solution of O in Si is in the supersaturated state and the possibility of its decomposition is eliminated owing to the low O diffusivity. Because of this, heating to temperatures at which the diffusion of O atoms becomes substantial leads to a variety of phenomena which accompany the process of formation of the second phase [50]. The initial stage O precipitation occurs at temperatures $T_{ann} \approx 350–450°C$ and, specifically, leads to the formation of quenched-in donors, specifically, double He-like quenched-in donors *TDD* [18, 50], which are formed at the initial stages of annealing. The ESR spectrum Si–*NL*8 corresponds to positive charge state TDD^+ of these donors [51, 52]. During prolonged thermal treatment of the samples ($T_{ann} = 400–470°C$), the shallow-level H-like donors *STD* are formed; the ESR spectrum Si–*NL*10 corresponds to these donors [53, 54]. The incorporation of O atoms into the structure of *TDD* and *STD* centers was proved [54, 55] as well as the incorporation of additional Al or H atoms into certain *STD* centers [18, 53]. The structure of quenched-in donors has not been established exactly. However, the process of their formation (growth) is rigorously correlated, as indicated by a high symmetry (C_{2v}) of the *TDD* and *STD* defects.

On incorporation of H atoms by ion implantation [56, 57] or thermal treatment in a hydrogen atmosphere [58, 59] with subsequent irradiation with neutrons, protons, or α particles, the donors are also formed after heat treatment at $T_{ann} = 300–400°C$. Their properties are very close to those of O quenched-in donors.

(1) The annealing (300–400°C, 20 min) of H-implanted Si samples is accompanied by the shift of the Fermi level from the midgap to the conduction band, irrespective of the sample conduction type prior to implantation. The emergence of the ESR spectrum ($S = 1/2$) Si–*AA*1 with the C_{2v} symmetry of a *g* tensor is simultaneously observed. The *AA*1 spectrum was identified with that emerging from the double donor in the positive charge state HDD^+ with the ionization energy of ~160 meV [14, 60]. The parameters of the *g* tensor for *AA*1 (Fig. 5a) are actually identical to those for the ESR spectrum of O quenched-in donors TDD^+ Si–*NL*8 obtained following a ~100 h thermal treatment of the samples [51]. The width of the individual line (~0.5 mT) for the *AA*1 and *NL*8 spectra is also identical. Any hyperfine splitting is absent in both spectra. Finally, both defects are double donors with close ionization energies of electrons. However, we note that the response of the *AA*1 and *NL*8 centers to the uniaxial compression of the sample is substantially different

(Fig. 5b) [52, 59]. This conclusively points to a distinction in the microscopic structure of the centers.

(2) Further annealing (T_{ann} = 350–450°C) leads to the disappearance of the signal of the HDD^+ $AA1$ spectrum and to clearly pronounced n-type conduction with the donor level at $\sim E_c$ – (0.026–0.035) eV [56, 60]. The concentration of shallow-level donors SHD rises with increasing implantation dose and levels off at the level of $\sim 10^{17}$ cm^{-3} for the concentration of incorporated H equal to $\sim 10^{19}$ cm^{-3}. In such samples, the ESR spectrum SHD is observed [14, 61]. It almost coincides with the spectrum Si-NL10 of shallow-level O quenched-in donors STD. At least a fraction of the SHD centers possess bistability properties [60, 61].

(3) In optical measurements, an entire family of H-initiated shallow-level SHD donors is detected. In studies [58, 62], as many as seven various donors were observed. In studies [63, 64], the lines of electron transitions whose spectra are close to those for O quenched-in donors were observed in the ranges of 400–500 and 600–1100 cm^{-1}. The observation of the isotopic shift with the substitution of ^{2}H for H [62] points to the presence of H atoms in the structure of donors.

Thus, the processes which are observed for H-implanted Si during thermal treatment are generally similar to the phenomena occurring at the initial stages of O precipitation and clustering. The electron structure of donors, which are induced by the implantation of H atoms, is almost identical to O quenched-in donors. However, there are significant distinctions. Thus, the highest SHD concentration is formed by annealing at 450°C for 20 min, whereas the samples should be thermally treated for $\sim$100 h in order to form the STD centers. The participation of O atoms in the structure of HDD and SHD centers can be excluded entirely. The reason is that the H-induced clusters with the concentration of $\sim 10^{17}$ cm^{-3} are formed in high-purity Si (FZ-Si) with low O content ($<10^{16}$ cm^{-3}). The response of the $AA1$ and $NL8$ spectra to the uniaxial compression is substantially different [59]. This also proves the different molecular structure of the centers.

Thus, it is firmly established that only the presence of H atoms and intrinsic defects in the sample are necessary for the formation of H-induced donors. Qualitatively, the generation of microclusters of self-interstitials responsible for the formation of shallow-level donors can be described as follows. It is known [10, 36, 38] that H atoms occupy dangling bonds in the H-ion implanted Si or in the irradiated hydrogenated Si. The strongest Si–H bonds are formed with dangling Si bonds in the vicinity of vacancy defects [65]. Some of the Si–H bonds are stable to $\sim$600°C [10, 36]. On heating the sample to 300–400°C, most of the defects become mobile. In this case, hydrogen-free vacancy- and interstitial-type defects are annihilated, whereas the annihilation is inhibited for vacancy defects passivated by H atoms. Thus, on annealing the samples, strong Si–H bonds prevent the annihilation of defects
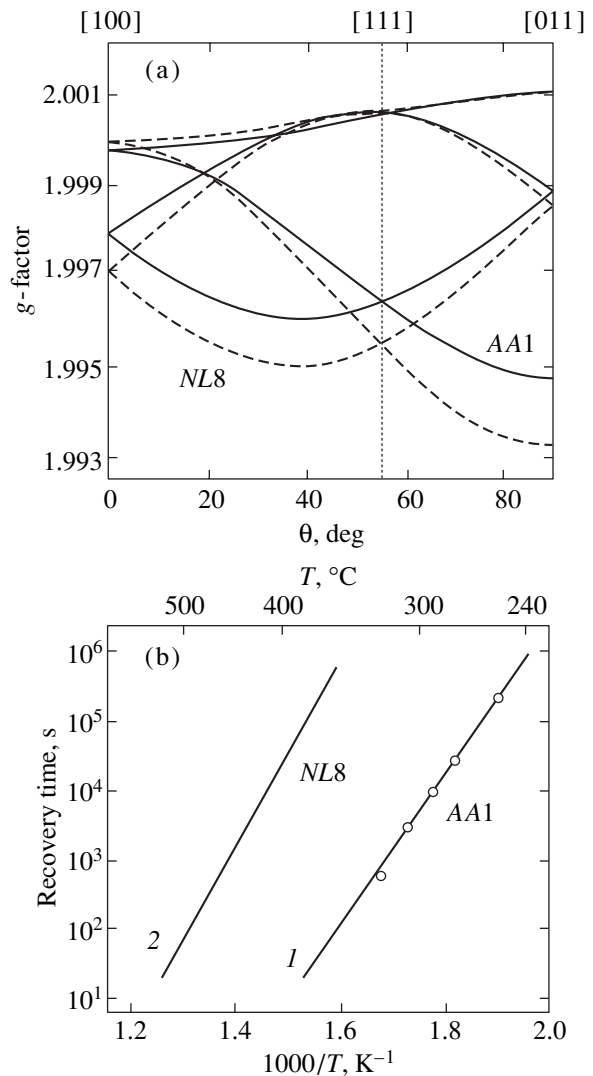

Fig. 5. (a) Angular dependence of the ESR spectrum $AA1$. T = 77 K, magnetic field **H** in the (011) plane, g_1[110] = 1.9947, g_2[111] = 2.0009, and g_3[001] = 1.9997 ($\pm$0.0003). For comparison, the angular dependence for the Si-$NL8$ spectrum is shown [51]. (b) Temperature dependences of the time of atomic reorientation of the centers Si-$NL8$ [52] $\tau^{1/2}$ [s] = 2 × 10^{-16}exp(2.7 eV/kT) and Si-$AA1$ τ [s] = 3 × 10^{-17}exp(2.3 eV/kT).

and thereby stimulate the precipitation and clustering of self-interstitials. In addition, when H atoms occupy dangling bonds, the electrical activity of these bonds is inhibited.

The properties of donors induced by the implantation of H atoms point to their emergence from the interstitial-type defects. Thus, no hyperfine interactions, which are characteristic of the dangling bond in the vicinity of vacancy defects in Si, are observed in either the $AA1$ spectrum or in the $NL8$ spectrum. In addition, the energy of atomic reorientation of the defect is very large (2.3 eV) (Fig. 5) and significantly exceeds the reorientation energy for all known vacancy defects.
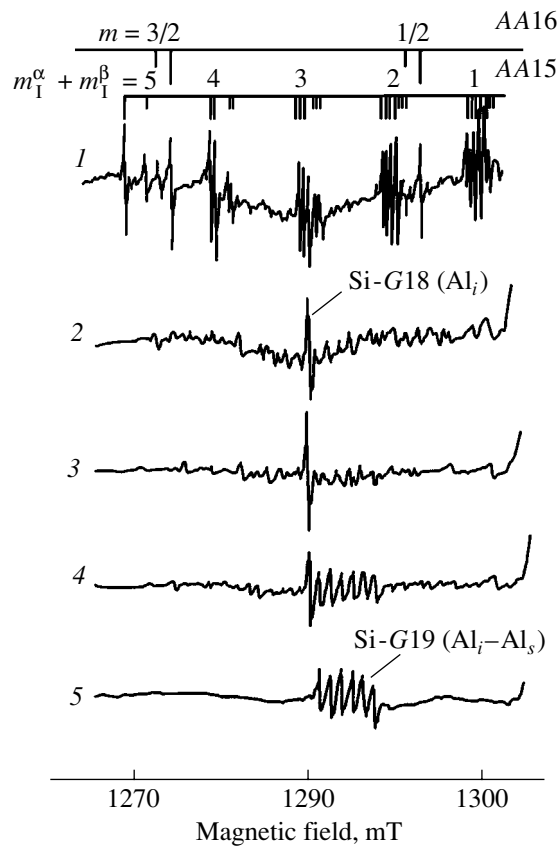
Fig. 6. ESR spectra of the FZ-Si:Al samples, which were H-implanted at 80 K at a dose of (*1*) 3×10^{15} and (*2–5*) 1×10^{16} cm^{-2} and then annealed for 10 min at temperature (*1*) 180 K, (*2*) 195 K, (*3*) 100°C, (*4*) 160°C, and (*5*) 185°C. On the side of weak magnetic field, 5 of 11 groups of the *AA*15 spectrum, 2 of 6 groups of the *AA*16 spectrum, 1 of 6 lines of the *G*18 spectrum, and 1 of 6 groups of the *G*19 spectrum are shown. The complex ESR spectrum of Al clusters is also shown. The measurement temperature was *T* = 77 K, the frequency was 37.2 GHz, and the magnetic field was **H** ∥ ⟨100⟩.

A high frequency factor of atomic reorientation (~10^{16} s^{-1}), which is characteristic of extended defects, considerably exceeds the frequency of local vibrations (~10^{13} s^{-1}). The data of piezospectroscopic investigations demonstrate that, compared to the conventional Si lattice, the structure of the *AA*1 defect is more closely packed along the [001] axis as well as along [110] axis. The comparison of the components of the piezospectroscopic tensor with those for known defects is also indicative of the interstitial nature of the cluster [25, 26].

Thus, we have drawn the conclusion on the formation of clusters of interstitial-type intrinsic defects in hydrogenated Si, which contains radiation defects, in the course of the thermal treatment of the sample. The electronic structure of these defects, which reflects their internal structure, is very close to the structure of known O quenched-in donors. However, the O impurity does not participate in their formation, whereas the role of H atoms is the determining one. The data of

piezospectroscopic investigations and high symmetry (C_{2v}) of the centers *HDD AA*1 are indicative of coordinated cluster growth in the course of precipitation of self-interstitials. Such clusters apparently consist of a chain along the ⟨011⟩ direction [59] or a group in the {001} plane [66, 67] of four self-interstitials, which are split along the ⟨001⟩ direction. Both models of the cluster are consistent with the symmetry of the center and with the data of piezospectroscopic measurements. Hydrogen atoms are incorporated in clusters, at least in those which create shallow-level donor states *SHD* [62], and also act as catalysts in the formation of clusters from smaller defects.

5. IMPURITY CLUSTERS OF DEFECTS

As noted above, the solution of the O impurity in Si, which was grown by pulling from the melt, is supersaturated. Oxygen precipitation, which occurs at temperatures above 450°C and up to 1200°C, has been extensively studied for a long time. It was found that the presence of H atoms considerably enhances O diffusivity (by a factor of 200 at 300°C [16–18]) and promotes the formation of quenched-in donors as well as O dimers [18, 68]. Theoretical calculations [19, 20] are also indicative of a decrease in the energy barrier for the migration of interstitial O atoms in the presence of H atoms in the vicinity of the defect. Thus, the O precipitates in the hydrogenated Si are formed more rapidly; however, their structure and properties are similar to those in the absence of hydrogen.

Impurity clusters, which are different from those known previously, are formed due to H-enhanced migration of Al atoms to the hydrogenated Al-doped Si. It is known that interstitial Al$_i$ atoms, which are formed by irradiation, migrate at 200°C [43]. In the conditions of the injection of minority carriers, the Al$_i$ atoms migrate at room temperature [69]. The detection of a new ESR Si-*AA*15 spectrum in FZ-Si:(Al, H) samples was quite unexpected [70]. This spectrum (Fig. 6, curve *1*) was observed subsequent to the low-temperature (80 K) implantation of H into the FZ-Si:Al samples. It was also observed in the samples subjected to high-temperature (1250°C) treatment in water vapor with subsequent irradiation with protons or α particles at 80 K with heating to 180–200 K. The spectrum vanished following short-term heating to room temperature. The hyperfine structure of the *AA*15 spectrum is unambiguously indicative of the presence of defects including two almost equivalent atoms with the nuclear spin $I = 5/2$. The ^{27}Al nuclei are the only ones which can be such nuclei in FZ-Si:Al samples. Although the Al–Al pairs can be present even in as-grown samples for the Al concentration used (~10^{17} cm^{-1}), their concentration cannot be high relative to the total Al concentration. On the other hand, the estimations demonstrate that the density of *AA*15 defects is of the same order of magnitude as the Al concentration; i.e., a substantial fraction of shallow-level acceptors participates

in the pair formation. For this reason, the pairs can be formed only by means of the low-temperature migration of Al atoms. It is not improbable that the migration occurs during the irradiation at ~80 K, whereas heating to 200 K leads to the emergence of the ESR spectrum. However, it is more probable that the migration occurs at 180–200 K, when the Si-AA15 spectrum emerges. The reason is that the H atoms, which occupy the BC sites following implantation, become mobile at these temperatures [14].

The necessity of the presence of H for the formation of the Al–Al pairs (AA15 center) indicates that Al atoms can migrate in the form of the (Al–H)$_i$ complex. The ESR center AA16 can be considered as a good candidate for the role of the (Al–H)$_i$ complex, which is mobile at 200 K. This center emerges simultaneously with the AA15 center but has a narrow thermal range of stability [71]. The hyperfine structure of the Si-AA16 spectrum suggests that an atom with the nuclear spin $I = 5/2$ is incorporated into the structure of the defect. This atom resides close to the point with T_d symmetry and undergoes trigonal distortion. The Al atom, which occupies the T_d interstice and has the charge state (++), can be a possible model of the AA16 defect (Fig. 7a). In this case, trigonal distortion can be induced by the H$^-$ atom, which occupies the neighboring T_d interstice. It is known from theoretical calculations [72] that the Al$_i$ atom migrates by hopping between tetragonal and hexagonal interstices. The presence of the H atom can decrease the energy-barrier height for passage through the hexagonal interstice and can lead to the low-temperature mobility of the (Al–H)$_i$ complex. This explanation of the H-enhanced migration of Al atoms necessitates theoretical calculations.

The concentration of Al–Al pairs (ESR centers AA15) increases with an increase in the implantation dose of H in the range from 1×10^{15} to 5×10^{15} cm^{-2}. However, for higher H implantation doses, $~1 \times 10^{16}$ cm^{-2}, which correspond to the bulk Al concentration of $~2 \times 10^{18}$ cm^{-3}, or for repetitive implantation of the samples containing the AA15 defects, the intensity of the AA15 spectrum considerably decreases or the spectrum is not formed at all. After the low-temperature implantation at 80 K and subsequent heating of the samples to 195 K, the complex ESR spectrum is formed (Fig. 6, curve 2). This spectrum is observed in the magnetic field range of 1270–1310 mT at a frequency of 37 GHz. The centroid of the spectrum lies in the region of the g factor values of ~2.04. After short-term annealing at room temperature, the spectrum vanishes. Further annealing leads to the emergence of a new complex center (Fig. 6, curves $3–5$), whose lines are located in a wider range of magnetic fields. The spectrum undergoes continuous modification up to the annealing temperature of ~200°C, at which it vanishes. Simultaneously, the Al$_i$ (Si-G18) center is annealed out and the ESR spectrum Si-G19 is formed. This spectrum can be identified with that associated with the Al$_i$–Al$_s$ defect [73]. The general prop-
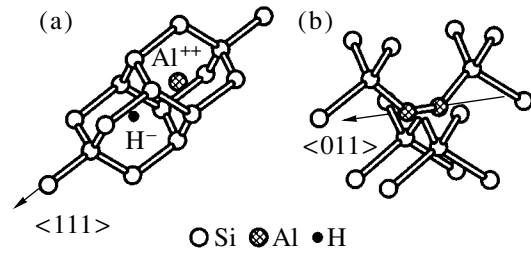

Fig. 7. Models suggested for defects (a) AA16 and (b) AA15.

erty of the complex spectra observed is the absence of any pronounced structure (as, for example, for AA15, G18, G19). In addition, they are detected only if the magnetic field is oriented along the crystallographic direction $\langle 001 \rangle$. With the deviation of 2–3° from the $\langle 001 \rangle$ direction, the spectra were broadened rapidly; in other main directions, the spectra were undetectable. For this reason, the symmetry of the spectra was not determined. However, we may conclude that it is low.

The properties of defects, which determine the emergence of complex ESR spectra for H-implanted FZ-Si:Al, make it possible to assume that these defects are clusters which contain more than two Al atoms. Actually, the solid solution of Al in Si for the concentration of $~10^{17}$ cm^{-3} at a temperature close to 295 K is supersaturated. Its decomposition is limited by low Al diffusivity. For this reason, the prerequisites for the formation of impurity interstitials of Al-enriched microprecipitates arise with the formation of mobile (Al–H)$_i$ defects. Such precipitates should have a low symmetry. In addition, they should be stable until the Al$_i$ atoms entering the cluster become mobile. The characteristics expected for such clusters are consistent with the properties of the defects observed.

6. CONCLUSION

The presence of H impurities in crystalline Si significantly affects the character of diffusion and migration of atoms of other impurities and defects, and leads to the clustering of vacancies, self-interstitial atoms, and impurity atoms.

Vacancy clusters observed by the ESR method are characterized by the presence of two equivalent Si atoms with dangling bonds. These atoms are arranged along the $\langle 111 \rangle$ axis at a distance of ~12 Å. The planar {111} hexavacancy is located between these atoms. The data on the IR absorption are indicative of the presence of extended defects consisting of several SiH$_2$ groups. The most plausible model of these defects is the completely passivated Si$_6$H$_{12}$ hexavacancy. The results of DLTS investigations indirectly demonstrate the presence of extended traps for self-interstitial atoms in hydrogenated Si samples. These can be planar defects (platelets), which were observed previously using electron microscopy and Raman spectroscopy [45–47]. It is

not improbable that the same defect is detected by various methods at various stages of detect formation. Specifically, for relatively low H concentrations, only the partially passivated vacancy defect (*AA*17) is observed; with increasing H concentration, the defect is passivated completely; and extended vacancy clusters are formed for high concentrations of H atoms and defects. Thus, the vacancy clusters, which are observed by the ESR and IR spectroscopies, can be the precursors or fragments of giant planar defects [74, 75].

In the course of the precipitation of intrinsic radiation defects at 300–500°C in hydrogenated Si, the formation of clusters of self-interstitial-type defects is also observed. Their electronic structure, which reflects the internal structure, is close to the structure of known O quenched-in donors. However, the O impurity is not involved in the formation of these defects, whereas the role of H is the determining one. Hydrogen atoms are incorporated into clusters (at least into those introducing the shallow-level donor states *SHD*) and act as the catalyst in the formation of clusters from smaller defects.

The presence of H atoms enhances the diffusion of some impurities in Si. The H-enhanced O precipitation was reported previously. Aluminum in Si is another impurity whose diffusion is enhanced in the presence of H atoms. However, in this case, the presence of radiation defects is also necessary. The specific feature is the low temperature (~180–200 K) at which the enhanced diffusion is observed. As a result of such diffusion, the supersaturated solid solution of Al in Si decomposes with the formation of Al-enriched precipitates. The formation of such nanoclusters can spatially modulate the sample conduction, which may be used in practice.

Thus, highly diverse behavior of H in Si is observed. On the formation of the supersaturated H solution in the course of low-temperature proton implantation, an isolated H atom can be observed. This atom begins to move over the lattice even at ~200 K and to interact with impurity atoms and radiation defects. As a result, H precipitates emerge in the form of passivated complexes. With increasing temperature, the H precipitation continues, the unstable configuration begins to vanish, and H atoms find the sites for firm bonding to the defects with higher thermal stability. In this case, for example, hydrogen first partially and then completely passivates the hexavacancy or forms the interstitial donor centers. At high temperatures, H precipitation is completed by the formation of molecules which agglomerate and give rise to voids. The voids grow and can lead to disruption of the sample at ~700–800°C. This effect forms the basis of "Smart" silicon-on-insulator technology, which has been developed recently [76].

REFERENCES

1. *Hydrogen in Semiconductors*, Ed. by J. I. Pancove and N. M. Johnson (Academic, San Diego, 1991).

2. S. J. Pearton, J. W. Corbett, and M. Stavola, *Hydrogen in Crystalline Semiconductors* (Springer-Verlag, Berlin, 1992).

3. *Hydrogen in Semiconductors II*, Ed. by N. H. Nickel (Academic, San Diego, 1999).

4. S. J. Uftring, M. Stavola, P. M. Williams, and G. D. Watkins, Phys. Rev. B **51**, 9612 (1995).

5. J. Weber, in *Proceedings of the 24th International Conference on Physics of Semiconductors*, Ed. by D. Gershoni (World Scientific, Singapore, 1999), p. 209.

6. V. P. Markevich, M. Suezawa, and K. Sumino, Mater. Sci. Forum **196–201**, 915 (1995).

7. R. E. Pritchard, M. J. Ashwin, J. H. Tucker, *et al.*, Phys. Rev. B **56**, 13118 (1997).

8. R. E. Pritchard, M. J. Ashwin, J. H. Tucker, *et al.,* Semicond. Sci. Technol. **12**, 1404 (1997).

9. I. S. Zevenbergen, T. Gregorkiewicz, and C. A. J. Ammerlaan, Phys. Rev. B **51**, 16746 (1995).

10. H. J. Stein, J. Electron. Mater. **4**, 159 (1975).

11. Yu. V. Gorelkinskii, Kh. A. Abdullin, and B. N. Mukashev, Physica B (Amsterdam) **273–274**, 171 (1999).

12. B. N. Mukashev, S. Zh. Tokmoldin, M. F. Tamendarov, and V. V. Frolov, Physica B (Amsterdam) **170**, 545 (1991).

13. M. Suezawa, Physica B (Amsterdam) **273–274**, 224 (1999).

14. Yu. V. Gorelkinskii and N. N. Nevinnyi, Physica B (Amsterdam) **170**, 155 (1991).

15. N. M. Johnson, C. Herring, and C. G. Van de Walle, Phys. Rev. Lett. **73**, 130 (1994).

16. R. Murray, Physica B (Amsterdam) **170**, 115 (1991).

17. M. J. Binns, C. A. Londos, S. A. McQuaid, *et al.*, J. Mater. Sci.: Mater. Electron. **7**, 347 (1996).

18. R. C. Newman, J. Phys.: Condens. Matter **12**, R335 (2000).

19. R. Jones, S. Öberg, and A. Umerski, Mater. Sci. Forum **83–87**, 551 (1992).

20. S. K. Estreicher, Phys. Rev. B **41**, 9886 (1990).

21. Y. H. Lee, Y. M. Kim, and J. W. Corbett, Radiat. Eff. **15**, 77 (1972).

22. Y. H. Lee, N. N. Gerasimenko, and J. W. Corbett, Phys. Rev. B **14**, 4506 (1976).

23. Y. H. Lee and J. W. Corbett, Phys. Rev. **8**, 2810 (1974).

24. Y. H. Lee and J. W. Corbett, Phys. Rev. **13**, 2653 (1976).

25. G. D. Watkins and J. W. Corbett, Phys. Rev. **134**, A1359 (1964).

26. G. D. Watkins and J. W. Corbett, Phys. Rev. **138**, A543 (1965).

27. K. L. Brower, Radiat. Eff. **8**, 213 (1971).

28. A. A. Kaplyanskiĭ, Opt. Spektrosk. **16**, 329 (1964).

29. G. D. Watkins, Phys. Rev. B **12**, 5824 (1975).

30. J. L. Hastings, S. K. Estreicher, and P. A. Fedders, Phys. Rev. B **56**, 10215 (1997).

31. A. S. Kaminskii, E. V. Lavrov, V. A. Karasyuk, and M. L. W. Thewalt, Phys. Rev. B **50**, 7338 (1994).

32. A. N. Safonov and E. C. Lightowlers, Mater. Sci. Eng. B **58**, 39 (1999).

33. B. Hourahine, R. Jones, A. N. Safonov, *et al.*, Physica B (Amsterdam) **273–274**, 176 (1999).

34. B. Hourahine, R. Jones, A. N. Safonov, *et al.*, Phys. Rev. B **61**, 12594 (2000).

35. N. N. Gerasimenko, M. Rolle, L. J. Cheng, *et al.*, Phys. Status Solidi B **90**, 689 (1978).

36. B. N. Mukashev, M. F. Tamendarov, and S. Zh. Tokmoldin, Mater. Sci. Forum **38–41**, 1039 (1989).

37. S. Zh. Tokmoldin, B. N. Mukashev, Kh. A. Abdullin, and Yu. V. Gorelkinskii, Physica B (Amsterdam) **273–274**, 204 (1999).

38. B. B. Nielsen, L. Hoffmann, and M. Budde, Mater. Sci. Eng. B **36**, 259 (1996).

39. L. C. Kimerling, Inst. Phys. Conf. Ser. **31**, 221 (1977).

40. Y. H. Lee, K. L. Wang, A. Jaworowski, *et al.*, Phys. Status Solidi A **57,** 697 (1980).

41. L. C. Kimerling, M. J. Asom, J. L. Benton, *et al.*, Mater. Sci. Forum **38–41**, 141 (1989).

42. P. V. Kuchinskiĭ, V. M. Lomako, and A. P. Petrunin, Fiz. Tekh. Poluprovodn. (Leningrad) **23**, 1625 (1989) [Sov. Phys. Semicond. **23**, 1006 (1989)].

43. G. D. Watkins, Mater. Sci. Forum **143–147**, 9 (1994).

44. A. Endrös, W. Krühler, and J. Grabmaier, Mater. Sci. Eng. B **4**, 35 (1989).

45. N. M. Johnson, F. A. Ponce, R. A. Street, and R. J. Nemanich, Phys. Rev. B **35**, 4166 (1987).

46. S. Muto, S. Takeda, and M. Hirata, Mater. Sci. Forum **143–147**, 897 (1994).

47. J. N. Heyman, J. W. Ager, E. E. Haller, *et al.*, Phys. Rev. B **45**, 13363 (1992).

48. Ch. G. Van de Walle, P. J. H. Denteneer, Y. Bar-Yam, and S. T. Pantelides, Phys. Rev. B **39**, 10791 (1989).

49. S. B. Zhang and W. B. Jackson, Phys. Rev. B **43**, 12142 (1991).

50. *Early Stages of Oxygen Precipitation in Silicon*, Ed. by R. Jones (Kluwer, Dordrecht, 1996).

51. S. H. Muller, M. Sprenger, E. G. Sieverts, and C. A. J. Ammerlaan, Solid State Commun. **25**, 987 (1978).

52. J. M. Trombetta, G. D. Watkins, J. Hage, and P. Wagner, J. Appl. Phys. **81**, 1109 (1997).

53. R. C. Newman, J. H. Tucker, N. G. Semaltianos, *et al.*, Phys. Rev. B **54**, R6803 (1996).

54. T. Gregorkiewicz, D. A. van Wezep, H. H. P. Th. Bekman, and C. A. J. Ammerlaan, Phys. Rev. B **35**, 3810 (1987).

55. J. Michel, J. R. Niklas, and J.-M. Spaeth, Phys. Rev. B **40**, 1732 (1989).

56. Y. Ohmura, Y. Zohta, and M. Kanazawa, Phys. Status Solidi A **15**, 93 (1973).

57. Yu. V. Gorelkinskii, V. O. Sigle, and Zh. S. Takibaev, Phys. Status Solidi A **22**, K55 (1974).

58. J. Hartung and J. Weber, J. Appl. Phys. **77** (1), 118 (1995).

59. Yu. V. Gorelkinskii, N. N. Nevinnyi, and Kh. A. Abdullin, J. Appl. Phys. **84**, 4847 (1998).

60. Yu. V. Gorelkinskii and N. N. Nevinnyi, Nucl. Instrum. Methods **209/210**, 677 (1983).

61. Yu. V. Gorelkinskii, Semicond. Semimet. **61**, 25 (1999).

62. J. Hartung and J. Weber, Phys. Rev. B **48**, 14161 (1993).

63. S. Zh. Tokmoldin, B. N. Mukashev, Kh. A. Abdullin, *et al.*, Mater. Sci. Eng. B **71**, 263 (2000).

64. R. C. Newman, M. J. Ashwin, R. E. Pritchard, and J. H. Tucker, Phys. Status Solidi B **210**, 519 (1998).

65. Ch. G. Van de Walle and R. A. Street, Phys. Rev. B **49**, 14766 (1994).

66. M. Kohyama and S. Takeda, Phys. Rev. B **60** (11), 8075 (1999).

67. B. J. Coomer, J. P. Goss, R. Jones, *et al.*, Physica B (Amsterdam) **273–274**, 505 (1999).

68. V. P. Markevich, L. I. Murin, J. L. Lindström, and M. Suezawa, Fiz. Tekh. Poluprovodn. (St. Petersburg) **34** (9), 1039 (2000) [Semiconductors **34**, 998 (2000)].

69. J. R. Troxell, A. P. Chatterjee, G. D. Watkins, and L. C. Kimerling, Phys. Rev. B **19**, 5336 (1979).

70. Kh. A. Abdullin, B. N. Mukashev, and Yu. V. Gorelkinskii, Appl. Phys. Lett. **71**, 1703 (1997).

71. Yu. V. Gorelkinskiĭ, B. N. Mukashev, and Kh. A. Abdullin, Fiz. Tekh. Poluprovodn. (St. Petersburg) **32**, 421 (1998) [Semiconductors **32**, 375 (1998)].

72. G. A. Baraff and M. Schlüter, Phys. Rev. B **30**, 3460 (1984).

73. G. D. Watkins, in *Radiation Damage in Semiconductors: Proceedings of the Radiation Damage Symposium, Paris, 1964* (Academic, New York, 1965), p. 97.

74. J. N. Heyman, J. W. Ager, E. E. Haller, *et al.*, Phys. Rev. B **45**, 13363 (1992).

75. N. H. Nickel, G. B. Anderson, N. M. Johnson, and J. Walker, Phys. Rev. B **62**, 8012 (2000).

76. M. Bruel, Electron. Lett. **31**, 1201 (1995).

Translated by N. Korovin

Rapid Thermal Annealing of Gallium Arsenide Implanted with Sulfur Ions

V. M. Ardyshev and M. V. Ardyshev*

Kuznetsov Siberian Physicotechnical Institute at Tomsk State University, pl. Revolyutsii 1, Tomsk, 634050 Russia
*e-mail: detector@mail.tomsknet.ru
Submitted July 30, 2001; accepted for publication October 13, 2001

Abstract—Sulfur ions were implanted into semi-insulating GaAs. A SiO_2 film was deposited by either of two methods onto the implanted surface. The samples were then subjected to either rapid thermal annealing (using halogen lamps) for 10–12 s at 805°C or to conventional thermal annealing for 30 min at 800°C. The content of GaAs components in the film was determined from the spectra of Rutherford backscattering. The electron-concentration profiles were plotted using the measurements of the capacitance–voltage characteristics. It is shown that sulfur diffuses in two directions, i.e., towards the surface and into the GaAs bulk. The former process is stimulated by vacancies formed near the semiconductor surface during the deposition of SiO_2. The coefficients of the "volume" diffusion of S and of the diffusion of S towards the surface are two orders of magnitude larger upon rapid thermal annealing than upon conventional thermal annealing, with the degree of S activation also being higher. © 2002 MAIK "Nauka/Interperiodica".

1. INTRODUCTION

It has been shown [1, 2] that the rapid halogen-lamp or electron-beam anneals of GaAs implanted with an amphoteric ^{28}S i impurity induces a diffusive redistribution of silicon and an increase in the degree of the electrical activation of silicon; these effects are more pronounced than in the case of conventional thermal annealing (CTA). The effect of conditions at the interface between the semiconductor and the surrounding medium on the above processes has been reported [3]. It is of interest to study these phenomena for impurities of different chemical nature, for example, for ^{32}S. Among donor impurities in GaAs, ^{32}S features the highest diffusive mobility in the course of CTA, the highest sensitivity to physicochemical conditions at the insulator–semiconductor interface, and a comparatively low degree of electrical activation. In this context, we report in this paper the results of studying the behavior of S implanted into GaAs when the ion-implanted samples are subjected to rapid thermal annealing (RTA).

2. EXPERIMENTAL

In our experiments, we used the wafers of single-crystal semi-insulating GaAs, which was doped with Cr to a concentration of 10^{16} cm^{-3} and had a resistivity of $>10^7$ Ω cm, a dislocation density of $<8 \times 10^4$ cm^{-2}, and an electron mobility of ~4300 cm^2 V^{-1} s^{-1} at 300 K. The surface of the wafers was oriented parallel to the (100) plane.

The samples were treated in the $H_2SO_4 : H_2O_2 : H_2O = 1 : 1 : 100$ etchant prior to implantation. The ^{32}S ions were implanted with an energy of 100 keV and a dose of 2×10^{13} cm^{-2} at a temperature of 150°C. We took measures to eliminate the axial and planar channeling during implantation [1]. Prior to annealing, the samples were divided into two groups. The SiO_2 film was formed at 400°C by plasma-chemical deposition (henceforth, SiO_2-PCD) on the surface of wafers of the first group (wafers 1). The SiO_2 film was grown on the surface of wafers II using a film-forming solution doped with samarium to ~8 at. % [4] (henceforth, SiO_2:Sm). The insulator-film thickness was 0.1 μm for performing the RTA and 0.3 μm in the case of CTA. Rapid thermal annealing at 805°C was carried out for 10–12 s using an Impul's-5 setup equipped with halogen lamps; during annealing, the samples were exposed to a flow of nitrogen with the dew point no higher than –65°C. Conventional thermal annealing was performed under hydrogen flow for 30 min at a temperature of 800°C in a resistance furnace.

Before and after annealing, we measured the content of the GaAs components in the SiO_2 films using Rutherford backscattering spectroscopy [5]. After removal of the insulator film, we determined the electron-concentration profiles from the measurements of the capacitance–voltage (C–V) characteristics using the Schottky barriers, which were 100×100 μm^2 in area and were surrounded by ohmic contacts. As the metallic coating in the fabrication of the Schottky barriers and ohmic contacts, we used an AuGe + 14%Ni alloy deposited by vacuum evaporation.

3. RESULTS AND DISCUSSION

In Fig. 1, we show the electron-concentration profiles $N(x)$ in the ion-implanted GaAs:S layers after RTA (in Fig. 1a, the protective insulator was SiO_2-PCD, henceforth, this RTA is referred to as RTA-1; in Fig. 1b, the protective insulator was SiO_2:Sm, henceforth, this RTA is referred to as RTA-2), after CTA (see Fig. 1c; the protective insulator was SiO_2-PCD), and also the implanted-sulfur concentration profile calculated using the Lindhard–Scharff–Sciött theory [6].

It can be seen that a dip is formed in the electron-concentration profile at a depth near R_p (the projected range of ^{32}S ions) as a result of RTA-1. The shape of the curve $N(x)$ indicates that this dip is caused by sulfur diffusion in two directions, i.e., towards the surface and into the GaAs bulk. In the case of diffusion into the bulk, a broadening of the profile relative to the calculated profile is observed, although this broadening is slight. In fact, the same broadening of $N(x)$ also occurs as a result of RTA-2; however, in this case, there is no "outward" diffusion of sulfur, which is observed as a result of RTA-1. The largest broadening is observed after the CTA, although, in this case, the dip in the dependence $N(x)$ is poorly pronounced; nevertheless, an increase in the electron concentration indicates, as in the case of RTA-1, that there are two, oppositely directed diffusion fluxes.

The effect of the insulator–GaAs interface on redistribution of S as a result of conventional thermal annealing has been reported in many publications (see, for example, [7, 8]). In particular, the surface-directed diffusion of S has been related [8] to the interaction of S with excess vacancies in the vicinity of the interface, which are formed during diffusion of Ga (or As) atoms from the semiconductor to the insulator film, with this process depending on the composition of the insulator and the method used for its deposition.

In Table 1, we list data on the content of Ga (As) atoms in the insulators before and after RTA and CTA; these data were obtained from the Rutherford backscattering spectra. It can be seen that, immediately after formation of an SiO_2-PCD film, the content of Ga (As) atoms is considerable in this film. In the SiO_2:Sm films, the Ga (As) atoms were not detected using Rutherford backscattering spectroscopy. CTA treatment enhanced the concentration of GaAs components in the SiO_2-PCD insulator; RTA did not affect this concentration. Since the escape of Ga (As) atoms is accompanied by the formation of vacancies (V) in the corresponding sublattices, we may conclude that diffusion of sulfur during RTA towards the surface is caused by a high concentration of these vacancies in the vicinity of the SiO_2–GaAs interface. We note that these vacancies are formed during the deposition of the SiO_2-PCD film.

It follows from experimental data that the concentration profile of sulfur is governed by the dependence
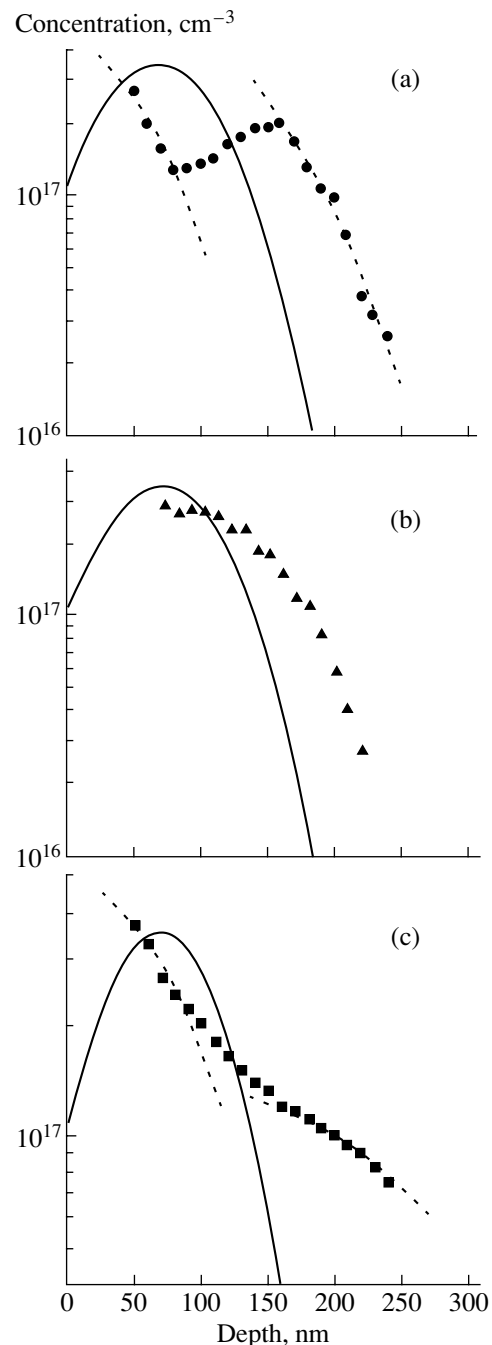

Fig. 1. Concentration profile of sulfur ions after implantation (100 keV, 2×10^{13} cm^{-2}); the profile was calculated using the theory [6] (the solid lines). Experimental electron-concentration profiles $N(x)$ (points) and the results of processing the experimental curves using formula (1) (dotted lines) are also shown. Annealing: (a) RTA-1 (with SiO_2-PCD protective insulator); (b) RTA-2 (with SiO_2:Sm protective insulator); and (c) CTA (with SiO_2-PCD protective insulator).

$[V](x, t)$ at the depths $x < R_p$ and by the sulfur diffusion into the GaAs bulk for $x > R_p$. In the latter case, the necessary condition is an excess of the sulfur diffusion coefficient over the diffusion coefficient of vacancies

Table 1. Concentrations of Ga(As) atoms in SiO_2 before and after rapid thermal annealing (RTA) and conventional thermal annealing (CTA)

Insulator	Concentration of Ga(As) atoms, at. %		
	Before annealing	CTA (800°C/30 min)	RTA (805°C/12 s)
SiO_2–PCD	0.73–0.79	0.86	0.75
SiO_2:Sm	At the background level	No data	At the background level

Table 2. Parameters of electron-concentration profiles after rapid thermal annealing (RTA) and conventional thermal annealing (CTA) of GaAs:S with the surface protected by SiO_2 film

Type of annealing	$\eta_1 N_{V_0}$, cm^{-2}	D_1, cm^2 s^{-1}	η_2, %	D_2, cm^2 s^{-1}
CTA	4.1×10^{20}	1.3×10^{-14}	27.5	6.3×10^{-14}
RTA-1	2.7×10^{20}	1.2×10^{-12}	44.0	1.3×10^{-12}

(these are the vacancies the interaction with which imparts donor properties to sulfur). Taking into account the above points and assuming that the diffusion of vacancies during RTA is described in terms of diffusion from a thin layer with surface concentration N_{V0}, whereas the sulfur diffusion corresponds to the model of diffusion suggested in [9, 10], the final electron-concentration distribution can be represented as

$$N(x) = \frac{\eta_1 N_{V0}}{\sqrt{\pi D_1 t}} \exp\left(-\frac{x^2}{4D_1 t}\right) + \frac{\eta_2 F}{\sqrt{2\pi(\Delta R_p^2 + 4D_2 t)}}$$
$$\times \exp\left(-\frac{(x - R_p)^2}{2\Delta R_p^2 + 4D_2 t}\right), \quad (1)$$

where η and D are the degree of electrical activation and the diffusion coefficient of sulfur, respectively; F is the implantation dose; ΔR_p is the standard deviation of the projected range; and t is the annealing duration. Subscripts 1 and 2 correspond to the diffusion fluxes of sulfur towards the surface and into the GaAs bulk, respectively.

In Figs. 1a and 1c, we also show the results of processing the experimental curves $N(x)$ obtained after RTA-1 and CTA, respectively, using formula (1); in Table 2, the parameters appearing in (1) and ensuring the best fit of calculated and experimental dependences $N(x)$ are listed.

It follows from Table 2 that the larger diffusion coefficients D_1 and D_2 and higher degrees of electrical activation of S in GaAs η_1 and η_2 are attained by RTA rather than by CTA. The values of D_2 are approximately

the same as for Si diffusion from an implanted GaAs layer subjected to RTA [1, 2]. It can also be seen from Fig. 1 that, in the region of depths down to $x \approx 100$ nm, which corresponds to the impurity diffusion towards the surface, a discrepancy between the experimental data is observed; this discrepancy is more pronounced for RTA than for CTA. The cause of this effect may be related to thermoelastic stresses that exist in the surface layers of the semiconductor and immobilize the impurity. These stresses originate owing to a difference between the thermal-expansion coefficients in the film and in GaAs and are not accounted for in expression (1). In the case of comparatively long CTA, the stresses have time to partially relax, whereas they are maximal for short-term RTA. The descrepancy between the calculated and experimental curves in the region of the dip can be explained by the fact that the term accounting analytically for the escape of the impurity to the region of the high vacancy concentration [9] is not included in expression (1); this escape is rapid in the case of RTA (a pronounced dip) and slow in the case of CTA (a poorly pronounced dip).

4. CONCLUSION

We ascertained that the rapid thermal annealing of GaAs implanted with S induces a diffusion-related redistribution of the impurity towards the surface and into the semiconductor bulk. The former process is caused by the interaction of sulfur with vacancies formed in GaAs during the deposition of the SiO_2 film onto the surface, whereas the latter process is related to the enhanced sulfur diffusion (as in the case of silicon impurity, see [1, 2]). In both cases, the diffusion coefficient is two orders of magnitude larger during rapid thermal annealing than during conventional thermal annealing; the degree of electric activation of the impurity is also higher in the case of RTA.

REFERENCES

1. V. M. Ardyshev and M. V. Ardyshev, Fiz. Tekh. Poluprovodn. (St. Petersburg) **32**, 1153 (1998) [Semiconductors **32**, 1029 (1998)].

2. V. M. Ardyshev, M. V. Ardyshev, and S. S. Khludkov, Fiz. Tekh. Poluprovodn. (St. Petersburg) **34**, 28 (2000) [Semiconductors **34**, 27 (2000)].

3. V. M. Ardyshev, M. V. Ardyshev, and S. S. Khludkov, Fiz. Tekh. Poluprovodn. (St. Petersburg) **34**, 70 (2000) [Semiconductors **34**, 70 (2000)].

4. V. M. Ardyshev, L. A. Kozlova, O. N. Korotchenko, and A. P. Mamontov, USSR Inventor's Certificate No. 235899 (1986).

5. V. M. Ardyshev, I. E. Burkova, and A. A. Yatis, Poverkhnost, No. 3, 77 (1985).

6. J. Lindhard, M. Scharff, and H. Schiøtt, K. Dan. Vidensk. Selsk. Mat. Fys. Medd. **33**, 1 (1963).

7. F. H. Eisen and B. M. Velch, in *Ion Implantation in Semiconductors* (Plenum, New York, 1977), p. 79.

8. V. M. Ardyshev, Author's Abstracts of Candidate's Dissertation (Tomsk, 1987).

9. E. D. Gornushkina, I. V. Kirillova, and R. Sh. Malkovich, Fiz. Tverd. Tela (Leningrad) **24**, 1088 (1982) [Sov. Phys. Solid State **24**, 616 (1982)].

10. M. V. Ardyshev, Author's Abstracts of Candidate's Dissertation (Tomsk, 2000).

Translated by A. Spitsyn

ELECTRONIC
AND OPTICAL PROPERTIES
OF SEMICONDUCTORS

The Preexponential Factor in Mott's Law for Variable-Range-Hopping Conduction in Lightly Compensated p-Hg$_{0.8}$Cd$_{0.2}$Te Crystals

V. V. Bogoboyashchiĭ

Kremenchug State Polytechnical University, Kremenchug, 39614 Ukraine
Submitted May 8, 2001; accepted for publication June 28, 2001

Abstract—Hopping conduction with variable range was studied in undoped p-Hg$_{0.8}$Cd$_{0.2}$Te crystals with the Hg-vacancy concentration varying from 10^{16} to 4×10^{17} cm^{-3} in the temperature range of 4.2–125 K. The temperature and concentration dependences of the preexponential factor ρ_{0M} in Mott's law was determined. It is found that the temperature dependence of ρ_{0M} is in good agreement with the theoretical calculations performed in the one-particle approximation. At the same time, ρ_{0M} depends heavily on the Hg-vacancy concentration and parameter T_0 in Mott's law, which is in contradiction with this theory. The experimental dependence of ρ_{0M} on both parameters has a power-law form; the exponent is equal to 2.3–2.4. It is assumed that the concentration dependence of ρ_{0M} is typical of double-charged acceptors. This fact can be explained by the capture of a second hole by the Hg vacancy. © *2002 MAIK "Nauka/Interperiodica".*

1. INTRODUCTION

The study of hopping conduction is a convenient method for gaining insight into the energy states in the semiconductor band gap. Narrow-gap Hg$_{1-x}$Cd$_x$Te crystals are of especial interest for this type of study [1–4]. Hopping conduction is observed in these crystals at unusually high temperatures (up to 10–20 K), and it preserves an activation character for high acceptor concentration (up to 10^{17}–10^{18} cm^{-3}). This circumstance provides favorable conditions for such a study. This material has also other unusual properties. For example, the hopping conduction parameters of the p-Hg$_{1-x}$Cd$_x$Te crystals depend on the type of acceptor. Specifically, ε_3 conduction with a fixed activation energy is observed for ordinary acceptors (Cu). In this case, the probability of a hop is defined by the localization radius of a heavy hole [3]. On the contrary, double-charged native acceptors (mercury vacancies V_{Hg}) cause the hopping conduction with variable range described by Mott's law [5], with the parameters defined by the light-hole localization radius [4]. In this case, both the energy of the acceptor state and its radius are independent of the acceptor concentration up to the metal–insulator transition in the impurity band [4, 6], though traditional notions about wave function behavior near this transition imply the reverse [7]. The contradiction is so serious that it should be properly discussed.

For this purpose we continued the study of hopping conduction in nonstoichiometric p-Hg$_{1-x}$Cd$_x$Te crystals (see [4]). Special attention has been given to studying the concentration and temperature dependences of the preexponential factor in Mott's law. In contrast to the exponent, this factor has received little attention

though the exponent can give only part of the information concerning the impurity states. Unfortunately, investigations of p-Hg$_{1-x}$Cd$_x$Te [3, 4] have shown that the values of the exponent both in Mott's law and in the Arrhenius law for the ε_3 conduction are quite conventional from the theoretical point of view [7, 8]. Due to this fact, it is impossible to understand the special features of this semiconductor on the basis of such studies. Thus, we assumed that investigation of the preexponential factor could help to obtain additional information about the hopping conduction in this semiconductor.

2. RESULTS

Several single-crystal wafers of undoped n-Hg$_{1-x}$Cd$_x$Te ($x = 0.22 \pm 0.005$) were cut from different ingots with the electron concentration of $n = (3 \pm 1) \times 10^{14}$ cm^{-3}.

For homogenization, selected wafers were annealed in Hg vapors at $T = 600$°C and vapor pressure (p) of 10 atm for one week. Then, part of the wafers were annealed at p = 2.5 atm for 24 h. As a result, we obtained Te-enriched wafers. Wafers were cut into samples and annealed isothermally in the saturated Te vapors in the temperature range of 240–490°C. The duration of this annealing stage was sufficient for the achievement of two-phase equilibrium with the Te precipitates. The other wafers were also cut into samples and then annealed in the Hg vapor in the temperature range 420–520°C at various pressures within the homogeneity region. The annealing time was sufficient for attaining equilibrium with the vapor phase.

In addition, a large number of annealed crystals, which were cut from the Hg$_{1-x}$Cd$_x$Te ($x = 0.22 \pm 0.02$)

ingots, were studied. Some of these ingots were intentionally In-doped up to the concentrations of 10^{15}–5×10^{16} cm^{-3}, whereas the other ingots contained only residual impurities.

As a result, a set of p-Hg$_{0.78}$Cd$_{0.22}$Te crystals with the concentration of electrically active Hg vacancies varying from 10^{16} to 4×10^{17} cm^{-3} was obtained. Samples annealed in the Hg vapors were single-phase. The other crystals were heterophase; they contained ~10^{18} cm^{-3} of excess Te in the form of small second-phase inclusions.

The Hg-vacancy concentration was determined from the hole concentration obtained from the Hall coefficient measurements at $T = 77$ K in the magnetic field $B = 1$ T. The field dependence of the Hall coefficient and the concentration dependence of the average degree of ionization of vacancies were taken into account. The method of calculating the V_{Hg} concentration in p-Hg$_{1-x}$Cd$_x$Te crystals has been described in detail in [9, 10].

According to the procedure mentioned above, typical $\rho(T)$ dependences for unannealed and annealed p-Hg$_{0.8}$Cd$_{0.2}$Te crystals with various V_{Hg} concentrations were reported in [1, 2] and [4], respectively. In all cases, hopping conduction with variable hopping range was observed at low temperatures. This conductivity obeys Mott's law; i.e.,

$$\rho = \rho_{0M} \exp(T_0/T)^{1/4}. \tag{1}$$

According to [4], the parameter T_0 increases only slightly with $[V_{Hg}]$ for a low V_{Hg} concentration in the crystal ($N_A \equiv [V_{Hg}] < 4 \times 10^{17}$ cm^{-3}). At the same time, the resistivity decreases very rapidly.

According to [8], the ρ_{0M} factor in (1) is, in the general case, a power function of temperature with the exponent depending on the wave function of the bound state. The $\rho_{0M}(T)$ dependence affects only slightly the function $\rho(T)$. The difference between the experimental curves and formula (1) is within the experimental error in T measurements caused by inaccuracy in thermometer calibration. On the other hand, neglecting this dependence can cause significant errors in ρ_{0M} and T_0 calculations by extrapolation to infinite temperature, particularly at small T_0.

Due to this circumstance, we experimentally determined the exponent in the $\rho_{0M}(T)$ dependence. We chose several pairs of samples so that T_0 should differ by an order of magnitude for the samples from the same pair. The resistivity was simultaneously measured for each pair in the temperature range of 4.2–16 K. In this case, each pair of experimental points ρ_1 and ρ_2 corresponds to the same temperature. Thus, data combination can be described by the parametric dependence $\rho_2 = f(\rho_1)$. We thereby avoided the effect of errors in T measurements. To provide sufficient sensitivity of this method to the $\rho_{0M}(T)$ function, the resistivity was measured to within 0.3%.
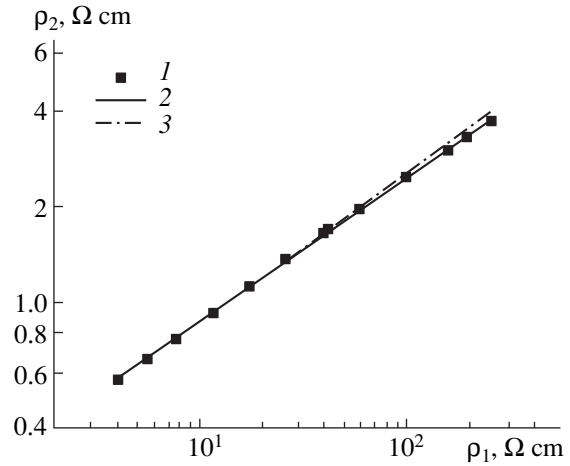
Fig. 1. Parametric dependence of resistivity for two p-Hg$_{0.8}$Cd$_{0.2}$Te samples obtained from simultaneous measurements. (*1*) Experiment, (*2, 3*) calculation for $n = 1$ and $n = 0$, respectively (see Eq. (2)).

If the law (1) with constant factor ρ_{0M} is satisfied, then it can be easily seen that the dependence $\rho_2(\rho_1)$ plotted on the log–log scale can be approximated by a straight line. If ρ_{0M} is a power function of T, the curve will be bent. In this case, the magnitude and sign of inflection will define the exponent of this function.

The experimental results for one of these pairs are shown in Fig. 1 (dots). One can see that the $\rho_2(\rho_1)$ dependence is very close to linear. Fitting the experimental data to the function

$$\rho = \rho_{0M}^* (T_0/T)^{n/4} \exp(T_0/T)^{1/4} \tag{2}$$

gives the best agreement for $n = 1 \pm 0.2$ (Fig. 1, curve *2*).

The dependence (2) plotted for $n = 0$ (line *3*) illustrates the accuracy of determining the parameter n.

The factor ρ_{0M}^* was obtained from the experimental dependence $\rho(T)$. It turned out that ρ_{0M}^* varied in a wide range, and it depended on all experimental parameters: x, $[V_{Hg}]$, T_0, and others. For this reason, experimental data were subjected to the two-factor analysis of variance. We assumed that ρ_{0M}^* simultaneously depended on the Hg vacancy concentration and characteristic temperature T_0.

The ρ_{0M}^* values normalized, according to the relation (2), to T_0 (for the dependence of ρ_{0M}^* on $[V_{Hg}]$) or to $N_A = [V_{Hg}]$ (for the dependence of ρ_{0M}^* on T_0) are displayed in Figs. 2 and 3. In this procedure the experimental values of ρ_{0M}^* were multiplied by $(T_0/T_0^*)^{2.3}$ or by $([V_{Hg}]/N_A^*)^{2.4}$, where $N_A^* = 10^{17}$ cm^{-3} and $T_0^* = 10^5$ K. One can see a distinct correlation of ρ_{0M}^* both with
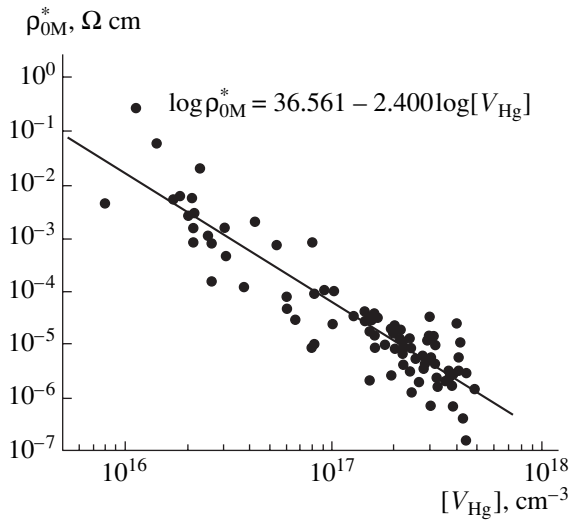
Fig. 2. Concentration dependence of the ρ_{0M}^* factor normalized to $T_0 = 10^5$ K. Experimental data (dots); interpolation according to the formula shown in the figure (straight line).
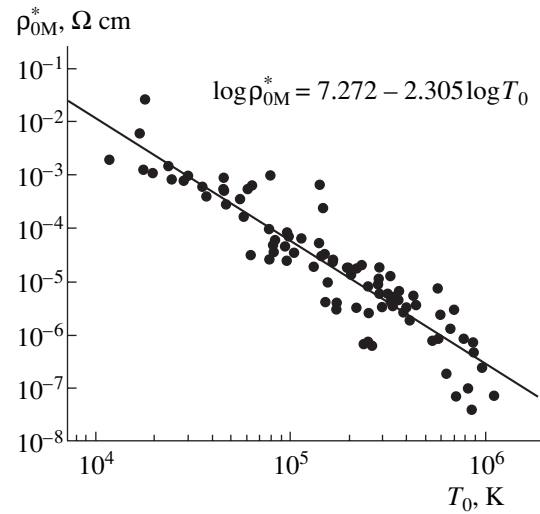

Fig. 3. The factor ρ_{0M}^* dependence on the parameter T_0 normalized to the value $N_A = [V_{Hg}] = 2 \times 10^{17}$ cm^{-3}. Experimental data (dots); interpolation from the formula displayed in the figure (straight line).

$[V_{Hg}]$ and with T_0. Both dependences can be approximated by the power functions. Processing the experimental data by the least-squares method, we obtain the following interpolation relation:

$$\rho_{0M}^* = 5.7 \times 10^{-5} \left(\frac{[V_{Hg}]}{N_A^*}\right)^{-2.4} \left(\frac{T_0}{T_0^*}\right)^{-2.3} \Omega \text{ cm.} \quad (3)$$

The dependence of ρ_{0M}^* on x was weak, and it was ignored.

3. THEORY

It is accepted that ρ_{0M} can be computed on the basis of the percolation theory [8]. In particular, these calculations are performed for semiconductors with hydrogen-like centers [8]. Unfortunately, these results cannot be directly used for comparison with experimental data described above, because the acceptor wave function in the diamond-like semiconductors differs considerably from that in the hydrogen-like one. Due to this fact, we evaluated ρ_{0M} for the narrow-gap diamond-like semiconductor of the p-type.

We used the variational method for calculation of ρ_{0M}. Test wave functions have the following features.

First, two spatial scales in the diamond-like semiconductor in which the hole masses significantly differ characterize the wave function of the acceptor state. One part of the hole density of states is located near the defect forming the core with a specific scale of a_h (the heavy hole localization radius). The other part forms the asymptotic tail of the density of states. In this region, the wave function diminishes exponentially as the distance to the acceptor increases. The specific

dimension here is $a_l = a_h / \sqrt{\beta}$, where $\beta = m_{lh}/m_{hh}$ is the ratio of the light (m_{lh}) and heavy (m_{hh}) effective hole masses. The formulas for a_h and a_l were obtained in [4] for the double-charged native acceptor in the semiconductor with $\beta \ll 1$. In particular, $a_h \approx 2.0$ nm and $a_l \approx 16$ nm for the Hg vacancy in the narrow-gap Hg$_{1-x}$Cd$_x$Te with $x = 0.22 \pm 0.005$ ($\beta \approx 0.015$) [4].

Second, due to the degeneracy of the valence band, the radial part of the bound-hole wave function has two components (R_0 and R_2) in a diamond-like semiconductor [8]. These functions differ near the acceptor, but away from it ($r \gg a_l$) they are identical: $R_0 \approx R_2$.

Based on this, the radial wave functions of an isolated acceptor can be expressed as

$$R_j = A_j R_{j0} + B\sqrt{2\beta^3/a_h^3}\exp(-r/a_l), \quad (4)$$

where R_{j0} is the function R_j ($j = 0$; 2) for $\beta = 0$. The variational calculation showed that, in this case, the extremum of the Hamiltonian average value of a bound hole is attained for $B \approx 1$. In this case, $A_0 \approx A_2 \approx 1$ if $\beta \ll 1$.

To estimate the overlap integral I_{ij}, we ignored the angular dependence of the wave function and assumed that $B = 1$. Then, we have the relation

$$I_{ij} = \frac{2}{3}\frac{e^2}{\varepsilon_0 a_h}\frac{r_{ij}}{a_h}\exp\left(-\frac{r_{ij}}{a_h}\right) + 2\beta^{3/2}\frac{e^2}{\varepsilon_0 a_h}\exp\left(-\frac{r_{ij}}{a_l}\right) \quad (5)$$

for $r_{ij} \gg a_l$, where r_{ij} is the distance between two acceptors. Here, the first term describes the core overlap, and the second one accounts for the overlap of the core and the tail wave functions belonging to different acceptors. As it is easy to calculate, it is possible to neglect the first

term in (5) and its contribution to the probability of a hole hop if the following relation is valid:

$$r_{ij}/a_l - \ln(r_{ij}/a_l) > -\ln 3\beta^{3/2}. \qquad (6)$$

Assuming that condition (6) is satisfied, we performed calculations of ρ_{0M} similar to [8] and obtained the following result:

$$\rho_{0M} = \rho_{0M}^*(T_0/T)^{\nu/4} \approx \frac{1}{9}\beta^{-7/2}\rho_0'(T_0/T)^{\nu/4}. \qquad (7)$$

Here, ν is the critical index ($\nu \approx 0.9$). The factor ρ_0' was calculated in [8]. It depends only on the core radius of the energy-state wave function and on the semiconductor characteristics. This quantity equals $\rho_0' \approx 3 \times 10^{-8}\ \Omega$ cm for the mercury vacancy in $Hg_{0.8}Cd_{0.2}Te$.

4. DISCUSSION

If we neglect the overlapping of the acceptor-core wave functions, the evaluations of ρ_{0M} are valid. In this case, the distance between acceptors should be fairly large. The second term in (5) is dominant only at $r_{ij} > 7a_l$ if $\beta \approx 0.015$ for p-$Hg_{0.8}Cd_{0.2}Te$. If Mott's law is satisfied (1), provided that a specific hop range is equal to $a_l(T_0/T)^{1/4}$, this inequality is equivalent to the condition $T_0 > 2500T \approx 10^4$ K. This requirement was satisfied in the investigated samples (Fig. 3). Therefore, we expected good agreement between the results of ρ_{0M} calculations and the experiment.

Actually, part of the ρ_{0M} temperature dependence is well described by expression (7), which is in close agreement with experimental dependence (2) within the measurement error. Substituting $\beta \approx 0.015$ and $\rho_0' \approx 3 \times 10^{-8}\ \Omega$ cm (typical of the narrow-gap $Hg_{0.8}Cd_{0.2}Te$) in (7), we obtain $\rho_{0M}^* \approx 0.01\ \Omega$ cm. This value matches, by an order of magnitude, the experimental data in the region of low vacancy concentration $[V_{Hg}] \approx 10^{16}$ cm^{-3} (Fig. 2).

However, in our experiment we observed a heavy concentration dependence of ρ_{0M}^*, which could be described by the empirical relation (3), though formula (7) did not contain either $[V_{Hg}]$ or T_0 in an explicit form (except for the ratio T_0/T)

Such ρ_{0M}^* behavior is rather unexpected. In fact, the majority of vacancies are neutral at low temperatures in the samples under study. Their energy states are located well above the Fermi level. According to this, the neutral vacancies should not affect the hopping charge transport. At the same time, the strong ρ_{0M}^* dependence on the $[V_{Hg}]$ concentration indicates that vacancies are involved in this phenomenon. The dependences of ρ_{0M}^* on T_0 (or on the acceptor density of states g_F near the

Fermi level which is inversely proportional to T_0) are also unexpected.

According to [8], ρ_{0M}^* is defined in the overlap integral by the correlation radius of the critical sublattice and by the preexponential factor. On the other hand, it follows from Fig. 2 that ρ_{0M}^* decreases by more than four orders of magnitude as the V_{Hg} concentration increases. This can be explained by the correlation radius variation, because it decreases insignificantly. Otherwise, it should be smaller than the hop range, which makes no sense [8]. Therefore, the ρ_{0M}^* behavior is primarily caused by the variation of the preexponential factor in the overlap integral.

This situation is still more unusual, because ρ_{0M}^* should be independent of the vacancy concentration if conduction over ordinary impurity acceptors, observed in [4] for $[V_{Hg}] > 4 \times 10^{17}$ cm^{-3}, takes place. In this case, ρ_{0M}^* is, on average, equal to 0.01 and 0.03 Ω cm for Te- and Hg-saturated crystals. This result is similar to $\rho_{0M}^* \approx 0.05\ \Omega$ cm obtained from (7) (i.e., for $a_l \approx 26$ nm).

The conclusion suggests itself that the phenomenon observed in this study is typical of conduction over Hg vacancies. In the neutral state, each of these vacancies binds two holes, in contrast to the impurity acceptors each of which binds one hole. Probably, the mutual influence of these holes manifests itself in this way by the hop of one of them to a free vacancy. In fact, the true wave function of the ground state defines the lowest binding energy. Because the maximum of the hole density is located near the core of the acceptor state, its energy depends only slightly on the wave function in the tail. Due to this fact, even insignificant variation in the bound hole interaction can cause appreciable variations in the hole density away from the acceptor core. It is possible that the ρ_{0M}^* value is defined by the collective interaction; i.e., the probability of a hop is simultaneously determined by all holes bound by vacancies arranged along the transport path. The ρ_{0M}^* dependence both on the $[V_{Hg}]$ concentration and the density of states g_F near the Fermi level supports this assumption.

In any case, we can state on the basis of our results and results obtained in [4] that the decrease in ρ_{0M}^* is caused by the increase in the overlap integral. If we assume that this is the result of an increase in the hole density in the tail of the acceptor states, which remains low, then almost all special features of the hopping conduction in p-$Hg_{0.8}Cd_{0.2}Te$ become understandable.

First, low hole density in the tail of the acceptor state may indeed cause the difference between the hopping conductivity in the nonstoichiometric p-$Hg_{0.8}Cd_{0.2}Te$ samples and in the crystals doped with Cu. In this material, the probability of a hop between the neighboring

centers ($r_{ij} \approx N_A^{-1/3}$; the region of ε_3 conductivity) is solely defined by the overlapping of the core wave functions if $[V_{Hg}] > 10^{15}$ cm^{-3} or if the Cu concentration $N_A > 10^{14}$ cm^{-3}, i. e., for all acceptor concentrations used in the experiment. On the contrary, for conduction with a variable hopping range, the second term is dominant in relation (5) and $r_{ij} = a_l(T_0/T)^{1/4}$. According to the calculations, the conductivity with a variable hopping range will prevail over the ε_3 conductivity for rather low acceptor concentrations at the temperatures when band conductivity is negligible. Vanishing of ε_3 conduction should be observed for a single-charged acceptor (Cu) for $N_A \approx 10^{16}$ cm^{-3}, whereas for a double-charged vacancy (whose state is more compact), for the concentration $[V_{Hg}] \approx 10^{17}$ cm^{-3}.

The concentration of Cu in the doped p-Hg$_{0.8}$Cd$_{0.2}$Te crystals was higher than 10^{16} cm^{-3}; due to this circumstance, the ε_3 conductivity was dominant in the experiment [3]. If the hole density remained unchanged in the region of $r \gg a_l$, then ε_3 conduction would also be observed in the nonstoichiometric crystals with $[V_{Hg}] > 10^{17}$ cm^{-3}. However, an increase in the hole density for $r \gg a_l$ leads to the prevalence of the conductivity with a variable hopping range in such crystals. This is also true for crystals with $[V_{Hg}] < 10^{17}$ cm^{-3}).

Second, the hole density in the tail is still low for $[V_{Hg}] < 4 \times 10^{17}$ cm^{-3}. Due to this fact, its increase has virtually no affect on the core wave function. The binding energy and both radii (a_h and a_l) also remain unchanged. This is consistent with the experimental results obtained in [3, 4].

Third, the high transition temperature to the hopping conduction which was observed in the undoped p-Hg$_{0.8}$Cd$_{0.2}$Te crystals with Hg vacancies can be easily explained by small values of ρ_{0M}^*.

Fourth, high acceptor concentrations at which the Mott transition occurs in the p-Hg$_{0.8}$Cd$_{0.2}$Te crystals is related to low hole density in the asymptotic tail of the wave function. In this case, overlap in the tails of the impurity states is not sufficient for formation of a wide acceptor band.

5. CONCLUSION

Therefore, the following conclusions can be drawn from our experimental results.

(1) The Preexponential factor ρ_{0M}^* in Mott's law for the hopping conduction in lightly compensated p-Hg$_{0.8}$Cd$_{0.2}$Te crystals has a complex dependence on the acceptor concentration and the acceptor density of states near the Fermi level. The temperature dependence of ρ_{0M}^* is satisfactorily described within the conventional model of the hopping charge transport. At the same time, contrary to expectations, we observed a strong ρ_{0M}^* concentration dependence. The ρ_{0M}^* value rapidly decreases due to an increase in the overlap integral as the acceptor concentration increases. This effect predetermines the existence of high-temperature hopping conductivity of the p-Hg$_{0.8}$Cd$_{0.2}$Te crystals with a high concentration of Hg vacancies.

(2) In the diamond-like semiconductors with a small mass of light holes, the main part of the hole density is concentrated in the core of the wave function of the isolated acceptor. The hole density in the asymptotic tail forms about $\beta^{3/2}$ of the total hole density, where $\beta = m_{lh}/m_{hh}$ is the ratio of light and heavy hole effective masses.

REFERENCES

1. A. I. Elizarov and V. I. Ivanov-Omskiĭ, Fiz. Tekh. Poluprovodn. (Leningrad) **15**, 927 (1981) [Sov. Phys. Semicond. **15**, 531 (1981)].

2. A. I. Elizarov, V. V. Bogoboyashchiĭ, and N. N. Berchenko, Fiz. Tekh. Poluprovodn. (Leningrad) **18**, 455 (1984) [Sov. Phys. Semicond. **18**, 283 (1984)].

3. V. V. Bogoboyashchiĭ, S. G. Gasan-Zade, and G. A. Shepel'skiĭ, Fiz. Tekh. Poluprovodn. (St. Petersburg) **34** (4), 411 (2000) [Semiconductors **34**, 398 (2000)].

4. V. V. Bogoboyashchiĭ, Fiz. Tekh. Poluprovodn. (St. Petersburg) **35**, 34 (2001) [Semiconductors **35**, 33 (2001)].

5. N. F. Mott, J. Non-Cryst. Solids **1**, 1 (1968).

6. V. V. Bogoboyashchiĭ, Fiz. Tekh. Poluprovodn. (St. Petersburg) **34**, 955 (2000) [Semiconductors **34**, 916 (2000)].

7. N. F. Mott and E. A. Davis, *Electronic Processes in Non-Crystalline Materials* (Clarendon, Oxford, 1979; Mir, Moscow, 1982), Vol. 1.

8. B. I. Shklovskiĭ and A. L. Efros, *Electronic Properties of Doped Semiconductors* (Nauka, Moscow, 1979; Springer-Verlag, New York, 1984).

9. V. V. Bogoboyashchiy, Proc. SPIE **3486**, 325 (1997).

10. V. V. Bogoboyashchiĭ, Kondens. Sredy Mezhfazn. Granitsy **2** (2), 132 (2000).

Translated by I. Kucherenko

ELECTRONIC
AND OPTICAL PROPERTIES
OF SEMICONDUCTORS

E_0 Photoreflectance Spectra of GaAs: Identification of the Features Related to Impurity Transitions

R. V. Kusmenko and É. P. Domashevskaya

Voronezh State University, Universitetskaya pl. 1, Voronezh, 394693 Russia
e-mail: roman@ftt.vsu.ru

Abstract—In the room-temperature photoreflectance spectra of moderately doped crystalline GaAs wafers near the fundamental E_0 critical point, components corresponding to impurity transitions were identified. This was done by phase analysis of the spectra, and their variation with the laser-excitation density was examined. The dependences of the impurity component magnitude and the retardation phase on the excitation density were determined experimentally. It was established that the impurity component is strongly affected by the condition of the sample surface. © 2002 MAIK "Nauka/Interperiodica".

Photoreflectance (PR) spectroscopy is widely used as a modulation optical technique for the nondestructive study of the electronic, optical, and structural properties of semiconductor crystals and their surfaces and interfaces. However, extremely high sensitivity of the PR spectra to the experimental conditions and to the sample parameters often leads to ambiguities in their interpretation. In particular, although observation of PR features in the energy region below the fundamental transition is reported rather frequently, there is still no general understanding of their nature. Originally, it was assumed that either band broadening caused by the Franz–Keldysh effect or modulation processes in the region of exciton transitions were responsible for the appearance of a low-energy structure [1, 2]. However, studies of electroreflectance and photoreflectance spectra reported over the last fifteen years [3–11] revealed that, in certain cases, the shape of the low-energy features cannot be described in the context of the above models, with the energy position of these features varying from the exciton-transition region to 30–70 (!) meV below E_0. In so far as the magnitude of the low-energy spectral components is comparable to that of the electromodulation component, their assignment to the modulation processes in the impurity-transition region seemed to be unjustified (for nondegenerate semiconductors, the density of states in the allowed bands is at least several orders of magnitude higher than the density of impurity states). Nevertheless, theoretical analysis revealed that, even for relatively low impurity densities (10^{15} cm^{-3} and higher), modulation of one of the impurity level parameters (transition energy, occupancy, or broadening) can result in the appearance of a structure in the modulation spectra which is comparable in magnitude with the component originating from valence-to-conduction band transitions. Then, the question arises as to why the number of reports on the observation of impurity features in modulation spectra is so small. For instance, after the first observation of such features in the electroreflectance spectra by Seraphin in 1966 [12], a detailed analysis of impurity components was undertaken only in 1985 [6].

We believe that, in many instances, impurity components do arise in electroreflectance and photoreflectance spectra of direct-gap semiconductors. However, they can strongly overlap with the broad E_0 PR component originating from intrinsic states, in which case either they are not visually observed in the spectral curves or are, incorrectly, attributed to excitonic transitions. In this study, we suggest methods that make it possible to identify impurity components in the situation when there is strong spectral overlap. It will be demonstrated that the behavior of impurity features cannot be explained by taking into consideration only the electromodulation mechanism, and it will be shown that their presence in the spectra is strongly affected by the condition of the sample surface.

The PR spectra ($\Delta R/R = f(E)$) were recorded at room temperature using the setup described in [13]. Either a red He–Ne laser ($\lambda = 632.8$ nm) or a blue He–Cd laser ($\lambda = 442.5$ nm) was used to modulate the sample reflectance. The intensities of the laser beam were in the range $L = 0.5$–4 W/cm^2. The measurements were carried out for Si-doped n-GaAs wafers ($E_0 = 1.424$ eV, charge carrier density $n \sim 10^{16}$ cm^{-3}) passivated by Ga$_2$Se$_3$. The thickness of the passivating layer was about 10 nm. Phase analysis of the spectra [14] was performed using an SR850 lock-in amplifier.

Figure 1 shows the PR signal (both in X and Y quadrature channels) measured near the E_0 gap on a Ga$_2$Se$_3$-passivated n-GaAs wafer ($n = 5 \times 10^{15}$ cm^{-3}) using a blue He–Cd laser beam modulated at 2500 Hz; in this recording, the lock-in phase is arbitrary. Obser-
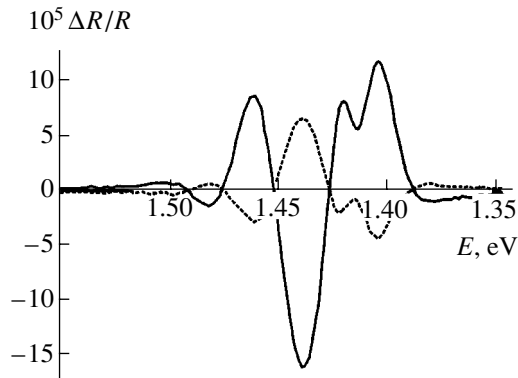
$10^5 \, \Delta R/R$

Fig. 1. X and Y quadrature channel records (solid and broken lines, respectively) of E_0 photoreflectance spectrum of a Ga_2Se_3-passivated n-GaAs wafer ($n = 5 \times 10^{15}$ cm^{-3}).
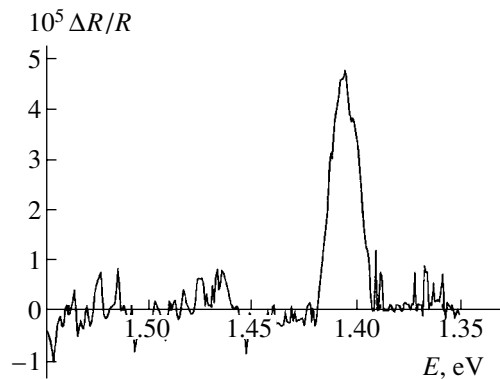
$10^5 \, \Delta R/R$

Fig. 2. Low-energy component separated by presetting the lock-in phase.

$10^5 \, \Delta R/R$
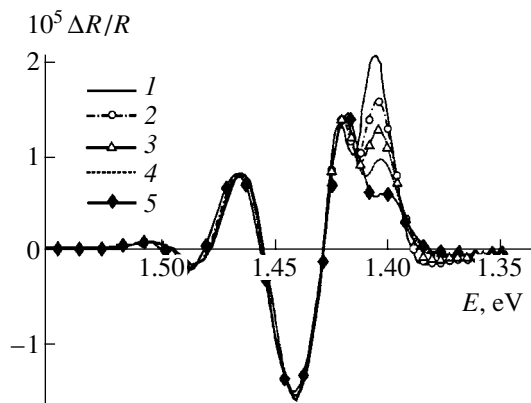
Fig. 3. Photoreflectance spectra recorded in the X channel for laser-excitation densities of (*1*) 2.8, (*2*) 1.74, (*3*) 1.26, (*4*) 0.89, and (*5*) 0.53 W/cm^2.

vation of the Franz–Keldysh oscillations in the high-energy region is evidence of the presence of the electromodulation E_0 component, originating from the valence-to-conduction band transitions and detected under the

mean-field conditions. The low-energy shoulder of the main peak of this component overlaps with the low-energy spectral component. Plotting of the phase diagram yields a loop-shaped phase line [14], which indicates that the spectrum contains two components with different retardation phases or, in other words, different time constants (which, to a first approximation, represent delay time of the modulation response with respect to the excitation signal).

Since the spectrally overlapping components have different phases, they can be separated using phase analysis. To do this, the phase of the PR signal was determined in the energy range where only the electromodulation component is present. Next, the lock-in phase was preset in such a way that this component was suppressed in the X channel. Then, the undistorted low-energy component was recorded (see Fig. 2). The lineshape of the low-energy feature qualitatively coincides with the so-called "first-derivative spectral shapes", characteristic of impurity components [3, 6, 8, 9, 11], and does not coincide with the low-field shape typical of exciton-related components. However, since the spectral position of this feature is very close to the E_0 gap (the peak being in the region of excitonic transitions), the lineshape alone cannot be considered as convincing proof of its impurity-transition origin.

As a next step in the identification of the nature of the low-energy component, we recorded a series of spectra varying the laser-excitation power density. The discrepancy between the phases of the low-energy and the mean-field electromodulation components indicates that they originate either in different regions of the sample or are due to different modulation processes. In both cases, different dependences of the component magnitudes on the excitation density should be expected.

The PR spectra recorded in the X channel under excitation intensities L varying from 2.8 to 0.53 W/cm^2 are shown in Fig. 3. Since the magnitudes of both components decrease with a reduction in the laser-excitation density, the curves were normalized to the amplitude of the second Franz–Keldysh oscillation. One can see that the contribution of the low-energy component falls off rapidly as the excitation density is reduced. At the same time, the spectral shape of this component remains unchanged, which was established by the measurements performed under preset lock-in phase.

In order to analyze quantitatively the dependence of the magnitudes of the low-energy and electromodulation components in the PR spectrum on the laser-excitation density, we define the amplitudes, or amplitude factors, A for both of them. In so far as the shape of the low-energy component is independent of the excitation density, the peak height can be used as an amplitude factor. The shape of the mean-field component changes with the level of surface field modulation, which makes it more complicated to introduce the amplitude factor in this case. However, calculations carried out in the con-

text of a generalized multilayer model [15] indicate that, for low and moderate levels of electric field modulation, the shape, period, and spectral position of the Franz–Keldysh oscillations remain virtually unchanged and depend only on the field strength in the dark. On the contrary, the magnitude of the signal in this region depends only on the surface-field modulation level. Thus, we can use the magnitude of the Franz–Keldysh oscillations as an amplitude factor for the mean-field electromodulation signal. In our estimations, we defined A as the magnitude of the second positive oscillation. The dependences $A(L)$ for the two components are shown in Fig. 4. It can be seen that both amplitude factors vary logarithmically with the laser-excitation density.

The observed behavior of the low-energy component cannot be explained under the assumption of its excitonic nature. First, the level of the surface electric field modulation varies with the variation in the excitation level, which should manifest itself in a varying spectral shape of the exciton-related PR feature. Second, experimental results on the behavior of the excitonic component with the laser-excitation density indicate that its relative strength with respect to the electromodulation component decreases with increasing laser intensity [16]. Thus, the origin of the low-energy component should be attributed to the modulation processes taking place in the region of impurity electron transitions. Observation of the more rapid increase in the magnitude of the impurity component with respect to the electromodulation E_0 component was also reported in [4].

Next, we determined the phases of the components for different laser-excitation densities. It was found that the phase of the E_0 component is very sensitive to excitation density, while the phase of the impurity component is not (see Fig. 5). This difference suggests that the process responsible for the appearance of the impurity component is directly related to the generation of high-density nonequilibrium charge carriers, in contrast to the indirect process responsible for the electromodulation component. Such a weak dependence of the phase of the impurity component on the excitation density correlates well with the assumption that the impurity PR signal is related to the recharging of the impurity centers [6, 9].

Unfortunately, we cannot make any conclusions from our data about the type of impurity state which the low-energy component originates from. Seeing as the sample under study is doped with Si, this PR feature should apparently be assigned to a transition involving an Si impurity level. The authors of [7] observed an impurity peak in the electroreflectance spectra in the same energy region and assigned it to the Si donor level.

Similar spectra are obtained when the sample is excited by the red laser (in the same range of excitation power densities); however, the low-energy component
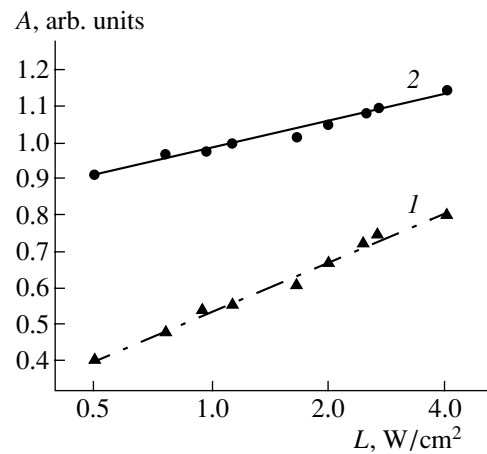

Fig. 4. $A(L)$ dependences for (*1*) low-energy and for (*2*) electromodulation E_0 components.
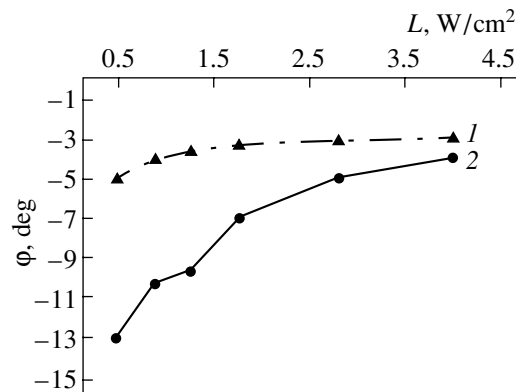

Fig. 5. Dependences of the retardation phase on the laser-excitation density for (*1*) low-energy and for (*2*) electromodulation E_0 components. The phase angles are shown negative to indicate that both signals are delayed with respect to the excitation.

is less pronounced. Since, in this case, the region where nonequilibrium charge carriers are generated is deeper, we assume that impurity states responsible for the low-energy PR feature are located near the surface. To check this assumption, we compared the spectra recorded at different spots on the sample surface and found strong variations in the magnitude of the impurity component. Finally, the measurements were carried out on the sample with the passivating layer removed. Analysis of the obtained spectrum, whose lineshape was the same as that reported in [16], revealed that the impurity component is no longer present; however, a strong excitonic component appears in the low-energy region. Although the reasons for the disappearance of the impurity component are not clear, this obviously occurs due to a modification of the sample surface. This means that the impurity components appear in the PR spectrum due to purely surface phenomena or because they are related to the states located in close proximity

to the surface. Correlation between the condition of the surface and the appearance of the impurity component was also observed in [5, 8].

It is interesting to note that, as a rule, the impurity components are not present in the PR spectra simultaneously with the excitonic components. Thus, it can be concluded that modulation processes responsible for them compete with each other.

To summarize, the use of combined techniques in this study enabled us to identify the impurity component in the PR spectra of GaAs. Its lineshape and retardation phase were determined, and the dependence of its amplitude and retardation phase on the laser-excitation power density was examined. The phase of the impurity component is smaller and has a weaker dependence on the excitation density than the phase of the electromodulation component, which makes it possible to assume that the process responsible for the appearance of the former feature is directly related to the generation of high-density nonequilibrium charge carriers. It was established that the condition of the sample surface is important for the observation of the impurity component.

REFERENCES

1. E. Gutsche and H. Lange, Phys. Status Solidi **22**, 229 (1967).
2. D. E. Aspnes, Surf. Sci. **37**, 418 (1973).
3. S. K. Brierley and D. S. Lehr, J. Appl. Phys. **67**, 3878 (1990).
4. C. Durbin, J. P. Estrera, R. Glosser, *et al.*, Appl. Phys. Lett. **61**, 1549 (1992).
5. M. Gal, R. Shi, and J. Tann, J. Appl. Phys. **66**, 6196 (1989).
6. O. J. Glembocki, N. Bottka, and J. E. Furneaux, J. Appl. Phys. **57**, 432 (1985).
7. L. Kassel, J. W. Garland, P. M. Raccah, *et al.*, Appl. Surf. Sci. **56–58**, 356 (1992).
8. S. L. Mioc, P. M. Raccah, and J. W. Garland, Mater. Res. Soc. Symp. Proc. **261**, 45 (1992).
9. A. N. Pikhtin, V. M. Airaksinen, H. Lipsanen, and T. Tuomi, J. Appl. Phys. **65**, 2556 (1989).
10. M. Sydor, J. Angelo, J. J. Wilson, *et al.*, Phys. Rev. B **40**, 8473 (1989).
11. R. L. Tober and J. D. Bruno, J. Appl. Phys. **68**, 6388 (1990).
12. B. O. Seraphin, J. Appl. Phys. **37**, 721 (1966).
13. S. Hildebrandt, M. Murtagh, R. Kusmenko, *et al.*, Phys. Status Solidi A **152**, 147 (1995).
14. A. V. Ganzha, W. Kircher, R. V. Kuz'menko, *et al.,* Fiz. Tekh. Poluprovodn. (St. Petersburg) **32**, 272 (1998) [Semiconductors **32**, 245 (1998)].
15. R. V. Kuz'menko, A. Ganzha, É. P. Domashevskaya, *et al.*, Fiz. Tekh. Poluprovodn. (St. Petersburg) **34**, 1086 (2000) [Semiconductors **34**, 1045 (2000)].
16. R. V. Kuz'menko, A. Ganzha, J. Schreiber, and S. Hildebrandt, Fiz. Tverd. Tela (St. Petersburg) **39**, 2123 (1997) [Phys. Solid State **39**, 1900 (1997)].

Translated by M. Skorikov

ELECTRONIC
AND OPTICAL PROPERTIES
OF SEMICONDUCTORS

Temperature Dependence of Thermoelectric Power in *n*-InSb in a Transverse Quantizing Magnetic Field

M. M. Gadzhialiev

Amirkhanov Institute of Physics, Dagestan Scientific Center, Russian Academy of Sciences, Makhachkala, 367003 Russia
e-mail: Kamilov@datacom.ru
Submitted July 8, 2001; accepted for publication August 27, 2001

Abstract—The thermoelectric power in *n*-InSb in a transverse quantizing magnetic field has been studied in the temperature range 67–160 K. The dependence of the electronic component of the thermoelectric power on the magnetic field is accounted for in terms of a quantum theory taking into account the spin splitting of Landau levels. © *2002 MAIK "Nauka/Interperiodica".*

The thermoelectric power in *n*-InSb and *n*-InAs in a transverse quantizing magnetic field has been the subject of several experimental studies [1–5]. Both the electron and the phonon components of the thermoelectric power were shown to grow in a transverse magnetic field under the conditions of orbital quantization of the carrier motion ($\Omega\tau \gg 1$, $\hbar\Omega \gg kT$, $\Omega = eH/m^*c$, where *e* is the elementary charge, *H* is the magnetic field intensity, m^* is the carrier effective mass, τ is the relaxation time of the electronic momentum, *c* is the speed of light, *T* is temperature, and *k* is the Boltzmann constant), with the rise in the phonon component constituting a major part of the total increase in the thermoelectric power.

According to the quantum theory of thermomagnetic effects developed in [6], the diffusion (electronic) component of the thermoelectric power in a quantizing magnetic field, found with spin splitting of the Landau levels (SSLL) taken into account, is lower than the thermoelectric power in the case when spin is disregarded.

The influence of SSLL on transport phenomena would be expected if the above-mentioned conditions are supplemented with the inequality $g\mu_B H > kT$, where *g* is the spectral splitting factor of the electron energy and μ_B is the Bohr magneton.

As emphasized in [7, 8], the effect of spin splitting on the transverse thermoelectric power is not observed in the experiment for reasons which are not clear. For the effect of SSLL on the thermoelectric power to be detected, it is necessary that, first, the thermoelectric power in the magnetic field be carefully measured with account of the mutual arrangement of the plane in which the potential probes lie and the direction of the applied magnetic field, and, second, the measurement be performed under the conditions when the phonon drag component $\alpha_{xx}^{\mathrm{ph}}$ of the measured thermoelectric power is zero [9].

If, in the experiment, we are dealing with the purely diffusion-limited thermoelectric power α_{xx}^{e}, reliable conclusions concerning the effect of spin on the diffusion component of the thermoelectric power can be made by comparing its change in a magnetic field with that predicted by the theory that takes the SSLL into account. $\alpha_{xx}^{\mathrm{ph}}$ can be excluded in the experiment in two ways: by changing the concentration so that the system of charge carriers becomes degenerate, or by performing the experiment in a temperature range selected so that there is no electron–phonon interaction. As shown in [4, 5, 8], the phonon drag is absent in the case of a degenerate electronic subsystem and at relatively high temperatures (*T* > 100 K for InSb).

In [10], the thermoelectric power was measured in a transverse magnetic field in *n*-InAs samples with high electron density ($n = 10^{16}$ cm^{-3}), in which there is no phonon drag because of the strong degeneracy. Interpretation of the results of [10] in terms of the theory developed in [6] demonstrated that the thermoelectric power in a magnetic field is in agreement with the formula derived with account of SSLL.

It should be noted that the most favorable situation for verifying the effect of SSLL on the thermoelectric power is that when the phonon component $\alpha_{xx}^{\mathrm{ph}}$ is absent owing to the negligible electron–phonon interaction at any electron density. This situation was implemented in an experimental study of *n*-InSb ($n_{77} = 2 \times 10^{13}$ cm^{-3}) in transverse magnetic fields of up to 80 kOe with *T* > 160 K [11]. It was shown that, in the temperature range with zero phonon drag, the variation of the electronic component α_{xx}^{e} of the thermoelectric power with magnetic field is explained by the theory that takes the SSLL into account.

In the present study, the thermoelectric power of *n*-InSb ($n_{77} = 2 \times 10^{13}$ cm^{-3}) was measured in transverse
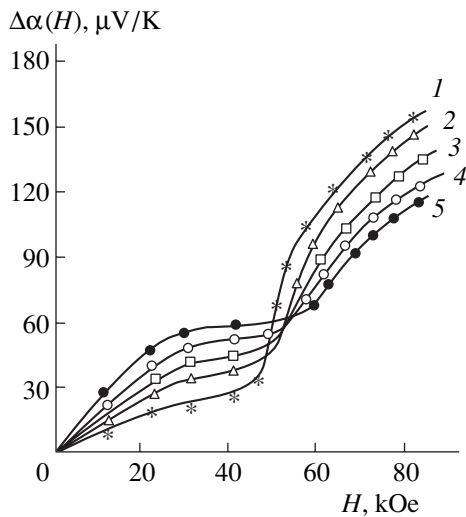
Fig. 1. Changes in thermoelectric power in n-InSb in a transverse magnetic field at temperatures of (*1*) 67, (*2*) 83, (*3*) 110, (*4*) 120, and (*5*) 160 K.

Fig. 2. Quantum additions $\delta\alpha_{xx}(H)$ to the leveled-off thermoelectric power α_∞ at temperatures of (*1*, *3*, *4*) 67 and (*2*, *5*, *6*) 160 K. (*1*, *2*) Experiment; (*3*, *5*) theory with spin disregarded; (*4*, *6*) theory with spin taken into account.

magnetic fields of up to 80 kOe at temperatures of 67, 83, 110, 120, and 160 K (Fig. 1) in order to investigate the effect of SSLL on the thermoelectric power in a wide temperature range.

As seen in Fig. 1, at any temperature, the thermoelectric power first grows then levels off (α_∞) when the strong-field condition ($\Omega\tau \gg 1$) is satisfied; it then rises sharply again when the condition $\hbar\Omega \gg kT$ is met. It is also seen that the threshold of the quantum rise in the thermoelectric power shifts to higher magnetic fields with increasing temperature, which is understandable in that whether or not the condition $\hbar\Omega \gg kT$ is satisfied depends on temperature.

Figure 2 shows the quantum rise in the thermoelectric power, $\delta\alpha_{xx}(H)$, measured at two limiting temperatures, 67 and 160 K. In plotting these curves, the thermoelectric power in a classically strong magnetic field at a given temperature, (α_∞), was used as the reference point for $\delta\alpha_{xx}(H)$. The figure also presents the quantum rise in the electronic component of the thermoelectric power, $\delta\alpha_{xx}^e(H)$, calculated for the above temperatures with the SSLL disregarded,

$$\delta\alpha_{xx}^e(H) = -\frac{k}{6e}v^2, \tag{1}$$

or taken into account,

$$\delta\alpha_{xx}^e(H) = -\frac{k}{e}\left[\frac{1}{6} - \frac{1}{8}\left(\frac{m^*}{m_0}g\right)^2\right]v^2. \tag{2}$$

Here, m_0 is the free electron mass and $v = \hbar\Omega/2kT$.

As can be seen in Fig. 2, the dependence $\alpha_{xx}^e(H)$ is in qualitative agreement with the theory which disregards the SSLL, at $T = 67$ K, and in quantitative agreement with the theory taking account of the SSLL, at
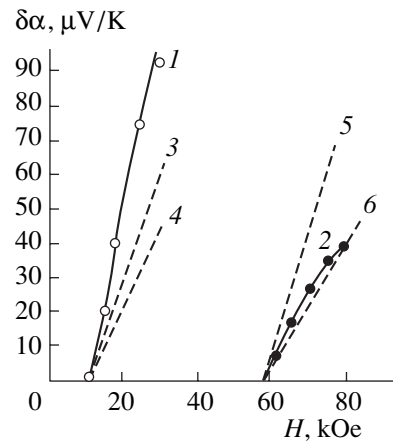
160 K. Therefore, with temperature rising above 100 K, the phonon drag completely disappears and the observed $\delta\alpha_{xx}^e(H)$ value is a purely diffusion-limited thermoelectric power, whose behavior in a magnetic field is described by the theory taking the SSLL into account.

REFERENCES

1. Kh. A. Amirkhanov, R. I. Bashirov, and M. M. Gadzhialiev, Fiz. Tverd. Tela (Leningrad) **3**, 3743 (1961) [Sov. Phys. Solid State **3**, 2713 (1962)].
2. I. V. Mochan, Yu. N. Obraztsov, and T. V. Smirnova, Fiz. Tverd. Tela (Leningrad) **4**, 1021 (1962) [Sov. Phys. Solid State **4**, 754 (1962)].
3. I. L. Drichko and I. V. Mochan, Fiz. Tverd. Tela (Leningrad) **6**, 1902 (1964) [Sov. Phys. Solid State **6**, 1498 (1964)].
4. S. M. Puri and T. H. Geballe, Phys. Rev. **136**, 1767 (1964).
5. S. M. Puri, Phys. Rev. **139**, 995 (1965).
6. A. N. Ansel'm and R. G. Tarkhanyan, Fiz. Tverd. Tela (Leningrad) **6**, 3357 (1964) [Sov. Phys. Solid State **6**, 2685 (1965)].
7. I. M. Tsidil'kovskiĭ, *Electrons and Holes in Semiconductors* (Nauka, Moscow, 1972).
8. V. M. Askerov, *Electronic Transport Phenomena in Semiconductors* (Nauka, Moscow, 1985).
9. M. M. Gadzhialiev, Fiz. Tekh. Poluprovodn. (Leningrad) **6**, 754 (1972) [Sov. Phys. Semicond. **6**, 653 (1972)].
10. M. M. Gadzhialiev, Izv. Vyssh. Uchebn. Zaved., Fiz., No. 4, 104 (1997).
11. M. M. Gadzhialiev and V. G. Badyul, Izv. Vyssh. Uchebn. Zaved., Fiz., No. 2, 97 (2000).

Translated by D. Mashovets

Effect of Annealing in Oxygen Radicals on Luminescence and Electrical Conductivity of ZnO:N Films

A. N. Georgobiani*, A. N. Gruzintsev**, V. T. Volkov**, and M. O. Vorob'ev*

* Lebedev Physical Institute, Russian Academy of Sciences, Leninskiĭ pr. 53, Moscow, 119991 Russia
e-mail: georg@sci.lebedev.ru
** Institute of Microelectronic Technology and High Purity Materials,
Chernogolovka, Moscow oblast, 142432 Russia
e-mail: gran@iptm-hpt.ac.ru
Submitted July 3, 2001; accepted for publication September 4, 2001

Abstract—It is shown that the introduction of a nitrogen acceptor impurity when growing zinc oxide films can result in the formation of hole conduction only after annealing in atomic oxygen vapor. Annealing affects not only electrical properties but also the luminescence of ZnO:N. The bands in the photoluminescence spectrum, which are related to nitrogen, appear in the ultraviolet and visible regions. © 2002 MAIK "Nauka/Interperiodica".

INTRODUCTION

Zinc oxide, by virtue of its piezoelectrical properties, its high electrical conductivity, and its optical transparency has found widespread application in various optoelectronic devices. The advances made in the last two years [1–3] in the preparation of ZnO of the *p*-type conduction with a hole concentration of $>10^{19}$ cm^{-3} by doping with acceptor impurities of Group V (N, P, and As) suggest that this material is one of the most promising in the family of wide-gap semiconductors of the II–VI and III–V groups. Zinc oxide doped by donor impurities of Al and Ga is traditionally used as a transparent contact with high radiation, chemical, and thermal resistance. Thus, high electron and hole conductivity in combination with a wide direct band gap (3.4 eV) make zinc oxide a promising material for the production of semiconductor sources of visible and ultraviolet emission.

Attempts at obtaining light-emitting diodes based on zinc oxide doped by donor and acceptor impurities have already been made [4, 5]. However, the diodes reported in these papers either did not luminesce at all, or had a very weak electroluminescence in the red region of the spectrum, whereas the undoped ZnO films usually have an intense ultraviolet photoluminescence in the region of bound excitons at the wavelength $\lambda \approx$ 370 nm [6]. Consequently, it is necessary to activate the doping impurity so that it does not only ensure the required value and type of conductivity, but also does not reduce the luminescence intensity, distort the emission spectrum, or diminish the transparency of zinc oxide. Only in one study [2], authors succeeded in obtaining *p*-type conduction using nitrogen dopant. In this case, doping was achieved by the addition of nitro-

gen oxide N$_2$O and the simultaneous employment of gallium oxide as an coactivator in the course of zinc oxide growth. The use of gaseous nitrogen as a transport gas did not result in hole conduction. It was concluded [2] that it is necessary to incorporate a donor impurity into the semiconductor for the enhancement of nitrogen solubility. However, the results indicate that double doping results in a sharp decrease in the carrier mobility by five orders of magnitude (to 0.05 cm^2 V^{-1} s^{-1}). In our opinion, the use of nitrogen and gallium oxides yields good results, first and foremost, due to the introduction of excess oxygen into a film. The reason for this is that the deficiency of oxygen in ZnO results in the appearance of intrinsic donor-type defects (interstitial zinc atoms and oxygen vacancies), which compensate acceptors caused by nitrogen.

The aim of this study was to gain insight into the effect of annealing on the conductivity of ZnO:N in a high-pressure atomic oxygen atmosphere, as well as to gain insight into the luminescent properties of this material. Employment of radicals (atoms) of oxygen [7–9] gives the highest possible effective pressure of oxygen above the film and allows us to shift the stoichiometry of the material in the direction of oxygen excess, thereby reducing the concentration of intrinsic defects of the donor type.

2. EXPERIMENTAL

We studied the photoluminescence and electrical properties of ZnO:N films prepared by the method of magnetron high-frequency sputtering onto amorphous substrates of thermally oxidized silicon SiO$_2$. Doping of the films was carried out by exposing the growing films to gaseous oxygen and nitrogen plasmas with var-
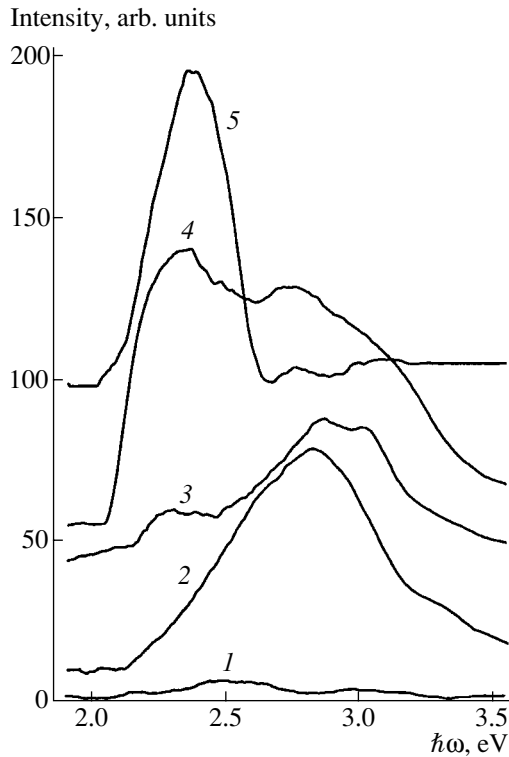
Intensity, arb. units

Fig. 1. Photoluminescence spectra of ZnO:N films (0.1 at. %) at 80 K before (*1*) and after annealing for 1 h in the atmosphere of conventional oxygen at the temperatures $T_a =$ (*2*) 400, (*3*) 500, (*4*) 600, and (*5*) 700°C.
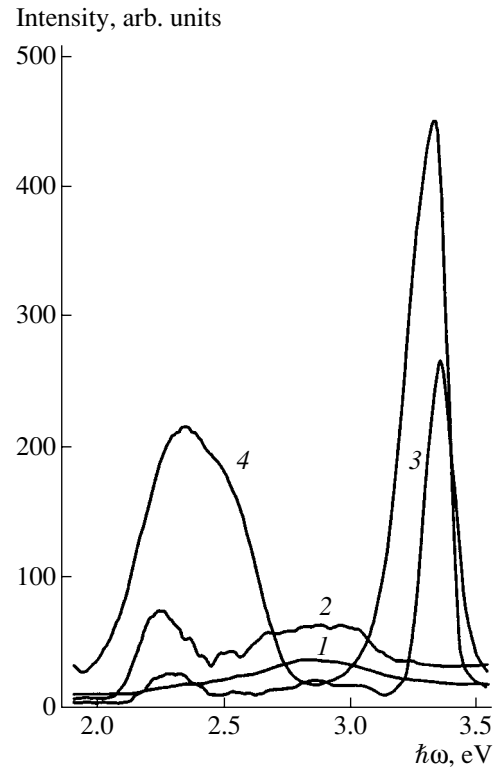
Intensity, arb. units

Fig. 2. Photoluminescence spectra of ZnO:N films (0.1 at. %) at 80 K after annealing for 1 h in the oxygen radicals at the temperatures $T_a =$ (*1*) 400, (*2*) 500, (*3*) 600, and (*4*) 700°C.

ious proportions of components. The analysis of the impurity content of unannealed films by secondary-ion mass spectrometry showed the presence of nitrogen in an amount dependent on the nitrogen partial pressure in the course of sputtering. For definiteness, we further studied ZnO:N films with a nitrogen content of 0.1 and 1 at. %. The use of oxygen as one of the components of magnetron plasma resulted in the required composition of ZnO in the films. Immediately after the deposition, owing to the large energy of sputtered ions, the films were amorphous, insulating, and did not luminesce. Their further annealing was required for crystallization, controlling the composition of point defects, and shifting of stoichiometry in the direction of oxygen excess.

ZnO:N films were annealed for various periods of time in the oxygen atmosphere (at the pressure of 10^{-2} Torr) and in the oxygen radicals (according to the technique described in [7]) at various temperatures. The photoluminescence (PL) spectra of the films were measured at liquid-nitrogen temperature under excitation with an LGI-505 pulsed nitrogen laser. Luminescence was analyzed using an MDR-6 double monochromator controlled by computer, which ensured a spectral resolution not worse than 1 meV for the slits employed. The film thickness was measured by a quartz thickness gauge in the course of sputtering and was 0.5 μm. In studies of crystalline structure and film surface mor-

phology, a JEOL-2000 transmission electron microscope was used. The conduction type was determined by measuring the thermoelectric power with the subsequent measurement of the carrier mobility of the best samples using the Hall method. The value of the conductivity was measured by the four-point probe method. The indium contacts were deposited for the films of *n*-conduction, and the gold contacts, for the films of *p*-conduction.

3. RESULTS

The analysis of PL spectra showed the presence of ultraviolet exciton (at the photon energy $\hbar\omega = 3.3–3.35$ eV), blue ($\hbar\omega = 2.7–2.8$ eV), and yellow-green emission ($\hbar\omega = 2.2–2.4$ eV) for annealed ZnO:N samples. The positions of emission peaks and their intensities depended on the temperature and atmosphere of annealing. The unannealed films, in fact, did not luminesce.

The PL spectra of doped ZnO:N (0.1 at. %) films prior to and after annealing at various temperatures in the atmosphere of conventional oxygen are presented in Fig. 1. One may note that at a low annealing temperature (up to $T_a = 500$°C) a blue line peaked at $\hbar\omega = 2.8$ eV is dominant in the PL spectrum (curves *2, 3*). As the annealing temperature increases, a green line peaked at

$\hbar\omega = 2.4$ eV emerges. At $T_a = 700°C$, this line becomes dominant for the ZnO:N films with low nitrogen concentration (Fig. 1, curve *5*). The PL spectra of ZnO:N films (0.1 at. %) annealed in atomic oxygen (Fig. 2) differ radically from those shown in Fig. 1. Here, at a low annealing temperature, the luminescence blue line $\hbar\omega = 2.8$ eV (curves *1, 2*) is also dominant. However, at high annealing temperatures, $T_a = 600–700°C$, along with the green band, an intense ultraviolet emission appears with the peak at $\hbar\omega = 3.3–3.35$ eV.

Now, let us consider PL spectra of ZnO:N films with a high nitrogen content, 1 at. % (Figs. 3, 4). In this case, a low-temperature annealing in the atmosphere of conventional oxygen also results in the appearance of blue emission with the peak at $\hbar\omega = 2.8$ eV, but a short-wavelength shoulder exists at 3.0 eV (Fig. 3, curves *3, 4*), which transforms into a shoulder at 3.1 eV on the intense excitonic band $\hbar\omega = 3.3$ eV at the highest annealing temperature $T_a = 700°C$ (curve *5*). In the last case, similar to the spectra for low nitrogen concentrations, a green emission appears, but now it consists of two elementary bands with peaks at $\hbar\omega = 2.25$ and 2.6 eV. Annealing in the atmosphere of oxygen radicals results in the PL of ZnO:N (1 at. %) films, whose spectra are qualitatively similar to those of the films with low nitrogen concentration (Fig. 2). Here also, at low annealing temperatures, the blue line $\hbar\omega = 2.8$ eV is dominant, and, at high temperatures, the green emission at 2.4 eV and the ultraviolet excitonic emission at 3.3 eV are dominant.

We now turn our attention to the dependence of the conductivity of ZnO:N films on the annealing conditions; this dependence is listed in the table. First of all, we note a reduction of the film resistivity as a result of the low-temperature annealing in the oxygen atmosphere up to the temperature $T_a = 600°C$. In this case, the further increase of the annealing temperature to $T_a = 700°C$ results in a sharp increase in resistivity up to 10^6 Ω cm. It is important that, independent of the nitrogen impurity concentration in the film, annealing in the atmosphere of unactivated oxygen brings about the *n*-type conduction. The use of oxygen radicals in the atmosphere of annealing, in the opinion of the authors of [8], enhances the effective pressure of atomic oxygen by more than six orders of magnitude. This fact, as can be seen from the table, results in the change not only of the value, but also of the type of conduction of ZnO:N films. In this case, the holes are the majority charge carriers after film annealing at temperatures of 400–600°C. The ZnO:N (1 at. %) films of *p*-type conduction obtained after annealing at the temperature $T_a = 500°C$ have the lowest resistivity. The hole mobility measured by the Hall method was 5 cm^2 V^{-1} s^{-1} for these films. The further increase in the annealing temperature results in the resistivity increase and in the *n*-type conduction. Annealing at $T_a = 700°C$ in any oxy-
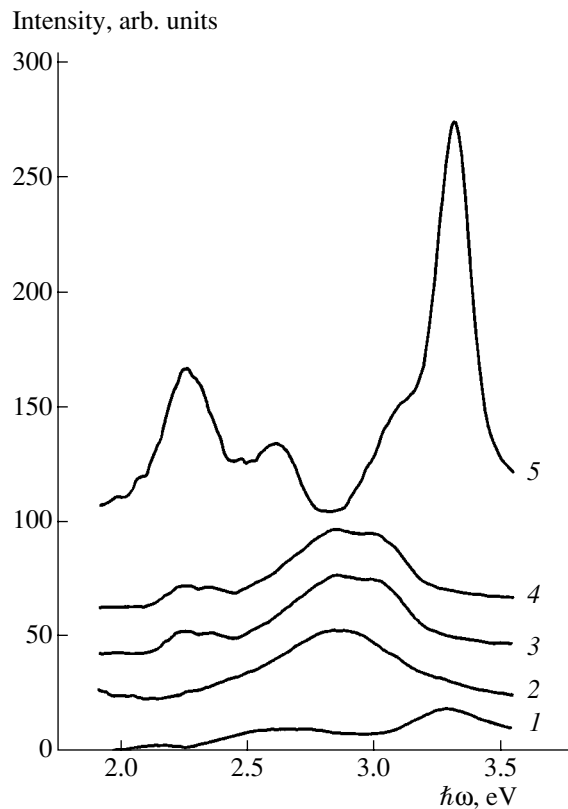
Fig. 3. Photoluminescence spectra of ZnO:N films (1 at. %) at 80 K before (*1*) and after annealing for 1 h in the atmosphere of conventional oxygen at the temperatures $T_a =$ (*2*) 400, (*3*) 500, (*4*) 600, and (*5*) 700°C.
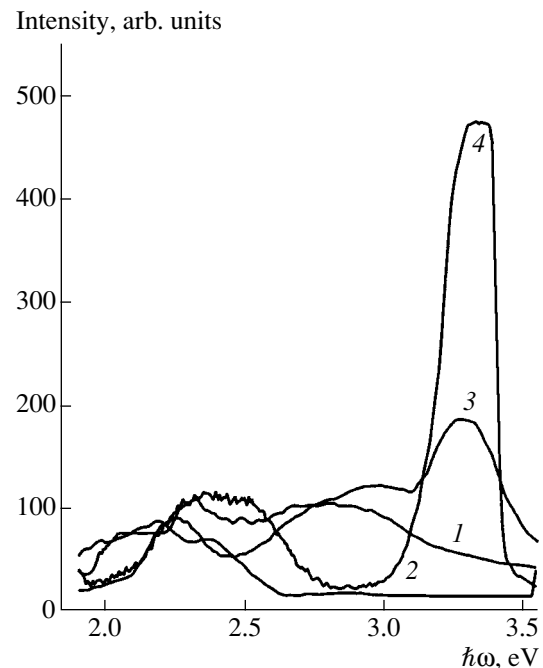

Fig. 4. Photoluminescence spectra of ZnO:N films (1 at. %) at 80 K after annealing for 1 h in the oxygen radicals at the temperatures $T_a =$ (*1*) 400, (*2*) 500, (*3*) 600, and (*4*) 700°C.

Resistivity (in Ω cm) and conduction type of ZnO:N films annealed under various conditions

Sample	Without annealing	Annealing conditions	T_a			
			400°C	500°C	600°C	700°C
ZnO:N (0.1 at. %)	1.3×10^3	Without radicals	4.2×10^4	6.2×10^2	6.2	1.2×10^6
ZnO:N (0.1 at. %)	1.3×10^3	In radicals	(*p*) 10^6	(*p*) 8.3×10^4	(*p*) 1.1×10^5	1.1×10^6
ZnO:N (1 at. %)	1.6×10^3	Without radicals	3.1×10^4	1.4×10^3	8.3	10^6
ZnO:N (1 at. %)	1.6×10^3	In radicals	(*p*) 1.2×10^6	(*p*) 7×10^4	(*p*) 9.8×10^4	1.1×10^6

gen atmosphere resulted in the formation of semiinsulating films.

4. DISCUSSION AND CONCLUSION

Thus, the results presented above testify to the heavy dependence of luminescent and electrical properties of ZnO:N films on the type of oxygen atmosphere and on the annealing temperature. One should note that the annealing duration of ~1 h is necessary for obtaining films of uniform thickness. Annealing for a longer time affected the luminescent characteristics only slightly. The PL spectrum changes of ZnO:N films in the course of annealing indicate that the dominant intrinsic or impurity point defects are also profoundly affected. According to the published data [10, 11], the green band with the peak at $\hbar\omega = 2.4$ eV in the pure ZnO is related to the oxygen vacancy V_O in the form of a F^+-center. The blue band in the region of 2.8–3.0 eV is caused by acceptors (zinc vacancies V_{Zn}) formed owing to the oxygen excess in the crystal lattice of ZnO. It is widely believed that ultraviolet emission in the region $\hbar\omega = 3.3$–3.35 eV is caused by the radiative recombination of bound excitons. A more detailed analysis of the excitonic emission requires the lowering of the PL measurement temperature to 4.2 K, especially as the excitonic bands in the films, as a rule, are broadened and shifted in comparison with peaks in crystals owing to the substrate influence.

In this context, we give considerable attention, first and foremost, to the analysis of the visible luminescence of our films. The predominance of blue emission at $\hbar\omega = 2.8$ eV at a low annealing temperature (no higher than 500°C) of ZnO:N films in the atmosphere of conventional oxygen and its radicals indicates that there is an oxygen excess in the film composition. Due to this fact, the contribution of intrinsic donor defects V_O and Zn_i to the film conductivity is negligible and is determined by impurity and intrinsic acceptors N_O and V_{Zn}. That is why it is possible to obtain the hole conduction by annealing in the atmosphere of oxygen radicals (see table). The annealing temperature increase up to $T_a = 600$–700°C results in the appearance of green

emission at $\hbar\omega = 2.4$ eV, which is related to oxygen vacancies. This means that the concentration of donor-type intrinsic defects increases, and they compensate acceptors.

There exists a critical annealing temperature which, being exceeded, does not result in hole conduction [8]. According to the data presented above, the ZnO:N films of *p*-type conduction are obtained by annealing in oxygen radicals in the temperature range $T_a = 400$–600°C. Consequently, the critical annealing temperature is within the range 600–700°C for a given density of the radical atmosphere. It is impossible to obtain the *p*-type conduction in the unactivated oxygen atmosphere.

At the high annealing temperature $T_a = 700$°C, the semi-insulating ZnO:N films with bright luminescence are obtained. The high PL intensity in this case is caused by the perfect polycrystalline structure of films with large-size grains (100 nm). At a low annealing temperature, the fraction of quasi-amorphous material is rather large and the sizes of crystallites are significantly smaller. This is confirmed not only by studies of our films using a transmission electron microscope, but also by the absence of excitonic lines in the spectra after low-temperature annealing. It can be seen from the PL spectra presented above that the excitonic ultraviolet band appears only as a result of annealing at the highest temperature $T_a = 700$°C. It is worthwhile to note also that at this annealing temperature and for a large nitrogen concentration in the film (1 at. %), the PL bands appear which are not characteristic of intrinsic defects, that is, a green band at $\hbar\omega = 2.6$ eV and a blue band at $\hbar\omega = 3.0$–3.1 eV (Fig. 3). Their appearance can be accounted for by the participation of impurity defects N_O in the radiative recombination: the former emission is caused by an electron transition from the level V_O to the level N_O, and the latter emission is related to the transition from the conduction band to this level. As noted above, conventional green and blue PL bands with peaks at $\hbar\omega = 2.4$ and 2.8 eV, respectively, are related to intrinsic defects (oxygen and zinc vacancies) in the zinc oxide.

REFERENCES

1. T. Yamamoto and H. Katayama-Yoshida, Jpn. J. Appl. Phys. **38**, L166 (1999).
2. M. Joseph, H. Tabata, and T. Kawai, Jpn. J. Appl. Phys. **38**, L1205 (1999).
3. K. Minegishi, Y. Kowai, Y. Kikuchi, *et al.*, Jpn. J. Appl. Phys. **36**, L1453 (1997).
4. Y. R. Ryu, W. J. Kim, and H. W. White, J. Cryst. Growth **219**, 419 (2000).
5. X. Guo, J. Choi, H. Tabata, and T. Kawai, Jpn. J. Appl. Phys. **40**, L177 (2001).
6. S. B. Zhang, S. H. Wei, and A. Zunger, Phys. Rev. B **63**, 075205 (2001).
7. T. V. Buthuzi, T. G. Chelidze, and A. N. Georgobiani, Phys. Rev. B **58**, 10692 (1998).
8. A. N. Georgobiani and M. B. Kotlyarevskii, Nucl. Phys. B **61**, 341 (1998).
9. A. N. Georgobiani, M. B. Kotlyarevskii, V. V. Kidalov, and I. V. Rogozin, Inorg. Mater. **33**, 185 (1997).
10. W. van Gool and A. P. Cleiren, Philips Res. Rep., No. 15, 238 (1960).
11. W. van Gool, Philips Res. Rep., No. 3, 61 (1963).

Translated by T. Galkina

Effective Exciton Mass in III–V Semiconductors

N. S. Averkiev and K. S. Romanov

Ioffe Physicotechnical Institute, Russian Academy of Sciences, ul. Politekhnicheskaya 26, St. Petersburg, 194021 Russia
e-mail: averkiev@pop.ioffe.rssi.ru
Submitted August 27, 2001; accepted for publication September 10, 2001

Abstract—Effective masses characterizing exciton subbands in semiconductors with a complex valence-band structure are calculated in the context of the zero-radius potential method. Good agreement is found between the results of these model calculations and previous numerical calculations for bulk GaAs. © *2002 MAIK "Nauka/Interperiodica"*.

INTRODUCTION

It is known that, in semiconductors with a complex band structure, motion of the exciton as a whole leads to a change in its binding energy. In addition, the exciton effective mass differs for different values of the total exciton angular momentum component along the direction of motion. The latter effect results in the splitting of the exciton ground state, depending on the direction and the magnitude of its momentum. Calculation of the dependence of the exciton binding energy on its total momentum, with exact Coulomb attraction between the electron and the hole taken into account, is a very complicated mathematical problem, and only the numerical solution can be obtained. However, in many cases we only need to know the effective mass. In this paper, the zero-radius potential model is used to calculate exciton levels and corresponding effective masses for semiconductors with a GaAs-like energy band structure. Effective mass dependence on the band-structure parameters is determined. To simplify the calculations, a spherical approximation for the complex valence band and the conduction band is used.

CALCULATION

In the context of the zero-radius potential model, it is assumed that Coulomb electron–hole interaction can be replaced by a δ-function interaction. Then, the Schrödinger equation takes the form

$$\hat{H}\psi(\mathbf{r}_e, \mathbf{r}_h) + V_0\delta(\mathbf{r}_e - \mathbf{r}_h)\psi = E\psi, \qquad (1)$$

where

$$\hat{H} = -\left\{-\frac{\hat{\mathbf{k}}_e^2}{2m_e} + \frac{1}{m_0}\left[-\left(\gamma_1 + \gamma\frac{5}{2}\right)\frac{\hat{\mathbf{k}}_h^2}{2} + \gamma(\hat{\mathbf{k}}_h\mathbf{J})^2\right]\right\}. \quad (2)$$

Here, $\mathbf{k}_e$ and $\mathbf{k}_h$ are the electron and the hole momentum operators, respectively; V_0 is the parameter characterizing the strength of electron–hole interaction; $\mathbf{J}$ is a 4×4 matrix; γ and γ_1 are Luttinger parameters for the Γ_8-type valence band [1]; m_e is the effective electron mass in the conduction band; and m_0 is the free-electron

mass. In the zero-radius potential model [2], the δ-function potential in the Schrödinger equation can be replaced by the following boundary condition:

$$\left.\frac{\frac{\partial}{\partial r}(r\psi_i(\mathbf{r}))}{r\psi_i(\mathbf{r})}\right|_{r \to 0} = -\alpha, \qquad (3)$$

where $\mathbf{r} = \mathbf{r}_e - \mathbf{r}_h$ is the spacing between the electron and the hole. To determine the eigenvalues and eigenfunctions of the Hamiltonian, it is convenient to consider the problem in the momentum representation. Introducing $\xi = \dfrac{\gamma_1}{\gamma}$ and $\eta = \dfrac{m_0}{\gamma m_e}$, we obtain

$$\hat{H} = -\frac{\gamma}{m_0}\left\{-\eta\frac{\mathbf{k}_e^2}{2} + \left[-\left(\xi + \frac{5}{2}\right)\frac{\mathbf{k}_h^2}{2} + (\mathbf{k}_h\mathbf{J})^2\right]\right\}. \quad (4)$$

Since the Hamiltonian is invariant under the time reversal, the solutions are doubly degenerate. Thus, among four linearly independent solutions, it is possible to find the two belonging to the same energy with the following property: one of the wave-function components equals zero, and the other one can be expressed in terms of the two remaining components. Such a solution has the form

$$\psi = \begin{pmatrix} a \\ b \\ -\dfrac{H_{41}}{H_{43}}a - \dfrac{H_{42}}{H_{43}}b \\ 0 \end{pmatrix}, \qquad (5)$$

where H_{ij} are the components of the Hamiltonian (4). The equation for a and b can be written as [3]

$$\begin{pmatrix} H_{11} - \dfrac{H_{41}}{H_{43}}H_{13} - \varepsilon & H_{12} - \dfrac{H_{42}}{H_{43}}H_{13} \\ H_{21} - \dfrac{H_{41}}{H_{43}}H_{23} & H_{22} - \dfrac{H_{42}}{H_{43}}H_{23} - \varepsilon \end{pmatrix}\begin{pmatrix} a \\ b \end{pmatrix} = \begin{pmatrix} A \\ B \end{pmatrix}, (6)$$

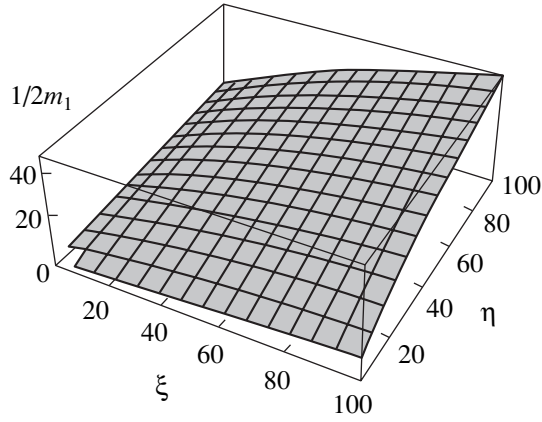where A and B are arbitrary constants.

Its solution can be represented as

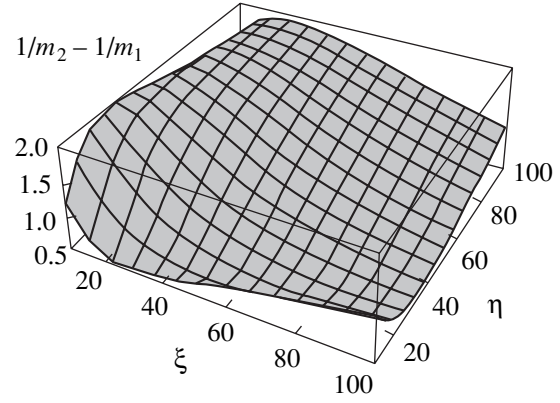**Fig. 1.** Exciton effective mass in the lower subband as a function of the band-structure parameters.

Fig. 2. Exciton subband splitting in relation to the parameters ξ and η.

$$\begin{pmatrix} a \\ b \end{pmatrix} = \begin{pmatrix} A\dfrac{-\dfrac{(\xi-1)}{2}k_h^2 - \dfrac{3}{2}k_{hz}^2 - \dfrac{\eta k_e^2}{2} - \varepsilon}{\Delta} + B\dfrac{3}{4}k_{h\perp}^2\dfrac{4k_{hz}^2 + k_{h\perp}^2}{\sqrt{3}k_{hz}(ik_{hx} - k_{hy})\Delta} \\ A\dfrac{\sqrt{3}k_{hz}(ik_{hx} - k_{hy})}{\Delta} + B\dfrac{-\dfrac{(\xi+1)}{2}k_h^2 + \dfrac{3}{2}k_{hz}^2 - \dfrac{\eta k_e^2}{2} - \varepsilon}{\Delta} \end{pmatrix}, \quad (7)$$

where Δ is the determinant of the set of Eqs. (6).

Next, we have to apply boundary condition (3). To do this, let us express the electron and hole momenta in terms of the total exciton momentum $\mathbf{p} = \dfrac{\mathbf{k}_h + \mathbf{k}_e}{2}$ and the relative motion momentum $\mathbf{k} = \dfrac{\mathbf{k}_h - \mathbf{k}_e}{2}$. The boundary condition takes the form

$$\left.\frac{\partial(a(\mathbf{r},\mathbf{p}))}{\partial r}\right|_{r\to 0} = -\alpha a(\mathbf{r},\mathbf{p})|_{r\to 0},$$

$$\left.\frac{\partial(b(\mathbf{r},\mathbf{p}))}{\partial r}\right|_{r\to 0} = -\alpha b(\mathbf{r},\mathbf{p})|_{r\to 0}, \quad (8)$$

where $a(\mathbf{r},\mathbf{p})$ and $b(\mathbf{r},\mathbf{p})$ are the Fourier transforms of a and b, respectively, over $\mathbf{k}$.

Since the conduction and the valence bands are assumed to be spherically symmetric, the calculations can be simplified by considering angle-averaged Fourier transforms. Thus, for the component a,

$$a(r,p) = 2\pi \int\limits_0^\pi \int\limits_0^\infty \int\limits_0^\pi e^{ikr\sin\Theta} a(k,\vartheta)\sin\vartheta\, d\vartheta\, dk\, d\Theta$$

$$= \frac{4\pi}{r}\int\limits_0^\infty \int\limits_0^\pi k\sin(kr)a(k,\vartheta)\sin\vartheta\, d\vartheta\, dk,$$

and similar calculations can be carried out for b.

Since (i) $a(-k,\vartheta)|_{-\mathbf{p}} = a(k,\vartheta)|_{\mathbf{p}}$ and (ii) due to spherical symmetry, only even orders of $\mathbf{p}$ will appear, for the purposes of calculating the exciton effective mass it is possible to retain only the terms of second order in $\mathbf{p}$. The wave functions for the two exciton states corresponding to different energies for $\mathbf{p} \neq 0$ can be determined from (7) setting first $A \neq 0$, $B = 0$ and then $A = 0$, $B \neq 0$. Expressions for the wave functions in the coordinate representation are very complicated, and we do not present them here.

Substituting expressions for $a(r, p)$ and $b(r, p)$ into corresponding boundary conditions, we determine first the energy ε_0 of the exciton at rest and then the energy ε of the exciton with $p \neq 0$. The expressions for the wave function for $p \neq 0$ and the dispersion equation are rather complicated. The dispersion equation has the form of a linear–fractional function, with ξ and η as parameters. It was found that the effective exciton mass is independent of α (α determines the exciton binding energy at $p = 0$).

The expression for ε can be written as

$$\varepsilon = -|\varepsilon_0| + \frac{p^2}{2m_{1,2}}, \quad (9)$$

where

$$\varepsilon_0 = \gamma \frac{\hbar^2\alpha^2}{m_0}\frac{2(\xi+\eta+2)(\xi+\eta-2)(\xi+\eta)^2}{((\xi+\eta+2)^{3/2} + (\xi+\eta-2)^{3/2})^2},$$

and m_1 and m_2 are the effective exciton masses.

The dependence of the coefficient $1/2m_1$ (expressed in units of $\hbar^2\gamma/m_0$ for the lower subband) on ξ and η is shown in Fig. 1. The difference of the inverse effective masses of the two subbands $1/2m_1 - 1/2m_2$ is plotted in Fig. 2.

It is of interest to compare the results obtained in this study with the numerical calculation of the effective exciton mass in GaAs [4]. According to [4], $1/m_1 \approx$ 3.45; the method suggested in this paper yields $1/m_2 \approx 4$. Such agreement should be considered as satisfactory.

CONCLUSION

Thus, in this study we calculated translational masses for two exciton subbands in bulk cubic-lattice III–V semiconductors. The results obtained can be applied to the analysis of the optical properties of these compounds, because translational masses do not depend on the initial binding energy. Furthermore, the suggested method can be used to estimate effective exciton masses in two-dimensional structures based on semiconductors with a complex band structure.

REFERENCES

1. J. M. Luttinger, Phys. Rev. **102**, 1030 (1956).

2. Yu. N. Demkov and V. N. Ostrovskii, *Zero-Range Potentials and Their Applications in Atomic Physics* (Leningr. Gos. Univ., Leningrad, 1975; Plenum, New York, 1988).

3. C. Kittel, *Quantum Theory of Solids* (Wiley, New York, 1963; Nauka, Moscow, 1967).

4. E. O. Kane, Phys. Rev. B **11**, 3850 (1975).

Translated by M. Skorikov

ELECTRONIC
AND OPTICAL PROPERTIES
OF SEMICONDUCTORS

Special Features of Charge Transport in PbGa$_2$Se$_4$ Crystals

B. G. Tagiev, N. N. Musaeva, and R. B. Dzhabbarov

Institute of Physics, Academy of Sciences of Azerbaijan, Baku, 370143 Azerbaijan
Submitted February 15, 2001; accepted for publication June 20, 2001

Abstract—The current–voltage (I–V) characteristics of PbGa$_2$Se$_4$ single crystals grown by the Bridgman–Stockbarger method with a resistivity of 10^{10}–10^{12} Ω cm were measured. The value of the majority carrier mobility $\mu = 14$ cm^2 V^{-1} s^{-1}, calculated by the differential method of analysis of I–V characteristics, makes it possible to evaluate a number of parameters: the carrier concentration at the cathode ($n_{c0} = 2.48$ cm^{-3}), the width of the contact barrier $d_c = 5.4 \times 10^{-8}$ cm, the cathode transparency $D_c^* = 10^{-5}$–10^{-4} eV, and the quasi-Fermi level $E_F = 0.38$ eV. It is found that a high electric field provides the charge transport through PbGa$_2$Se$_4$ crystals in accordance with the Pool–Frenkel effect. The value of the dielectric constant calculated from the Frenkel factor is found to be equal to 8.4. © *2002 MAIK "Nauka/Interperiodica".*

The ternary chalcogenide compound PbGa$_2$Se$_4$ is a photosensitive material and is of great interest as a material for manufacturing photodetectors and photoconverters operating in a wide spectral range (0.4–1.20 µm) [1].

The temperature dependences of dark and photon-induced currents, the energy levels of recombination centers, and the band gap corresponding to the direct and indirect allowed optical transitions in PbGa$_2$Se$_4$ single crystals have been studied in our previous publications [1, 2].

In this paper, we preset the results of the measurements of the current–voltage (I–V) characteristics of PbGa$_2$Se$_4$ single crystals with a resistivity of 10^{10}–10^{12} Ω cm (at $T = 300$ K). Samples 50 to 200 µm in thickness were prepared for the measurements. Indium contacts were deposited on the cleaved surfaces of crystals. Prior to measurements, the samples were heated to 380 K; then they were slowly cooled to 300 K in the dark during two hours in high vacuum.

The I–V characteristics typical of all samples are shown in Fig. 1. It can be seen that the current through the In–PbGa$_2$Se$_4$–In structure increases by 3–4 orders of magnitude with an increase in the electric field from 10^2 to 10^5 V/cm depending on temperature. As the temperature is lowered, the dependence of current on voltage becomes more pronounced, and the I–V characteristics shift to stronger electric fields. A steep increase in current with increasing voltage ($I \propto U^n$) is observed in the initial portion the I–V characteristics. Then, at the voltages of up to 120 V, depending on temperature, the rate of current increase reduces.

The current in a sample is limited by a contact acting as a barrier in the blocking direction; thus, a minor increase in voltage (≈ 10 V) may produce the breakdown of a barrier due to the impact ionization in the

space-charge region, which causes a rapid increase at low voltages.

Above 40 V, the current increases relatively slowly, which is caused by the trapping of injected electrons by the empty levels $E_t = 0.72$ eV. This process continues until the voltage reaches a limiting magnitude corresponding to the complete filling of traps. However, if
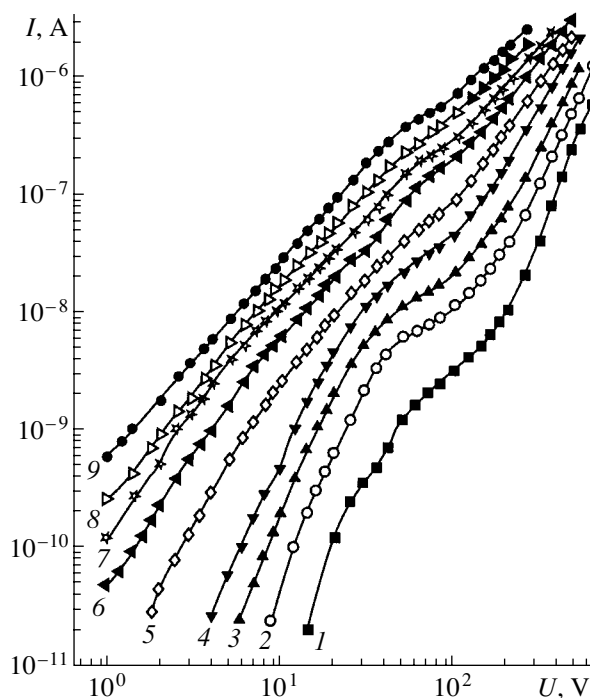

Fig. 1. Current–voltage characteristics of PbGa$_2$Se$_4$ single crystal $L = 120$ µm in thickness at $T = $ (*1*) 125, (*2*) 161, (*3*) 181, (*4*) 189, (*5*) 230, (*6*) 248, (*7*) 340, (*8*) 360, and (*9*) 380 K.
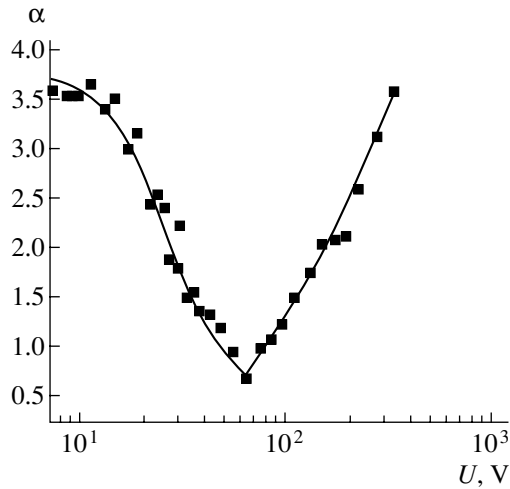
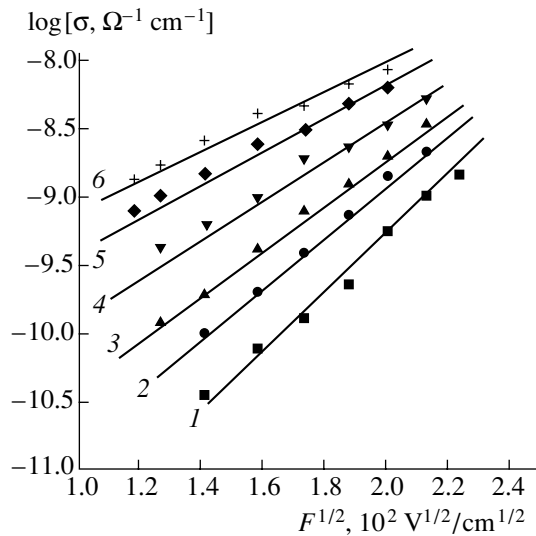**Fig. 2.** Dependence of α on U at $T = 181$ K for PbGa$_2$Se$_4$ single crystal.

Fig. 3. Dependence of $\log\sigma$ on $\sqrt{F}$ for PbGa$_2$Se$_4$ single crystal at $T = (1)$ 125, (2) 161, (3) 181, (4) 198, (5) 230, and (6) 248 K.
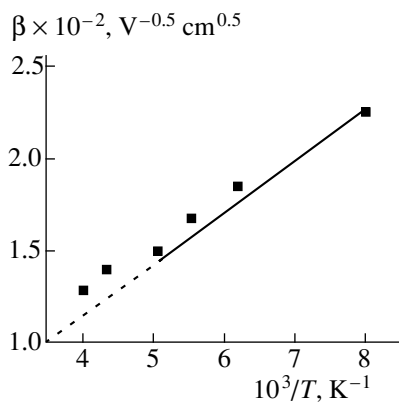

Fig. 4. Dependence of β on $10^3/T$ for PbGa$_2$Se$_4$.

the sample includes a pronounced inhomogeneity with increased resistance, the conductance of this inhomogeneous region reduces with increasing voltage.

Several approximate methods are known for the analytical description of the I–V characteristics. The dependence of a current I on U for In–PbGa$_2$Se$_4$–In structures in our study was analyzed in terms of the power law ($I \propto U^\alpha$) [3, 4]:

$$\alpha = \frac{d\log I}{d\log U} = \frac{dI}{dU}\frac{U}{I}. \quad (1)$$

The dependence $\alpha(U, I)$ at a temperature of 181 K has one extremum ($\alpha_{min} = 0.66$ at $U_{min} = 65$ V ($I_{min} = 1.37 \times 10^{-8}$ A)) (Fig. 2).

According to the theory suggested in [3], the activation energy of deep levels is described by the formula

$$E_t = kT\ln\left[2\left(\frac{2\pi m_n kT}{h^2}\right)^{3/2}\frac{3(1+\alpha_m)e\mu SV_m}{2\alpha_m^2(5-8\alpha_m^2)LI_m}\right], \quad (2)$$

where $2\left(\frac{2\pi m_n kT}{h^2}\right) \approx 10^{19}$ cm^{-3}, $\left(\frac{m_n}{m}\frac{T}{300\text{ K}}\right)^{3/2} = N_c$ is the effective density of states in the conduction band, $m_n = 0.5m_e$ is the effective mass, h is Planck's constant, k is the Boltzmann constant, T is the absolute temperature, L is the sample thickness, and S is the contact area. Using the values E_t obtained from the temperature dependences of conductivity, the mobility of the majority carrier was calculated as $\mu = 14$ cm^2 V^{-1} s^{-1}. This makes it possible to determine such parameters as $n_{c0} = 2.48 \times 10^8$ cm^{-3} (the concentration of carries at the cathode), $d_c = 5.4 \times 10^{-8}$ cm (the width of the contact barrier), $D_c^* = 10^{-5}–10^{-4}$ eV (the cathode transparency), and $E_F = 0.38$ eV (the quasi-Fermi level) [4, 5].

As can be seen in Fig. 1, after passing the region of slow growth, the current again begins to increase, which indicates that thermal and field ionization of traps occurs. In order to verify the validity of this mechanism for PbGa$_2$Se$_4$ crystals, we used the Pool–Frenkel theory [6], which suggests the following relation between the electrical conductivity σ in strong electric fields ($F \neq 0$) and the electric field F:

$$\sigma = \sigma_0\exp(\beta\sqrt{F}).$$

Here, σ_0 is the conductivity for $F = 0$ or in the region of the validity of Ohm's law, $\beta = \dfrac{\sqrt{e^3}}{kT\sqrt{\pi\varepsilon\varepsilon_0}}$ is the Frenkel factor, e is the electron charge, and ε is the dielectric constant of a semiconductor.

The $\log\sigma$ as a function of $\sqrt{F}$ for an In–PbGa$_2$Se$_4$–In structure at various temperatures is shown in Fig. 3. One can easily see that the slope β of the straight lines $\log\sigma = f(\sqrt{F})$ increases with a decrease in temperature

(Fig. 4). This indicates that the ionization of traps in strong electric fields depends only on temperature. The magnitude of ε for PbGa$_2$Se$_4$ determined from the experimental value of β was found to be equal to 8.4.

REFERENCES

1. B. G. Tagiev, O. B. Tagiev, R. B. Dzhabbarov, and N. N. Musaeva, Neorg. Mater. **35**, 33 (1999).

2. B. G. Tagiev, N. N. Musaeva, and R. B. Dzhabbarov, Fiz. Tekh. Poluprovodn. (St. Petersburg) **33**, 39 (1999) [Semiconductors **33**, 34 (1999)].

3. A. N. Zyuganov and S. V. Svechnikov, *Injection-Contact Phenomena in Semiconductors* (Naukova Dumka, Kiev, 1981).

4. Z. V. Berishvili, A. N. Zyuganov, S. V. Svechnikov, and P. S. Smertenko, Poluprovodn. Tekh. Mikroélektron., No. 28, 23 (1978).

5. A. N. Zyuganov, P. S. Smertenko, and E. P. Shul'ga, Poluprovodn. Tekh. Mikroélektron., No. 29, 48 (1979).

6. Ya. I. Frenkel', Zh. Éksp. Teor. Fiz. **8**, 1292 (1938).

Translated by A. Zalesskiĭ

Efficiency of the Intercalation of Aluminum Atoms under a Monolayer and Submonolayer Two-Dimensional Graphite Film on a Metal

N. R. Gall*, E. V. Rut'kov, and A. Ya. Tontegode

Ioffe Physicotechnical Institute, Russian Academy of Sciences, Politekhnicheskaya ul. 26, St. Petersburg, 194021 Russia
*e-mail: gall@ms.ioffe.rssi.ru
Submitted May 21, 2001; accepted for publication May 28, 2001

Abstract—Intercalation of aluminum atoms under a two-dimensional graphite film on a metal was studied by high-resolution Auger spectroscopy. The spectra were recorded directly from the highly heated (up to 2100 K) sample. It is shown that the efficiency of this process increases significantly if the film is of the island type, rather than continuous, and if part of the metal surface is not covered with graphite. It is concluded that the graphite-island boundaries are the defects via which the intercalating atoms penetrate under the graphite film. © 2002 MAIK "Nauka/Interperiodica".

1. INTRODUCTION

Intercalation, i.e., spontaneous penetration of adsorbed particles under two-dimensional (2D) graphite films on metals, was first observed in 1981 [1] and was later described in detail in reviews [2, 3] and in a monograph [4]. Two-dimensional graphite films on metals are remarkable objects, which differ radically in their properties from other forms of adsorbed carbon. Such films were observed at the surfaces of many metals (Ir, Re, Pt, Ni, Rt, and Mo); these films can be envisaged as a graphite monolayer that consists of strongly bonded carbon atoms (a "graphite carpet"); this monolayer is located at the metal surface and retains its specificity and structure, which is supported by the measurements using tunneling and atomic-force microscopies [5, 6]. Like the layers in a graphite crystal, the 2D graphite film is linked to the surface only by weak Van der Waals forces without electron exchange [1–9].

Specific features of intercalation under 2D graphite films are virtually independent of the substrate but depend heavily on the type of intercalating particle. In order to describe quantitatively the above process, we have introduced the term "intercalation efficiency," which is the fraction of particles penetrated under the film in reference to all adsorbed particles. The atoms with low ionization potentials (Cs, K, and Na) intercalate under the film at a temperature of $T \approx 300$ K with an efficiency close to 0.5 and accumulate there only up to the monolayer concentration. As T increases, the process efficiency decreases sharply; at $T > 800$ K, intercalation has not been observed. In contrast, the atoms with large ionization potentials (Pt, Ni, Si, and Au) intercalate only at $T \geq 1000$ K with an efficiency close to unity and form multilayer films under graphite. As T increases, the intercalation efficiency also decreases

drastically and is no higher than several percent at 1500 K.

The objective of this study was to gain insight into the intercalation of a 2D graphite film by atoms with the intermediate ionization potential $V_i \approx 6$ eV. We chose aluminum atoms with $V_i = 5.94$ eV; we also selected two metals (iridium and rhenium), which differed in the formation mechanisms of 2D graphite film at the surface, as the substrates.

2. EXPERIMENTAL

The experiments were carried out in an ultrahigh-vacuum chamber under the residual pressure $P < 10^{-10}$ Torr in a high-resolution electron Auger spectrometer equipped with a prism energy analyzer [10]. For the samples, we used directly heated rhenium and iridium ribbons with an area of 50×1 mm^2 and a thickness of 0.02 mm with the faces of $(10\bar{1}0)$ and (111) at the surface, respectively. We were able to record the Auger spectra directly from the sample heated to a temperature as high as $T \approx 2100$ K.

The ribbons were cleaned and texturized by heating by an alternating current first in an oxygen atmosphere at $T = 1500$ K and then in ultrahigh vacuum at $T = 2300$ K. After cleaning, we did not observe any peaks in the Auger spectrum except for those of the corresponding metals; the work functions for the ribbons were found to be 5.15 and 5.75 eV and were typical of the above faces. The ribbon surface was uniform with respect to the work function. The sample temperature was measured using a micropyrometer; the sample temperature in the range unaccessible for pyrometric measurements was determined using a linear extrapolation of the heater-current dependence of the temperature.

Aluminum was deposited uniformly over the entire operating area of the ribbons using a specially designed getter source. The principle of the source operation consisted in the preliminary dissolution of an aluminum charge in the iridium or platinum ribbon (with an aluminum mass amounting to 5–10% of the ribbon mass) with subsequent thermal desorption of Al atoms segregating at the surface.

3. PRODUCTION AND CHARACTERIZATION OF A TWO-DIMENSIONAL GRAPHITE FILM ON THE (111) Ir AND ($10\bar{1}0$) Re SURFACES

A two-dimensional graphite film on the iridium surface was formed by adsorption of benzene molecules using the method described elsewhere [3]. The benzene molecules arriving at the metal-sample surface decompose at $T = 1500$–1800, hydrogen is desorbed, and carbon remains in the adsorption layer. Carbon atoms are not dissolved in the iridium bulk and form 2D graphite islands at the surface; when these islands merge together, they form a continuous graphite film with a strictly monolayer thickness. The two-dimensional character of the film is ensured automatically because the C_6H_6 molecules do not decompose at a passive graphite layer, and the arrival of carbon atoms to the adsorption layer ceases. In the case of rhenium, the formation of a 2D graphite film is preceded by saturation of the ribbon with carbon to the limiting-solubility level. After saturation with carbon, the benzene vapors are pumped out, and all subsequent measurements are performed under ultrahigh-vacuum conditions.

As has been shown [2], physicochemical properties of 2D graphite films are nearly independent of the substrate; thus, the choice of iridium or rhenium is governed only by convenience of the experiment. A 2D graphite film on iridium is stable at $T < 1900$ K, whereas the thermal stability of a 2D graphite film on rhenium is limited by $T < 1200$ K (for higher T, carbon can diffuse from the bulk, which results in the growth of a multilayer graphite film). However, this drawback can turn out to be an advantage, because a submonolayer 2D graphite film with a specified fraction of the surface area s covered with graphite islands can be formed easily and reproducibly on the rhenium substrate (see [10]).

INTERACTION OF ALUMINUM WITH THE RHENIUM AND IRIDIUM SURFACES

We conducted a detailed study of the interaction of aluminum with the ($10\bar{1}0$) rhenium surface; this was also described in [11]. Deposition of Al on Re at 1100–1300 K brings about the formation of a surface aluminide AlRe with the Al atom density of $N_{Al} \approx 1.8 \times 10^{15}$ cm^{-2}; right up to the point of the surface-aluminide formation, all aluminum atoms arriving at the surface remain there, whereas after the surface-aluminide for-

mation is completed, all the new atoms arriving at the surface are dissolved in the metal bulk. At higher temperatures, the surface aluminide is decomposed owing to thermal desorption; the surface becomes free of adsorbed aluminum at $T > 1550$ K.

We determined the absolute concentration of Al atoms in surface aluminide by comparing our data with those reported by Parschan *et al.* [11], in which case the absolute calibration of surface aluminide was performed using the results of low-energy electron diffraction. Assuming that there is 100% adherence of Al atoms to the metal surface at room temperature, we determined the absolute value of the Al atom flux density. Experiment showed that the source we used made it possible to obtain density-stable fluxes in the range of 10^{11}–10^{14} cm^{-2} s^{-1}.

We also performed a detailed study of the adsorption of Al at the Ir(111) surface in a wide temperature range. On the Ir surface, like on the Re surface, a surface aluminide is formed; however, in the case of Ir, the surface aluminide composition is different (Ir$_5$Al) and the Al density is equal to $N_{Al} \approx 3.5 \times 10^{14}$ cm^{-2} (surface aluminide on rhenium served as the reference). The Al adatoms are removed from the surface at $T = 1500$–1600 K owing apparently to thermal desorption.

The above data make it possible to relate the heights of the aluminum Auger peaks to the absolute amount of aluminum in the absorption layer, at least as long as all the adsorbed aluminum atoms are within a single monolayer. Such a growth mode, in fact, occurs in the course of high-temperature ($T > 1000$ K) deposition of aluminum on metals but not on a graphite film.

5. INTERCALATION OF ALUMINUM UNDER A TWO-DIMENSIONAL GRAPHITE FILM ON METALS

Deposition of 2D graphite films onto iridium or rhenium at room temperature brings about the growth of three-dimensional (3D) Al islands over graphite, in accordance with the data reported in [12]. In this case, any substantial intercalation of aluminum under the film is not observed, as follows from an identical decrease in the Auger signal intensities related to carbon and to the substrate of the growing adsorbate film.

The results of the annealing out of the 3D aluminum islands ($N_{Al} \approx 2 \times 10^{15}$ cm^{-2}) on the 2D graphite films on iridium are shown in Fig. 1a. It can be seen that, at temperatures as high as ≈ 700 K, the system remains virtually the same. At higher temperatures, the Al Auger signal starts to decrease and the signal related to carbon becomes larger, whereas the signal that originated from the substrate remains unchanged at first and then also decreases somewhat. At $T > 1200$ K, all three Auger signals level off and remain constant up to 1500 K. At higher temperatures, the signal corresponding to aluminum vanishes, the signal corresponding to
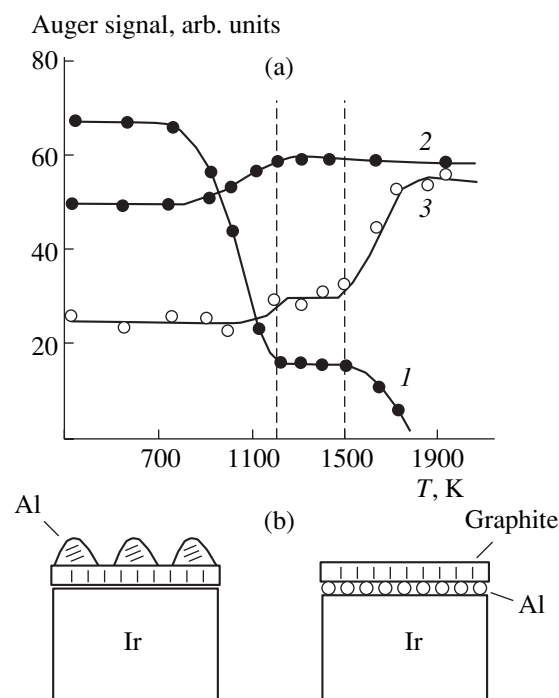
Auger signal, arb. units

Fig. 1. (a) The Auger signals of (*1*) aluminum, (*2*) carbon, and (*3*) iridium measured in the course of isochronous annealing (with the temperature step of 100 K) of Al film sputtered onto 2D graphite film deposited on (111) Ir at 300 K; the initial surface density of aluminum was ~2 × 10^{15} cm^{-2}, and the data acquisition time was 15 s at each point. (b) Schematic representation of transformation of the adsorption layer as a result of annealing: from 3D aluminum islands adsorbed on 2D graphite film to a layer of Al atoms intercalated under the graphite film.

iridium increases almost twofold, and that corresponding to carbon remains unchanged.

An explanation of the observed variations in the Auger signal can be derived from Fig. 1b. The rearrangement of the adsorption layer starts at $T = 700$ K and is completed at 1200 K; during this rearrangement, the 3D Al islands located above the graphite layer are dissolved, and the released Al atoms are partially evaporated and partially intercalate under the 2D graphite film. At $T > 1200$ K, there is no aluminum at the outer surface of the 2D graphite film; the carbon Auger signal has the same intensity as before the aluminum deposition. In contrast, the Auger signal of the substrate is significantly reduced owing to screening by both the graphite layer and intercalated aluminum; compared to the initial value, the intensity of this signal is almost two times lower (before the Al deposition, we used the iridium Auger signal with an energy of $E = 54$ eV).

With further heating ($T > 1500$ K), aluminum leaves the adsorption layer, apparently owing to thermal desorption and possibly also owing to its partial dissolution in the substrate bulk; as a result, the aluminum Auger signal vanishes. At the same time, the iridium

Auger signal increases to its initial value and the carbon Auger signal remains unchanged (Fig. 1a).

In order to determine the absolute amount of aluminum intercalated under the film, we should know the true intensity of the aluminum Auger signal which would correspond to the signal intensity without the screening effect of 2D graphite film. In order to determine this quantity, we have to measure δ, which characterizes quantitatively a decrease in the aluminum Auger peak due to the graphite monolayer. The value of δ depends primarily on the Auger transition energy and was determined previously for the nickel Auger peak [13]; the latter had an Auger transition energy which was close to the Auger transition energy for aluminum and amounted to δ = 2.5 ± 0.2. This makes it possible to recover the "true" value of the Auger signal for aluminum under the 2D graphite film. Comparing this value with the reference value (corresponding to surface aluminide on rhenium), we found that the surface aluminide Ir$_3$Al with an adsorbate density of $N_{Al} \approx 5 \times 10^{14}$ cm^{-2} is formed under the graphite layer; i.e., this aluminide is somewhat enriched with aluminum compared to that at the free surface. This is not surprising because a 2D graphite film retards the desorption of adatoms from the intercalated state.

Direct deposition of Al onto a 2D graphite film at $T > 950$ K leads to the situation where aluminum ceases to accumulate over the graphite layer; rather, it intercalates under this layer. This is shown by the constancy of the carbon Auger signal, whereas the aluminum Auger signal increases and the iridium signal diminishes, although insignificantly. This means that aluminum penetrating into the adsorption layer does not accumulate above the graphite layer and, correspondingly, does not reduce the Auger signal coming from this layer; rather, aluminum accumulates between the graphite film and the metal surface.

Using these data, we determined the efficiency of aluminum intercalation under a 2D graphite film on the iridium (111) surface; i.e., we determined the fraction of particles penetrating under the film in relation to the total number of atoms incident on the surface. The corresponding experimental data are shown in Fig. 2; in fact, we show a variation in the substrate Auger signal I_{Ir} (normalized to its initial value I_{Ir}^0) in the course of deposition of Al on the pure Ir and on the 2D graphite film on Ir at several temperatures. A decrease in the Auger signal is caused by screening of the substrate by aluminum, which accumulates in the adsorption layer. Estimations showed that the intercalation efficiency was ~14% at 1000 K and decreased to 7% at 1100 K. The same values are also obtained when the rhenium substrate is used, which corroborates the above conclusion that the properties of 2D graphite films are nearly independent of the type of metal on which the graphite film is formed. The ultimate amount of aluminum accumulated in the intercalated state on the rhenium surface also corresponds to the surface ReAl aluminide.
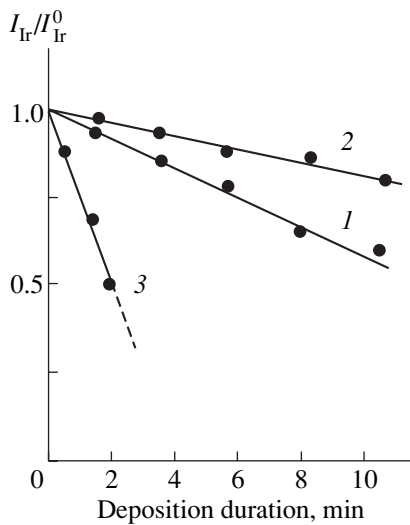
Fig. 2. Variations in attenuation of the iridium Auger signal in the course of deposition of Al atoms onto 2D graphite film on (111) Ir at (*1*) 1000 and (*2*) 1100 K and (*3*) in the course of deposition of Al atoms onto the clean (111) Ir surface at 1000 K. The flux density of Al atoms was $\nu_{Al} = 1.6 \times 10^{13}$ cm^{-2} s^{-1}.

Fig. 3. Variation in the aluminum Auger signal in the course of deposition of Al atoms onto 2D graphite film on ($10\bar{1}0$) Re at 1100 K. The fraction of the surface covered by the graphite layer $s = (1)$ 0, (*2*) 90, and (*3*) 100% (a continuous monolayer film). The flux density of Al atoms was $\nu_{Al} = 3.6 \times 10^{13}$ cm^{-2} s^{-1}.

Apparently, a low efficiency of intercalation is related to desorption of the major fraction of aluminum that arrives at the graphite-film surface. It was of interest to investigate whether the intercalation efficiency would change if the 2D graphite film did not cover the entire metal surface. To this end, we successively grew the graphite film on the rhenium substrate, so that the film covered a fraction of the metal-surface area equal to $s = 40, 70$, and 90%, and we studied the intercalation process. We assumed that the fraction of the substrate surface area covered by graphite is proportional to the intensity of the carbon Auger signal coming from the graphite film.

Variation in the aluminum Auger signal in the course of Al deposition using the same Al flux incident on the 2D graphite film at the ($10\bar{1}0$) Re surface at 1100 K for differing coverage s of the surface with the graphite layer is illustrated in Fig. 3. For all curves, the carbon Auger signal remains unchanged during the entire experiment. The final stage of each deposition consists in the formation of surface aluminide both on the surface areas of the substrate free of graphite and on the areas with a 2D graphite film in an intercalated state; after this stage, the intensity of the aluminum Auger signal remains unchanged. Differences in the intensities of the aluminum Auger signals at the final stages are governed by the fact that, each time, different fractions of aluminum are found to be adsorbed at the free surface and under the 2D graphite film, where its signal is attenuated substantially owing to the screening effect of the graphite layer. We draw attention to the fact that even an insignificant growth of the layer's "degree of discontinuity" induces a drastic rise of the Al Auger
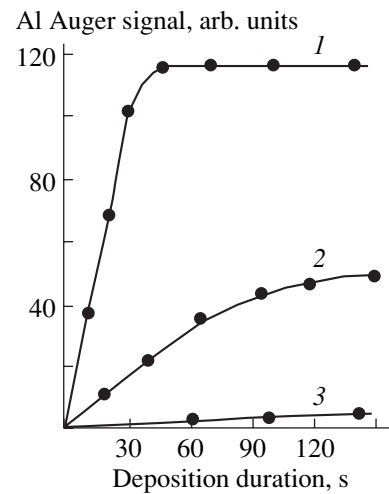
signal. This means that we observe a drastic increase in the number of Al atoms that remain in the adsorption layer and, in particular, are intercalated under the 2D graphite film.

6. DISCUSSION OF THE RESULTS

Let us discuss the results shown in Fig. 3. By comparing the data that are represented by curves *2* and *3* and illustrate the intercalation of aluminum under the continuous monolayer and under the film covering 90% of the surface area, we can see that transition to a submonolayer film induces a drastic increase in the frac-
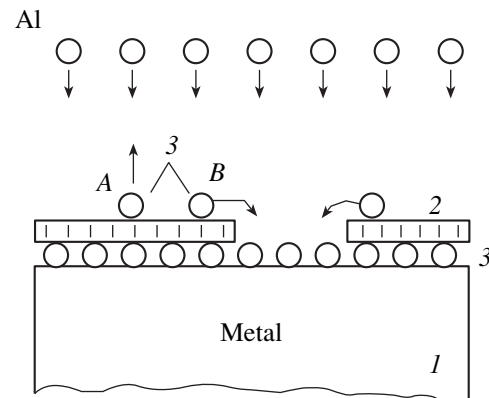

Fig. 4. Schematic representation of adsorption layer on the (*1*) Ir or Re substrate involving the areas both (*2*) covered by the 2D graphite film and free of it. The aluminum atoms adsorbed on the free surface and intercalated under the graphite layer are shown by circles *3*.

tion of aluminum atoms remaining in the adsorption layer in the intercalated state. A submonolayer graphite film consists of islands; apparently, it is the emergence of a large number of island boundaries that enhances the drain of atoms under the layer and results in an increase in the intercalation efficiency.

A schematic representation of an adsorption layer containing areas both covered by a 2D graphite film and free of it is shown in Fig. 4. An aluminum atom incident on the central part of the island (site *A*) has no time to migrate to the island boundary, is desorbed, and is detected by electron Auger spectroscopy. In contrast, an atom adsorbed closer to the island boundary (site *B*) migrates over the surface and intercalates under the graphite island.

We now attempt to estimate the intercalation efficiency for a submonolayer film. To this end, we first of all make clear what quantitative information is represented by amplitudes of the aluminum Auger signal shown in Fig. 3. We introduce the following designations: s, for the surface-area fraction covered by the 2D graphite film; ν, for the density of the aluminum-atom flux incident on the surface; t, for the process duration; N, for the aluminum surface concentration (N_{fr}, at the free surface; and N_{int}, in the intercalated state); I_{Al}, for the intensity of the aluminum Auger signal; and K, for the elemental-sensitivity coefficient defined so that, on the metal surface free of 2D graphite films, we have

$$I_{Al} = KN. \tag{1}$$

The following relation is then valid:

$$I_{Al} = KN_{fr}(1-s) + KsN_{int}\delta^{-1}. \tag{2}$$

Until the surface concentration corresponding to surface aluminide at the metal surface free of 2D graphite film is attained, all the incident aluminum atoms presumably remain on the adsorption layer, whereas the number of these atoms under the 2D graphite film is fewer by W times, where W is the intercalation efficiency. In the general case, the quantity W should be defined as the ratio between the number of intercalated atoms and the total number of atoms incident on the surface covered by the graphite film; i.e.,

$$W = N_{int}/\nu t; \tag{3}$$

consequently,

$$I_{Al} = K\nu t(1-s) + KsW\nu t\delta^{-1}. \tag{4}$$

We assume that aluminum atoms incident on the surface area free of the 2D graphite film do not intercalate under the graphite islands; rather, they form an independent surface aluminide. We also assume that the main transport of aluminum to the intercalated state is accomplished by the migratory drain of aluminum atoms from the outer surface of graphite islands via defects in the film.

Relation (4) is a linear form with respect to time and, naturally, cannot describe the curves with leveling off, which are observed experimentally. This leveling off is caused by dissolution of aluminum arriving at the surface in amounts in excess of those necessary for formation of surface aluminide; this process is not described in terms of the above simple model. However, formula (4) should describe the initial stages of the process until the onset of dissolution. Indeed, it can be seen that the initial portions of all dependences shown in Fig. 3 are rectilinear. The slopes of these lines, dI_{Al}/dt, are represented by the following expression [which can be easily derived from formula (4)]:

$$dI_{Al}/dt = K\nu(1-s) + KsW\nu\delta^{-1}. \tag{5}$$

Formula (5) makes it possible to determine the intercalation efficiency for a submonolayer graphite film. Indeed, we determine the quantities s and δ from independent experiments, whereas the product $K\nu$ can be derived from curve *1* in Fig. 3; this curve describes the variation in the aluminum Auger signal when the latter is deposited on pure rhenium by a constant flux with known density.

Calculations show that, to within experimental accuracy, the intercalation efficiency is almost independent of the amount of aluminum that already intercalated under the film. However, this efficiency depends on the fraction of the surface area covered by islands; thus, at $T = 1100$ K, the efficiency increases from $W = (0.35 \pm 0.1)$ for $s = 90\%$ to $W \approx 1$ for $s < 70\%$. It is noteworthy that the obtained values are much larger than the efficiency of intercalation of aluminum atoms under a continuous 2D graphite film with monolayer thickness.

It is reasonable to assume that the quality of the graphite layer itself is independent of whether it is continuous or of the island type. However, in the latter case, the number of island boundaries increases drastically; it is possible that the island size decreases as well. In fact, destruction of graphite islands proceeds from their boundaries [3]; this is not surprising if we take into account that an individual carbon atom is bound within the layer with an energy of ~9 eV [4], whereas this bonding is much weaker at the island boundaries: the bonding energy is ~3 eV for rhenium [10] and ~4.5 eV for iridium [3]. Apparently, an appreciable difference between the efficiencies of intercalation under the monolayer and submonolayer films indicates that it is the boundaries of graphite islands which act as the defects responsible for intercalation of atoms under the 2D graphite film, as has been suggested previously [14]. When the islands merge together and give rise to a continuous monolayer, the permeability with respect to intercalating atoms diminishes. In contrast, an increase in the intercalation efficiency to the value close to unity indicates that the island size becomes close to the migration length of aluminum atoms during their lifetime on the graphite surface at a given temperature. According to the data of scanning tunneling micros-

copy, the mean island size amounts to 3000–8000 Å; therefore, the migration length of aluminum atoms has the same order of magnitude at 1000–1100 K.

It is highly probable that the aforementioned increase in the intercalation efficiency is universal and will be observed for many types of intercalating particles.

CONCLUSION

We ascertained for the first time that aluminum atoms intercalate under a two-dimensional graphite film on (111) iridium and ($10\bar{1}0$) rhenium surfaces; we also determined the efficiency of this process. We detected a new effect that consists in the drastic increase in the efficiency of intercalation of foreign atoms under the two-dimensional graphite film on metals when this film is transformed from a monolayer state (covering the entire surface) to a submonolayer island one. If 10% of the surface area of a metal (rhenium) becomes free of the graphite layer, the intercalation efficiency for aluminum atoms increases by five times at 1100 K. We developed a physical model and suggested a mechanism of the observed phenomenon, which is apparently universal. The above-reported results make it possible to state with a high degree of confidence that it is the graphite-island boundaries, rather than other types of defects, which represent the "channels" through which intercalation occurs.

ACKNOWLEDGMENTS

REFERENCES

1. E.V. Rut'kov and A. Ya. Tontegode, Pis'ma Zh. Tekh. Fiz. **7**, 1122 (1981) [Sov. Tech. Phys. Lett. **7**, 480 (1981)].

2. E. V. Rut'kov and A. Ya. Tontegode, Usp. Fiz. Nauk **163**, 57 (1993) [Phys. Usp. **36**, 1053 (1993)].

3. N. R. Gall, E. V. Rut'kov, and A. Ya. Tontegode, Int. J. Mod. Phys. B **11**, 1765 (1997).

4. A. Ya. Tontegode, Prog. Surf. Sci. **38**, 201 (1991).

5. M. Eizenberg and J. M. Blakely, Surf. Sci. **82**, 228 (1979).

6. L. Bolotov, N. R. Gall, I. V. Makarenko, *et al.*, Fiz. Tverd. Tela (Leningrad) **40**, 1570 (1998) [Phys. Solid State **40**, 1423 (1998)].

7. N. R. Gall, I. V. Makarenko, A. N. Titkov, *et al.*, Poverkhnost, No. 7, 39 (1999).

8. Hu Zi-Pu, D. F. Ogletree, M. A. Van-Hove, and G. A. Somorjai, Surf. Sci. **180**, 433 (1987).

9. R. Rossei, M. De Crescenzi, F. Sette, *et al.*, Phys. Rev. B **28**, 1161 (1983).

10. N. R. Gall, S. N. Mikhailov, E. V. Rut'kov, and A. Ya. Tontegode, Surf. Sci. **191**, 185 (1987).

11. M. Parschan and K. Cristmann, Surf. Sci. **347**, 63 (1996).

12. S. Srivastava and J. Almlof, Surf. Sci. **255**, L509 (1991).

13. N. R. Gall, E. V. Rut'kov, and A. Ya. Tontegode, Carbon **38**, 663 (2000).

14. A. Ya. Tontegode, Pis'ma Zh. Tekh. Fiz. **15** (7), 57 (1989) [Sov. Tech. Phys. Lett. **15**, 271 (1989)].

Translated by A. Spitsyn

Simulation of Hydrogen Penetration into *p*-Type Silicon under Wet Chemical Etching

O. V. Feklisova, E. B. Yakimov*, and N. A. Yarykin

*Institute of Microelectronics Technology and Ultrahigh-Purity Materials, Russian Academy of Sciences,
Chernogolovka, Moscow oblast, 142432 Russia*
*e-mail: yakimov@ipmt-hpm.ac.ru
Submitted March 26, 2001; accepted for publication June 28, 2001

Abstract—Penetration of hydrogen into *p*-Si and formation of hydrogen-containing defects under wet chemical etching were simulated. The simulated concentration profiles of hydrogen-containing defects were compared to the measured profiles. It is shown that the hydrogen-distribution relaxation after termination of etching is important in the crystals with a low trap concentration. Consideration of such relaxation makes it possible to describe all experimental profiles without assuming that the hydrogen diffusivity is anomalously high. However, the experimental profiles can also be described assuming that the hydrogen diffusivity is high, with the effect of relaxation being less important in this case. It is shown that a comparative analysis of concentration profiles for the hydrogen-containing centers makes it possible to determine the number of hydrogen atoms in these centers in the cases where these profiles are either formed mainly in the course of etching or are modified significantly by transient hydrogen diffusion. © *2002 MAIK "Nauka/Interperiodica".*

INTRODUCTION

It is known [1–4] that hydrogen can penetrate into silicon to a fairly large depth at 295 K and even lower temperatures; in addition, hydrogen can efficiently interact with crystal-lattice defects during its diffusion. In order to study the behavior of hydrogen at room temperature, wet chemical etching is most often used [1, 3–7]. It has been shown [4] that, after wet chemical etching, the distribution of hydrogen-containing defects AH_i (here, i corresponds to the number of hydrogen atoms in a defect) over the distance z from the etched surface is described by the exponential dependence $[AH_i] \propto \exp(-iz/L)$, which can be used to determine experimentally the values of i and L [4, 6, 7]. The quantity L, which plays the role of the hydrogen diffusion length measured from the crystal boundary that moves in the course of etching, is the same for all defects in the sample under investigation and is equal to

$$L = \left(\frac{V}{2D_H} + \sqrt{\frac{1}{L_0^2} + \frac{V^2}{4D_H^2}} \right)^{-1}, \qquad (1)$$

where V is the etching rate, L_0 is the hydrogen diffusion length in the as-grown crystal, and D_H is the hydrogen diffusion coefficient. As can be seen from expression (1), the measurement of L can also be used to determine the hydrogen diffusion coefficient, the value of which is reported in various publications with a spread amounting to several orders of magnitude [8]. However, a number of assumptions were made when deriving formula (1) in [4]; these assumptions, being valid for *n*-Si where the interaction of hydrogen with the dopant is

comparatively weak, are justified in *p*-Si only at large distances from the surface where the hydrogen concentration is low. We primarily refer to the assumption that hydrogenation does not significantly affect the concentration of the centers that trap hydrogen. In *p*-Si, the most effective traps are the shallow-level acceptor impurities, the radius of hydrogen capture by which is so large (~4 nm [2]) that they can form neutral pairs composed of hydrogen and a shallow-level acceptor. As a result, the formed depth-nonuniform distribution of the dopant can not only bring about a violation of the assumption that L_0 is uniform over depth but also give rise to an the electric field, which can affect the hydrogen transport, because hydrogen atoms have a positive charge in *p*-Si [9]. In addition, it has not been taken into account [4] that, at the instance of termination of etching, a fraction of the hydrogen may be in the free state. If the amount of free hydrogen is fairly large, the relaxation-related diffusion of free hydrogen until it is captured by traps may distort the defect-concentration profiles formed under wet chemical etching.

In this paper, we report the results of numerical simulation of hydrogen penetration into *p*-Si under wet chemical etching; we also simulated the distribution of the hydrogen-containing centers. In simulations, we took into account the nonuniform distribution of traps, the effect of an electric field caused by this distribution on the hydrogen transport, and also the hydrogen-distribution relaxation after termination of the wet chemical etching. The results of calculations were compared with experimentally measured concentration profiles for electrically active acceptor impurities, which made it possible to verify the adequacy of the used model

with experimental data and estimate the effect of the transient hydrogen diffusion on the impurity distribution after the wet chemical etching was terminated.

SIMULATION OF HYDROGEN PENETRATION UNDER WET CHEMICAL ETCHING

We numerically solved the following set of equations that describe hydrogen penetration into Si under wet chemical etching and account for the aforementioned factors:

$$\frac{\partial [H]}{\partial t} = D_H \frac{\partial^2 [H]}{\partial z^2} + \frac{eD_H}{kT} \frac{\partial}{\partial z}\left([H]\frac{\partial \varphi}{\partial z}\right)$$

$$+ V\frac{\partial [H]}{\partial z} - \frac{[H]}{\tau}\frac{N_B}{N_{B0}} - \frac{[H]}{\tau_2},$$

$$\frac{\partial^2 \varphi}{\partial z^2} = \frac{4\pi e}{\varepsilon} N_{B0}\left[\frac{N_B}{N_{B0}} - \exp(-e\varphi/kT)\right],$$

$$\frac{\partial N_B}{\partial t} = V\frac{\partial N_B}{\partial z} - \frac{[H]}{\tau}\frac{N_B}{N_{B0}},$$

$$\frac{1}{\tau} = 4\pi D_H r_B N_{B0},$$

$$F_0 = \left.\frac{\partial [H]}{\partial z}\right|_{z=0} = \text{const.}$$

(2)

Here, [H] is the hydrogen concentration, N_B is the concentration of electrically active boron, $1/\tau$ is the rate of capture of hydrogen by boron in the as-grown crystal, N_{B0} is the initial boron concentration, r_B is the radius of capture of hydrogen by boron, φ is the electrostatic potential, and ε is the dielectric constant of Si. The terms containing the etching rate V appear in the equations because the depth z is measured from the moving (as a result of etching) surface. Relaxation of hydrogen distribution after termination of etching was described by the same equations with $V = 0$ and $F_0 = 0$.

It was assumed that the diffusion or drift of hydrogen was accompanied with its capture by boron as a result of the formation of stable, electrically inactive pairs and also with the capture (with a constant capture time τ_2) by other traps. The introduction of the latter was motivated by experimentally observed differences in the depths of hydrogen penetration into similarly doped crystals grown by the Czochralski (Cz) method and by the floating-zone (FZ) method. The depth of hydrogen penetration in Cz-Si is invariably smaller than that in FZ-Si, which is indicative of the presence of additional traps for hydrogen in Cz-Si; these traps are possibly related to oxygen. The capture time for these traps, τ_2, determined from a comparison of several similarly doped pairs of Cz- and FZ-Si crystals, was found to be on the order of 100 s under the assumption that such traps are absent in FZ-Si.

Since one of the objectives of this study was to analyze the distribution of the complexes containing one or several hydrogen atoms, we also considered the capture of hydrogen by traps A, which form stable complexes with one or two hydrogen atoms. The concentration of traps A was assumed to be low compared to that of the doping impurities, which made it possible to calculate the hydrogen distribution with the effect of these impurities disregarded; we then calculated the distribution of the AH_i complexes using the approach suggested in [6] and based on evaluating the total hydrogen concentration Φ; i.e.,

$$\frac{\partial [A]}{\partial \Phi} = -r_0^A[A],$$

$$\frac{\partial [AH_i]}{\partial \Phi} = r_{i-1}^A[AH_{i-1}] - r_i^A[AH_i],$$

(3)

$$\Phi = 4\pi D_H \int_0^t [H]dt,$$

where r_i^A and $[AH_i]$ are the capture radius and the concentration of complexes containing i hydrogen atoms, respectively. It is worth noting that the assumption about the low concentration of centers A does not in fact restrict the use of the results of simulation, because the experimental study of concentration profiles of the deep-level centers is typically performed using the method of deep-level transient spectroscopy; this method can be used correctly only if the concentration of the centers under investigation is much lower than that of the dopant.

COMPARISON OF SIMULATED AND EXPERIMENTAL PROFILES

For the sake of comparison with the results of simulation, we measured the concentration profiles of electrically active boron in a number of Cz- and FZ-Si samples with the initial boron concentration N_{B0} in the range of 3.5×10^{13}–1.4×10^{16} cm^{-3}. Hydrogen was introduced into the surface of crystals under wet chemical etching in a solution of hydrofluoric and nitric acid (HF : HNO$_3$ = 1 : 7) at room temperature (the etching rate was equal to 2–4 μm/min). The concentration profiles of charge carriers were determined from the capacitance–voltage characteristics of the Schottky barriers formed by thermal deposition of Al in a vacuum chamber.

The measured concentration profiles of electrically active boron for three samples differing significantly in their doping level are shown in Fig. 1. A decrease in the boron concentration near the surface occurs as a result of the formation of neutral boron–hydrogen pairs, the distribution of which can be calculated as the difference between the initial boron concentration (equal to the boron concentration in the bulk of the samples) and the
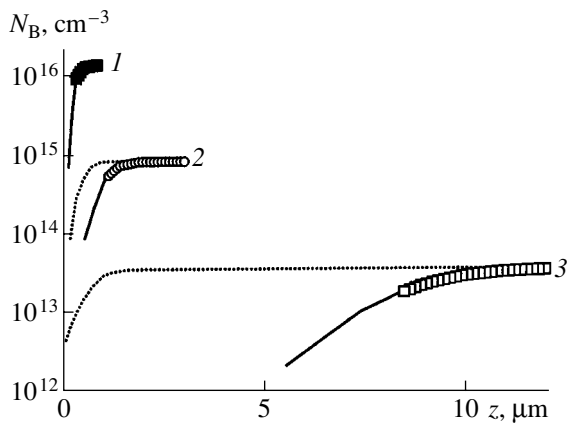
N_B, cm^{-3}

Fig. 1. The measured (the points) and calculated (the solid lines) concentration profiles of electrically active boron in the (*1*, *2*) Cz- and (*3*) FZ-Si samples after wet chemical etching. Dotted lines represent the profiles calculated for the instance of termination of etching. The boron concentration was equal to N_B = (*1*) 1.4×10^{16}, (*2*) 8.2×10^{14}, and (*3*) 3.5×10^{13} cm^{-3}.

concentration profile of electrically active boron. If we approximate the falloff of the concentration of the boron–hydrogen pairs with the depth of the samples by the exponential dependence $\exp[-(z - z_0)/L]$, we can use the experimental distributions of boron to determine the quantity z_0, which specifies the hydrogen penetration depth (the region of almost complete boron passivation), and the quantity L, which is governed by the rate of decrease in the hydrogen concentration. In the samples under investigation, both quantities decreased approximately proportionally to $(N_{B0})^{-1/2}$ with increasing boron concentration.

If it is assumed that the hydrogen redistribution after etching is insignificant, all experimental profiles can be adequately fitted by the profiles calculated using Eqs. (2) for any $D_H > 2 \times 10^{-9}$ cm^2/s and the values of the capture radius r_B that ranged from 2.0 to 3.0 nm for all the samples under investigation. These values of r_B are in good agreement with the values of 3.5–4 nm obtained previously [2, 10] by other methods, especially if we take into account that the value of L in all samples was comparable to the spatial resolution typical of the method for the determination of the impurity distribution from the analysis of the capacitance–voltage characteristics.

The above estimate of D_H is in good agreement with the value $D_H \geq 5 \times 10^{-9}$ sm^2/s obtained in studies of *n*-Si [6]. However, it is noteworthy that these values of D_H exceed, by more than an order of magnitude, the value $(8 \times 10^{-11}$ cm^2/s) obtained by extrapolating the results of measuring D_H at high temperatures [11]. From this, it is natural that the question arises as to whether it is also possible to describe theoretically the experimentally measured boron concentration profiles for $D_H < 10^{-9}$ cm^2/s. It was found that the experimental boron

profiles that we measured in the lightly doped crystals cannot be described adequately using the above values of the diffusion coefficients without taking into account the transient hydrogen diffusion, the magnitude of which is governed by the concentration of free hydrogen at the instant the wet chemical etching is terminated.

Calculations using Eqs. (2) with allowance made for relaxation-related diffusion showed that the experimental penetration depths of hydrogen z_0 can be accounted for by varying D_H in a wide range and by compensating variation in the hydrogen flux to the surface (F_0). A variation in F_0 results in a change in the concentration of free hydrogen. For $D_H > 7 \times 10^{-9}$ cm^2/s, this concentration is so low that the hydrogen relaxation upon completion of etching virtually does not affect the concentration profiles of hydrogen-containing defects for all the boron concentrations used in this study. As the value of D_H decreases, the effect of relaxation-related diffusion becomes more pronounced. Nevertheless, for $D_H > 10^{-9}$ cm^2/s, the effect of the relaxation-related diffusion of hydrogen on the concentration profiles of hydrogen-containing defects can manifest itself only in the crystals with a very low boron concentration and may be ignored for the crystals with $N_{B0} > 5 \times 10^{14}$ cm^{-3}.

As D_H decreases further, the relaxation-related diffusion of hydrogen starts to significantly modify the profiles. Nevertheless, the experimental profiles can be adequately described theoretically using the same capture radius r_B as for larger values of D_H even for fairly low concentrations of N_{B0}. Some of the profiles calculated for $D_H = 8 \times 10^{-11}$ cm^2/s are shown in Fig. 1. The calculated profiles corresponding to the instant of the etching termination (dotted lines) and those corresponding to the completion of the transient hydrogen diffusion (the solid lines) are shown. The rate of hydrogen incorporation into silicon, F_0, which was obtained by fitting the calculated profiles to those measured for $D_H = 8 \times 10^{-11}$ cm^2/s varies from 1.5×10^9 to 6.6×10^{10} cm^{-2}/s as the boron concentration changes from 3.5×10^{13} to 1.4×10^{16} cm^{-3}; i.e., F_0 varies approximately in proportion to $(N_B)^{1/2}$. In this case, the hydrogen concentration at the surface is no higher than 4×10^{15} cm^{-3}.

Numerical experiments showed that, for the adopted etching rates, the quasi-steady boron distribution is formed over several minutes under wet chemical etching. If the hydrogen-diffusion coefficient is sufficiently large, the boron concentration profile is predominantly formed even during the wet chemical etching, and the effect of transient hydrogen diffusion is, experimentally, virtually undetectable. In the opposite case (i.e., for a small value of D_H), relaxation-related diffusion proceeds rather slowly and may significantly affect the boron concentration profile, especially in lightly doped crystals. For example, for $D_H = 8 \times 10^{-11}$ cm^2/s, such relaxation in Si with a B concentration on the order of 10^{16} cm^{-3} is completed in a matter of minutes, with the
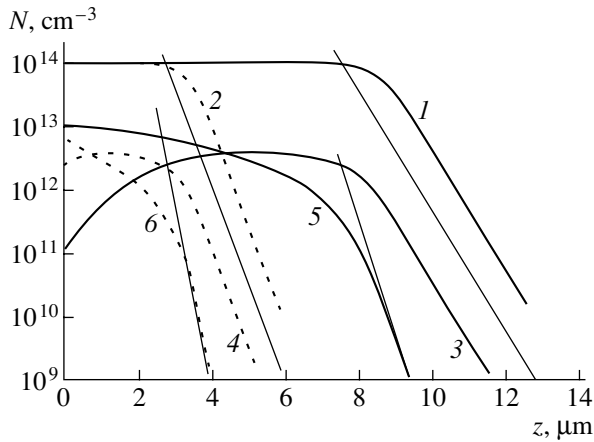
N, cm^{-3}

Fig. 2. Calculated concentration profiles for the (*1, 2*) boron–hydrogen pairs and the centers containing (*3, 4*) a single or (*5, 6*) two hydrogen atoms immediately after wet chemical etching (dotted lines *2, 4, 6*) and after relaxation (the solid lines *1, 3, 5*). The thin solid lines approximate the concentration falloff by the exponential law.

value of L changing by less than 10%. In the samples with boron concentration $N_B = 3.5 \times 10^{13}$ cm^{-3}, both the penetration depth of hydrogen z_0 and its diffusion length L increase significantly (by more than a factor of 3) as a result of relaxation (Fig. 1). In this case, the relaxation lasts for as long as 60 min, which basically makes it possible to detect experimentally.

In order to resolve the question as to whether the method for determining the number of hydrogen atoms in a hydrogen-containing complex from the analysis of the defect-concentration profiles under the conditions of significant transient hydrogen diffusion is justified, the corresponding profiles were calculated for the centers that can capture one or two hydrogen atoms. It was assumed that the concentration of boron-trapping centers [A] is lower by a factor of 10 than the boron concentration and that $r_i^A = 0.5$ nm for both the A centers and their complexes with hydrogen. The results of simulation for the boron–hydrogen pairs and the complexes containing one or two hydrogen atoms are shown in Fig. 2. It can be seen that the values of L for the boron–hydrogen pairs (a single hydrogen atom) and the complexes consisting of traps A with a single hydrogen atom coincide both before and after relaxation, whereas the values of L for a complex with two hydrogen atoms are, in both cases, smaller by a factor of 2. Thus, although the transient hydrogen diffusion may significantly affect the concentration profiles of hydrogen-containing centers, the ratio between the values of L for the centers containing different numbers of hydrogen atoms remains unchanged. Consequently, the approach suggested previously [4] is also applicable to situations where the profiles are modified significantly as a result of the hydrogen distribution relaxation.

CONCLUSION

Thus, we simulated the penetration of hydrogen into silicon under wet chemical etching. We show that it is impossible to determine the diffusion coefficient of hydrogen solely from the analysis of the concentration profiles for the hydrogen-containing centers; the experimental profiles can be approximated both on the assumption that the diffusion coefficient is anomalously large and using the diffusion coefficient extrapolated from the high-temperature measurements if we take into account the effect of the transient hydrogen diffusion after termination of wet chemical etching. It is shown that the method used for determination of the number of hydrogen atoms in the centers, which is based on the comparative analysis of their concentration profiles, can be employed not only if the profiles are formed in the course of etching but also under conditions when these profiles are markedly modified by the transient hydrogen diffusion.

ACKNOWLEDGMENTS

REFERENCES

1. A. J. Tavendale, A. A. Williams, S. Alexiev, and S. J. Pearton, Mater. Res. Soc. Symp. Proc. **104**, 285 (1988).

2. C. H. Seager, R. A. Anderson, and D. K. Brice, J. Appl. Phys. **68**, 3268 (1990).

3. A. L. Parakhonskiĭ, O. V. Feklisova, S. S. Karelin, and N. A. Yarykin, Fiz. Tekh. Poluprovodn. (St. Petersburg) **30**, 670 (1996) [Semiconductors **30**, 362 (1996)].

4. O. V. Feklisova and N. Yarykin, Semicond. Sci. Technol. **12**, 742 (1997).

5. E. Ö. Sveinbjörnsson, G. I. Andersson, and O. Engström, Phys. Rev. B **49**, 7801 (1994).

6. N. Yarykin, J.-U. Sachse, H. Lemke, and J. Weber, Phys. Rev. B **59**, 5551 (1999).

7. J.-U. Sachse, J. Weber, and E. Ö. Sveinbjörnsson, Phys. Rev. B **60**, 1474 (1999).

8. S. J. Pearton, J. W. Corbett, and M. Stavola, in *Hydrogen in Crystalline Semiconductors* (Springer-Verlag, Heidelberg, 1992), p. 200.

9. A. J. Tavendale, D. Alexiev, and A. A. Williams, Appl. Phys. Lett. **47**, 316 (1985).

10. T. Zundel and J. Weber, Phys. Rev. B **46**, 2071 (1992).

11. A. van Wieringen and N. Warmoltz, Physica (Amsterdam) **22**, 849 (1956).

Translated by A. Spitsyn

Internal Ionization Energy in II–VI Compounds

**A. V. Komashchenko, V. N. Komashchenko*, K. V. Kolezhuk, G. I. Sheremetova,
V. D. Fursenko, and Yu. N. Bobrenko**

Institute of Semiconductor Physics, National Academy of Sciences of Ukraine, Kiev, 03028 Ukraine
* e-mail: komas@isp.kiev.ua
Submitted June 25, 2001; accepted for publication July 11, 2001

Abstract—The dependence of sensitivity of surface-barrier p-$Cu_{1.8}S$/n-II–VI heterostructures on the energy of exciting photons or of accelerated monoenergetic electrons was studied. The method of the determination of the mean energy ε of internal ionization for the direct-gap II–VI compounds is suggested, and the ε values are found experimentally. The relationship between ε and the band gap of a semiconductor is found to be expressed as $\varepsilon = 2.5 E_g$. © 2002 MAIK "Nauka/Interperiodica".

INTRODUCTION

The internal ionization energy ε required for the formation of nonequilibrium charge carriers, the electrons and holes, is one of the important parameters of a material, because it governs the efficiency of the conversion of the ionizing radiation [1]. However, the values of ε for many semiconductors have not been determined experimentally, or they are ambiguous as, e.g., for the wide-gap II–VI compounds, which hold promise for the fabrication of sensors for ultraviolet and beta radiation [1, 2].

The aim of this study was to determine the energy of the formation of an electron–hole pair in II–VI compounds by comparing the results obtained from the photon and electron excitations of the heterostructures based on these compounds.

EXPERIMENT

The surface-barrier heterostructures of the p-$Cu_{1.8}S$/n-II–VI type [3, 4] were used as samples. The thickness of the base polycrystalline II–VI films was about 3 μm, and the thickness of copper sulfide, about 350 Å. For the measurements of the optical and electrical parameters of copper sulfide, the heterostructures were prepared by simultaneous deposition of the $Cu_{1.8}S$ films onto reference quartz glasses. The concentration of majority carriers was $p = 5 \times 10^{21}$ cm^{-3} in $Cu_{1.8}S$ and $n < 10^{15}$ cm^{-3} in II–VI. The sample area was about 25 mm^2. The sample surface covered with copper sulfide was subjected to radiation. A modernized electron EM-4 diffractometer was used as a source of monoenergetic accelerated electrons with the energy of $E_\beta = 3$–30 keV. The current density in the electron beam was measured in the range $i_\beta = 10^{-11}$–10^{-8} A/cm^2 using a Faraday cup. The photocurrent spectra at the photon excitation were measured using an SF-26 spectrophotometer. The samples were studied in the barrier-layer mode at 300 K. The short-circuit currents I and I_β were measured at the photon and electron excitations, respectively.

The characteristic feature of the structures under consideration is that they have a highly asymmetric p–n junction with a space-charge region (SCR) located completely within the base layer (in II–VI compound), and copper sulfide does not contribute to the photocurrent (except for the situation considered in [5]). It is reasonable to assume that the copper sulfide would be also inactive under electron irradiation. The extent of the photosensitive region is $d = W + L_p$, where W is the SCR width and L_p is the hole diffusion length in II–VI. The magnitude of d obtained from the capacitance–voltage and spectral characteristics was 0.8–1.0 μm, the magnitude of L_p being a fraction of a micrometer.

The electron penetration depth and electron absorption in $Cu_{1.8}S$ and II–VI were calculated by the method suggested in [6, 7] using the Bethe equation. It was found that the penetration depths for electrons penetrating into the base region of the heterostructures were about 0.1, 1.0, and 4.5 μm for the energies $E_\beta = 3$, 12, and 30 keV, respectively. Therefore, the electrons with the energies $E_\beta < 15$ keV are absorbed in II–VI compounds at a depth approximately corresponding to d. The absorption coefficient K_β for electrons with energies $E_\beta > 6$ keV in a thin film of copper sulfide is small ($K_\beta < 0.05$). The effect of copper sulfide is significant if the electron penetration depth becomes comparable with the thickness of $Cu_{1.8}S$, that is, at $E_\beta < 6$ keV.

The effect of the electron energy on the current I_β was studied under the condition when the density of generated electrons and holes was close to the magnitudes corresponding to the excitation by photons and remained constant. This condition was satisfied by keeping constant the power of the exciting electron beam $P_\beta = i_\beta E_\beta / q$, where q is the electron charge.

BACKGROUND

It is known that the photons with an energy higher than the band gap $h\nu \gtrsim E_g$ are absorbed by a semiconductor with the formation of electron–hole pairs. The quantum yield of the inner photoeffect is equal to unity; i.e., one absorbed photon produces one electron–hole pair, and the expression for photocurrent may be written as [8]

$$I = qF_{opt}\eta = qP_{opt}\eta/h\nu, \qquad (1)$$

where F_{opt} is the density of a photon flux incident on the sample surface per unit time, η is the quantum yield equal to the ratio of the photogenerated pairs to the number of incident photons, and P_{opt} is the power of incident irradiation.

For the heterostructures under study, the following relation is valid:

$$\eta = T_{opt}\eta_1\eta_2, \qquad (2)$$

where the factor T_{opt} accounts for the photon losses due to the reflection from the surface of the structure and the nonphotoactive absorption; for $Cu_{1.8}S$, it is equal to the transmission coefficient of a copper sulfide film. The factor η_1 characterizes the efficiency of the separation of thermalized nonequilibrium carriers by the $p–n$ heterojunction; the factor η_2 accounts for the losses caused by the surface and bulk recombination within a quasi-neutral region, at the interface of the heterostructure, and so on.

In the case of electron excitation, the number of electron–hole pairs generated in a semiconductor during the slowing-down of a single electron with the energy E_β is determined by the multiplication coefficient α_p:

$$\alpha_p = E_\beta/\varepsilon. \qquad (3)$$

The current generated in the structures under investigation can be expressed as

$$I_\beta = qF_\beta\alpha_p\eta_\beta = i_\beta\alpha_p\eta_\beta, \qquad (4)$$

where F_β is the density of electron flux incident on the sample surface per unit time. The parameter η_β is actually equivalent to a quantum efficiency of photoconversion η and represents the probability that the monoenergetic electrons are slowed down in a semiconductor with the production of $F_\beta\alpha_p$ pairs, which subsequently become separated by the barrier electric field and contribute to the generated current.

The efficiency of the conversion of monoenergetic electron beams can be expressed as

$$\eta_\beta = (1 - R_\beta)(1 - K_\beta)\eta_1\eta_2. \qquad (5)$$

Here, the factor $(1 - R_\beta)(1 - K_\beta)$ characterizes the probability of the penetration of excitation electrons into a photosensitive layer of the converter, where R_β is the coefficient of electron reflection from the surface of a structure. It should be noted that, since we used copper

sulfide films with nanometer dimensions, the experimental results could be analyzed by using the values of R_β for the bulk base material of p-$Cu_{1.8}S/n$ II–VI heterostructures. Under the same conditions of the generation of nonequilibrium carriers, one may assume that in both processes the coefficients η_1 and η_2 in (2) and (5) are identical. The following arguments count in favor of this assumption.

Thermalized nonequilibrium carriers generated by the light or accelerated electrons are indistinguishable. Moreover, the concentrations of these carriers in our experiments were kept equal. We should also mention that for the direct gap II–VI semiconductors the effective penetration depth of the light from the fundamental band, as well as of the electrons with the energy $E_\beta < 15$ keV, is close and comparable with the width of the photosensitive region.

Taking into account the above, we can use (2) and (5) to obtain

$$\eta_\beta = \eta(1 - R_\beta)(1 - K_\beta)/T_{opt}. \qquad (6)$$

The sensitivities S and S_β of the heterostructures under photon and electron excitations, respectively, depend on the energies of quanta and electrons in the following way:

$$S = I/P_{opt} = q\eta/h\nu, \qquad (7)$$

$$S_\beta = I_\beta/P_\beta = q\alpha_p\eta_\beta/E_\beta. \qquad (8)$$

Expressions (7) and (8) have similar forms. Since dependence (8) is measured under the same density of the generated electron–hole pairs ($P_\beta = $ const), the amplitude of a signal is a function of the depth of the formation of pairs. Thus, this characteristic can be considered as an analogue of the spectral characteristic of the photoeffect. However, in contrast to the latter, for which the sensitivity deep within the absorption band [see (7)] falls off with increasing photon energy, the magnitude of S_β within a certain energy range remains constant with increasing E_β. Indeed, substituting (3) into (8), we obtain the expression which does not contain the dependence of S_β on E_β:

$$S_\beta = q\eta_\beta/\varepsilon. \qquad (9)$$

We now use (9) and (6) to obtain the following final expression for the energy of inner ionization:

$$\varepsilon = q\eta(1 - R_\beta)(1 - K_\beta)/S_\beta T_{opt}. \qquad (10)$$

The value ε can be readily obtained from expression (10). Since the values of η, S_β, and T_{opt} can be measured, the value of K_β can be calculated, and the value of R_β can be taken from the published data.

RESULTS

The samples for the experiments were chosen according to the requirement that, in a fairly wide range of $h\nu$ and E_β, they should have regions with $\eta = $ const
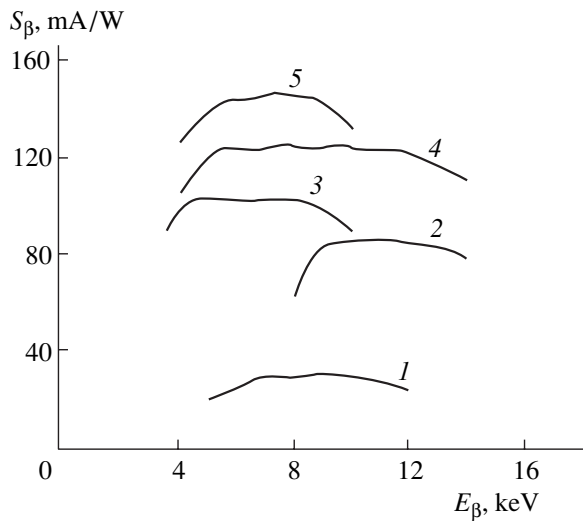
Fig. 1. Energy characteristics of heterostructures: (*1*) p-Cu$_{1.8}$S/n-ZnS, (*2*) p-Cu$_{1.8}$S/n-ZnSe, (*3*) p-Cu$_{1.8}$S/n-CdS, (*4*) p-Cu$_{1.8}$S/n-CdSe, and (*5*) p-Cu$_{1.8}$S/n-CdTe.

and η_β = const under the photon and electron excitation, respectively.

The typical $S_\beta = f(E_\beta)$ dependences, the so-called energy characteristics, for various II–VI compounds are shown in Fig. 1. It can be seen that the sensitivity of the converters remains constant within the region of electron energies $E_\beta < 15$ keV. The increase in E_β results in an increase in the depth of the electron penetration into the base region of a structure. In the course of this process, some of the generated pairs cannot be separated by the field of a p–n junction; as a result, the sensitivity decreases. The presence of an insensitive layer of copper sulfide is the cause of the decrease in S_β at low electron energies. The above arguments explain the fact that the conversion efficiency η_β = const at the values E_β corresponding to the total absorption of electrons within a photosensitive region.

The spectral characteristics of the quantum yield of the photoeffect in the heterostructures are shown in Fig. 2. It can be seen that the samples of all types have regions with η = const. We should note that, according to calculations, the fraction of the drift component in a photocurrent is dominant (>90%); i.e., nonequilibrium
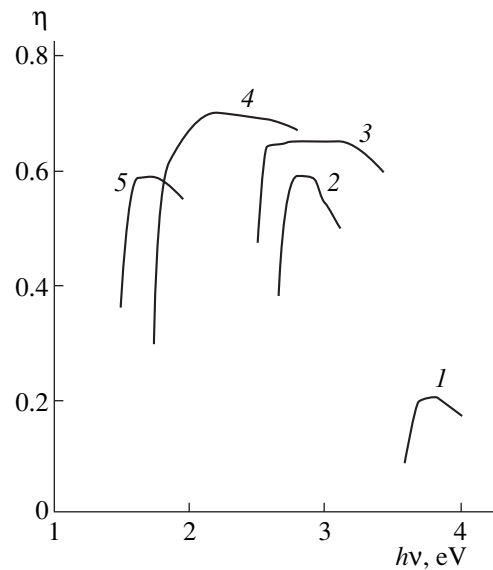

Fig. 2. Spectral characteristics of the quantum yield for the heterostructures: (*1*) p-Cu$_{1.8}$S/n-ZnS, (*2*) p-Cu$_{1.8}$S/n-ZnSe, (*3*) p-Cu$_{1.8}$S/n-CdS, (*4*) p-Cu$_{1.8}$S/n-CdSe, and (*5*) p-Cu$_{1.8}$S/n-CdTe.

carriers are generated predominantly in the SCR of converters.

Analysis of the results confirms the idea that the recombination losses of nonequilibrium carriers accounted for in (2) and (5) for the photon and electron excitations as the coefficients η_1 and η_2 are the same within the energy range considered. This follows from the constancy of η and η_β at the photon and electron energies which correspond to their total absorption in the photosensitive region of heterostructures. The above arguments allow us to calculate ε using expression (10).

The values of internal ionization energy ε for II–VI compounds averaged over the measurements for five samples of each type are listed in the table. The values of E_g and R_β for II–VI compounds (published data) and the value T_{opt} for Cu$_{1.8}$S, corresponding to the photon energies $h\nu$ at which η = const (obtained from the experiment), are also listed in the table. Satisfactory agreement can be seen between the results obtained and the published data on ε for CdS and CdSe [11, 12] (the ε data for the remaining II–VI materials are not available to us).

The mean ionization energy does not depend on the type of ionizing irradiation. It is determined by the width of a band gap and exceeds it by a factor of 2.5–3 [1, 2]. The analytical expression of this relationship is given in [13–15]: $\varepsilon = 2.67E_g \pm 0.87$ eV.

The dependence $\varepsilon = f(E_g)$ obtained from the data given in the table is shown in Fig. 3. It can be seen that the experimental points satisfactorily fit a straight line with a slope of 2.5. This allows the relationship between

Parameters of II–VI compounds

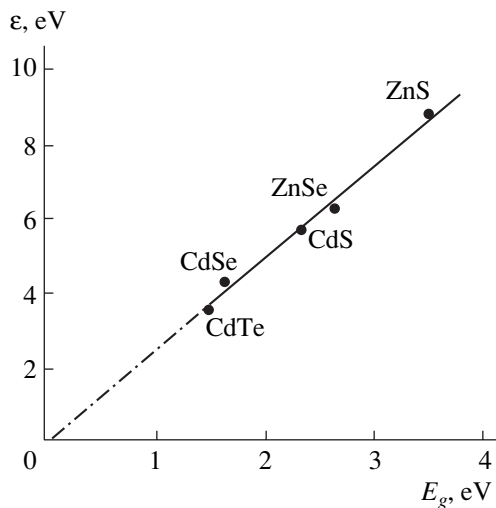| Para-meter	Compound				
	CdS	CdSe	CdTe	ZnS	ZnSe
E_g, eV	2.4 [9]	1.7 [8]	1.5 [9]	3.6 [9]	2.7 [9]
R_β [10]	0.29	0.30	0.33	0.20	0.29
T_{opt}	0.74	0.85	0.74	0.57	0.73
ε, eV	5.8	4.4	3.5	8.9	6.4

ε, eV

Fig. 3. Internal-ionization energy as a function of band gap for II–VI compounds.

the mean ionization energy and the energy gap of II–VI compounds to be represented as

$$\varepsilon = 2.5 E_g. \qquad (11)$$

It should be emphasized that the magnitudes of ε obtained may be somewhat underestimated. This may be caused by the fact that the actual coefficient of reflection of the accelerated electrons from the surface of polycrystalline samples is obviously smaller than those given in [10] for single crystals. Also, if one uses for the calculation of ε the value $R_\beta = 0.2$ [10] for copper sulfide (instead of the base II–VI material), dependence (11) takes the form $\varepsilon = 2.7 E_g$. The main distinction of expression (11) from those published in [13–15] is that the dependence of the mean energy of internal ionization on the band gap does not contain an additional term and the straight line $\varepsilon = f(E_g)$ runs (at the extrapolation) through the origin of coordinates. This distinction is of fundamental importance and reflects the fact that $\varepsilon = 0$ for the materials with $E_g = 0$ as, for instance, in metals.

CONCLUSION

Thus, a method for the determination of the internal ionization energy of the direct-gap II–VI compounds

being irradiated with accelerated electrons is suggested in this study, and the values of this energy are obtained experimentally. It is shown that the mean values of ε for CdS, CdSe, CdTe, ZnS, and ZnSe are equal to 5.8, 4.4, 3.5, 8.9, and 6.4 eV, respectively. The experimental data are described satisfactorily by the empirical expression $\varepsilon = 2.5 E_g$.

REFERENCES

1. V. S. Vavilov, Usp. Fiz. Nauk **164** (3), 287 (1994) [Phys. Usp. **37**, 269 (1994)].
2. A. N. Georgobiani, Usp. Fiz. Nauk **113** (1), 129 (1974).
3. S. Yu. Pavelets, A. V. Komashchenko, V. D. Fursenko, and P. P. Gorbik, Optoélektron. Poluprovodn. Tekh. **34**, 36 (1999).
4. A. V. Komashchenko, K. V. Kolezhuk, P. P. Gorbik, *et al.*, Pis'ma Zh. Tekh. Fiz. **26** (5), 1 (2000) [Tech. Phys. Lett. **26**, 179 (2000)].
5. Yu. N. Bobrenko, A. M. Pavelets, S. Yu. Pavelets, and V. M. Tkachenko, Pis'ma Zh. Tekh. Fiz. **20** (12), 9 (1994) [Tech. Phys. Lett. **20**, 477 (1994)].
6. A. G. Rokakh and V. A. Smolyar, Izv. Akad. Nauk SSSR, Ser. Fiz. **33** (3), 473 (1969).
7. R. P. Joshi, K. H. Schoenbach, C. Molina, and W. W. Hofer, J. Appl. Phys. **74** (3), 1568 (1993).
8. S. Sze, *Physics of Semiconductor Devices* (Wiley, New York, 1981; Mir, Moscow, 1984), Vol. 2.
9. *Physicochemical Properties of Semiconducting Materials: A Reference Book* (Nauka, Moscow, 1979).
10. C. A. Klein, Appl. Opt. **5** (12), 1922 (1966).
11. S. V. Svechnikov and V. G. Chalaya, Fiz. Tverd. Tela (Leningrad) **8** (10), 3108 (1966) [Sov. Phys. Solid State **8**, 2486 (1966)].
12. P. P. Gorbik, N. O. Maĭ, A. V. Komashchenko, *et al.*, Dopov. Akad. Nauk Ukr. **12**, 85 (1999).
13. V. S. Vavilov and N. A. Ukhin, *Radiation Effects in Semiconductors and Semiconductor Devices* (Atomizdat, Moscow, 1969).
14. V. S. Vavilov, N. P. Kekelidze, and L. S. Smirnov, *Effects of Radiation on Semiconductors* (Nauka, Moscow, 1988).
15. C. A. Klein, J. Phys. Soc. Jpn. **21**, 307 (1966).

Translated by A. Zalesskiĭ

SEMICONDUCTOR STRUCTURES, INTERFACES, AND SURFACES

Influence of the Misfit-Dislocation Screw Component on the Formation of Threading Dislocations in Semiconductor Heterostructures

E. M. Trukhanov*, A. V. Kolesnikov, A. P. Vasilenko, and A. K. Gutakovskiĭ

Institute of Semiconductor Physics, Siberian Division, Russian Academy of Sciences,
pr. Akademika Lavrent'eva 13, Novosibirsk, 630090 Russia
* e-mail: trukh@isp.nsc.ru
Submitted June 25, 2001; accepted for publication July 12, 2001

Abstract—In heterostructures with the (001) interface and diamond and sphalerite crystal lattices, the total relief of mismatch stresses by introducing two mutually perpendicular arrays of 60° misfit dislocations (MDs) was shown to be possible only if their screw components were of the same type. In the opposite case, it was necessary to introduce additional MD arrays that increased the probability of formation of threading dislocations in an epitaxial film. When the process is nonoptimal and two mutually perpendicular arrays are introduced with opposite types of screw components, excess energy of long-range shear stresses is accumulated. Examples of nonoptimal introduction of misfit dislocations are the operation of the Frank–Read and Hagen–Strunk modified dislocation sources. The relaxation process was simulated and investigated experimentally. © 2002 MAIK "Nauka/Interperiodica".

1. INTRODUCTION

In semiconductor epitaxial structures, a mismatch in lattice parameters of interfaced layers gives rise to a mechanical-stress field. The control of the relaxation process for the stressed state represents a serious experimental and theoretical problem of current epitaxial technology. The most conventional variant of relaxation consists in the introduction of misfit dislocations (MDs) into the film–substrate interface, which is possible for a film thickness h exceeding a critical value h_c when the transition of the film from a pseudomorphic state into a dislocation one becomes energetically favorable [1–3]. The preferred mechanism of MD formation is gliding, because it proceeds at lower temperatures compared to the dislocation climb. This circumstance facilitates the forming of abrupt interfaces and decreases the number of defects in the heterostructure as a whole. In the process of introducing a misfit dislocation, one of its edges (or both) bends from the interface and emerges on the free surface of the film. As a result, a dislocation section arises that threads throughout the epitaxial film and, gliding over the interface, extends the MD. In an ideal case, all the mobile threading dislocation sections are brought out to lateral faces of the heterostructure after the relaxation process is completed, and the MD mean length is comparable to the interface diameter. In such a heterosystem, the film and the substrate have an identical structural-defect density in the crystal lattice after the total relief of mismatch stresses.

The realization of this idealized situation might make it possible to solve the problem of obtaining a defect-free substrate material for a wide class of semiconductors on the basis of bulk silicon, because this material is the most perfect of bulk crystals produced artificially. Reasonably thick, perfect epitaxial layers in which the mismatch stresses are relieved can be further used as the nucleating substrates for obtaining new semiconductor compounds.

When the relaxation proceeds in real structures, there is always the probability of stopping the gliding dislocation section far from the film edge, as a result of which immobile threading dislocations (TDs) arise. If the mismatch parameter f is of the order of 1% or more for the interfaced crystal lattices in the film and the substrate, the formation of immobile TDs is virtually inevitable. For current epitaxial technology, the production of highly perfect structures with a large mismatch is possible only in the case of pseudomorphic layers when the introduction of MDs is either energetically unfavorable ($h < h_c$) or cannot occur due to kinetic restrictions for $h > h_c$ [4, 5].

The generation of immobile TDs is conducive in certain situations to the generation of new MDs [6–9] and to the process of relief of mismatch stresses; however, this phenomenon, as a whole, should be thought of as undesirable. This is associated with a considerable degradation of structural properties of the heterostructure containing these defects. In such structures, the values of electrical parameters corresponding to the perfect bulk crystals are unattainable in a number of cases. Moreover, the electron and optical properties predicted theoretically also prove to be unattainable. After the process of the relief of mismatch stresses is

completed, the density of immobile TDs decreases steadily as the film thickness increases; this is due to the mutual annihilation of dislocations with opposite Burgers vectors $\mathbf{b}$ [10]. The lesser the number of MD arrays introduced into the interface, the more favorable the conditions for the annihilation of immobile TDs. For the heterosystems with a crystal lattice of the diamond or sphalerite types and the (001) interfaces, the variant of relaxation is possible when only two mutually perpendicular arrays of 60° MDs (60°-MDs) with the common vector $\mathbf{b}$ are formed. The formation of such an MD network maximally facilitates the TD annihilation; a keen interest in the mechanisms of its formation has persisted for decades worldwide [11–15]. However, the influence of the type of the screw dislocation component on such a relaxation process and on the generation of threading dislocations has been unstudied until now.

In this paper, this influence is considered in greater detail for the process of introducing mutually perpendicular arrays with common $\mathbf{b}$; however, other mechanisms of MD formation are also discussed. We investigated semiconductor heterosystems with a diamond and sphalerite crystal lattice and a (001) interface, which are most widely used in experimental and technological practice. In this study, we also showed that it is the high symmetry of the cubic crystal lattice that is favorable for the generation of immobile threading dislocations when introducing MDs into the given interface.

2. GENERATION OF IMMOBILE THREADING DISLOCATIONS AS A RESULT OF INTERACTION BETWEEN IMMOBILE DISLOCATION SECTIONS

The mobile threading dislocation sections, which extend the misfit dislocations during their gliding, can interact, thus generating immobile TDs. Because the [001] direction coincides with the fourth-order symmetry axis, eight 60°-MD arrays can be equiprobably introduced into the (001) interface for $h > h_c$. They are listed in the table. Four arrays, 1–4, are in parallel with the [1$\bar{1}$0] direction; and four arrays, 5–8, are in parallel with the [110] axis.

To analyze the influence of the interaction between gliding threading dislocation sections on the generation of immobile TDs, we assume that an extension of MD array 1 occurs in the [$\bar{1}$10] direction. According to the table, such an MD has the Burgers vector $\mathbf{b}_1 = (a/2)[101]$. The mobile threading section of this misfit dislocation can meet a similar section which glides in the opposite [1$\bar{1}$0] direction and extends one more MD. If the spacing between the meeting MDs is less or is on the order of b/f, four interaction variants, I–IV, are possible between them. In case I, the misfit dislocation extending in the opposite [1$\bar{1}$0] direction belongs also to array 1. Therefore, the total annihilation of meeting

Parameters of 60° MDs located in the (001) interface of heterostructures with the diamond and sphalerite crystal lattices. The types of screw dislocation components correspond to the case when the lattice parameter of the film exceeds the lattice parameter of the substrate ($a_d < a_s$). In the opposite case, when $a_d < a_s$, the types of screw dislocation components must be changed to the opposite ones

Number of an array	Glide plane	Direction of the Burgers vector, $\mathbf{b}$	Direction of the dislocation line, ξ	Type of screw dislocation component
1	($\bar{1}\bar{1}$1)	[101]	[$\bar{1}$10]	Left-hand
2	($\bar{1}\bar{1}$1)	[011]	[$\bar{1}$10]	Right-hand
3	(111)	[$\bar{1}$01]	[1$\bar{1}$0]	Left-hand
4	(111)	[0$\bar{1}$1]	[1$\bar{1}$0]	Right-hand
5	(1$\bar{1}$1)	[011]	[$\bar{1}\bar{1}$0]	Left-hand
6	(1$\bar{1}$1)	[$\bar{1}$01]	[$\bar{1}\bar{1}$0]	Right-hand
7	($\bar{1}$11)	[0$\bar{1}$1]	[110]	Left-hand
8	($\bar{1}$11)	[101]	[110]	Right-hand

dislocation sections is possible, and the probability of the generation of an immobile threading dislocation is lowest. If the initial mobile section of array 1 meets the gliding dislocation section of array 2 (case II) or the section of array 3 (case III), these sections are stopped in positions of stable dislocation equilibrium, and two immobile TDs arise. Their mutual annihilation by means of dislocation reactions is impossible.

In case IV, when the misfit dislocation extending in the opposite direction belongs to array 4, i.e., $\mathbf{b}_4 = (a/2)[0\bar{1}1]$, the reaction with the generation of a pure-edge Lomer MD is possible between the misfit dislocations extending towards one another. Because the directions of dislocation lines for arrays 1 and 4 are taken as mutually opposite ($\xi_1 = -\xi_4$) in the table, the Burgers vector of the Lomer MD is calculated as $\mathbf{b} = \mathbf{b}_1 - \mathbf{b}_4 = a/2[110]$. In the case of the origination of the Lomer MD, the relief of mismatch between the crystal layers of the heterostructure proceeds most efficiently, but this is a rare situation. As a rule, the fraction of pure edge MDs is small, and it increases with temperature and mismatch parameters. Only in exceptional cases is it possible to obtain 100% of the Lomer MDs, but, in this case, it is necessary to introduce them according to the climb mechanism [16]. If the reaction generating the Lomer MDs takes place, after the mobile dislocation sections are met, one of them or both continue gliding in their initial directions and, while moving, transform two previously introduced 60°-MDs into a single 90°-MD. If both mobile TDs are involved in the reaction and it is brought to completion, the arisen 90°-MD has a length equal to the sum of the lengths of the initial 60°-MDs.

In this case, the ends of the arisen Lomer dislocation are connected with the film surface by the pair of dislocation sections instead of a single TD. Such a structure is caused by the specific feature of the emergence of the 90°-MD, because we consider its generation not as the result of the climb, but as the mechanism of gliding of the dislocations in two different {111} planes.

For the annihilation of the stopped TDs in case I and the reaction with the generation of 90°-MDs in case IV to set in, the transverse gliding of the given TDs or their climb is often necessary, because two MDs extending in opposite directions are typically arranged along different atomic rows in the interface. If no annihilation occurs in case I, and two immobile TDs are formed, the probability of their annihilation increases with increasing film thickness [17].

In situations I–IV, the threading dislocation sections move in parallel directions. For the dislocations moving in perpendicular directions along the interface, the positions of stable dislocation equilibrium are also possible, which can lead to the generation of immobile TDs. This is true if the gliding section of a dislocation from array *1* encounters the section of any of the arrays *5–7*. The most interesting variant of the meeting of the mobile TDs gliding in perpendicular directions is the meeting of threading sections of arrays *1* and *8*, because their annihilation is possible. As a result, the so-called *L*-shaped dislocation is formed in the interface. From the considered interaction between the threading dislocations, it follows that this is merely a single array of 60°-MDs in the $[\bar{1}10]$ direction and a single array in the [110] direction that should be introduced into the (001) interface of a semiconductor heterosystem for decreasing the density of immobile TDs. It seems that the combinations of perpendicular arrays, which have identical **b** and form the *L*-shaped dislocations, are optimal. According to the table, these are arrays *1* and *8*, *2* and *5*, *3* and *6*, and *4* and *7*.

From the literature, various mechanisms of the generation of the *L*-shaped dislocations are known. We discuss some of them. At the initial stage of the relaxation process, the first 60°-MDs are generated as a result of the bending and the subsequent motion of dislocation sections threading into the film from the substrate [1, 18]. If, during the phenomenon under consideration, a mobile TD is trapped by a crystal-lattice defect in the film, a certain section of this dislocation can begin to move in the {111} secondary glide plane. This is possible both for the upper [6, 7] and lower [8] sections of the TD trapped by a defect. The situation is also possible when one section of the TD glides in the secondary plane, while another glides in the primary plane [9]. If the trapping effect occurs repeatedly, a broken line involving a rectilinear, mutually perpendicular dislocation segments arises. In the case when such segments intersect, the fourfold dislocation node arises. This node can be divided into two double nodes because the Burgers vectors **b** of the intersecting dislocations are

identical. As a result, two *L*-shaped misfit dislocations are formed [2, 19, 20]. Each of them contains two mutually perpendicular dislocation rays, whose glide planes are the intersecting {111} planes. The rays have a common point, which we will call a kink of the *L*-shaped dislocation. Far from the kink, the dislocation ray constitutes an MD segment arranged in the interface. Near the kink, this beam is a dislocation section bent in the glide plane. One of the kinks of two *L*-shaped MDs that arose during the decomposition of the fourfold dislocation node moves from the interface to the film as a result of the prismatic gliding, while another node moves into the substrate. Since the Burgers vector **b** is tilted to the interface, the lengths of these sections decreases when the segments of *L*-shaped dislocations deflect from the interface. It is this effect that induces the energy gain in the decomposition reaction of the fourfold dislocation node. Such a dislocation reaction was theoretically predicted by Read [21] and was first experimentally observed in studies [19, 20]. The motion of the kink of the *L*-shaped MD inside the film can give rise to the Hagen–Strunk dislocation source [11, 18] or its modified variant [12]. As to the motion of such a kink inside the substrate, it gives rise to a modified Frank–Read source [13–15, 18]. During the operation of these sources, additional *L*-shaped MDs with the same Burgers vector are formed, and this provides favorable conditions for the annihilation of immobile TDs in the process of the further relaxation of the heterostructure [10]. Thus, on the basis of the published data, the formation of the 60°-MD network with identical **b** can be considered as a promising variant for controlling the process of relieving the mismatch stresses with the aim of reducing the density of immobile TDs. However, this conclusion is obtained without consideration of the effect of the type of the MD screw component on the relaxation of mismatch stresses. Such an effect is taken into account in the next section.

3. INFLUENCE OF THE SCREW COMPONENT OF MISFIT DISLOCATION ON THE PLASTIC RELAXATION OF MISMATCH STRESSES

We evaluated the relaxation process using the $Ge_{0.25}Si_{0.75}/Si$ heterosystem with the (001) interface as an example. It was assumed that two mutually perpendicular 60°-MD arrays were introduced, with their linear density $1/D$ being identical. Here, D is the spacing between the neighboring dislocation arrays. For the given film thickness h, we calculated the heterostructure energy as a function of D. The value of this function minimum was taken as the heterostructure energy E_{hs}, which corresponded to a given value of h provided that the process is quasi-steady.

The calculation model is similar to that we used in [22] with the modification that we consider 60°-MDs instead of the array of pure edge MDs. The type of screw component of the dislocation was taken into account by choosing the corresponding sign of the

stress components. The $E_{hs}(h)$ dependence is shown in Fig. 1. Curve *1* corresponds to the case of introducing the mutually perpendicular MDs with different types of screw components, and curve *2* refers to the case when the screw components coincide. For comparison, in Fig. 1, we show a change in the heterostructure energy (curve *3*) obtained in terms of the Matthews model [1]. It can be seen that all three dependences coincide for $h < h_c$, which is close to 10 nm. For h close to 30 nm, dependence *2* levels off, while dependence *1* becomes a virtually linear increasing function.

Elastic residual strains in the film were defined as $\varepsilon_d = f/(1 - D/D_0)$. The value $h_c = 8.3$ nm calculated in terms of our model is close to the value of 9.8 nm calculated according to the model [1]. The results of calculating $\varepsilon_d(h)$ are shown in Fig. 2. The designations for the curves in Figs. 1 and 2 coincide. It can be seen from the table that arrays *1* and *8*, which can generate the L-shaped MDs, have different types of screw components. For this reason, their introduction is described by curve *1*. From the data in Fig. 2, it can be seen that, if the value of elastic residual strains reaches below a certain level ($\varepsilon_d < 0.8\%$ for the $Si_{0.75}Ge_{0.25}$ heterostructure), the relaxation proceeds nonoptimally. Therefore, it becomes energetically favorable to introduce dislocations from other arrays between the generated dislocation. For example, if these are the generated L-shaped dislocations containing the left-hand screw components of array *1* and the right-hand screw components of array *8*, it is possible to additionally introduce both the right-hand-screw MDs from arrays *2* or *4*, which are parallel to array *1*, and the left-hand-screw MDs from arrays *5* or *7*, which are parallel to array *8*. In the case of introducing additional dislocation arrays, the relaxation process approaches the optimal variant (curve *2*); however, the probability of the generation of immobile TDs increases in this case as was considered in Section 2.

The decrease in the heterostructure energy upon introducing additional dislocation arrays is considerable. If it is assumed that only two mutually perpendicular arrays, i.e., *1* and *8*, are introduced for an arbitrary h, the heterostructure energy amounts to a substantial fraction (25–40%) of the energy of a structure containing an overstressed pseudomorphic film for $h > 30$ nm, which is much higher than the energy of an optimally relaxing structure. For comparison, curve *4* in Fig. 1 represents the energy of the heterosystem for which the film is in the pseudomorphic state independently of the value of h. An almost linear increase in heterostructure energy (curve *1*) is associated with the accumulation of excess elastic energy of the long-range shear stresses [23–25]. In the heterosystem with completely relieved mismatch stresses, when the spacing between the neighboring 60°-MDs is $D_0 = 0.5b/f$, these long-range stresses are equal to

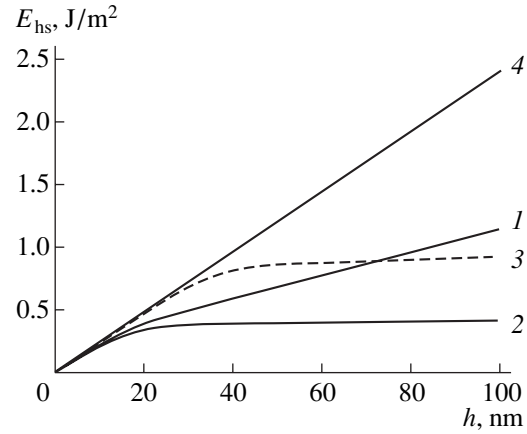$$\sigma_{xy} = Gb/D_0 = 2Gf, \qquad (1)$$

Fig. 1. Variation in energy of heterostructure with increasing film thickness determined in terms of various models. Curves *1* and *2* correspond to the model proposed and used for the case of the introduction of two mutually perpendicular 60° MD arrays (*1*) with different types of screw components and (*2*) with identical types; curve (*3*) was calculated in terms of the Matthews model [1]; and curve (*4*) represents the case of an overstressed pseudomorphic film.
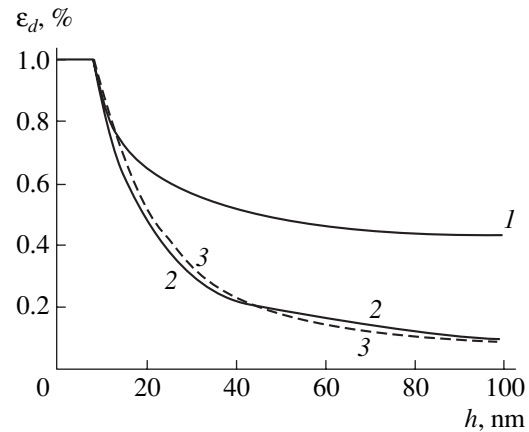

Fig. 2. Influence of the type of screw component of misfit dislocations on the relaxation process. The designation of curves is the same as in Fig. 1.

which amounts to a considerable fraction of stresses in the initial pseudomorphic film

$$\sigma_{yy} = \sigma_{xx} = 2Gf\frac{(1+v)}{(1-v)}.$$

The generation of these stresses accounts for the asymptotic approach of the $E_{hs}(h)$ dependence to a linear one with increasing h (curve *1* in Fig. 1). When determining the components σ_{xy} of the stress tensor, the Oz axis was directed perpendicular to the (001) interface, while the Ox and Oy axes were parallel to the [110] and [$\bar{1}$10] directions. If we rotate the Ox and Oy directions in the interface plane through 45°, i.e., make them parallel to the [100] and [010] directions, the act-
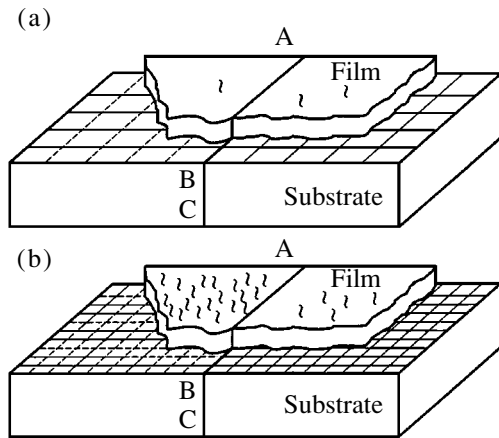
Fig. 3. Schematic illustration of the influence of the screw-component type of a misfit dislocation (MD) on the formation of immobile threading dislocations. To the right of the ABC cross section, two MD arrays are introduced with identical types of screw components throughout the relaxation process (a and b). To the left of the ABC cross section, two MD arrays with the common **b** and opposite types of screw components are introduced (a) at the initial stage of the process; at the next stages, several arrays are introduced. Short zigzag lines denote the threading dislocations. The solid and dashed lines denote the misfit dislocations with the screw components of different types.

ing field is described in terms of the compressive–tensile stresses as

$$\sigma_{yy} = -\sigma_{xx} = 2Gf. \tag{2}$$

The above additional introduction of right-hand-screw MD arrays *2* and *4*, which are parallel to array *1*, and also the introduction of left-hand-screw MD arrays *5* and *7*, which are parallel to array *8*, is one of the methods of relaxation for the field of long-range stresses. If the relaxation is insufficiently efficient, the origination of a fragmentary structure or cracks is possible [23–26].

The field of stresses written as (1) or (2) is the superposition of two fields, each of which is generated by a single array of 60°-MDs. In particular, array *1* of the left-hand-screw misfit dislocations distributed with a linear density $1/D_0$ generates the long-range field of stresses, which is equal to the halved value defined by expression (1) or (2). This field can be completely compensated by the long-range stresses of arrays *2* or *4* of the right-hand-screw dislocations, which are parallel to array *1* and are distributed with the same linear density. If we want to use the MD array which lies in the perpendicular direction for the purpose of compensating the long-range field of stresses generated by array *1* of the left-hand-screw misfit dislocations, these dislocations must be the left-hand-screw ones. These can be dislocations from either array *5* or array *7* distributed with the same linear density of $1/D_0$.

The above analysis makes it possible to formulate the requirements for the 60°-MD arrays ensuring a minimum density of immobile TDs at various stages of the

relaxation process in a heterostructure with the (001) interface. If it is necessary to grow an epitaxial film in which the mismatch stresses are relieved only partially ($\varepsilon_d > 0.8f$), it is expedient to introduce two mutually perpendicular MD arrays with the common Burgers vector. In semiconductor technology, a more often encountered problem is the production of a film with few defects in which the mismatch stresses are completely relieved. A possible variant of its optimal solving is the introduction of two mutually perpendicular MD arrays with identical types of screw components. It is necessary to introduce either two arrays of the left-hand-screw MDs or two arrays of the right-hand-screw MDs.

It should be noted that the screw-component type is not taken into account in the Matthews model or its various modifications [1–3]. The process of relaxation calculated in terms of this model is illustrated by dashed curve *3* in Fig. 2, which runs rather close to curve *2* plotted for the case of the identical screw-component types. As follows from our data shown in Fig. 1, the value of elastic energy accumulated by the heterostructure to the end of relaxation is approximately twice as high in the case of curve *3* than in the case of curve *2*. As a result, curve *3* runs closer to curve *1* than to curve *2* for the region of thicknesses used in plotting Fig. 1 ($h \lesssim 100$ nm).

The influence of the screw-component type on the generation of immobile TDs is illustrated on the schematic drawing in Fig. 3. The misfit dislocations with different screw-component types are shown by the solid and dashed lines. At the initial stage of relaxation (Fig. 3a), two mutually perpendicular MD arrays with a common Burgers vector (for example, the dislocations from arrays *1* and *8*) are introduced into the region of the interface arranged to the left of the ABC cross section, and two mutually perpendicular MD arrays with screw components of the same type are introduced into the region to the right of this cross section. These can be two MD arrays with the left-hand screw component or two arrays with the right-hand screw component. In the right-hand region of the structure, the perpendicular MD arrays have different Burgers vectors; therefore, the annihilation of the threading dislocations proceeds here less efficiently than in the left-hand region, and the density of immobile threading dislocations is higher at the initial stage (Fig. 3a). For the further relaxation in the left-hand region of the structure, the introduction of additional dislocation arrays is necessary, which is favorable for increasing the density of immobile TDs (Fig. 3b). As was shown in [25], in this case, even a redistribution of the previously introduced MDs is possible. However, in the right-hand region of the structure, the introduction of the same arrays as those in Fig. 3a is retained throughout the relaxation process. As a result, a substantially lower TD density can be attained at the final stage. It should be noted that, if two mutually perpendicular MD arrays with different Burgers vectors and different

screw components (for example, dislocations from arrays *1* and *6*) were introduced at the initial stage to the left of the ABC cross section, it would have been necessary to show identical densities of threading dislocations to the left and to the right of the ABC cross section.

Using Fig. 3, we illustrate two conditions which ensure a reduced density of immobile threading dislocations at various stages of relieving the mismatch stresses. For the initial stage, such a favorable condition is the requirement that the Burgers vector is common for two mutually perpendicular MD arrays. At the remaining stages of the process, it is necessary that the types of screw components are identical for these arrays.

4. SPECIAL FEATURES OF THE GENERATION OF THREADING DISLOCATIONS FOR VARIOUS MECHANISMS OF FORMATION OF MISFIT DISLOCATIONS

As was shown in Section 2, it is the high symmetry of the cubic crystal lattice that is favorable for the generation of immobile threading dislocations if the MDs are introduced into the (001) interface of a semiconductor heterostructure. In the first approximation, the data displayed in Fig. 2 describe the quasi-steady relaxation in the case of introducing MDs into interfaces with (001) vicinal orientations. It should be noted that, when we pass from a singular orientation of the (001) interface to an arbitrary vicinal orientation, the number of MD arrays to which the common value of h_c corresponds becomes less than 8. Therefore, provided that the process is quasi-steady, the probability of TD generation decreases. It is evident that, when describing the relaxation process, it is necessary to consider only the MD arrays to which the minimum values of h_c correspond. According to [26], if a vicinal plane is obtained by the rotation about a direction of the $\langle 100 \rangle$ type, two mutually perpendicular MD arrays are introduced for a minimum critical thickness, and these arrays have opposite screw components. Therefore, the process is described by curve *1* in Fig. 2 and characterized by the accumulation of excess elastic energy and, as a consequence, requires the introduction of additional MD arrays. If a vicinal plane orientation is obtained by rotation about a direction of the $\langle 110 \rangle$ type, there are two pairs of mutually perpendicular arrays that are introduced. In every pair, one array is a dislocation with the left-hand screw component, while the other one is a dislocation with the right-hand screw component. As a result, the process is described by curve *2* (Fig. 2), but the probability of TD generation increases due to the large number of the arrays introduced. It is possible to show that, if the (001) vicinal orientations are obtained by rotations about some of the other axes, the probabilities of the formation of immobile TDs are lower than in the case of orientations obtained by the rotations about the $\langle 110 \rangle$ directions and higher than in the case of

the orientations obtained by the rotations about the $\langle 110 \rangle$ directions. Thus, if we consider the entire set of (001) vicinal orientations, the probability of the formation of immobile TDs under conditions of the quasi-steady proceeding of the relaxation is highest for the orientations obtained by the rotations about the $\langle 110 \rangle$ directions. We noted that it is these deviated orientations which are the most widespread in technological applications.

Of the MD-introduction mechanisms known from the available publications, the most frequently discussed are the homogeneous origination of dislocation half-loops at random sites of the heterosystem and the activation-free introduction of MDs from the dislocations previously existing in the substrate. In the case of the former mechanism, the conditions considered when Fig. 3 was discussed, and shown to ensure a lowered density of immobile TDs, are not fulfilled for the equiprobable introduction of various dislocation arrays at any stage of the process. In the case of the latter mechanism, the density of immobile TDs depends on the nature of dislocations in the substrate. If all the dislocations have the same Burgers vector, only two arrays of mutually perpendicular MDs with common **b** are introduced at the initial stage of relaxation; at this stage of the process, the probability of generating immobile TDs is lowered (Fig. 3a, the left-hand region). At subsequent stages of the process, this probability increases due to introducing additional arrays. If it is equiprobable to detect a dislocation with an arbitrary Burgers vector in the initial substrate, there are no prerequisites for reducing the density of immobile TDs.

The search for the factors ensuring the introduction of two mutually perpendicular arrays with identical types of screw components is also of importance for the stage of formation of an equilibrium MD network [18]. If such arrays are introduced, we can rely on the formation of a relatively flat dislocation network. It is likely that the greater the number of dislocation arrays involved in the relaxation process, the larger the volume that occupies the equilibrium dislocation network and the higher the energy of such a network. Moreover, as will be shown below using the experimental data, an increase in the number of arrays involved in the relaxation process promotes the additional formation of immobile TDs at the final stage of the relaxation process.

Examples of three-dimensional dislocation networks, which arise when several dislocation arrays are introduced in the mutually perpendicular directions, are shown in the electron microscopy photographs (Fig. 4). In Fig. 4a, numbers *1* and *2* denote the kinks of *L*-shaped MDs, and numbers *3* and *4* indicate the short bridges of the dislocation network, which connect two triple MD nodes. Kinks *1* and *2*, as well as bridges *3* and *4*, are oriented differently in the space. This means that the interaction between at least four MD arrays
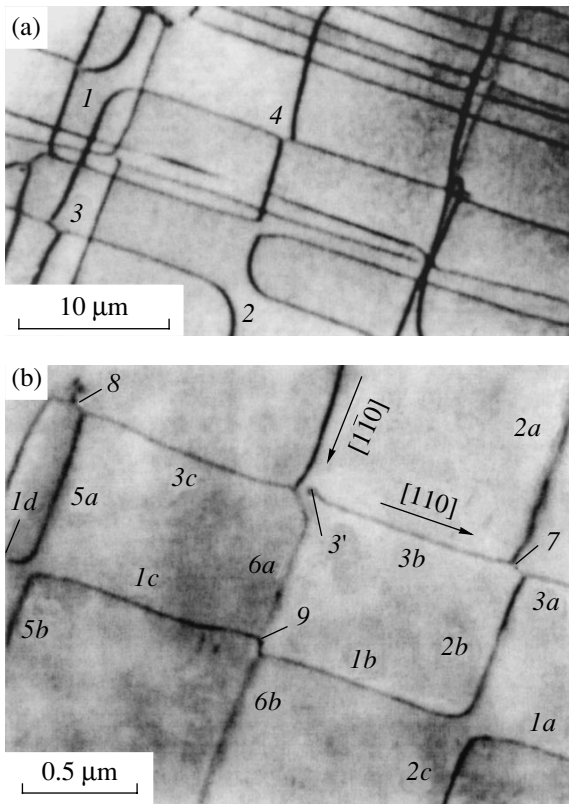
Fig. 4. Electron-microscopy photographs of the three-dimensional dislocation network near the interface of the InGaAs/(001)GaAs heterostructure. In Fig. 4a, numbers *1* and *2* denote the pairs of *L*-shaped misfit dislocations (MDs), and numbers *3* and *4* denote short bridges in the dislocation network connecting two triple nodes of the MDs. In Fig. 4b, number *3'* denotes the immobile threading dislocation appearing at the stage of formation of the network. For dislocations *1–8* in Fig. 4b, the Burgers vectors are $\mathbf{b}_{1,2,4,5} = (a/2)[101]$, $\mathbf{b}_3 = (a/2)[01\bar{1}]$, and $\mathbf{b}_{6,7,8} = (a/2)[110]$.

listed in the table are necessary to form the dislocation structure displayed in Fig. 4a.

The pattern of the three-dimensional dislocation network shown in Fig. 4b was obtained using the diffraction vector $\mathbf{g} = [2\bar{2}0]$. The identical numbers denote the network elements with identical Burgers vectors. Various letter additions to identical numbers denote the network elements, which likely composed previously a single extended misfit dislocation. The Burgers vectors of various dislocation elements of the network are given in the caption to Fig. 4. For their determination, we used the following two special features of behavior of the dislocation contrast. The first of these consists in the fact that the image of a dislocation disappears if the conditions $\mathbf{gb} = 0$ and $\mathbf{g}(\mathbf{b} \times \boldsymbol{\xi}) = 0$ are met simultaneously; here, $\boldsymbol{\xi}$ is the unit vector parallel to the dislocation line. According to the second feature, the image of a dislocation becomes binary if $\mathbf{gb} = 2$ and if the images are obtained under conditions when the Ewald

sphere passes strictly through a reciprocal lattice site corresponding to the vector $\mathbf{g}$. In order to investigate the dislocation structure, we also obtained electron-microscopy photographs for the same area of the heterosystem (Fig. 4b) using the vectors $\mathbf{g} = [\bar{2}20]$, [400], and [040]. This enabled us to establish that the origination of this dislocation network is associated with dislocation reactions. Network elements *1–5* are the 60° MDs. Elements *6*a and *6*b are the Lomer 90° MDs. Their contrast disappears for $\mathbf{g} = [\bar{2}20]$. Two pairs of *L*-shaped dislocations are observed: one of them is represented by dislocations *1*a, *2*c, and *1*b, *2*b, and the other, by dislocations *1*c, *5*b, and *1*d, *5*a. Short dislocation bridges connecting the triple network nodes are denoted as *7–9*.

At an early stage of formation of this stable structure, dislocation *4* was apparently more extended along the $[1\bar{1}0]$ direction and occupied the positions of elements *6*a and *6*b. As a result of reactions between continuous dislocation *3*, which involved sections *3*a, *3*b, *3*c, and dislocations *2*, *4*, *5*, dislocation segments *7* and *8* arose as well as the immobile threading dislocation *3'*. Analysis shows that a mobile TD also arose during the generation of dislocation *3'* and this TD glided in the $[1\bar{1}0]$ direction and transformed the 60° dislocation *4* into Lomer dislocation *6*. For generating the mentioned threading dislocations, a segment of gliding dislocation *3* emerged on the free surface of the film near its intersection with dislocation *4*. This resulted in an increase in the energy of the system; however, the subsequent formation of the Lomer MD compensated this expenditure and additionally decreased the energy. The decrease in the energy as a result of the dislocation reaction that transformed the 60° MD into the Lomer dislocation is also associated with the fact that the component of the edge constituent of the Burgers vector along the [110] direction is twice as large for dislocation *6* than for dislocation *4*. It should be noted that, as a result of this reaction, the level of shear stresses in the heterostructure decreases, which is favorable for the proceeding of this reaction. According to the data in Fig. 4b and the table, three neighboring parallel dislocations, *2*, *4*, and *5*, have an identical Burgers vector and the same type of screw component. Therefore, the substitution of 60° dislocation *4* by edge dislocation *6* decreases the mean level of shear stresses in their neighborhood. An important result of the above analysis is the conclusion that the appearance of immobile TDs is possible near the interface where the three-dimensional dislocation network is formed.

5. CONCLUSION

We investigated the influence of the type of dislocation screw component on the relaxation process of relieving the mismatch stresses and on the formation of threading dislocations in an epitaxial film. This investigation enabled us to formulate the requirements on the

60°-MD arrays ensuring the lowest density of immobile threading dislocations. If the technological problem is to obtain an overstressed epitaxial film, when partial plastic relaxation is admissible, it is expedient to introduce two mutually perpendicular MD arrays with a common Burgers vector. If the problem is to obtain a low-defect film in which the mismatch stresses are completely relieved, a possible variant of its optimal solution is the introduction of two mutually perpendicular MD arrays with identical types of screw components.

ACKNOWLEDGMENTS

REFERENCES

1. J. W. Matthews, J. Vac. Sci. Technol. **12**, 126 (1975).
2. E. A. Fitzgerald, Mater. Sci. Rep. **7** (3), 87 (1991).
3. Yu. B. Bolkhovityanov, O. P. Pchelyakov, and S. I. Chikichev, Usp. Fiz. Nauk (in press).
4. Yu. B. Bolkhovityanov, A. L. Alperovich, A. S. Jaroshevich, *et al.*, J. Cryst. Growth **146**, 310 (1995).
5. J. C. Bean, L. C. Feldman, A. T. Fiory, and S. Nakahava, J. Vac. Sci. Technol. A **2**, 436 (1984).
6. M. Hohnisch, H.-J. Herzog, and F. Schäfferu, J. Cryst. Growth **157**, 126 (1995).
7. B. Beanland, J. Appl. Phys. **77**, 6217 (1995).
8. J. Washburn and E. P. Kvam, Appl. Phys. Lett. **57**, 1637 (1990).
9. C. G. Tuppen, C. J. Gibbings, M. Hockly, and S. G. Roberts, Appl. Phys. Lett. **56**, 54 (1990).
10. R. E. Romanov, W. Pompe, S. Mathis, *et al.*, J. Appl. Phys. **85**, 182 (1999).
11. H. Strunk, W. Hagen, and E. Bauser, Appl. Phys. **18**, 67 (1979).
12. R. Beanland, J. Appl. Phys. **72**, 4031 (1992).
13. A. Lefebvre, C. Herbeaux, C. Bouillet, and J. Dr Persino, Philos. Mag. Lett. **63**, 23 (1991).
14. F. K. LeGoues, B. S. Meyerson, J. F. Morar, and P. D. Kirchner, J. Appl. Phys. **71**, 4230 (1992).
15. K. W. Shwarz, J. Appl. Phys. **85**, 108 (1999).
16. A. Trampert and K. H. Ploog, Appl. Phys. Lett. **66** (17), 2265 (1995).
17. J. S. Speck, M. A. Brewer, G. Beltz, *et al.*, J. Appl. Phys. **80**, 3808 (1996).
18. V. I. Vdovin, Phys. Status Solidi **171**, 239 (1998).
19. E. M. Trukhanov, E. B. Gorokhov, and S. I. Stenin, Phys. Status Solidi A **33**, 435 (1976).
20. S. I. Stenin, O. P. Pchelyakov, and E. M. Trukhanov, in *Properties of Metal-Dielectric-Semiconductor Structures* (Nauka, Moscow, 1976), p. 222.
21. W. T. Read, *Dislocations in Crystals* (McGraw-Hill, New York, 1953; Nauka, Moscow, 1957).
22. E. M. Trukhanov, K. B. Fritzler, and A. V. Kolesnikov, Appl. Surf. Sci. **123/124**, 664 (1998).
23. A. Tkhorik and L. S. Khazan, *Plastic Deformations and Misfit Dislocations in Heteroepitaxial Structures* (Kiev, 1983).
24. E. M. Trukhanov, Poverkhnost, No. 2, 13 (1995).
25. E. M. Trukhanov, Poverkhnost, No. 2, 22 (1995).
26. E. M. Trukhanov and A. V. Kolesnikov, Appl. Surf. Sci. **123/124**, 669 (1998).

Translated by V. Bukhanov

Optical Properties of Ultradisperse CdSe$_x$Te$_{1-x}$ (0 ≤ x ≤ 1) Particles in a Silicate Glass Matrix

I. V. Bodnar*, V. S. Gurin**, A. P. Molochko*, N. P. Soloveĭ*,
P. V. Prokoshin**, and K. V. Yumashev***

* Belarussian State University of Information Science and Radio Engineering, Minsk, 220027 Belarus
** Research Institute for Physicochemical Problems, Belarussian State University, Minsk, 220080 Belarus
*** International Laser Center, Belarussian State Polytechnical Academy, Minsk, 220012 Belarus
Submitted May 30, 2001; accepted for publication July 11, 2001

Abstract—Ultradisperse particles of CdSe$_x$Te$_{1-x}$ (0 ≤ x ≤ 1) were formed in the matrix of a silicate glass by introduction of corresponding prepared compounds into a mixture of SiO$_2$ and Ca, Na, K, and Li oxides. Initially produced particles with an average size of 10–15 nm grow by a factor of 2–3 after additional thermal treatment of the glasses; the optical absorption spectra are noticeably changed only in the case of CdSe$_x$Te$_{1-x}$ (x = 0.8 or 0.4) solid solutions, but not in the case of CdSe and CdTe binary compounds. All glasses synthesized exhibit similar luminescence bands in the visible region of the spectrum. The features observed are interpreted under the assumption that two crystalline modifications (wurtzite and sphalerite) are separated in the process of thermal treatment of glasses activated by solid solutions. © 2002 MAIK "Nauka/Interperiodica".

1. INTRODUCTION

Interest in new optical materials containing ultradisperse particles of semiconductors has not waned despite a large number of studies in this field. This interest is caused by the diversity of optical properties, which is due to the presence of nanoparticles of semiconductors exhibiting size-dependent physical properties [1–5]. The optical characteristics of such materials directly depend on the nature of a semiconductor, particle size, and the character of particle localization in a glass matrix and can have typical bands in a wide region of the spectrum: from ultraviolet to infrared (IR) [1, 2, 6–8].

Silicate glasses activated by II–VI compounds, in particular, by cadmium chalcogenides, span the visible region of the spectrum and are used for the fabrication of industrial optical filters. In addition, corresponding cadmium compounds are quite stable and are inert to glass; moreover, their semiconductor properties have been adequately studied. In spite of detailed studies of the conditions for the formation of semiconductor nanocrystals of this class in glasses [3–5, 9–14], deep insight into their optical properties is absent owing to the numerous factors which affect the state of nanocrystals and glass matrices. Among cadmium chalcogenides, the least studied are the telluride and telluride-based solid solutions. Both in crystalline structure and in chemical behavior, CdTe differs markedly from CdSe and CdS; thus, one should expect the behavior of CdSe$_x$Te$_{1-x}$ to differ from that of a Cd–S–Se system. Thus, the most characteristic crystalline structure of CdTe under conventional conditions is cubic (sphaler-

ite), whereas the most stable lattice for CdS and CdSe is hexagonal (wurtzite) [15]. Quantum-mechanical size effects for CdTe manifest themselves most distinctly in the series of chalcogenides under consideration due to a large exciton Bohr radius (a_B = 7.5 nm for CdTe and 5.4 nm for CdSe [16]) and low effective electron masses (0.11m_e for CdTe and 0.13m_e for CdSe [15]). The above facts indicate that the study of glasses activated by CdTe, CdSe nanoparticles and their solid solutions is relevant. We should also note that the main method of preparing such glasses is the fusion of the batch containing the basis of the vitreous matrix (silicon oxides, oxides of alkali metals, and other glass-forming components) with cadmium oxide and selenium/tellurium; the formation of chalcogenides occurs during an annealing in the reducing atmosphere [17–24]. The method we used for preparation of glasses activated by CdSe$_x$Te$_{1-x}$ consists in the introduction of corresponding prepared compounds in a batch, the composition of which permits its sufficient solubility [25–27]. Such a method is productive for the formation of glasses with ternary compounds and their solid solutions CuMX$_2$, where X = S, Se, or Te, and M is a Group IIIa element. In the case of ternary compounds, the controllable realization of chemical reactions of chalcogenides with oxides of metals in the course of annealing is difficult since the oxides of copper and IIIa metals have markedly differing reaction characteristics.

The aim of this study was to ascertain the conditions for the formation of ultradisperse particles of the CdSe$_x$Te$_{1-x}$ semiconductor phase (x = 0–1) in the matrix of a silicate glass and to determine their microstructure and optical properties.

2. EXPERIMENTAL

The activated materials studied were prepared on the basis of glass matrices in a SiO$_2$–CaO–M$_2$O (M = Li, Na, K) system. Such matrices are characterized by high optical transmission in the visible and IR spectral regions. The edge of their intrinsic absorption is located near the wavelength λ = 300 nm. We previously studied [25–27] the synthesis of glasses doped with ternary semiconductor compounds I–III–VI and their solid solutions; these studies allowed us to optimize the composition of glass matrices, improve their technical specifications, and lower the synthesis temperature to 1620 ± 10 K. The rather high melting temperatures of the corresponding compounds (>1623 K for CdSe and 1314 K for CdTe) and their stability and inertness to the glass substantiate the possibility of the direct introduction of CdSe and CdTe into the glass matrices in a dispersed form. In spite of the complete transparency of such glass matrices (without a semiconductor) in the visible region of the spectrum, their composition profoundly affects the optical properties of semiconductor nanocrystals localized in these matrices. In particular, the type of alkali metal cation has a special significance, as it exerts a different polarizing effect upon the components introduced. The particles of a semiconductor have a tendency to concentrate at the regions of the glass matrix enriched with alkali-metal ions [28], and one can assume that, in the case of a glass matrix with three alkali-metal oxides, there will be more favorable conditions for the nucleation and growth of the nanocrystalline phase of a semiconductor.

Crystalline CdSe$_x$Te$_{1-x}$ compounds were synthesized from the elements in a single-zone vertical furnace with subsequent prolonged (150–300 h) thermal annealing to provide homogenization. The crystal structure of the synthesized crystals was identified by X-ray diffraction studies. A set of X-ray diffraction patterns is presented in Fig. 1 for compounds used in comparison with published data for some modifications of CdTe, CdSe, and Te (insignificant quantities of the latter were present in the tellurium-containing species). It is noteworthy that the transformation of the hexagonal modification (wurtzite) more typical of CdSe into a cubic one (sphalerite) occurs only for the ratio [Te]/[Se] ≥ 4.

The founding of glasses with the addition of the aforementioned semiconductor compounds introduced in the amount of 0.75 wt % was carried out in a corundum crucible in a gas-flame furnace under reducing conditions. To prevent the oxidation of the semiconductor compounds, activated charcoal (2 wt %) was introduced into the batch. The synthesis temperature varied in the range of 1620 ± 20 K depending on the glass composition with exposure to a maximum temperature for 1 h. The melts, after synthesis, were rapidly cooled and subjected to annealing with subsequent natural cooling. The annealing temperature was selected with allowance made for the softening temperature of glasses (693 K).

X-ray studies of the powder-like semiconductors were carried out with a YZG4A diffractometer using CuK_α radiation with an Ni filter (λ = 0.154 nm).

The microstructure was studied by transmission electron microscopy (TEM) using an electron microscope (UEMV-100LM) with scanning the "carbon replica with extraction" taken off from the as-etched glass on which a carbon film 10–20 nm thick was evaporated. The optical spectra were measured for polished samples 0.25–0.5 mm thick using Specord M40 and CARY-17D spectrophotometers, and the photoluminescence spectra were measured using a Fluoromax-2 fluorimeter.

RESULTS AND DISCUSSION

The appearance of a characteristic color of the glasses as a result of introduction of semiconductor compounds into a charge was indicative of the formation of activated glasses by the method used; however, the presence of compounds in such a small amount did not result in changes in the X-ray patterns conventional for glasses. These patterns were characterized only by a broad halo from the amorphous glass matrix.

TEM data (Fig. 2) are unambiguously indicative of the formation of solid-phase particles inside the glass matrix, which affect optical characteristics. The particles observed have average sizes in the range of 10–15 nm, which depend little on the CdSe$_x$Te$_{1-x}$ solid-solution composition. The particles are localized in specific segregation regions, which are usually observed in glasses in the presence of formations of other chemical compositions.

As a result of an additional thermal treatment of glasses at 550 and 600°C (optical characteristics somewhat change in this case, see below), the particle size increases, on average, by 2–3 times and the concentration remains virtually unchanged. This is connected with the special features of nanoparticle formation in a glass matrix by the method indicated. In the course of the melt cooling, continuous nucleation with the simultaneous growth of nanocrystals occurs, which results in a sharp decrease in the supersaturation factor. Such a type of growth is characteristic of the stage of coalescence of particles [30, 31]. As a result, a depleted zone is formed around the growing nucleus of the nanocrystal; the supersaturation is low in this zone, the probability of the appearance of new nuclei decreases drastically, the growth process ceases, and the particles of a certain average size are formed. The calculations carried out in [32] show that, as a result of the transition from the growth stage to coalescence, the average radius of particles stabilizes under these conditions. Thus, in the course of additional heat treatment, the formation of new particles probably does not occur, and their resulting concentration actually coincides with that formed during high-temperature synthesis and cooling of the melt. It is worthwhile to note that the process of ultradisperse particle formation in this method
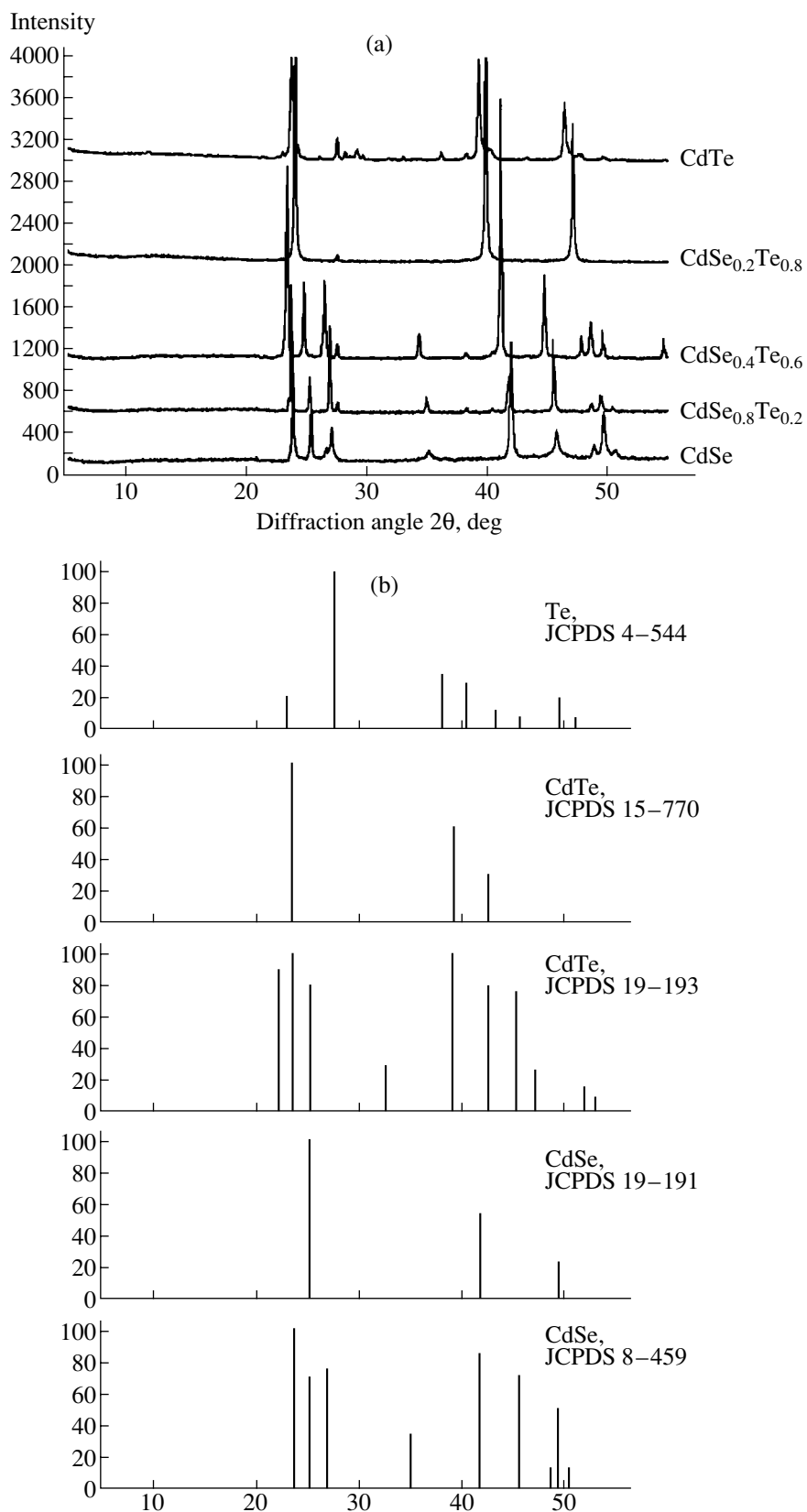
Fig. 1. Set of X-ray diffraction patterns of crystalline compounds of $CdSe_xTe_{1-x}$ series with various x employed for synthesis of activated glasses (a) in comparison with line X-ray diffraction pattern of JCPDS data [29] (b).
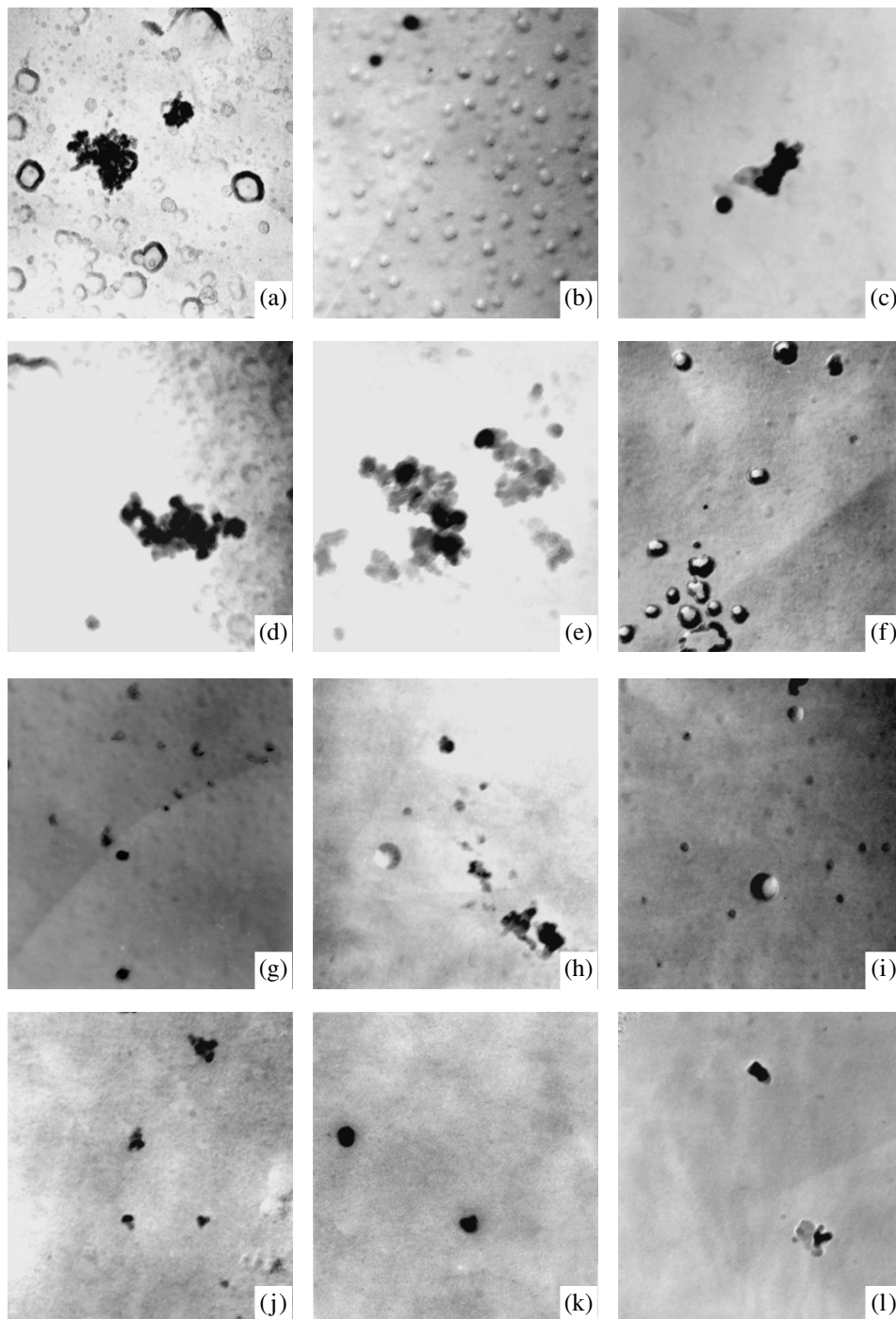
Fig. 2. Micrographs of particles formed in glass samples activated by CdSe$_x$Te$_{1-x}$ with various x without additional heat treatment (a, d, g, j) and after heat treatment (for 6 h) at temperatures of 550 (b, c, h, k) and 600°C (c, f, i, l). (a–c) The micrographs for CdSe; (d–f), for CdSe$_{0.8}$Te$_{0.2}$; (g–i), for CdSe$_{0.4}$Te$_{0.6}$; and (j–l), for CdTe. Magnification 40 000 X.

of activated glass preparation includes dispersion of the crystalline material and its melting and dissolution in the glass at high temperature with subsequent crystallization by cooling. Taking into account the aforementioned melting temperatures for CdSe and CdTe, we may assume that a solid phase is present in the process of the melt cooling, and the smallest sized particles have time to grow; as a consequence, we do not observe the fractions of particles with sizes less than 10 nm. The effect of heat treatment for the activated glasses under study is also minimal, because the material for the further growth of particles is absent within the glass matrix, in contrast to traditional methods of particle formation for the CdS–CdSe–CdTe composition in
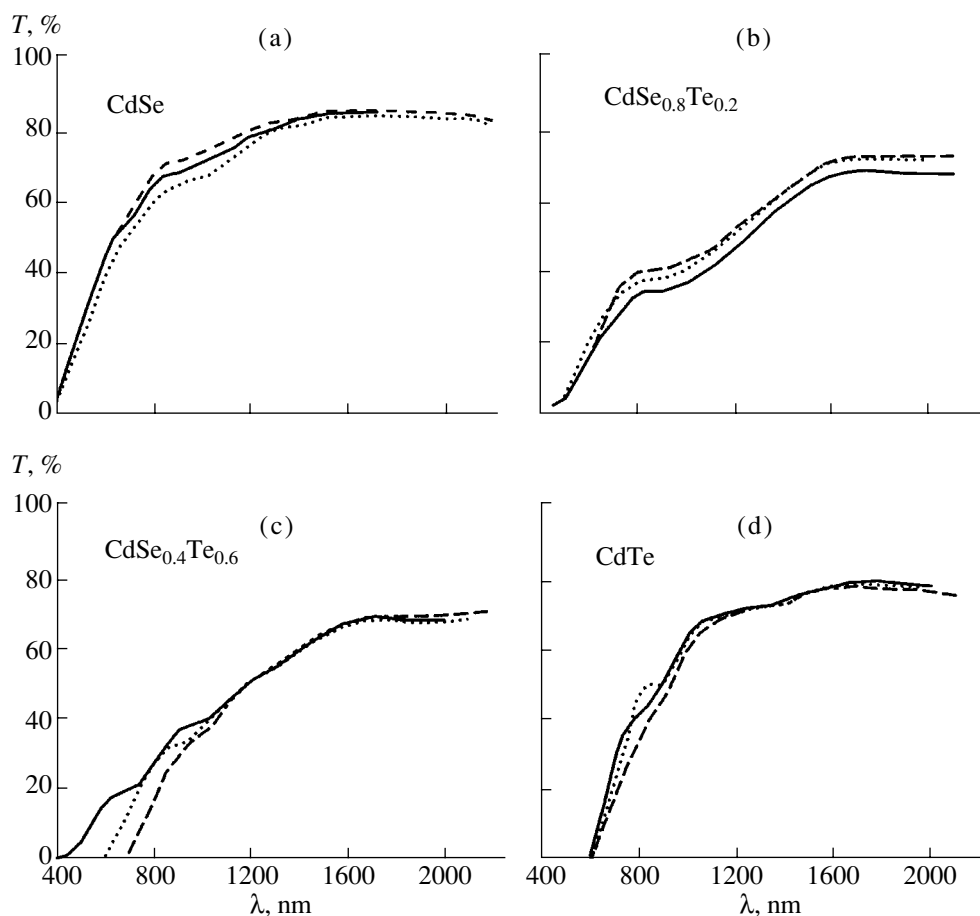
Fig. 3. Transmission T spectra in the long-wavelength region of the spectrum for glasses activated by $CdSe_xTe_{1-x}$ with various x, without additional heat treatment (the solid line) and after heat treatment (for 6 h) at temperatures of 550 (dashed line) and 600°C (dotted line): (a) corresponds to CdSe; (b), to $CdSe_{0.8}Te_{0.2}$; (c), to $CdSe_{0.4}Te_{0.6}$; and (d), to CdTe. The thickness of glass samples was 0.5 mm.

glasses, when cadmium oxide in a matrix is present after the primary melting and reacts with a chalcogenide during additional heat treatment. Thus, the glasses of the type under study are more stable, retain their microstructure, and one can expect the manifestation of more stable optical properties.

The absorption spectra of the series of the glasses under study immediately after founding and after additional heat treatment at 550–600°C are shown in Fig. 3 (in the transmission T scale for a near-IR region) and in Fig. 4 (on the scale of optical density D for a visible spectral region). Such a separate presentation of spectra for two regions of wavelengths is necessary due to the fact that the optical density for a similar glass thickness differs in the spectral range under study by several times; therefore, in order to observe the structure of the absorption spectrum, we used samples of glasses with various thicknesses (0.5 and 0.25 mm for the data in Figs. 3 and 4, respectively).

There are no pronounced absorption bands in the samples with CdSe and $CdSe_{0.8}Te_{0.2}$ nanoparticles prior to heat treatment (Figs. 3a, 3b, 4a, 4b): the spectra are

gently sloping, with a steady increase in the absorption to shorter wavelengths typical of glasses. After the heat treatment of $CdSe_{0.8}Te_{0.2}$ samples (but not CdSe), a peak appears near $\lambda = 555$ nm (Fig. 4b). The peaks in CdSe and $CdSe_{0.4}Te_{0.6}$ samples, which are similar in shape and position, are present in the spectra both prior to and after heat treatment (Figs. 4c, 4d); moreover, a noticeable difference is observed in the behavior of transmission curves in the IR region for these samples (Figs. 3c, 3d). The aforementioned peak is usually observed in the glasses with CdTe nanoparticles [19–24] and can be related to the first ($1s$–$1s$) exciton transition, shifted to the higher energies owing to the quantum-mechanical size effect. However, this shift is rather significant for the particles of the sizes observed (larger than 1 nm), which exceed the Bohr radius in CdTe. Therefore, we may assume that the other characteristics of particles (along with their sizes) are responsible for the significant high-energy shift. One such characteristic is the crystalline structure, which for CdSe and $CdSe_{0.8}Te_{0.2}$ particles (prior to heat treatment) differs from the structure of $CdSe_{0.4}Te_{0.6}$ and CdTe and does

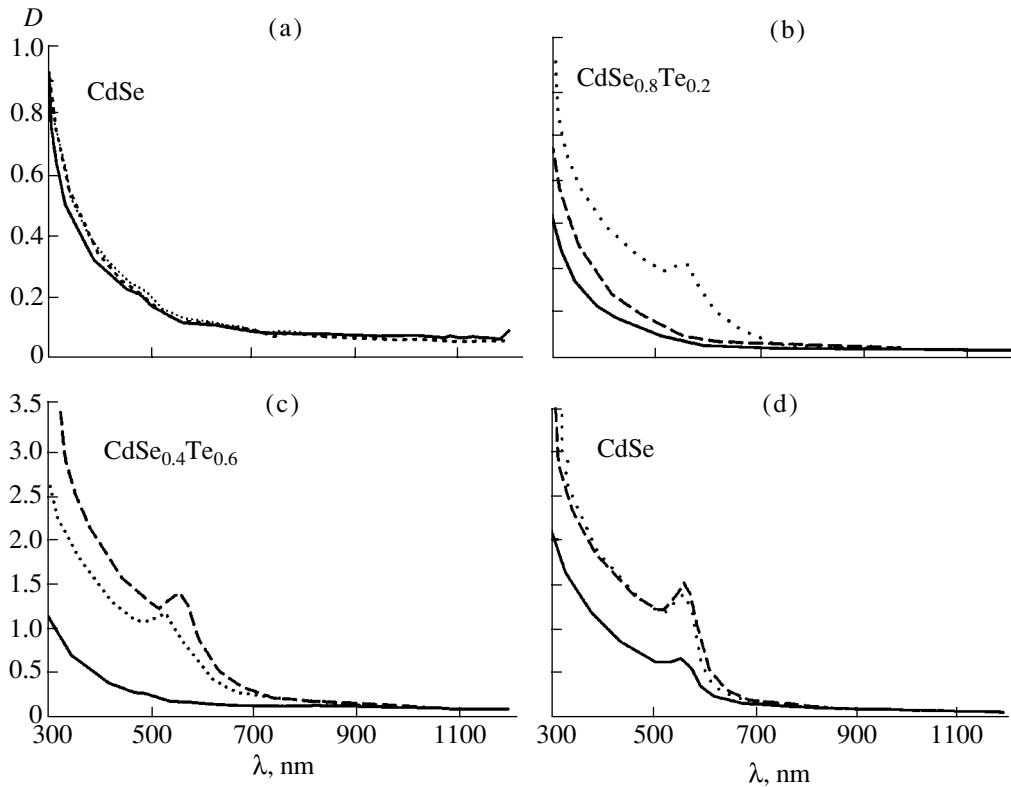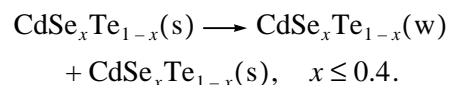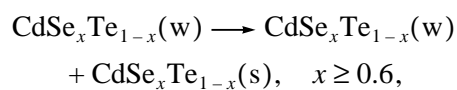**Fig. 4.** Absorption spectra (optical density D) of glasses activated by CdSe$_x$Te$_{1-x}$ semiconductors with various x, without an additional heat treatment (the solid line) and after heat treatment (for 6 h) at temperatures of 550 (dashed line) and 600°C (dotted line): (a) corresponds to CdSe; (b), to CdSe$_{0.8}$Te$_{0.2}$; (c), to CdSe$_{0.4}$Te$_{0.6}$; and (d), to CdTe. The thickness of glass samples was 0.2 mm.

not give rise to the exciton absorption peak. The structure of sphalerite, which is expected for the latter, results in a more pronounced quantum-mechanical size effect. Another characteristic of particles, which is difficult to determine directly by experiment, may be the presence of imperfections in particles (deviations from the perfect stoichiometry Cd : X = 1 : 1).

One should note that the largest effect of heat treatment is observed in the spectra of CdSe$_{0.8}$Te$_{0.2}$ and (especially) CdSe$_{0.4}$Te$_{0.6}$ solid solutions. Specifically, the absorption peaks, which are initially present in the spectra of the samples with CdTe nanoparticles, increase only by heat treatment, and, in the samples with solid solutions, they manifest themselves and attain a magnitude similar to that in CdTe. For CdSe$_{0.4}$Te$_{0.6}$, the peak shift to longer wavelengths as a result of the heat treatment is as large as 100 nm; however, in the case of CdTe, the shift is virtually absent. When passing from the samples with a high content of selenium (CdSe$_{0.8}$Te$_{0.2}$) to the samples without Se (CdTe), the shift becomes no larger than 10 nm. This shift is fairly small when compared to that which can be expected on the basis of the band gap value E_g for bulk CdSe and CdTe (1.7 and 1.5 eV, respectively); i.e., the shift of the absorption edge should be ~100 nm. However, according to these peak positions, one can conclude that a noticeable quantum-mechanical size effect takes place and causes a high-

energy shift (~0.5 eV) of the absorption edge for CdTe particles, compared with the absorption edge of the bulk semiconductor. The fact that the positions of absorption peaks for the samples with different stoichiometric compositions are rather close can be explained on the assumption that, in all cases, either CdTe particles or CdSe$_x$Te$_{1-x}$ solid-solution particles with a crystal structure similar to that of CdTe are responsible for the presence of peaks, since in the samples with CdSe particles the peaks are not observed at all. Then, in the case of solid solutions, a violation of their initial stoichiometry and a change in their crystal structure can occur. As was shown above (Fig. 1), for the series of crystalline CdSe$_x$Te$_{1-x}$ samples, the stoichiometry change is followed by a transition from the wurtzite lattice (w) (CdSe and solid solutions with high content of Se) and the sphalerite lattice (s) (CdTe and solid solutions with high content of a mixed lattice). Consequently, we may assume that the following processes take place:
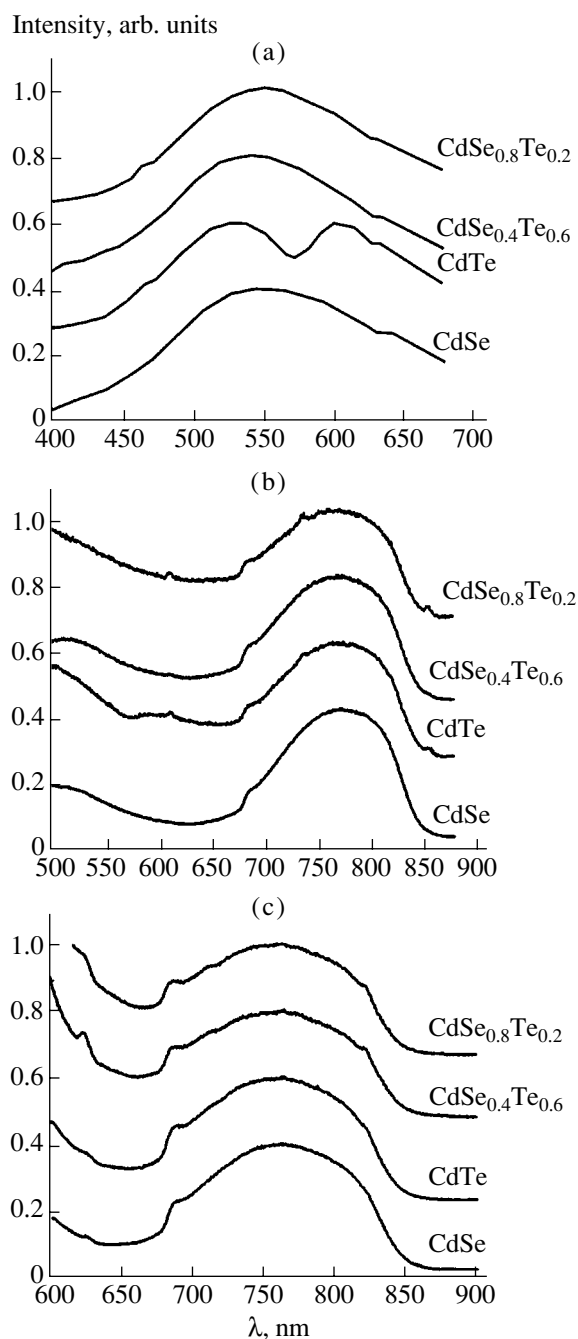
$$CdSe_xTe_{1-x}(w) \longrightarrow CdSe_xTe_{1-x}(w)$$
$$+ CdSe_xTe_{1-x}(s), \quad x \ge 0.6,$$

$$CdSe_xTe_{1-x}(s) \longrightarrow CdSe_xTe_{1-x}(w)$$
$$+ CdSe_xTe_{1-x}(s), \quad x \le 0.4.$$

Intensity, arb. units

Fig. 5. Luminescence spectra of glasses activated by $CdSe_xTe_{1-x}$ with various x, without an additional heat treatment; luminescence was excited by light with the wavelengths λ_{ex} = (a) 350, (b) 400, and (c) 570 nm. The thickness of glass samples was 0.2 mm.

In this case, the phase with the contribution of the wurtzite structure to the absorption spectrum manifests itself only as a gradual falloff of absorptivity (Fig. 4a), and the additional absorption from the sphalerite phase forms the peak observed in all other cases (Figs. 4b–4d). The spectra of samples with CdTe nanoparticles contain the contribution only of a single sphalerite phase, with which the insignificant changes in the spectra in the course of heat treatment are associated. On the other hand, for the particles of solid solutions, the heat treatment favors the process of phase separation, which adds complexity to the shape of spectra for the samples with solid solutions by heat treatment both in the visible and IR regions and, in particular, the appearance of the peak in the wavelength region λ = 550–600 nm.

The fact that the excess surface energy of nanoparticles can differently affect the stability of various crystalline modifications can be a cause of changes in the stoichiometry and in the crystal structure of the solid solution, as a result of which CdSe and CdTe become incompletely miscible compounds. Thus, in contrast to CdSe–CdS, there is a narrow two-phase region in the CdSe–CdTe system [33] in which two individual phases with a crystal lattice of wurtzite and sphalerite coexist in a macroscopic state. However, as the sizes of particles increase, the difference in the crystal lattice energies can increase owing to the surface energy contribution, and the two-phase wurtzite–sphalerite system can turn out to be more thermodynamically favorable within a wider range of component ratios.

The measurement of photoluminescence (PL) spectra using excitation with light of various wavelengths within the absorption region of semiconductor compounds (Fig. 5) yielded additional information about the state of nanoparticles of the semiconductor phase present in the glasses. The results of measurements are presented here for the samples prior to heat treatment. There are two quite intense PL bands in all samples (the luminescence signal of similar glasses without a semiconductor is small compared to the signal from the samples under study, and, therefore, its subtraction is not required). One of the peaks is observed in the region of λ = 530–550 nm for the excitation wavelength λ_{ex} = 350 nm (Fig. 5a); the position of this peak depends on the compound composition. If the PL is excited by light with longer wavelengths, λ_{ex} = 400 (Fig. 5b) and 570 nm (Fig. 5c), a peak at λ = 765–770 nm is observed in all samples. The peak seems to be split in Fig. 5a for the CdTe sample, which is associated with the reabsorption of the PL signal, since the maximum absorption of this sample is within this region. For convenience of comparison, the normalized spectra shown in Fig. 5 are shifted in the vertical direction by an arbitrary value. However, one should note that for an insignificant difference in the sizes and thicknesses between glass samples used in the measurements, the PL intensity of glasses containing CdSe and having low absorption throughout the entire range of wavelengths studied is no lower than for all types of glasses with pronounced peaks in the absorption spectra in the visible region. It follows from the above that the PL signals observed are not associated directly with the absorption in the region λ = 550–600 nm described above, and the relaxation of interband or exciton excitation corresponding to this peak occurs nonradiatively. The similarity of emission spectra for the samples differing by their type of chalcogenide X of semiconductor CdX can be indicative of

the fact that the PL bands observed are associated with defects formed predominantly from the participation of cadmium ions. There are, at least, two types of such defects represented by traps of different depths and responsible for the appearance of two bands: a broader band peaked at $\lambda \approx 550$ nm and excited by short-wavelength light (Fig. 5a) and a narrower band peaked at $\lambda \approx 770$ nm and excited to the same extent by light with wavelengths $\lambda = 400$ and 570 nm (Figs. 5b, 5c). Such defects can be produced during synthesis of activated glasses, owing to the partial chalcogenide decomposition (fairly insignificant, without violating the corresponding phase composition of the binary compound or solid solution) due to the high volatility of Se or Te. In other words, vacancies of Se^{2-} or Te^{2-} can exist, as well as excess interstitial Cd ions or surface defects also associated with excess Cd^{2+} ions. The anomalously large shift of exciton absorption peaks discussed above can then be explained taking into account this assumption about the excess of cadmium ions. A high concentration of these kinds of defect energy can bring about a heavier dependence of the energy of states on the size (similarly, e.g., to the influence of acceptor impurities in GaAs [34]) and a large shift of absorption exciton lines. In other words, self-doping of CdTe and CdSe$_x$Te$_{1-x}$ solid solutions after heat treatment of glasses may be the cause of a more pronounced manifestation of the quantum-mechanical size effect.

Luminescence bands, whose spectrum position is close to those bands observed by us, were observed for CdTe nanoparticles in zeolites (563 and 750 nm) [35] also without shorter wavelength peaks, which in many cases are characteristic of the excitonic luminescence of particles with sizes giving rise to quantum-mechanical effects,. In addition, a similar long-wavelength band was also observed repeatedly for CdTe nanoparticles. However, in the case of particles which fall within the range of "strong quantization", the position of such bands, which are associated with luminescence occurring from the involvement of traps (e.g., surface atoms), vary depending on the size of particles [36–38].

CONCLUSION

(1) A method for the synthesis of silicate glasses activated with CdSe$_x$Te$_{1-x}$ compounds ($0 \leq x \leq 1$) was developed; this method makes it possible to form a semiconducting phase with average particle sizes of 10–15 nm in the glass bulk. The basic distinctive feature of the method is the introduction of prepared compounds in the mixture of glass-forming substances.

(2) The results of studying the visible-region absorption spectra for a number of activated glasses and the changes in these spectra resulting from heat treatment suggest that the final product of the synthesis of glasses activated by CdSe$_x$Te$_{1-x}$ solid solutions are particles which consist of mixed phases of wurtzite and sphalerite structures. Individual phases of solid solutions obtained immediately as a result of founding the

glasses become mixed after heat treatment. In the case of CdSe and CdTe binary compounds, the average particle size increases only slightly without an appreciable shift of the absorption bands.

(3) The glasses obtained feature fairly pronounced luminescence bands with peaks at 550 and 770 nm. The position of such peaks is virtually independent of the type of semiconductor compound used for the activation of glasses. The luminescence bands are related to the existence of traps formed by excess Cd ions.

ACKNOWLEDGMENTS

REFERENCES

1. U. Woggon, *Optical Properties of Semiconductor Quantum Dots* (Springer-Verlag, Berlin, 1996).

2. S. V. Gaponenko, *Optical Properties of Semiconductor Nanocrystals* (Cambridge Univ. Press, Cambridge, 1998).

3. A. P. Alivisatos, J. Phys. Chem. **100** (31), 13226 (1996).

4. A. Eychmuller, J. Phys. Chem. B **104** (28), 6514 (2000).

5. V. I. Klimov, J. Phys. Chem. B **104** (26), 6112 (2000).

6. G. T. Petrovskiĭ, A. A. Zhilin, V. S. Shashkin, and A. A. Onushchenko, Opt. Zh. **65** (12), 29 (1998) [J. Opt. Technol. **65**, 974 (1998)].

7. L. L. Beecroft and Ch. K. Ober, Chem. Mater. **9** (6), 1302 (1997).

8. N. R. Kulish, V. P. Kunets, and M. P. Lisitsa, Opt. Eng. **34** (4), 1054 (1995).

9. Yu. V. Vandyshev, V. S. Dneprovskiĭ, and V. I. Klimov, Zh. Éksp. Teor. Fiz. **101** (1), 270 (1992) [Sov. Phys. JETP **74**, 144 (1992)].

10. M. Müller and U. Woggon, Ber. Bunsenges. Phys. Chem. **100** (9), 1446 (1996).

11. A. A. Onushchenko and É. L. Raaben, Fiz. Khim. Stekla **23** (1), 122 (1997).

12. A. I. Ekimov and I. A. Kudryavtsev, Izv. Akad. Nauk, Ser. Fiz. **56** (2), 20 (1992).

13. S. G. Konnikov, A. A. Lipovskiĭ, N. V. Nikiforov, *et al.*, Fiz. Tekh. Poluprovodn. (St. Petersburg) **29** (8), 1473 (1995) [Semiconductors **29**, 767 (1995)].

14. V. A. Gaĭsin, S. V. Karpov, E. V. Kolobkova, *et al.*, Fiz. Tverd. Tela (St. Petersburg) **41** (8), 1505 (1999) [Phys. Solid State **41**, 1378 (1999)].

15. *Physics and Chemistry of II–VI Compounds*, Ed. by M. Aven and J. S. Prener (North-Holland, Amsterdam, 1967; Mir, Moscow, 1970).

16. A. D. Yoffe, Adv. Phys. **42** (2), 173 (1993).

17. L.-Ch. Li, M. J. Kim, S. H. Risbud, and R. W. Carpenter, Philos. Mag. B **63** (3), 769 (1991).

18. B. G. Potter, Jr. and J. H. Simmons, J. Appl. Phys. **68** (3), 1218 (1990).

19. V. Esch, B. Fluegel, G. Khitrova, *et al.*, Phys. Rev. B **42** (12), 7450 (1990).

20. C. R. M. de Oliveira, A. M. de Paula, F. O. Plentz Filho, *et al.*, Appl. Phys. Lett. **66** (4), 439 (1995).

21. L. C. Barbosa, V. C. S. Reynoso, A. M. de Paula, *et al.*, J. Non-Cryst. Solids **219**, 205 (1997).

22. P. Lefebvre, T. Richard, J. Allegre, *et al.*, Superlattices Microstruct. **15** (4), 447 (1994).

23. M. L. Redigolo, W. A. Arellano, L. C. Barbosa, *et al.*, Semicond. Sci. Technol. **14** (1), 58 (1999).

24. Y. Liu, V. C. S. Reynoso, L. C. Barbosa, *et al.*, J. Mater. Sci. Lett. **14**, 635 (1995).

25. I. V. Bodnar', A. P. Molochko, and N. P. Solovĕ, Neorg. Mater. **29** (9), 1226 (1993).

26. I. V. Bodnar', A. P. Molochko, and N. P. Solovĕ, Neorg. Mater. **31** (8), 1030 (1995).

27. I. V. Bodnar', A. P. Molochko, and N. P. Solovĕ, Neorg. Mater. **33** (1), 23 (1997).

28. S. A. Kutolin and A. I. Neĭch, *Physical Chemistry of Stained Glass* (Stroĭizdat, Moscow, 1988).

29. *Powder Diffraction File* (JCPDS Int. Centre for Diffractional Data, Swarthmore, 1989).

30. I. M. Lifshits and V. V. Slezov, Zh. Éksp. Teor. Fiz. **35** (2), 479 (1958) [Sov. Phys. JETP **8**, 331 (1959)].

31. A. I. Ekimov, A. A. Efros, and A. A. Onushchenko, Solid State Commun. **56** (11), 921 (1985).

32. A. A. Onushchenko, G. T. Petrovskiĭ, and M. P. Shepilov, Dokl. Akad. Nauk **340** (2), 178 (1995) [Phys. Dokl. **40**, 19 (1995)].

33. *Physicochemical Basics of Synthesis of Single-Crystal Semiconductors of Solid Solutions of II–VI Compounds*, Ed. by I. B. Mizetskaya *et al.* (Naukova Dumka, Kiev, 1986).

34. G. T. Einevoll and Y.-Ch. Chang, Phys. Rev. B **40** (14), 9623 (1989).

35. E. S. Brigham, C. S. Weisbecker, W. E. Rudzinski, and Th. E. Mallouk, Chem. Mater. **8** (8), 2121 (1996).

36. M. Nogami, K. Nagasaka, and T. Suzuki, J. Am. Ceram. Soc. **75** (1), 220 (1992).

37. A. M. Kapitonov, A. P. Stupak, S. V. Gaponenko, *et al.*, Ber. Bunsenges. Phys. Chem. **101** (11), 1668 (1997).

38. T. Rajh, O. I. Micic, and A. J. Nozik, J. Phys. Chem. **97** (46), 11999 (1993).

Translated by T. Galkina

<div align="center">

LOW-DIMENSIONAL
SYSTEMS

</div>

Soliton Shape Stabilization in a Superlattice with Next-to-Nearest Neighbor Spectrum in a Field of a Nonlinear Wave

S. V. Kryuchkov and É. G. Fedorov*

Volgograd State Pedagogical University, Volgograd, 400013 Russia
*e-mail: eduard-f@mail.ru
Submitted June 18, 2001; accepted for publication September 4, 2001

Abstract—The effect of an electric field of a nonlinear (cnoidal) electromagnetic wave (pumping field) upon the shape of the solitary electromagnetic wave (soliton) in the quantum semiconductor superlattice with two harmonics of the electron spectrum is studied. Propagation of electromagnetic waves is shown in this case to be described by the modified double *sine*-Gordon equation. The possibility of the amplification of the pulse and its transformation into the dissipative soliton is noticed. The speed and width of a soliton depend on the presence of the second harmonic in the superlattice electron energy spectrum. The dependence of the dissipative soliton parameters on temperature and pumping field amplitude is also noticed. The possibility of propagation of electromagnetic waves described by solutions of the modified *sine*-Gordon equation in the superlattice with the spectrum under study is found. © *2002 MAIK "Nauka/Interperiodica"*.

1. It is well known that solitary electromagnetic (EM) waves (solitons) can propagate in solids [1–3]. Sufficiently moderate electric field strengths (~10^3 V/cm) are necessary in order to form solitons in quantum semiconductor superlattices (SL) [4]. That is why SLs are very appropriate media for the experimental study of solitons, which is interesting not only from the fundamental point of view. The phenomena related to soliton propagation in SLs can be used as a conceptual basis for new solid-state electronic devices (soliton memory shifting registers, for example). The search for simple and effective methods of amplification and stabilization of the shape of solitons propagating in SLs is necessary for creating such devices, because solitary waves formed in SLs show strong attenuation [5]. Stabilization of the soliton shape by applying a uniform external high-frequency electric field was proposed in [6]. A similar situation was considered in [7], where taking the SL electron energy spectrum second harmonic into account was shown to lead to fundamentally new results.

Stabilization of the soliton shape can be obtained by irradiation of an SL with an electromagnetic wave. However, it is known that an electromagnetic wave incident to an SL transforms into a nonlinear (cnoidal) wave [4]. That is why it is important to study the effect of a specified field of a nonlinear EM wave (pumping field) on the soliton propagation through an SL for which the electron dispersion law can be written in the form [7, 8]

$$\mathcal{E}(\mathbf{p})$$

$$= \frac{p_\perp^2}{2m} + \varepsilon_0[1 - \cos(p_x d/\hbar)] - \varepsilon_2 \cos(2 p_x d/\hbar), \quad (1)$$

where *m* is the electron effective mass related to motion in the plane of the layer forming the SL; *x* is the axis perpendicular to the SL layers; $\varepsilon_0 = \Delta$ (Δ is the half-width of the lower conduction miniband); *d* is the SL spacing; and $p_\perp$ and p_x are, respectively, transverse and longitudinal (relative to the SL axis) electron quasi-momentum components in the minizone.

2. Let the electron de Broglie wavelength and the SL spacing be small in comparison with the characteristic length along which the amplitude of the EM wave propagating through the SL changes; the electron mean free time is large in comparison with the characteristic time in which the electromagnetic field amplitude changes. Also let electron collisions with crystal lattice irregularities be negligibly rare. Then, propagation of the EM wave through the SL will be described by the double *sine*-Gordon equation (DSG) [7, 8]:

$$\frac{\partial^2 \Phi}{\partial t^2} - v^2 \frac{\partial^2 \Phi}{\partial z^2} + \omega_0^2 (\sin\Phi + \lambda \sin 2\Phi) = 0. \quad (2)$$

Here,

$$\omega_0 = \frac{\omega_p d}{\hbar} \sqrt{\varepsilon_0 m \frac{I_1}{I_0}}, \quad (3)$$

$$\lambda = 2\frac{\varepsilon_2 I_2}{\varepsilon_0 I_1}, \quad (4)$$

$$I_n = \frac{1}{\pi} \int_0^\pi \cos(nx) \exp\left[\frac{\varepsilon_0}{\Theta}\left(\cos x + \frac{\varepsilon_2}{\varepsilon_0}\cos 2x\right)\right] dx, \quad (5)$$

$\Phi = A_x ed/c\hbar$; where **A** is the vector potential of the EM wave related to the electric field by the well-known

expression $\mathbf{E} = -c^{-1}\partial\mathbf{A}/\partial t$; v is the velocity of the wave in the absence of electrons; ω_0 is the generalized plasma frequency in the lower conduction miniband; ω_p is the Langmuir frequency; and $\Theta = kT$ is the temperature expressed in the energy units.

Let us consider the effect of the cnoidal EM wave on the form of the pulse propagating through the SL. Here, we are interested in the solitary wave described by the kink solution of (2) [9]:

$$\Phi(t, z) = -2\arctan\left[\sqrt{\frac{2\lambda + 1}{\sinh(\xi/L)}}\right], \qquad (6)$$

where $\xi = z - ut$,

$$L = (v/\omega_0)\sqrt{1 - (u/v)^2}/\sqrt{2\lambda + 1},$$

and u is the kink velocity ($u/v < 1$).

The electric component of the pulse field has the form $\mathbf{E} = \{E, 0, 0\}$,

$$E(t, z) = E_0 \frac{\cosh(\xi/L)}{[2\lambda + \cosh^2(\xi/L)]}, \qquad (7)$$

where $E_0 = 2u\hbar(edL)^{-1}\sqrt{2\lambda + 1}$.

Notice that the solution (6), (7) transforms into the one-soliton solution of the *sine*-Gordon (SG) equation [1].

Let the nonlinear EM wave with the frequency $\omega_1 \gg \omega_0$ and the electric field $\mathbf{E}_1 = \{E_1, 0, 0\}$ amplitude $E_{1,0}$ propagate along the SL layers. Then, the electric current in the SL will be induced both by the soliton and the nonlinear wave.

We solve this problem using a quasi-classical approximation, which is justified if the conditions $\hbar\omega_1 \ll 2\Delta$, $E_0 ed \ll 2\Delta$, and $E_{1,0} ed \ll 2\Delta$, which we imposed, are satisfied. Since the characteristic length of a substantial change of the wave field amplitude is significantly larger than the electron mean free path, we disregard the spatial dispersion of the nonlinear wave electric field. This permits us to write the related axial component of the field in the form

$$E_1(t) = -\frac{1}{c}\frac{\partial A_{1x}}{\partial t} = -\frac{\hbar}{ed}\frac{\partial\Phi_1}{\partial t}, \qquad (8)$$

where A_{1x} is the axial component of the vector potential of the pumping field

$$\Phi_1(t) = \begin{cases} 2\arcsin\left\{\kappa\,\mathrm{sn}\left[\dfrac{2K(\kappa)}{\pi}\omega_1 t, \kappa\right]\right\}, & 0 < \kappa \leq 1, \\[4mm] 2\arcsin\left\{\mathrm{sn}\left[\dfrac{2K(\kappa^{-1})}{\pi}\omega_1 t, \kappa^{-1}\right]\right\}, & \kappa > 1, \end{cases} \qquad (9)$$

$$\omega_1 = \omega_0\frac{\beta}{\sqrt{\beta^2 - 1}}\begin{cases} \dfrac{\pi}{2K(\kappa)}, & 0 < \kappa \leq 1, \\[4mm] \dfrac{\kappa\pi}{2K(\kappa^{-1})}, & \kappa > 1, \end{cases} \qquad (10)$$

$$\kappa = \frac{eE_{1,0}d}{2\omega_0\hbar}\frac{\sqrt{\beta^2 - 1}}{\beta}, \qquad (11)$$

$$\beta = u_1/v,$$

where u_1 is the nonlinear wave phase velocity and K is the complete elliptic integral of the first kind.

Taking into account the specified pumping field formally means the substitution $\Phi \longrightarrow \Phi + \Phi_1$ in the expression for the current density that appears in the d'Alembert equation and is induced by the fields of the EM soliton and the cnoidal wave [7]. Averaging the current density over the pumping field period $T_1 = 2\pi/\omega_1$, we obtain the modified DSG equation describing the EM wave propagating through the SL under the influence of the cnoidal wave:

$$\frac{\partial^2\Phi}{\partial t^2} - v^2\frac{\partial^2\Phi}{\partial z^2}$$
$$+ \omega_0^2\sigma_0(\kappa)\left[\sin\Phi + \lambda\frac{\sigma_2(\kappa)}{\sigma_0(\kappa)}\sin 2\Phi\right] = 0. \qquad (12)$$

Here,

$$\sigma_0(\kappa) = \begin{cases} \left[2\dfrac{E(\kappa)}{K(\kappa)} - 1\right], & 0 < \kappa \leq 1, \\[4mm] \left\{1 - 2\kappa^2\left[1 - \dfrac{E(\kappa^{-1})}{K(\kappa^{-1})}\right]\right\}, & \kappa > 1, \end{cases} \qquad (13)$$

$$\sigma_2(\kappa) = 1 - 2$$

$$\times \begin{cases} \dfrac{\kappa^2}{K(\kappa)}\displaystyle\int_0^{4K(\kappa)} \mathrm{sn}^2(x, \kappa)\mathrm{dn}^2(x, \kappa)dx, & 0 < \kappa \leq 1, \\[5mm] \dfrac{1}{K(\kappa^{-1})}\displaystyle\int_0^{4K(1/\kappa)} \mathrm{sn}^2(x, \kappa^{-1})\mathrm{cn}^2(x, \kappa^{-1})dx, & \kappa > 1; \end{cases} \qquad (14)$$

K and E are the complete elliptic integrals of, respectively, the first and second kind.

The dependence $\sigma_2(\kappa)$ cannot be expressed in terms of tabulated functions and can be found using numerical integration. The functions $\sigma_0(\kappa)$ and $\sigma_2(\kappa)$ are alternating; $\sigma_0(\kappa)$ vanishes at $\kappa \approx 0.91$, and $\sigma_2(\kappa)$ passes through zero at $\kappa \approx 0.56$ and $\kappa \approx 0.97$.

Two fundamentally different situations can take place depending on the cnoidal wave parameters. For a pumping field such that $\sigma_0(\kappa) > 0$ and $\sigma_2(\kappa) > 0$, the

solution of (12) can be reduced to the kink solution of (6), (7) by means of renormalization:

$$\omega_0 \longrightarrow \omega_0\sqrt{\sigma_0(\kappa)} \quad \text{and} \quad \lambda \longrightarrow \lambda\sigma_2(\kappa)/\sigma_0(\kappa).$$

Then, the pulse width L and the related electric field amplitude vary nonmonotonically with κ.

However, if the pumping field parameters satisfy the conditions $\sigma_0(\kappa) < 0$ and $\sigma_2(\kappa) > 0$, (12) may have a solution corresponding to amplification of the pulse propagating through the SL [6, 7, 10]. The physical reason behind such amplification is the specific redistribution of electrons in the conduction miniband due to cnoidal wave influence. The expression for the energy of longitudinal (along the SL axis) electron motion averaged over the canonic ensemble and the pumping field period reads

$$\overline{\mathscr{E}} = \varepsilon_0\left\{1 - \sigma_0(\kappa)\frac{I_1}{I_0}\left[1 + \frac{\lambda\sigma_2(\kappa)}{2\sigma_0(\kappa)}\right]\right\}. \tag{15}$$

It is seen from (15) that if the condition

$$0 < \sigma_2(\kappa) < -2\frac{\sigma_0(\kappa)}{\lambda} \tag{16}$$

is satisfied, the mean energy of the electron longitudinal motion in the miniband is larger than its half-width ($\overline{\mathscr{E}} > \varepsilon_0 = \Delta$); i.e., the medium of the miniband electrons becomes inversely populated under the influence of the pumping field. It is known that amplification of pulses is possible in such media [6, 10].

The field of a pulse being amplified consists of separate subpulses with conserved total area. Similarly to the case of the soliton described by the SG equation, one can expect an increase of the frequency $\omega(z)$ and compression of the pulse as it propagates. The pulse is amplified so that the number of photons in it does not change, while its energy increases because of stimulated emission in the transition of electrons to the current energy $\hbar\omega(z)$ of the pulse field photons [6, 10].

3. An increase of the pulse frequency $\omega(z)$ can induce interminiband transitions which lead to dissipation of the pulse energy. This effect can be estimated introducing the term $\gamma\partial\Phi/\partial t$ into the left-hand side of (12), where γ is the phenomenological constant taking account of the soliton energy losses due to the interminiband transitions [6, 11, 12]:

$$\frac{\partial^2\Phi}{\partial t^2} - v^2\frac{\partial^2\Phi}{\partial z^2} + \gamma\frac{\partial\Phi}{\partial t}$$
$$+ \omega_0^2\sigma_0(\kappa)\left[\sin\Phi + \lambda\frac{\sigma_2(\kappa)}{\sigma_0(\kappa)}\sin 2\Phi\right] = 0. \tag{17}$$

The pulse frequency $\omega(z)$ increases until it becomes comparable to the interminiband electron transition frequency, after which the pulse propagation process becomes stationary, and the pulse transforms into the

dissipative soliton stabilized by the cnoidal wave field. The related solution of (17) reads

$$\Phi_D = -\arccos\{\tanh[(z - u_D t)/L_D]\}, \tag{18}$$

$$E_D = E_{D0}\operatorname{sech}[(z - u_D t)/L_D]. \tag{19}$$

Here,

$$u_D = v\left[1 + \lambda\frac{2\gamma^2\sigma_2(\kappa)}{\omega_0^2\sigma_0^2(\kappa)}\right]^{-1/2}, \tag{20}$$

$$L_D = \frac{\gamma v}{\omega_0^2|\sigma_0(\kappa)|}\left[1 + \lambda\frac{2\gamma^2\sigma_2(\kappa)}{\omega_0^2\sigma_0^2(\kappa)}\right]^{-1/2}, \tag{21}$$

$$E_{D0} = \frac{\hbar\omega_0^2}{ed\gamma}|\sigma_0(\kappa)|. \tag{22}$$

The velocity u_D, width L_D, and amplitude E_{D0} of the dissipative soliton are not interdependent parameters, unlike the case of solitons of completely integrable systems, being determined exclusively by the parameters of the medium [12].

For $d = 10^{-6}$ cm, $\varepsilon_0 = \Delta = 10^{-1}$ eV, $\varepsilon_2 = 3 \times 10^{-2}\varepsilon_0$, $\omega_0 = 10^{12}$ s^{-1}, and $T = 3 \times 10^2$ K, we find $\lambda \approx 4.0 \times 10^{-2}$ using (4) and (5). Thus, amplification of the pulse and its transformation into the dissipative soliton (18), (19) are possible in SL irradiation with a nonlinear wave whose electric field amplitude $E_{1,0} \approx 1.39 \times 10^4$ V/cm ($\beta - 1 = 5 \times 10^{-3}$, $\kappa \approx 1.05$; see (11)) and higher. For the given values of λ and $E_{1,0}$, condition (16) is satisfied with a safety margin. Assuming $v = 10^{10}$ cm/s, $\gamma = 10^{11}$ s^{-1}, $\beta - 1 = 5 \times 10^{-3}$, $E_{1,0} = 1.60 \times 10^4$ V/cm ($\kappa \approx 1.21$, $\sigma_0(\kappa) \approx -0.14$, and $\sigma_2(\kappa) \approx 0.03$), we obtain from (20), (21), and (22) for, respectively, the velocity, width, and amplitude of the stabilized pulse $u_D \approx 9.99 \times 10^9$ cm/s, $L_D \approx 7.14 \times 10^{-3}$ cm, and $E_{D0} \approx 9.23 \times 10^2$ V/cm.

It follows from relations (20) and (21) that the effect of the second harmonic of the SL electron energy spectrum leads to a decrease of the dissipative soliton velocity and width in comparison with the case of the one-harmonic spectrum. In the limit of $\lambda \longrightarrow 0$, the pulse velocity and width become, as would be expected, equal to the velocity (equal to the EM wave velocity in the absence of electrons) and width of the dissipative soliton propagating through the SL with the one-harmonic spectrum. It is also seen from (20)–(22) that the dependence of λ and ω_0 on T (see (3)–(5)) determines the temperature dependence of the velocity, width, and amplitude of the EM pulse (18), (19), which vary essentially with the amplitude of the electric field of the cnoidal wave.

If the pumping field parameters are such that $\sigma_2(\kappa) \longrightarrow 0$ (at $\kappa \approx 0.56$ and $\kappa \approx 0.97$), it would be expected that solitary EM waves described by the mod-

ified SG equation propagate through the SL under consideration:

$$\frac{\partial^2 \Phi}{\partial t^2} - v^2 \frac{\partial^2 \Phi}{\partial z^2} + \omega_0^2 \sigma_0(\kappa) \sin \Phi = 0, \qquad (23)$$

which takes account of the second harmonic in the electron energy spectrum and the temperature dependence of ω_0 in accordance with (3) and (5).

The condition $\sigma_0(\kappa) > 0$ holds at $\kappa \approx 0.56$, and the related solutions of (23) can be obtained from the known solutions of the SG equation [1, 4] via renormalization, i.e., $\omega_0 \longrightarrow \omega_0 \sqrt{\sigma_0(\kappa)}$. It follows from (11) that, at $d = 10^{-6}$ cm, $\omega_0 = 10^{12}$ s^{-1}, and $\beta - 1 = 5 \times 10^{-3}$, this relation is valid at the pumping field amplitude $E_{1,0} \approx 7.41 \times 10^3$ V/cm.

If $\kappa \approx 0.97$, then $\sigma_0(\kappa) < 0$; an amplification with the following stabilization of the pulse propagating through the SL is possible [6, 10]. This phenomenon can be observed in the SL irradiated by a nonlinear EM wave with the electric field amplitude $E_{1,0} \approx 1.28 \times 10^4$ V/cm at the same values of d, ω_0, and β.

REFERENCES

1. É. M. Épshteǐn, Fiz. Tverd. Tela (Leningrad) **19** (11), 3456 (1977) [Sov. Phys. Solid State **19**, 2020 (1977)].

2. A. P. Tetervov, Ukr. Fiz. Zh. **23** (7), 1182 (1978).

3. É. M. Belenov, L. A. Grechko, and A. P. Kanavin, Pis'ma Zh. Éksp. Teor. Fiz. **58** (5), 331 (1993) [JETP Lett. **58**, 333 (1993)].

4. F. G. Bass, A. A. Bulgakov, and A. P. Tetervov, *High-Frequency Properties of Semiconductors with Superlattices* (Nauka, Moscow, 1989).

5. É. M. Épshteǐn, Izv. Vyssh. Uchebn. Zaved., Radiofiz. **24** (10), 1293 (1981).

6. F. G. Bass, S. V. Kryuchkov, and A. I. Shapovalov, Fiz. Tekh. Poluprovodn. (St. Petersburg) **29** (1), 19 (1995) [Semiconductors **29**, 9 (1995)].

7. S. V. Kryuchkov and A. P. Shapovalov, Opt. Spektrosk. **84** (2), 286 (1998) [Opt. Spectrosc. **84**, 244 (1998)].

8. S. V. Kryuchkov and G. A. Syrodoev, Izv. Vyssh. Uchebn. Zaved., Radiofiz. **33** (12), 1427 (1990).

9. V. I. Ozhogin and V. L. Preobrazhenskiǐ, Usp. Fiz. Nauk **155** (4), 593 (1988) [Sov. Phys. Usp. **31**, 713 (1988)].

10. É. M. Belenov, P. G. Kryukov, A. V. Nazarkin, *et al.*, Pis'ma Zh. Éksp. Teor. Fiz. **47** (9), 442 (1988) [JETP Lett. **47**, 523 (1988)].

11. R. H. Pantell and H. E. Puthoff, *Fundamentals of Quantum Electronics* (Wiley, New York, 1969; Mir, Moscow, 1972).

12. S. V. Sazonov, Pis'ma Zh. Éksp. Teor. Fiz. **53** (8), 400 (1991) [JETP Lett. **53**, 420 (1991)].

Translated by S. Ktitorov

LOW-DIMENSIONAL SYSTEMS

Resonance Transitions between Split Levels in Three-Barrier Nanostructures and the Prospects of Using these Structures in Devices Operating in the Submillimeter-Wave Band

E. I. Golant and A. B. Pashkovskiĭ

State NPO Istok, Fryazino, Moscow oblast, 141190 Russia
Submitted August 29, 2001; accepted for publication September 9, 2001

Abstract—A model describing the coherent tunneling of electrons in a three-barrier quantum-well structure in a high-frequency (terahertz) electric field was developed. On the basis of this model, the frequency dependences of negative dynamic conductivity (intensities of quantum transitions) in three-barrier nanostructures with coherent tunneling of electrons via closely spaced split energy levels was studied qualitatively and quantitatively. It is shown that coherent quantum lasers operating in the far-infrared region of the spectrum and emitting at a wavelength of up to 60 μm (5 THz) can be developed on the basis of these structures. The electron lifetime at the lower resonance level is found to be five times shorter than the characteristic scattering time, the space-charge effect is insignificant, and the available power released in the structure exceeds severalfold the losses of power in the optical waveguide. © 2002 MAIK "Nauka/Interperiodica".

1. INTRODUCTION

Recently, considerable progress has been made in mastering the 5- to 12-μm range of the far-infrared (far-IR) region of the spectrum; this progress is based on using a new type of lasers operating by transitions between the size-quantization levels in semiconductor heterostructures with AlInAs barriers and GaInAs wells; these lasers are referred to as the so-called quantum cascade (QC) lasers [1–3].

At the same time, attempts aimed at extending the operation range of the QC laser to lower frequencies present serious difficulties related primarily to an increase in the laser's starting current with increasing wavelength of laser radiation.

At present, the longest wavelength of radiation emitted by a QC laser is λ = 17 nm; the emission was obtained in the pulsed mode at a temperature of 150 K [4]. Observations of electroluminescence [5, 6] and photoluminescence [7, 8] at the picowatt intensity level have been reported; the lasers operated by intersubband transitions in the region of 100 μm.

An important element of the physical mechanism for the operation of QC lasers is the noncoherent (with involvement of phonons) tunneling of electrons; in this case, there are several collisions with phonons, which disturb the coherence of the electron wave function for each electromagnetic-radiation quantum (photon) emitted by electron. The causes of the appreciable increase in the starting current of such lasers with increasing wavelength (decreasing frequency) of radiation have been considered recently [3].

At the same time, we have previously demonstrated [9] that it is basically possible to develop a quantum laser operating by coherent (ballistic) transport of electrons through the two-barrier resonance-tunneling structures at frequencies in the region of 30 THz (λ = 10 μm). This laser differs from a QC laser in the coherent mechanism of tunneling and in the appreciably smaller width of the potential barrier in the basic quantum-confinement structure.

On the other hand, classical microwave emitters based on negative dynamic resistance in the resonance-tunneling transit-time diodes operate in the electromagnetic-wave spectral region with longer wavelengths. However, the negative dynamic resistance of such diodes decreases with increasing frequency, and the highest available generation frequency of the resonance-tunneling transit-time diodes is about 700 GHz [10].

It has been shown [11, 12] that the use of resonance transitions in a two-barrier injecting resonance-tunneling transit-time diode in combination with coherent transport of electrons through the entire structure makes it possible, under certain conditions, to increase the oscillation frequency to 5 THz (λ = 60 μm); further attempts at increasing the frequency of these resonance-tunneling transit-time diodes have run into fundamental problems.

In this context, we analyzed certain basic physical factors that hinder the effective operation of lasers and resonance-tunneling transit-time diodes based on two-barrier resonance-tunneling structures with coherent electron transport in the submillimeter wavelength range (λ = 30–300 μm).

In addition, we suggest a rational approach to solving the problem of developing semiconductor lasers that operate in the above range. For lasing, we suggest using the electron transitions between closely spaced

split levels of size quantization in three-barrier resonance-tunneling structures under the conditions of coherent (collisionless) electron transport. By split levels, we mean here those the energy spacing between which decreases in proportion to the strength (the product of the height by width) of the average potential barrier. It is revealed that the electron transport through such structures has a number of interesting physical features, which make it possible to expect lasing with a wavelength of $\lambda \approx 65 \ \mu m$ if the design is appropriate.

2. PHYSICAL CAUSES OF THE FREQUENCY RESTRICTIONS

The first frequency restriction stems from the requirement for coherency of tunneling. This restriction is related to the finiteness of the tunneling electron lifetime at the resonance level: $\tau \sim \hbar/\Gamma$, where Γ is the resonance-level width. The lifetime should be shorter than the characteristic time of momentum relaxation for electrons τ_p with allowance made for all scattering mechanisms; it is notable that the lifetime at the upper resonance level, which is always broader than the lower level in the two- and three-barrier structure, is most important in the small-signal mode (it is in this approximation that the estimates have been previously obtained [11–13]), whereas the lifetime at the lower level is more important and brings about a more severe restriction in the large-signal mode. This presents a major problem for the use of two-barrier structures in both lasers and resonance-tunneling transit-time diodes at relatively low frequencies, because the ratio between the level widths is $(N/L)^3$, where N and L are the level numbers; the use of structures with large numbers of operating levels is impeded owing to a pronounced increase in the well width, which is undesirable for a number of reasons. In particular, even a low constant electric field in a wide well causes the well to become triangular instead of rectangular; as a result, the intensity of quantum transitions in such a well decreases drastically.

The second important limitation on the use of two-barrier resonance-tunneling structures in both lasers and the injector for resonance-tunneling transit-time diodes is related to the deleterious effect of the space-charge alternating component on the negative dynamic conductivity, which is proportional to the intensity of quantum transitions. As has been shown previously [14], the space charge in the two-barrier resonance-tunneling structures limits the largest magnitude of negative conductance of the active region (in transition from the first to the second resonance levels) by a value of $\sim 0.7 \omega \varepsilon \varepsilon_0$ (here, ε is the relative permittivity of the semiconductor, ε_0 is the permittivity of free space, and ω is the frequency). This restriction not only prevents the lasing frequency from being decreased, but, as was discovered, also makes it impossible to significantly increase the generation frequency of the resonance-tunneling transit-time diodes using the resonance transi-

tions in a quantum injector with very narrow quasi-levels [11, 12].

The third restriction, which is especially important for lasers where the electromagnetic wave propagates along the optical waveguide confined by the heterojunction boundaries, is related to the loss conductivity in the optical waveguide; in the case under consideration, this conductivity increases drastically as the frequency decreases. In the relaxation-time approximation, the conductivity related to ohmic losses can be evaluated as

$$\sigma_s \approx q\mu n/(1 + \omega^2 \tau_p^2), \qquad (1)$$

where q is the charge, n is the concentration, μ is the mobility, and τ_p is the momentum-relaxation time for an electron. In a structurally perfect GaAs with electron concentration $n = 10^{17} \ cm^{-3}$ and the electron mobility $\mu \approx 9.6 \times 10^4 \ cm^2 \ V^{-1} \ s^{-1}$ at $T = 77$ K, the momentum-relaxation time is equal to $\tau_p \approx 4 \times 10^{-13}$ s, which yields $\sigma_s \approx 0.03$ S/cm at a frequency of 30 THz.

As has been shown previously [9], the requirement for a sufficiently large optical-confinement coefficient (~ 0.8) is equivalent to the condition that the width of the optical waveguide should amount approximately to the wavelength in the waveguide, i.e., $w \approx \lambda/\kappa$, where $\kappa \approx 3.4$ is the refractive index of GaAs, and the active conductivity of the structure σ_a for the signal generation should satisfy the condition [9]

$$\sigma_a > \xi\frac{w}{a}\sigma_s \approx \frac{\xi}{\kappa}\frac{\lambda}{a}\sigma_s. \qquad (2)$$

Assuming that the characteristic size of the active region (the quantum well) $a = 10$ nm and $\lambda = 10 \ \mu m$ and setting in (2) $\xi = 1$ (this numerical coefficient, which is either smaller than or equal to unity, is related to the nonuniformity of distribution of an electric field in the wave), we determine the condition for amplification as $\sigma_a > 10$ S/cm.

It follows from the above formulas that a decrease in the lasing frequency to 10 THz ($\lambda = 30 \ \mu m$) at $n = 10^{17} \ cm^{-3}$ leads to the requirement that $\sigma_a > 270$ S/cm, which exceeds by severalfold the limiting (with respect to the alternating space charge) value $0.7 \omega \varepsilon \varepsilon_0 \approx 50$ S/cm. On the other hand, elementary estimations show that a decrease in ohmic losses by reducing the electron concentration may be difficult owing to a restriction on the lifetime at the resonance levels.

There are at least two methods that make it possible to overcome these difficulties. One of these methods is based on using materials with a narrower band gap, lower effective mass, higher mobility, and, consequently, a much longer momentum-relaxation time. In particular, the highest generation frequencies have been obtained [10] using the InAs-based resonance-tunneling transit-time diodes. For a two-barrier laser structure with $n = 10^{17} \ cm^{-3}$ and $a = 10$ nm, calculation yields the condition for lasing as $\sigma_a > 7$ S/cm at $T = 77$ K and a frequency $\nu = 10$ THz.

However, as was mentioned above, the obtained estimates hold true, strictly speaking, only for the small-signal mode, because a relatively mild condition for the coherent tunneling of electrons at the upper (broader) level is used. At the same time, a more rigid condition for electron coherence at the lower (narrower) level in the two-barrier resonance-tunneling structures should be used. Calculation shows that, in this practically important mode, the sole use of a narrow-gap InAs semiconductor cannot by itself completely solve the problem of the appreciable lowering of the oscillation frequency in lasers based on two-barrier resonance-tunneling structures. This problem can be solved to a large extent if one chooses the second method, which involves the use of resonance transitions between split levels in the InAs-based three-barrier structures. A feasible example of the solution will be considered below in detail.

3. DESCRIPTION OF THE MODEL

Let us consider an asymmetric three-barrier resonance-tunneling structure with thin (δ-shaped) barriers. We assume that a high-frequency (HF) electric field varying in time as $E(t) = E(e^{i\omega t} + e^{-i\omega t})$ is applied to this structure. For the sake of definiteness, we also assume that a monoenergetic electron beam is incident on the structure from the left. The time-dependent Schrödinger equation then has the following form:

$$i\hbar\frac{\partial\psi}{\partial t} = -\frac{\hbar^2}{2m^*}\frac{\partial^2\psi}{\partial x^2} + H(x)\psi + H(x,t)\psi,$$

$$H(x) = -U[\theta(x) - \theta(x-a)]$$
$$- U_1[\theta(x-a) - \theta(x-a-l)]$$
$$- U_2\theta(x-a-l) + \alpha\delta(x) + \alpha\rho\delta(x-a) + \alpha\gamma\delta(x-a-l), \quad (3)$$

$$H(x,t) = -qE\{x[\theta(x) - \theta(x-a-l)]$$
$$+ (a+l)\theta(x-a-l)\}(e^{i\omega t} + e^{-i\omega t}).$$

Here, q and m^* are the charge and mass of an electron; $\alpha = \varphi_b b$ is the strength of the first barrier, which has the height φ_b and width b; $\theta(x)$ is a unit function; γ and ρ are numerical coefficients; U, U_1, and U_2 are the magnitudes of discontinuities of the conduction-band bottom at the barriers (see Fig. 1); and a and l are the distances between the barriers.

In this case, the unperturbed wave function of electrons ψ_0 can be written as

$$\psi_0(x)$$
$$= \begin{cases} \exp(ik_0 x) + D_0\exp(-ik_0 x), & x < 0 \\ A_0\sin(kx) + B_0\cos(kx), & 0 < x < a \\ Z_0\sin[k_1(x-a)] + W_0\cos[k_1(x-a)], & a < x < a+l \\ C_0\exp[ik_2(x-a-l)], & x > a+l, \end{cases} \quad (4)$$
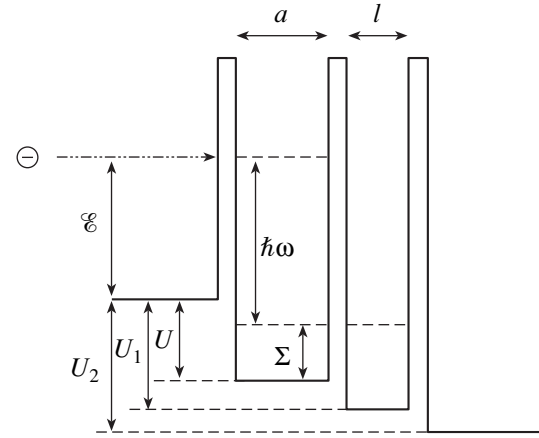
Fig. 1. Schematic representation of the energy-band diagram for the three-barrier structure under consideration.

where $k_0 = (2m^*\mathcal{E}/\hbar^2)^{1/2}$, $k = [2m^*(\mathcal{E} + U)/\hbar^2]^{1/2}$, $k_1 = [2m^*(\mathcal{E} + U_1)/\hbar^2]^{1/2}$, and $k_2 = [2m^*(\mathcal{E} + U_2)/\hbar^2]^{1/2}$ are the wave vectors of electrons; and $\mathcal{E}$ is the energy of electrons incident on the structure. In the small-signal approximation, the first-order correction ψ_1 to the ground-state wave function has the following time dependence [13]: $\psi_1 = \psi_+(x)e^{i(\omega_0 + \omega)t} + \psi_-(x)e^{i(\omega_0 - \omega)t}$ ($\omega_0 = \mathcal{E}/\hbar$); this dependence corresponds to the emission and absorption of a photon with an energy of $\hbar\omega$. In the specific case of a three-barrier structure, the wave functions $\psi_\pm$ are given by

$$\psi_\pm(x)$$
$$= \begin{cases} D_\pm\exp(-ik_{0\pm}x), & x < 0 \\ A_\pm\sin(kx) + B_\pm\cos(kx) + \varphi_\pm(x), & 0 < x < a \\ Z_\pm\sin[k_{1\pm}(x-a)] \\ + W_\pm\cos[k_{1\pm}(x-a)] + \chi_\pm(x), & a < x < a+l \\ C_\pm\exp[ik_{2\pm}(x-a-l)] \\ + P_\pm\exp[ik_2(x-a-l)], & x > a+l, \end{cases} \quad (5)$$

where

$$k_{0\pm} = [2m^*(\mathcal{E} \pm \hbar\omega)/\hbar^2]^{1/2},$$

$$k_\pm = [2m^*(\mathcal{E} + U \pm \hbar\omega)/\hbar^2]^{1/2},$$

$$k_{1\pm} = [2m^*(\mathcal{E} + U_1 \pm \hbar\omega)/\hbar^2]^{1/2},$$

$$k_{2\pm} = [2m^*(\mathcal{E} + U_2 \pm \hbar\omega)/\hbar^2]^{1/2}, \quad (6)$$

$$P_\pm = \mp\frac{qEa}{\hbar\omega}\psi_0(a+l),$$

$$\varphi_\pm, \chi_\pm = \mp\frac{qEa}{\hbar\omega}\psi_0(x) + \frac{qE}{m^*\omega^2}\psi_0'(x)$$

are the corresponding particular solutions to the equation for $\psi_\pm$ (see [13, 14]). A system of equations for the determination of the coefficients $A_\pm$, $B_\pm$, $C_\pm$, $D_\pm$, $Z_\pm$, and $W_\pm$ has the following form in the matrix representation:

$$
\begin{pmatrix}
1 & 0 & -1 & 0 & 0 & 0 \\
ik_{0\pm} - y & k_\pm & 0 & 0 & 0 & 0 \\
0 & \sin k_\pm a & \cos k_\pm a & 0 & -1 & 0 \\
0 & -k_\pm \cos k_\pm a & k_\pm \sin k_\pm a & k_{1\pm} & -\rho y & 0 \\
0 & 0 & 0 & \sin k_{1\pm} a & \cos k_{1\pm} a & -1 \\
0 & 0 & 0 & -k_{1\pm}\cos k_{1\pm}a & k_{1\pm}\sin k_{1\pm}a & ik_{2\pm} - \gamma y
\end{pmatrix}
\begin{pmatrix}
D_\pm \\ A_\pm \\ B_\pm \\ Z_\pm \\ W_\pm \\ C_\pm
\end{pmatrix}
$$

$$
=
\begin{pmatrix}
f_1 \\ f_2 \\ f_3 \\ f_4 \\ f_5 \\ f_6
\end{pmatrix}
=
\begin{pmatrix}
\varphi_\pm(0) \\
-\varphi'_\pm(0) \\
\chi_\pm(a) - \varphi_\pm(a) \\
\rho y \chi_\pm(a) - \chi'_\pm(a) + \varphi'_\pm(a) \\
P_\pm - \chi_\pm(a+l) \\
(\gamma y - ik_2)P_\pm - \chi'_\pm(a+l)
\end{pmatrix}.
$$

(7)

Here,

$$
y = \frac{2m^*\alpha}{\hbar^2}. \tag{8}
$$

The solution of the obtained system of equations yields the first-order correction to the electron wave function, which makes it possible to calculate the active conductance of the structure. The results presented below (Section 4) are based on the rigorous solution of this system.

For resonance transitions, certain general properties of three-barrier structures with fairly strong barriers, $y \gg k_{0\pm}, k_\pm, k_{1\pm}, k_{2\pm}$, can be studied using the example of a symmetric structure without discontinuities of the conduction-band bottom at the barriers, in which case $a = l$, $U = U_1 = U_2 = 0$, and $\gamma = 1$. For such a structure, the condition for resonance transit of electrons through the structure can be written as [13]

$$
|\cos k\alpha| \approx 1, \quad |\sin ka| \ll 1. \tag{9}
$$

For $\cos ka \approx -1$, we set

$$
\sin ka = -\frac{k}{y}\beta \tag{10}
$$

and find that the determinant of system (7) is at its minimum (the condition for resonance, see [13, 14] for more details) if

$$
\beta_1 = -1, \quad \beta_2 = -1 - 2/\rho; \tag{11}
$$

for $\cos ka \approx 1$, the minimum is attained if

$$
\beta_1 = 1, \quad \beta_2 = 1 + 2/\rho. \tag{12}
$$

Thus, instead of levels distant from each other, we have the pairs of closely spaced "split" levels (see Fig. 2).

The splitting of the levels can be easily explained if we envision the formation of a symmetric three-barrier structure as the emergence and growth of the third δ-shaped barrier at the center of a quantum well (QW) (with width $2a$) in the original two-barrier structure. The emergence of the third barrier does not distort the wave functions of the two-barrier structure, which vanish at the point corresponding to the growth of the barrier (the QW center). Therefore, the positions of the corresponding levels (the levels with even numbers) remain unchanged. In contrast, the resonance wave functions of the odd-numbered levels become profoundly distorted as the strength of the third barrier increases. For the zero strength of this barrier, a maximum of the odd-numbered wave function is located at the QW center. A zero of this function appears at this point if the barrier strength is infinite; the same is true of the next-in-number even wave function. Therefore, the values of the wave vectors of the odd-numbered wave functions approach those of the even-numbered wave functions; consequently, the energies of the corresponding levels approach each other.

The separation between the levels is equal to

$$
\hbar\omega = \frac{2k\Sigma}{\pi N \rho y}, \tag{13}
$$

where Σ, N, and k are the energy, number, and wave vector for a given pair of levels, respectively. It can be seen that, for fairly strong barriers (i.e., when $y \gg k$ and $\rho \sim 1$), the energy spacing between the split levels is much smaller than their energy, $\hbar\omega \ll \Sigma$; notably, the stronger the inner and outer barriers, the lower the fre-

quencies of transitions. Thus, in contrast to a two-barrier structure, in which the frequencies of transitions are governed by the longitudinal size of a QW and by the number of resonance levels, the frequencies of transitions in three-barrier structures can be controlled by varying the strength of the middle barrier.

It can be shown that the width of the Nth pair of levels in a three-barrier structure is given by

$$\Gamma \approx \frac{k_0 + k_2}{4k}\Gamma_{sym},$$

where

$$\Gamma_{sym} = \left(\frac{\pi\hbar^2 N}{m^*}\right)^3 \frac{1}{\alpha^2 a^4} \tag{14}$$

is the width of the Nth level in a symmetric two-barrier structure with the longitudinal QW size equal to the size of the first QW a in a three-barrier structure. For the structures with a constant height of the conduction-band bottom, $k_0 = k_2 = k$; consequently, we have $\Gamma = \Gamma_{sym}/2$. A remarkable special feature of split levels is their virtually identical widths (to within the parameter k/y). This property is very important, because, to a great extent, it facilitates the attainment of large magnitudes of negative differential conductivity (NDC) in such structures. In fact, the lower level in the two-barrier structures is always much narrower than the upper level; in addition, the feasibility of enhancing the structure conductance in the large-signal mode by increasing the effective width of the barriers is limited to a large extent by the necessity of maintaining the tunneling coherence at exactly the narrower lower level. In other words, the barrier width can be increased only as long as the tunneling lifetime does not exceed the mean time of scattering by phonons; this scattering disturbs the tunneling coherence. In addition, also because of the narrowness of the lower level, only an insignificant electron-current fraction (approximately equal to the ratio between the widths of the lower and upper levels) corresponding to tunneling of electrons through the upper level arrives at the lower level involved in the interaction with the HF field. At the same time, in transitions between the split levels equal in width, first, almost all electrons tunneling through the structure can interact with the HF field and supply energy to this field, and, second, the limitations in time are almost the same for both the upper and lower levels, which makes it possible to attain a much higher intensity of quantum transitions and, consequently, an NDC.

It is noteworthy that there is another important and very interesting special feature of transitions between the split levels in a symmetric three-barrier structure. In the case of transitions between the Kth and Nth resonance levels, the high-frequency conductivity of a two-
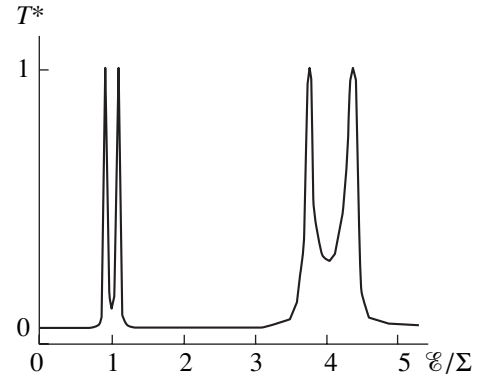
Fig. 2. The coefficient of transit T^* through a symmetric three-barrier InAs-based structure as a function of the ratio between the electron energy $\mathcal{E}$ and the energy of the first resonance level in a two-barrier structure with $\Sigma = 60.3$ meV (the distance between the barriers is $a = l = 150$ Å, and the hetero-barrier widths and heights are 11 Å and 2 eV, respectively.

barrier structure increases as the fourth power of the barrier strength α,

$$\sigma_{sym} = \pm\frac{8q^2 m^*\alpha^4}{\pi M\hbar^6\omega^3}n[1-(-1)^{K-N}] \tag{15}$$

(n stands for the electron concentration), whereas the emission frequency ω controlled by the energy spacing between the levels depends only slightly on α. As can be easily shown using system (7), in the case of transitions between the split levels, the high-frequency conductivity in three-barrier structures has the following form:

$$\alpha = \pm\frac{8q^2 k_0^2[\rho^2(U+U_2)+4\hbar(\omega_0-\omega)]^2}{a(k_0+k_2)^2(k_{0-}+k_{2-})m^*\rho^4\hbar^2\omega^3}n. \tag{16}$$

Here, the dependence of the frequency ω on the strength of the barriers (the outer barriers are assumed to be identical) is given by (13). For a structure whose conduction-band bottom has constant height, expression (16) is reduced to

$$\sigma = \pm\frac{16q^2(\omega_0-\omega)^2}{\pi Nm^*\rho^4\omega^3}n, \tag{17}$$

whereas expression (17), in view of (8) and conditions $k \ll y$ and $\omega \ll \omega_0$, transforms into the following expression:

$$\sigma = \pm\frac{q^2\pi^2 N^2 n}{4m^*\rho\omega_0}\left(\frac{y}{k}\right)^3 = \pm\frac{q^2\pi^2 N^2\alpha^3 n}{\rho}\left(\frac{m^*}{\hbar^{10}\omega_0^5}\right)^{1/2}. \tag{18}$$

Thus, it turns out that the high-frequency conductivity in the case of transitions between the split levels in three-barrier structures is proportional to the third power of the strength of the barriers.

4. RESULTS OF NUMERICAL CALCULATIONS

In Figs. 3–5, we show the results of numerical calculations for an asymmetric three-barrier structure (1);
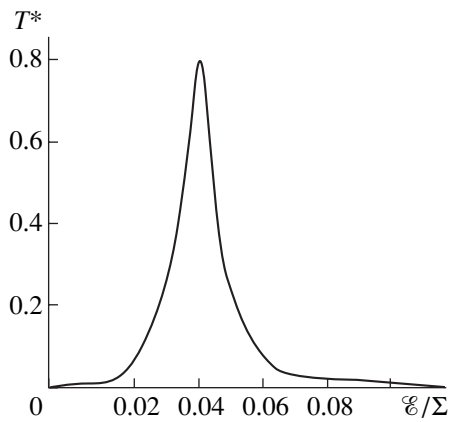
Fig. 3. The coefficient of transit $T*$ through the three-barrier structure under consideration as a function of the ratio between the electron energy $\mathscr{E}$ and the energy of the first resonance level in a two-barrier structure $\Sigma = 60.3$ meV.

we used the model described in Section 2. The same width is chosen for both QWs, i.e., $a = l = 150$ Å; the widths of the first, second, and third heterobarriers are 11, 5.5, and 16.5 Å, respectively; and the height of the barriers (2 eV) is governed by the magnitude of discontinuity of the bands (the height of the first resonance level in the structure with the 11-Å-wide barriers is $\Sigma = 60.3$ meV). In general, the properties of ultrathin heterobarriers have not been studied adequately; thus, the model we used for the barriers with widths on the order of several atomic layers is extremely approximate—the more so for a single atomic layer. However, the two-barrier resonance-tunneling structures with barriers with widths amounting to several atomic layers (of course, the exact height of these barriers is unknown)
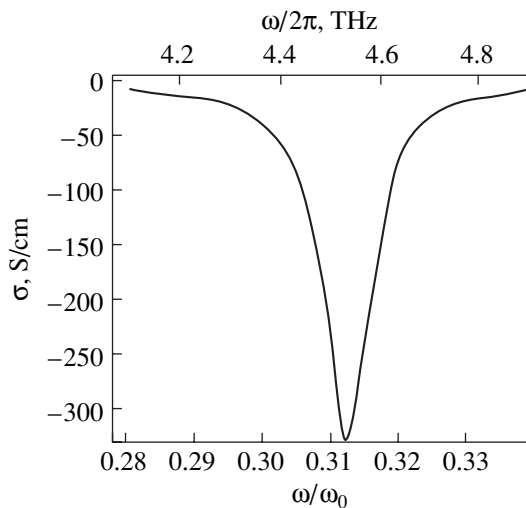
have already been reported [10]. It is noteworthy that an ultrathin and high middle barrier is conceptually equivalent to a lower and rather wide barrier of the same strength; the latter barrier can generally be fabricated without difficulties. The magnitude of discontinuity in the conduction-band bottom at the first and second barriers $U = U_1 = 65$ meV is chosen so that the first resonance level is below and the second resonance level is above the conduction-band bottom in the leftmost part of the three-barrier resonance-tunneling structure (Fig. 1). The magnitude of discontinuity in the conduction-band bottom at the third barrier $U_2 = 45$ meV is chosen in such a way so as to ensure the largest increase in the integrated (taking into account all electrons injected into the structure) HF conductance of the three-barrier resonance-tunneling structure.

In Fig. 3, we show the dependence of the static transit coefficient $T*$ on the energy of incident electrons. As can be seen, although the structure is highly asymmetric, the transit coefficient is reasonably large (~0.8) due to the fact that the third barrier is wider than the first one.

In Fig. 4, we show the frequency dependence of active high-frequency conductivity of a structure that has $n = 10^{16}$ cm^{-3} and is irradiated with monoenergetic electrons. It can be deduced from Fig. 4 that the width of the lower resonance level Γ is close to the width of the upper resonance level and amounts to ~0.6 meV. The corresponding lifetime at this level is nearly five times shorter than the characteristic time of the electron-momentum relaxation in InAs at $T = 77$ K; consequently, transport through the structure is collisionless (coherent).

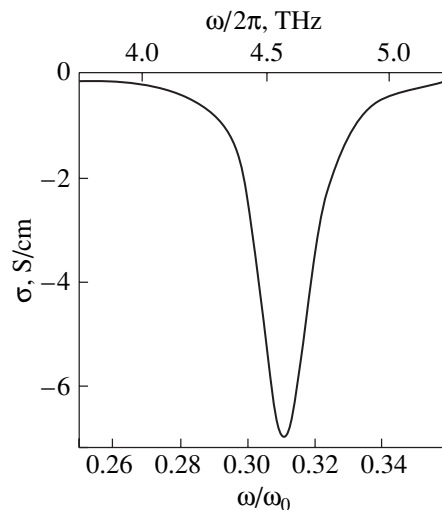Figure 5 represents the frequency dependence of integrated active conductivity of a three-barrier reso-

Fig. 4. Active conductivity of three-barrier structure σ that has an electron concentration of $n = 10^{16}$ cm^{-3} and is subjected to a monoenergetic electron beam passing through the resonance level as a function of the normalized frequency ω/ω_0 ($\omega_0 = \Sigma/\hbar$].

Fig. 5. Dependence of integrated active conductivity σ of the three-barrier structure under consideration with allowance made for the Fermi distribution of electrons on the normalized frequency ω/ω_0 ($\omega_0 = \Sigma/\hbar$, $a = l = 150$ Å, and $\Sigma = 60.3$ meV).

nance-tunneling structure with electron concentration $n = 10^{16}$ cm^{-3} at temperature $T = 77$ K with allowance made for the Fermi distribution of electrons incident on the structure input.

It can be seen that the conductivity attains its largest magnitude at the frequency $\nu = 4.5$ THz; this magnitude is equal to $\sigma_a = -7.3$ S/cm, which, on the one hand, exceeds by several times the lasing threshold (for the structure under consideration, this threshold is defined by the condition $-\sigma_a > 2$ S/cm) and, on the other hand, is several times smaller than the value $0.7\omega\varepsilon\varepsilon_0 \approx 20$ S/cm, above which neglect of the space-charge alternating component is justified. Thus, we may conclude that the oscillation frequency of a coherent quantum laser based on a three-barrier structure can basically be reduced to 5 THz in the large-signal mode without exceeding the considered physical mechanism of the laser's operation. It is clear that the successive cascade connection of such active three-barrier nanostructures (as is done in modern devices [1, 2]) can bring about an appreciable increase in both the quantum efficiency and the output power of a laser.

It is of interest to compare the characteristics of the suggested three-barrier InAs-based laser structure with those of a two-barrier InAs-based structure. Naturally, this comparison should be performed at a higher frequency, where, in principle, both structures operate.

The frequency of transitions between the split levels of a three-barrier structure can be increased both by increasing the energy of the levels and by decreasing the strength of the middle barrier. In Fig. 6, we show the frequency dependence of integrated active conductivity at $T = 77$ K for a three-barrier structure with $n = 10^{16}$ cm^{-3}, identical widths of both QWs, i.e., $a = l = 130$ Å, and the outer barriers with widths of 11 and 16.5 Å and a height of 2 eV. For the inner barrier, we assumed that its width and height were 5.5 Å and 1 eV, respectively (which was conceptually equivalent to a barrier with a width of 55 Å and a height of 0.1 eV); it was also assumed that $U = U_1 = 80$ meV and $U_2 = 60$ meV. The height of the first resonance level in a two-barrier structure with 11-Å-thick barriers is $\Sigma = 78.23$ meV. The width of the first resonance level was found to be the same as in the former case.

It can be deduced from the results of calculations that the integrated conductivity of the structure under consideration attains a maximum at the frequency $\nu = 9.5$ THz; the conductivity exceeds the threshold conductivity ~0.3 S/cm (starting from which the lasing sets in) by more than an order of magnitude for the aforementioned electron concentration. In order to obtain the same result using a two-barrier structure, we should make the width of the lower level smaller by a factor of about 5. In this case, the electron lifetime at this level will become virtually equal to the time of electron-momentum relaxation; correspondingly, the electron transport will no longer be coherent for finite amplitudes of the HF field and further reduction of the oper-
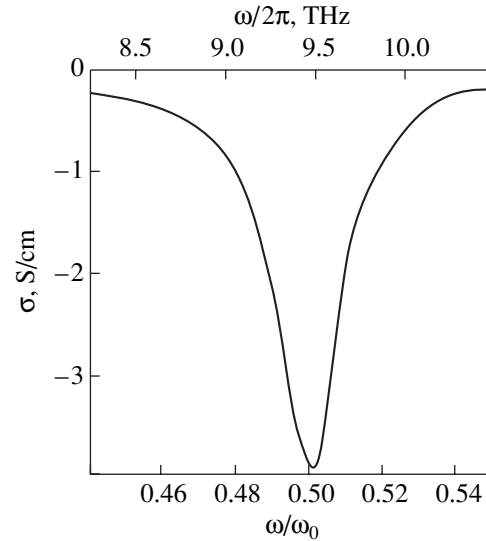

Fig. 6. Integrated active conductivity σ of the three-barrier structure under consideration as a function of normalized frequency ω/ω_0 ($\omega_0 = \Sigma/\hbar$, $a = l = 130$ Å, and $\Sigma = 78.23$ meV).

ating frequency will result in a drastic decrease in both the conductivity and quantum efficiency of the two-barrier structure.

5. CONCLUSION

Thus, calculations show that lasers operating by transitions between the split levels (subbands) in the far-IR region of the spectrum at frequencies up to 4.5 THz can be developed on the basis of three-barrier nanostructures with optimized widths of potential barriers, which ensure coherent electron transport.

Taking into account that (as shown previously [11, 12]) resonance-tunneling transit-time diodes with coherent tunneling in the two-barrier injector can have negative dynamic resistance, which exceeds the ohmic resistance of the passive diode regions, at frequencies up to 5 THz ($\lambda = 60$ μm), we can state that it is basically possible to span the entire frequency range from several gigahertz to tens of terahertz using active semiconductor devices based on nanostructures with coherent transport of electrons.

REFERENCES

1. J. Faist, A. Tredicicci, F. Capasso, *et al.*, IEEE J. Quantum Electron. **34** (2), 336 (1998).

2. C. Sirtori, J. Faist, F. Capasso, *et al.*, Appl. Phys. Lett. **69** (19), 2810 (1996).

3. G. Scamarcio, C. Gmachl, F. Capasso, *et al.*, Semicond. Sci. Technol. **13**, 1333 (1998).

4. A. Tredicucci, C. Gmachl, F. Capasso, *et al.*, Appl. Phys. Lett. **74** (5), 638 (1999).

5. M. Helm, P. England, E. Colas, *et al.*, Phys. Rev. Lett. **63**, 74 (1989).

6. M. Rochat, J. Faist, M. Beck, *et al.,* Appl. Phys. Lett. **73**, 3724 (1998).

7. I. Lyubomirsky, Q. Hu, and M. R. Melloch, Appl. Phys. Lett. **73**, 3043 (1998).

8. B. S. Williams, B. Xu, and Q. Hu, Appl. Phys. Lett. **75** (19), 2927 (1999).

9. E. I. Golant, A. B. Pashkovskiĭ, and A. S. Tager, Pis'ma Zh. Tekh. Fiz. **20** (21), 74 (1994) [Tech. Phys. Lett. **20**, 886 (1994)].

10. E. R. Brown, J. R. Soderstrom, C. D. Parker, *et al.*, Appl. Phys. Lett. **58** (20), 2291 (1991).

11. É. A. Gel'vich, E. I. Golant, A. B. Pashkovskiĭ, and V. P. Sazonov, Pis'ma Zh. Tekh. Fiz. **25** (10), 7 (1999) [Tech. Phys. Lett. **25**, 382 (1999)].

12. É. A. Gel'vich, E. I. Golant, A. B. Pashkovskiĭ, and V. P. Sazonov, Pis'ma Zh. Tekh. Fiz. **26** (13), 11 (2000) [Tech. Phys. Lett. **26**, 544 (2000)].

13. E. I. Golant and A. B. Pashkovskiĭ, Pis'ma Zh. Éksp. Teor. Fiz. **67** (6), 372 (1998) [JETP Lett. **67**, 394 (1998)].

14. A. B. Pashkovskiĭ, Pis'ma Zh. Éksp. Teor. Fiz. **64** (12), 829 (1996) [JETP Lett. **64**, 884 (1996)].

Translated by A. Spitsyn

<div align="center">

AMORPHOUS, VITREOUS,
AND POROUS SEMICONDUCTORS

</div>

Microwave Photoconductivity in Nanocrystalline Porous Titanium Oxide Subjected to Pulsed Laser Excitation

E. A. Konstantinova*, V. Yu. Timoshenko*, P. K. Kashkarov*, V. G. Kytin*,
V. Ya. Gaĭvoronskiĭ**, H. Porteanu***, Th. Dittrich***, and F. Koch***

* Faculty of Physics, Moscow State University, Vorob'evy gory, Moscow, 119899 Russia
e-mail: liz@vega.phys.msu.su
** Institute of Physics, National Academy of Sciences of Ukraine, pr. Nauki 144, Kiev, 252650 Ukraine
*** Technische Universität München, Physik Department E16, D-85748 Garching, Germany
Submitted June 5, 2001; accepted for publication June 26, 2001

Abstract—A contactless method of microwave photoconductivity was used to study the relaxation of photoexcited charge carriers in nanocrystalline porous titanium oxide. A decrease in the amplitude and a change in the microwave photoconductivity relaxation time is observed with reduction in the nanocrystal size, which is explained by localization of carriers due to dielectric confinement. Capture of holes by the traps on the TiO_2 surface increases the amplitude and prolongs the relaxation time of the microwave photoconductivity. © 2002 MAIK "Nauka/Interperiodica".

INTRODUCTION

Titanium oxide (TiO_2) is a wide-gap semiconductor that can have several crystallographic forms, rutile and anatase being the most widely known ones. TiO_2 finds various applications in science and technology: the manufacture of sensors [1] and catalysis in the production of oxygen and hydrogen [2] are some examples. Another promising application, proposed by Grätzel *et al.* [3, 4], is related to the injection solar cells based on porous TiO_2 (*por*-TiO_2) consisting of nanocrystals with the anatase structure. To date, the highest efficiency of the (*por*-TiO_2)-based solar cells has not exceeded 12%, which is still lower than that of silicon solar cells; however, in view of the low cost of *por*-TiO_2 production, this material is of certain practical interest [4].

Photovoltaic applications of *por*-TiO_2 call for an adequate understanding of the relaxation processes observed after photoexcitation of a sample. Although significant effort has been devoted to studying the electrical properties of *por*-TiO_2 (see, e. g., [5–7]), a comprehensive analysis of photoconductivity in this material is still lacking. It should also be taken into account that *por*-TiO_2 is an extremely complicated object, which may be thought of as a network of nanocrystals with their surfaces containing defects and various molecular complexes. Another difficulty that hinders investigation of the *por*-TiO_2 conductivity by conventional methods is the problem of forming a reliable electric contact to it. However, a contactless technique of microwave photoconductivity (MPC) [8] has proved to be promising for the investigation of relaxation processes in porous semiconductors. This method implies the detection of the photoexcited charge carriers using

a change in the transmission or reflection of the electromagnetic radiation in the gigahertz frequency range.

In this study, the MPC method is applied to investigate recombination processes in *por*-TiO_2 layers with nanocrystals of various sizes. To ascertain the role of the defects and molecular complexes on the *por*-TiO_2 crystal surface, the samples were subjected to thermal vacuum annealing and adsorption in ethanol vapors, the results being detected using the electron spin resonance (ESR) technique.

EXPERIMENTAL

To prepare the *por*-TiO_2 samples, glass substrates were coated with thin layers of a turpentine paste containing anatase nanocrystals. Then, the samples were annealed in air for 40–50 min at a temperature of 450°C. This treatment resulted in the complete removal of organic substances from the films and led to the formation of a nanoporous structure that consisted of a network of TiO_2 nanocrystals. Samples with average sizes of nanocrystals of about 16 and 6 nm (hereinafter denoted as A16 and A6, respectively) were selected for the experiments. The average size of the nanocrystals was determined from X-ray diffraction [7]. The porosity (P) and the thickness of layers amounted to about 70% and 1 μm, respectively. Along with the as-prepared *por*-TiO_2 samples, we also studied *por*-TiO_2 subjected to thermal vacuum annealing at a residual pressure of ~10^{-2} Pa at 450°C for 30–40 min. Furthermore, as-prepared samples exposed to saturated ethanol vapors were also examined. For many semiconductors, TiO_2 among them [9], ethanol molecules that adsorb on the surface are known to behave as donors; this fact was
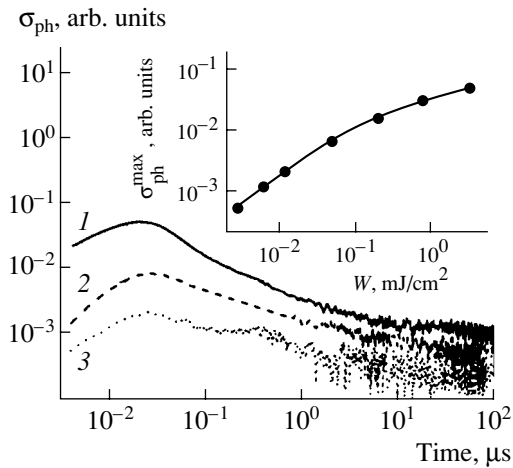
σ_{ph}, arb. units

Fig. 1. Kinetics of the microwave photoconductivity of as-prepared A16 samples for the excitation energy fluences $W = $ (*1*) 3, (*2*) 10^{-2}, and (*3*) 3×10^{-3} mJ/cm^2. The inset presents the W dependence of the σ_{ph} peak amplitude.

used to form trapping centers on the interior surface of (*por*)-TiO$_2$.

A pulsed nitrogen laser with a quantum energy of $h\nu = 3.7$ eV, a pulse duration of 5 ns, and a repetition rate from 1 to 5 Hz was employed for the excitation of nonequilibrium charge carriers in *por*-TiO$_2$. The reflection and absorption coefficients measured in the initial A16 layers at the given frequency of excitation radiation amounted to $R = 13\%$ and $\alpha = 3.7 \times 10^4$ cm^{-1}, respectively. After thermal vacuum annealing, the respective values increased to $R = 15\%$ and $\alpha = 4.3 \times 10^4$ cm^{-1}. Estimation of the band gap from the spectral dependence of α yielded $E_g = 3.4$ eV, which is approximately equal to E_g for single-crystal and polycrystalline anatase films [10]. The optical constants of A6 samples were not measurable because of appreciable scattering. The data obtained in [11] suggest that, due to the quantum-mechanical size effect, the E_g of an anatase nanocrystal 6 nm in diameter widens by about 0.1 eV with respect to that in a single crystal. This allows the absorption coefficients of as-prepared A6 samples and those subjected to thermal vacuum annealing to be estimated from the spectral dependence of α for A16 samples at 2×10^4 and 3×10^4 cm^{-1}, respectively. An increase in α of the *por*-TiO$_2$ after thermal vacuum annealing is caused by the formation of electron states of defects appearing in the TiO$_2$ band gap because of oxygen depletion, the so-called reduction, which is well known for TiO$_2$ single crystals [12].

ESR spectra of the *por*-TiO$_2$ layers separated from the substrates were recorded using a standard JEOL-JES-RE2X spectrometer with an operating frequency of 9.5 GHz and a sensitivity of 10^{11} spin/Gs.

The setup for measuring MPC kinetics consisted of a Gunn diode (35 GHz, with frequency stabilizer) as the microwave source, a waveguide, an attenuator, and a conventional microwave detector. The sample served as the end wall of the waveguide where a standing wave was formed. A microwave detector was used to measure the power of microwave radiation and its variation induced in the sample from the excitation by the nitrogen laser, i.e., the MPC signal. It should be noted that, according to [8], measurements in this arrangement yield results equivalent to those of intracavity measurements, where the photoinduced variation of the cavity Q factor is governed by a change in the microwave conductivity of the material. The kinetics of MPC was visualized using an HP-503 storage oscilloscope linked to a computer. The time resolution was 20 ns. Data obtained with excitation by individual laser pulses were accumulated and averaged over several hundred of these. The MPC-signal shape was the same for all experiments; i.e., no change introduced by the charge accumulation was revealed. The measurements were carried out at a temperature of 300 K.

It is known that MPC in *por*-TiO$_2$ may result either from the motion of the charge carriers induced by quanta with an energy exceeding E_g [8, 13] or, in view of the ionic character of TiO$_2$ bonds, from the photoinduced change in the dipole moment [14]. In the first case, the amplitude of the MPC signal is proportional to the density of photoexcited carriers and the slope of the MPC decay curve provides information about their recombination and capture in the studied samples. MPC of the second type is typical of optical excitation of *por*-TiO$_2$ when the quantum energy is below E_g [14]. In our experiment, the condition $h\nu > E_g$ was evidently met. Furthermore, the largest detectable signal of the photoinduced change in the Q factor of the system was two orders of magnitude smaller than its level in the dark. Thus, the measurements were performed with a slight modulation of the initial Q factor. The above considerations allow us to assume that the detected signal is proportional to the MPC value, which is, in turn, proportional to the density of the charge carriers induced in *por*-TiO$_2$ layers [8].

EXPERIMENTAL RESULTS

Figure 1 illustrates the kinetics of MPC $\sigma_{ph}(t)$ for as-prepared A16 samples at different laser energy fluences W. The maximal MPC signal σ_{ph}^{max} is attained at the trailing edge of the pulse. After the end of the pulse, the signal relaxes according to the nonexponential law, which depends on the level of excitation. For $W > 0.1$ mJ/cm^2, the initial decay of MPC (curve *1*) within the first 200 ns is a power time function of the t^{-p} type, where $p \approx 1$. With time, the MPC relaxation slows down and the signal is detectable up to hundreds of microseconds. For $W \lesssim 0.01$ mJ/cm^2, relaxation $\sigma_{ph}(t)$ is considerably slower (curves *2* and *3*) and, even at small times, the parameter p satisfies the inequality $p < 1$. Furthermore, for small W values, the shape of $\sigma_{ph}(t)$ curve is W-independent, which is indicative of the dominant role of lin-

ear mechanisms in the recombination and capture of nonequilibrium carriers.

The inset in Fig. 1 shows the dependence of σ_{ph}^{max} on W. It can be seen that, for $W < 0.1$ mJ/cm^2, the dependence $\sigma_{ph}^{max}(W)$ is linear, which supports the linear recombination mechanism inferred above from the analysis of the kinetics of MPC. Excitation with the pulse energy fluence $W > 0.1$ mJ/cm^2 results in a sublinear $\sigma_{ph}^{max}(W)$ dependence, thus suggesting that the nonlinear recombination mechanisms, which limit the density of the photoexcited carriers in *por*-TiO$_2$ layers, are prevalent.

For the sake of comparison, the curves corresponding to the MPC kinetics of as-prepared A16 samples and the same samples after thermal vacuum treatment or ethanol adsorption are plotted in Fig. 2. Even at high W values, a noticeable deviation of $\sigma_{ph}(t)$ from the inverse proportionality $\sigma_{ph} \propto t^{-1}$, typical of the as-prepared samples (curve *1*), was observed for the samples subjected to the thermal vacuum (curve *2*) and the adsorption (curve *3*) treatments. An especially pronounced slowing down of MPC kinetics was observed for *por*-TiO$_2$ exposed to ethanol vapors. This type of kinetics can be conceptually identified with the so-called persistent photoconductivity, which is typical of semiconductor systems with a high density of traps or with a spatially separated recombination of carriers. Note that, in our experiments with *por*-TiO$_2$ samples with adsorbed molecules of ethanol, persistent MPC was observed for as long as tens of microseconds. Another important effect produced by the ethanol adsorption is the increase in σ_{ph}^{max} compared to that of the initial samples. Note also that these effects of ethanol adsorption were completely reversible: after removal of the vapors, the initial form of the MPC signal was completely restored.

In order to ascertain the character of the MPC kinetics as a function of particle size, a similar analysis of the A6 samples was performed (Fig. 3). We found that, for as-prepared A6 samples, the MPC amplitude is lower than that for A16 samples. Moreover, the MPC kinetics measured in samples of these two types at the same W is different (compare curves *1* in Figs. 2 and 3). Thus, for A6 samples, power-law decay $\sigma_{ph}(t) \propto t^{-1}$ is observed for up to 1 μs; then, the curve flattens out and approaches a stationary value. Similar to the behavior observed for the A16 samples, thermal vacuum annealing of A6 samples causes an increase in the MPC relaxation time (compare curves *1* and *2* in Fig. 3), as does the ethanol adsorption, which also increases $\sigma_{ph}(t)$ in comparison with that of the as-prepared samples. However, the amplitude of the delayed MPC signal for A6 samples was about an order of magnitude smaller than that for the similarly treated A16 samples.
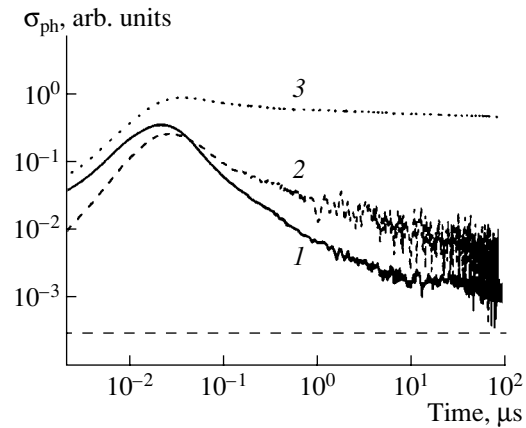
Fig. 2. Kinetics of microwave photoconductivity of (*1*) as-prepared A16 samples, (*2*) the same samples subjected to thermal vacuum annealing, and (*3*) after the adsorption of ethanol molecules. The excitation energy fluence $W = 1$ mJ/cm^2. Horizontal dashed line shows the noise level.
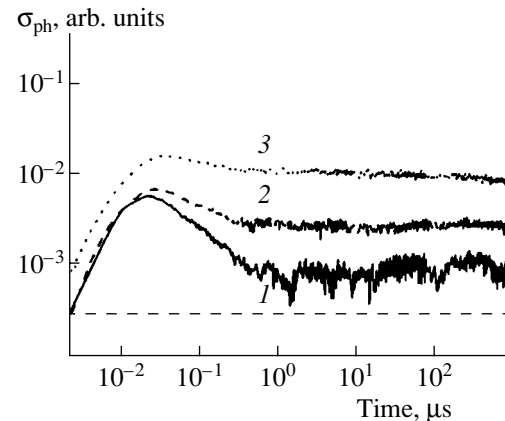

Fig. 3. The same as in Fig. 2 for sample A6.

The defect structure of the *por*-TiO$_2$ layer was analyzed by the electron spin resonance (ESR) technique. The ESR spectra of the as-prepared A16 samples, as well as for the same samples after thermal vacuum annealing and ethanol adsorption, are presented in Fig. 4. In [15], ESR spectral lines corresponding to *g*-factors of 2.0035, 2.009, and 2.020 are attributed to O$_2^-$ centers; the lines corresponding to $g = 2.006$, 2.009, and 2.013, to O$_3^-$ centers; and the lines with $g = 2.03$ and 2.002, to the (HO$_2$)$^\bullet$ radicals. According to [16], the lines with $g = 2.014$ and 2.003 indicate the presence of (OH)$^\bullet$ radicals, and the line with $g = 1.995$ indicates the presence of Ti^{3+} ions. Oxygen anion radicals can be formed naturally via the adsorption of molecular oxygen from air onto the TiO$_2$ crystal surface. The formation of (HO$_2$)$^\bullet$ and (OH)$^\bullet$ radicals occurs when a hole is captured by negatively charged O$_2$H$^-$ or OH$^-$ molec-
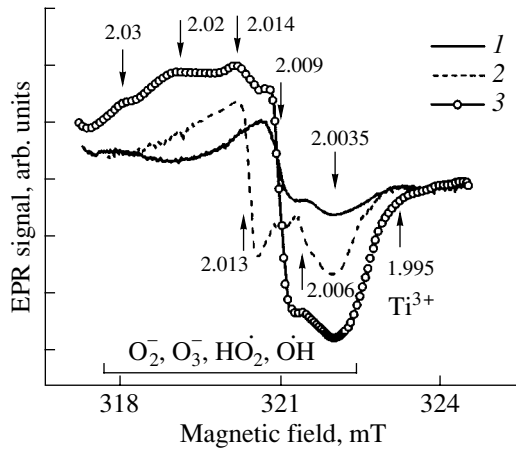
Fig. 4. Electron spin resonance spectra for *por*-TiO$_2$: (*1*) as-prepared sample, (*2*) the sample subjected to thermal vacuum annealing, and (*3*) the sample exposed to ethanol vapors. Numbers with arrows indicate the *g*-factor values.
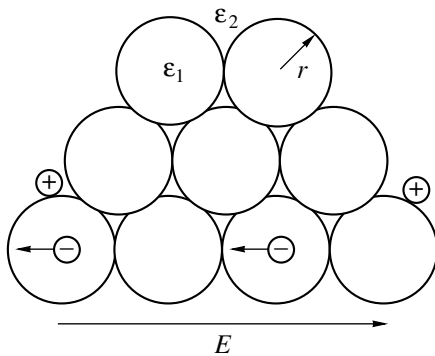

Fig. 5. Model of microwave photoconductivity in *por*-TiO$_2$ nanocrystals. **E** vector indicates the direction of the electric field of microwave radiation.

ular complexes, which are always present on the TiO$_2$ surface, with the exception of the samples subjected to thermal vacuum treatment at high temperatures (above 350–400°C) [15]. As one can conclude from Fig. 4, in as-prepared (*por*)-TiO$_2$ (curve *1*), O$_2^-$ and (HO$_2$)$^{\cdot}$ radicals prevail; in vacuum annealed samples (curve *2*), O$_2^-$ and O$_3^-$ radicals, as well as the Ti^{+3} centers, are present; and the samples exposed to ethanol vapors contain a variety of radicals connected with (HO$_2$)$^{\cdot}$ and (OH)$^{\cdot}$ hydroxyl groups (curve *3*). Total concentrations of the spin centers amounted to 1.5×10^{17} cm^{-3} in the as-prepared sample; 3×10^{17} cm^{-3}, in the sample after thermal vacuum annealing; and on the order of 10^{18} cm^{-3}, in the sample held in ethanol vapors.

DISCUSSION

In terms of the classical approach, the MPC observed in *por*-TiO$_2$ layers may be related to the motion of charge carriers in a system of connected TiO$_2$ nanocrystals in an electric field of microwave radiation, as shown schematically in Fig. 5. To simplify further analysis, nanocrystals will be considered as spherical. Since nanocrystals are much smaller than the wavelength of the microwave radiation used in experiment (9 mm), we may disregard spatial fluctuations of the field on the nanocrystal-size scale and assume that the charge carriers move in a field that is, on average, uniform. The fluctuations of the field arise from the dielectric inhomogeneity of the medium and conceptually present new barriers for the carrier motion, thus decreasing the cross section of carrier interaction with microwave radiation, i.e., lowering their mobility at the frequencies used in experiment. The carrier mobility as a function of nanocrystal size will be specially considered below.

Analysis of the kinetics of MPC presented above at a high excitation level should first and foremost account for the possibility of nonlinear recombination, which limits maximal concentration of the photoinduced carriers in the *por*-TiO$_2$ layers. Let us estimate this concentration under the assumption that, in view of the small diffusion coefficients of electrons (10^{-3}–10^{-5} cm^2/s) and holes (10^{-5}–10^{-7} cm^2/s) in *por*-TiO$_2$ [5–7], the photoexcited layer thickness may be taken to be on the order of α^{-1}. Then, the absorption of the laser pulse results in production of $n = \alpha W(1 - R)/h\nu$ electron–hole pairs. Using the values of α and R obtained from the optical measurements for the A16 samples, disregarding recombination, and considering the laser pulse with $W = 1$ mJ/cm^2, we estimate the density of the excited electron–hole plasma to be about 10^{20} cm^{-3}. Note that, for A6 samples, where α is somewhat smaller, the estimated density is lower by a factor of 1.5–2. The values obtained are sufficiently high to bring about the recombination processes whose rate is a quadratic (bimolecular radiative recombination) or a cubic (non-radiating Auger recombination) function of n. The Auger recombination lifetime τ_A can now be estimated using the obtained n. Taking the Auger recombination coefficient γ from the range typical of most wide-gap semiconductors ($\gamma = 10^{-29}$–10^{-30} cm^6/s [17]), we obtain $\tau_A = (\gamma n^2)^{-1} \approx 10^{-11}$–$10^{-9}$ s, which points to the significant role of Auger recombination as a factor limiting the density of carriers at a high level of excitation. This conclusion is supported by the experimentally observed sublinear dependence of σ_{ph}^{max} on W (see the inset in Fig. 1).

Another nonlinear recombination process that is likely to occur in TiO$_2$ nanocrystals is radiative bimolecular recombination. Unfortunately, no data on the probability coefficients and characteristic times of this process in TiO$_2$ are available. However, the experimentally observed power-law decay of the MPC signal t^{-p} with $p \approx 1$ clearly points to the fact that bimolecular recombination prevails within the time intervals from 20 to 200 ns for the samples with nanocrystals 16 nm in

size (Fig. 2, curve *1*) and from 20 nc to 1 μs for the samples with nanocrystals 6 nm in size (Fig. 3, curve *1*).

It is of interest to analyze the number of photoexcited electron–hole pairs per nanocrystal in the *por*-TiO$_2$ layer. The number of nanocrystals in a unit volume of the *por*-TiO$_2$ layer N can be expressed as

$$N = (4/3\pi r^3)^{-1}(1 - P),$$

where $P = 0.7$ is the porosity of the sample and $r = 8$ and 3 nm for A16 and A6 samples, respectively. Consequently, the corresponding values of N in A16 and A6 samples are approximately 10^{17} and 2×10^{18} cm^{-3}. Using the above estimates of n, maximal numbers of photoexcited nonequilibrium carriers per TiO$_2$ nanocrystal turn out to be about 1000 and 100 pairs in A16 and A6 samples, respectively. Nonlinear recombination evidently reduces the ultimate density of the electron–hole plasma. However, the estimations made above suggest that several tens of nonequilibrium electron–hole pairs are still present in every nanocrystal of the absorbing TiO$_2$ layer after the end of the laser pulse. These carriers can either recombine or be captured by defects on the nanocrystal surface. They can also diffuse into the depth of the layer, since the sample's thickness considerably exceeds the absorption length. We believe that these are the processes which govern the MPC kinetics on a time scale beginning from several microseconds.

In what follows, we discuss the decrease in the MPC signal for the samples with a smaller nanocrystal size. This effect may be caused either by an increase in the recombination rate, which lowers n, or by a decrease in the cross section of the carriers' interaction with microwave radiation in smaller nanocrystals. The former cause seems more probable. In fact, we observed a diminishing of the MPC signal in A6 samples even at the highest level of excitation (compare Figs. 2 and 3), where recombination via nonlinear mechanisms prevails. According to the above estimates, the rate of nonlinear recombination in A6 samples may even be lower than that in A16 samples. On the other hand, a decrease in the cross section of microwave interaction with smaller nanocrystals seems plausible in view of the two following circumstances. First, the period of charge carrier oscillations in the electric field of microwave radiation is about 30 ps; during this time interval, the carriers exhibit multiple scattering by the boundaries of nanocrystals. Therefore, the smaller the nanocrystal, the greater the number of scattering events and, hence, the less the cross section of interaction with microwave radiation, or, what is the same, the lower the mobility of carriers at the frequencies under study. Second, localization of the charge carriers in smaller sized nanocrystals is more pronounced due to both the quantum-mechanical size effect [11], which forces the carriers to overcome the barriers arising from fluctuations in nanocrystal size, and the so-called dielectric confine-

ment, which is associated with the potential of the image charges at the nanocrystal boundaries [18].

Dielectric confinement can be estimated from the following formula for the image energy of a point charge at the center of a dielectric sphere [19]:

$$U = \frac{e\varepsilon_1\varepsilon_2}{[r(\varepsilon_1 - \varepsilon_2)]},$$

where e is the elementary charge, and ε_1 and ε_2 are the respective dielectric constants of the material of the sphere and the surrounding medium (Fig. 5). Assuming that $\varepsilon_1 = 40$ (anatase) and $\varepsilon_2 = 10$ (the effective dielectric constant of *por*-TiO$_2$) [7], for $r = 8$ and 3 nm, we obtain a corresponding U value on the order of 20 and 50 meV. The latter value exceeds the thermal energy at room temperature, which hampers the transition of the carriers through the boundaries of 6-nm-large nanocrystals. On the one hand, this attenuates the MPC signal and, on the other, can amplify the effect of the persistent MPC. In fact, the most mobile carriers of the same sign (electrons), which diffused from the absorption region to the adjacent unexcited nanocrystals, cannot recombine there. Thus, their density remains constant for a long time, as was observed with the samples A6 (Fig. 3).

In our opinion, the thermal- and adsorption-induced slow down of the MPC relaxation in *por*-TiO$_2$ may be attributed to the holes' capture by the surface states formed as a result of annealing or adsorption. At the same time, the electrons may still retain their mobility and, hence, interact with the electric field of the microwave radiation (Fig. 5). It should be noted that, for all types of samples, the most typical defects are those capable of hole capture (O_2^-, O_3^-) or those which were initially negative and then captured a positive charge, such as the surface molecular $(HO_2)^{\cdot}$ and $(OH)^{\cdot}$ groups, i.e., the empty or filled hole traps. The highest concentration of defects in *por*-TiO$_2$ was detected in samples after treatment in ethanol vapors. It should be remembered that, in this case, the MPC signal was maximal and the decay times increased to tens of milliseconds. If holes are captured by the surface states and the electrons remain relatively free in the nanocrystal bulk, the recombination rate decreases. This, in turn, will cause an increase in both the amplitude and the relaxation time MPC, including the intensification of the persistent MPC (Figs. 2, 3).

CONCLUSION

Thus, a time-resolved MPC technique was employed to study relaxation of electron excitation in *por*-TiO$_2$ with various nanocrystal sizes. A decrease in the nanocrystal size was found to result in attenuation of the MPC signal, which is due to a restriction on carrier motion through the system of nanocrystals in the porous layer. It is demonstrated that, along with nonlin-

ear recombination, another mechanism of relaxation of the photoexcited carriers may consist in their capture by traps associated with adsorbed oxygen and hydroxyl molecular complexes at the surface of the TiO_2 nanocrystals. The production of hole traps in ethanol vapors amplifies the MPC signal and slows down its relaxation.

ACKNOWLEDGMENTS

REFERENCES

1. W. Göpel and G. Reinhard, in *Sensors Update*, Ed. by H. Baltes, W. Göpel, and J. Hesse (VHC, Weiheim, 1996), p. 47.
2. A. Fujishima and K. Honda, Nature **238**, 37 (1972).
3. B. O'Regan and M. Grätzel, Nature **353**, 737 (1991).
4. M. K. Nazeeruddin, A. Kay, I. Rodicio, *et al.*, J. Am. Chem. Soc. **115**, 6382 (1993).
5. Th. Dittrich, E. A. Lebedev, and J. Weidmann, Phys. Status Solidi A **165**, R5 (1998).
6. R. Könenkamp, Phys. Rev. B **61**, 11057 (2000).
7. Th. Dittrich, J. Weidmann, V. Yu. Timoshenko, *et al.*, Mater. Sci. Eng. B **B69-70**, 489 (2000).
8. M. Kunst and G. Beck, J. Appl. Phys. **60**, 3558 (1986).
9. V. F. Kiselev and O. V. Krylov, *Electron Processes in Adsorption and Catalysis on Semiconductors and Dielectrics* (Nauka, Moscow, 1979).
10. H. Tang, F. Levy, H. Berger, and P. E. Schmid, Phys. Rev. B **52**, 7771 (1995).
11. M. Anpo, T. Shima, S. Kodama, and Y. Kubokawa, J. Phys. Chem. **91**, 4305 (1987).
12. R. L. Kurtz, R. Stockbauer, T. E. Madey, *et al.*, Surf. Sci. **218**, 178 (1989).
13. R. Janes, M. Edge, J. Robinson, *et al.*, J. Mater. Sci. **33**, 3031 (1998).
14. H. E. Porteanu, V. Yu. Timoshenko, Th. Dittrich, and F. Koch, Phys. Status Solidi A **182**, 201 (2000).
15. A. R. Gonzalez-Elipe, G. Munuera, and J. Soria, J. Chem. Soc., Faraday Trans. 1 **75**, 748 (1979).
16. M. Anpo, T. Shima, and Y. Kubokawa, Chem. Lett., No. 12, 1799 (1985).
17. V. N. Abakumov, V. I. Perel, and I. N. Yassievich, *Nonradiative Recombination in Semiconductors* (North-Holland, Amsterdam, 1991), Series Modern Problem in Condensed Matter Science, Vol. 33.
18. L. V. Keldysh, Phys. Status Solidi A **164**, 3 (1997).
19. V. V. Batygin and I. N. Toptygin, *Problems in Electrodynamics* (Nauka, Moscow, 1970; Academic, London, 1964).

Translated by A. Sidorova-Biryukova

Special Features of Recombination of Nonequilibrium Charge Carriers in Porous Silicon with Different Nanostructure Morphologies

M. G. Lisachenko*, E. A. Konstantinov, V. Yu. Timoshenko, and P. K. Kashkarov

Moscow State University, Vorob'evy gory, Moscow, 119899 Russia

* e-mail: maxl@ofme.phys.msu.su

Submitted June 25, 2001; accepted for publication July 11, 2001

Abstract—Photoluminescence of porous silicon with different nanostructure morphologies and silicon monocrystalline wafers used as substrates was studied comparatively. The photoluminescence intensity of mesoporous and nanoporous silicon was established to be related to the excitation intensity by the quadratic and linear dependences, respectively. A model of recombination processes in the semiconductor nanocrystal systems is suggested. The experimental results are in good agreement with the model predictions. © 2002 MAIK "Nauka/Interperiodica".

INTRODUCTION

When passing from a bulk semiconductor to a system of separate nanocrystallites, the factors controlling recombinative processes in such objects significantly change. First, the role of the surface and related electron states of defects becomes more important. Second, carriers are found to be localized in a limited space region and cannot freely interact with each other. Therefore, the dependence of the luminescence of nanocrystalline and porous semiconductors on the pump intensity differs from that of bulk materials. For example, the dependence of interband photoluminescence (PL) of bulk semiconductors on the excitation intensity is known to obey the power law with the exponent defined by the relation between the concentrations of equilibrium and nonequilibrium free carriers [1]. The exponent can vary from 1 to 2 for the exciton PL of bulk semiconductors [1]. However, a linear or sublinear dependence of PL on the excitation intensity is typically observed for porous silicon (*por*-Si) consisting of silicon nanocrystals [2].

Varying the conditions of *por*-Si preparation, one can readily produce structures with different morphologies and a preset average size of a separate unit on the basis of a single material, i.e., silicon [3]. For example, if heavily doped silicon ($\rho \approx 10$ mΩ cm) is used to produce *por*-Si, the formed pores and silicon fragments have cross sections of about 10 and 5–10 nm, respectively. In this case, the quantum-mechanical size effect is insignificant and carriers can drift rather freely from one cluster to another. Such structures are referred to as mesoporous silicon (*mesopor*-Si) [3]. If *por*-Si is grown on a *por*-Si lightly doped substrate ($\rho \approx 10$ Ω cm), characteristic cross sections of pores and silicon filamentary fragments are 2–3 nm. In this case, the size quantization energy reaches a few electronvolts, and even moderate

(in absolute value) fluctuations (about 1 nm) of fragment cross sections lead to carrier localization in silicon nanocrystals. The carrier exchange between nanocrystals becomes inhibited. Such structures are referred to as microporous silicon [3] or, taking their pore size into account, nanoporous silicon (*nanopor*-Si). Notwithstanding the great number of works dedicated to *nanopor*-Si (see, for example [2–6]), *mesopor*-Si has been inadequately studied [7, 8]. Furthermore, the available publications contain no data that directly compare the PL of *por*-Si with different nanostructure morphologies (*mesopor*-Si and *nanopor*-Si), as well as with the PL of substrates on which this *por*-Si was formed. Such data are important for understanding the changes in recombinative processes as the silicon skeleton is varied from connected silicon nanocrystallites (*mesopor*-Si) to almost totally separate nanocrystallites (*nanopor*-Si).

Therefore, this study is dedicated to experimental and theoretical investigations of changes in the statistics of the recombination of nonequilibrium carriers in the *mesopor*-Si and *nanopor*-Si nanostructures.

RECOMBINATION MODEL

Before proceeding to the experimental results and discussion, we theoretically analyze recombination processes in bulk semiconductors and in a system of connected nanocrystals. We assume that the radiative recombination proceeds via binding of free carriers to an exciton and its subsequent annihilation in the time τ_r. Only free carriers can nonradiatively recombine at surface defects in the time τ_{nr}. We consider such excitation levels where Auger recombination can still be ignored. In this approximation, recombination of nonequilib-

rium carriers in a *p*-type semiconductor can be described by the following set of kinetic equations:

$$\frac{\partial n}{\partial t} = g - Cn(p + p_0) + AN - \frac{n}{\tau_{nr}},$$

$$\frac{\partial N}{\partial t} = Cn(p + p_0) - AN - \frac{N}{\tau_r}. \tag{1}$$

Here, n and p are the concentration of nonequilibrium electrons and holes (in the absence of attachment, $n = p$), p_0 is the concentration of equilibrium holes, N is the concentration of excitons, g is the rate of nonequilibrium-carrier generation, C is the coefficient proportional to the probability of free electron and hole binding to an exciton, and A is the probability of exciton thermal dissociation.

We consider the steady state $\left(\frac{\partial n}{\partial t} = 0, \frac{\partial N}{\partial t} = 0\right)$. Since the concentration n of nonequilibrium electrons in the majority of silicon-based systems is mainly controlled by the nonradiative recombination rate, the term related to the thermal dissociation of excitons in the first equation of set (1) can be neglected. Then, from (1), we find

$$n \approx \frac{-\tau^{-1} + \sqrt{\tau^{-2} + 4Cg}}{2C}, \tag{2}$$

$$N \approx \frac{C(n^2 + np_0)}{A + \tau_r^{-1}}, \tag{3}$$

where $\tau^{-1} \equiv \tau_{nr}^{-1} + Cp_0$. In the case of $Cg\tau^2 \ll 1$, formula (2) for the concentration of free nonequilibrium carriers is appreciably simplified: $n \approx g\tau$, and the exciton PL intensity, taking into account (3), is written as

$$I_{PL} = \frac{N}{\tau_r} \simeq \frac{C\tau}{1 + A\tau_r}(p_0 + \tau g)g. \tag{4}$$

From (4), we find that

$$I_{PL} \propto g, \quad \text{if} \quad n \ll p_0; \tag{5a}$$

$$I_{PL} \propto g^2, \quad \text{if} \quad n \gg p_0. \tag{5b}$$

Set (1) is valid if charges can freely drift in the system. If the carrier drift is confined by a small volume, any separate electron cannot interact with any hole in the crystal. The interaction proceeds only with a single charge occurring in the immediate proximity to the electron. As the third charge appears, the probability of the Auger process increases drastically, and such carriers are eliminated from radiative recombination. Hence, the probability of binding free carriers to an exciton appears proportional to the concentration of nonequilibrium carriers, rather than to the product of free electron and hole concentrations [9]. Thus, if each nonequilibrium electron–hole pair in the system is

located in a separate nanocrystal, kinetic Eqs. (1) should be replaced by

$$\frac{\partial n}{\partial t} = g - C*n + AN - \frac{n}{\tau_{nr}},$$

$$\frac{\partial N}{\partial t} = C*n - AN - \frac{N}{\tau_r}, \tag{6}$$

where $C*$ is the probability of free electron and hole binding to an exciton. In this case, the dependence of the PL intensity on the pump level should be linear.

EXPERIMENTAL

The *por*-Si samples were produced by electrochemical etching of silicon substrates in a fluoric acid-based electrolyte of HF(48%) : C_2H_5OH (1 : 1). *Mesopor*-Si was formed on substrates with the resistivity $\rho = 0.015\ \Omega$ cm at a current density of 25 mA/cm^{-2} and an etching duration of 15 min. *Nanopor*-Si layers were grown on substrates with the resistivity $\rho = 10\ \Omega$ cm at a current density of 40 mA/cm^{-2} within 15 min. The porosity of the samples in *mesopor*-Si and *nanopor*-Si was 45 and 70%, respectively. The *mesopor*-Si and *nanopor*-Si layer thickness was about 15 μm.

The structural properties (characteristic sizes and shapes of nanostructures) were determined from Raman spectra using an He–Ne laser beam (wavelength was 632.8 nm and power was 20 mW).

The PL was excited by the beam of a quasi-CW Cu vapor laser (wavelength was 511 nm, pulse length duration was 20 ns, and frequency rate was 12 kHz) or an He–Ne laser (wavelength was 632.8 nm and maximum power was 40 mW). The excitation intensity was varied from 10 mW/cm^2 to 20 W/cm^2. The PL was detected using an InGaAs photodiode with a synchronous detection scheme. This was done by modulating the laser beam using a chopper with a frequency of 400 Hz. The PL lifetime was measured with a fast InGaAs photodiode (time resolution was about 100 ns). The PL spectra were corrected with the setup spectral sensitivity taken into account. Furthermore, the defect concentrations in the studied samples were evaluated using a conventional ESR spectrometer with an operating frequency of 9.4 GHz and a sensitivity of 5×10^{10} spin/G^1. The measurements were carried out in a vacuum chamber (about 10^{-3} Torr) at room temperature.

RESULTS

The Raman spectra of the samples are shown in Fig. 1. An analysis of the spectra according to the model of phonon confinement in silicon nanocrystals [10] shows that the *mesopor*-Si structure contains filamentary nanocrystallites with a cross section of about 7–10 nm. The nanocrystallites in *nanopor*-Si are best approximated by spheres 2–4 nm in diameter.
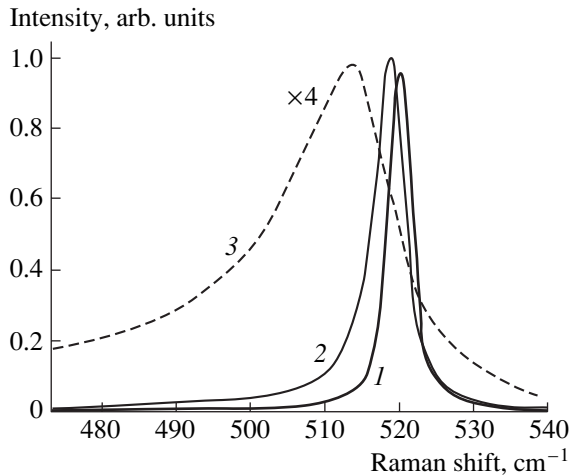
Intensity, arb. units

Fig. 1. Raman spectra of (*1*) crystalline, (*2*) mesoporous, and (*3*) nanoporous silicon.

PL intensity, arb. units
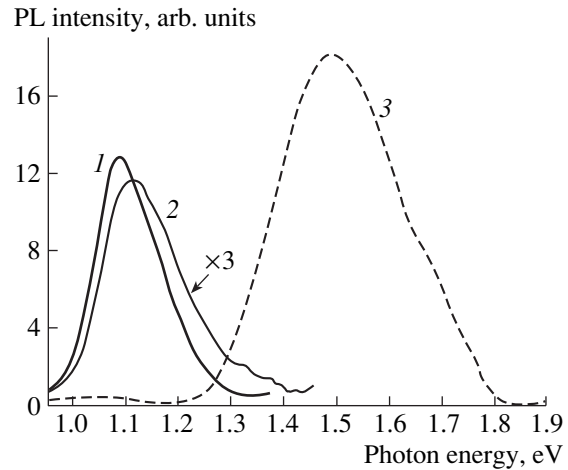
Fig. 2. Photoluminescence spectra of (*1*) crystalline, (*2*) mesoporous, and (*3*) nanoporous silicon.
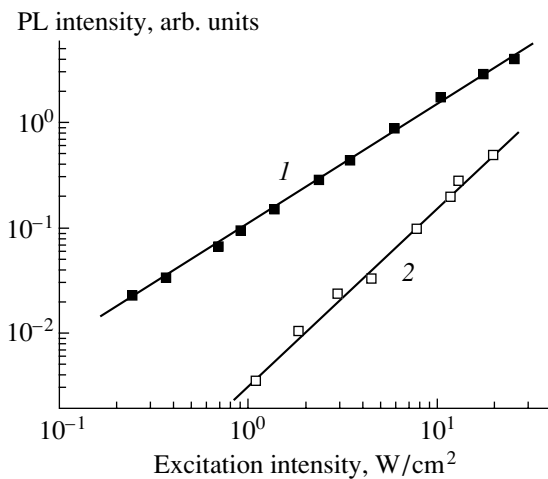
PL intensity, arb. units

Fig. 3. Dependence of the photoluminescence intensity of (*1*) crystalline silicon ($\rho = 0.015 \ \Omega$ cm) and (*2*) mesoporous silicon on the laser excitation intensity.
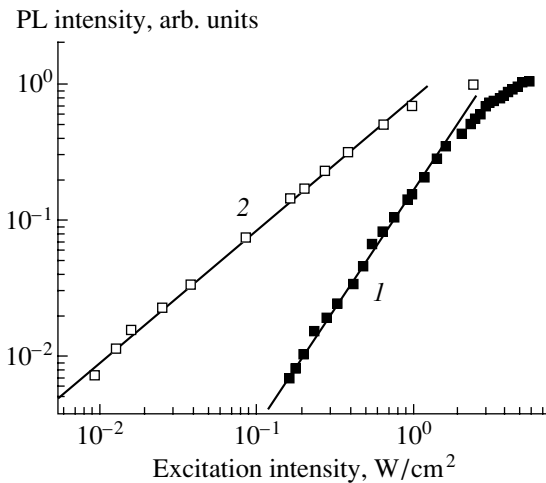
PL intensity, arb. units

Fig. 4. Dependence of the photoluminescence intensity of (*1*) crystalline silicon ($\rho = 10 \ \Omega$ cm) and (*2*) nanoporous silicon on the laser excitation intensity.

Characteristic PL spectra of crystalline Si, *mesopor*-Si, and *nanopor*-Si, excited by the copper vapor laser beam are shown in Fig. 2. The PL spectrum of crystalline Si has a peak at the quantum energy $h\nu_{max} = 1.07$ eV, which conforms well to the published data [11] on its interband luminescence. For *mesopor*-Si, $h\nu_{max}$ is shifted to higher energies by 0.04 eV. For *nanopor*-Si, the "blue" shift of $h\nu_{max}$ is about 0.4 eV.

The dependences of the PL intensity on the laser excitation intensity for the *mesopor*-Si and Si substrate are shown in Fig. 3. One can see that these dependences are quadratic and linear, respectively, as the excitation-beam power density varies from 1 to 10 W/cm². We note that the PL intensity of *mesopor*-Si was several times lower than that of its crystalline substrate.

In contrast to *mesopor*-Si, the PL intensity of *nanopor*-Si grows linearly as the excitation power increases (Fig. 4). The crystalline Si substrate, on which *nanopor*-Si was grown, has a quadratic dependence on the excitation power (Fig. 4). At low excitation intensities, the PL intensity of *nanopor*-Si was several times higher than that of its crystalline substrate. We note that the PL intensity dynamics of crystalline Si and *nanopor*-Si was independent of the type of excitation source. Due to the insufficient power of the He–Ne laser, all the measurements for *mesopor*-Si were carried out only with the Cu vapor laser.

The PL lifetime measurements have shown that the *mesopor*-Si and its crystalline substrate are characterized by times shorter than 10^{-7} s. Depending on the emission wavelength, the PL lifetimes of *nanopor*-Si vary from several to several tens of microseconds and are 10^{-5} s at the spectrum peak. The PL lifetime in the

studied samples of lightly doped crystalline Si was 2×10^{-5} s.

DISCUSSION

The shift of the PL spectrum peak in *nanopor*-Si by 0.4 eV to higher energies and the rather small (0.04 eV) shift of *mesopor*-Si with respect to the PL peak position of crystalline silicon (see Fig. 2) are well explained within the model of the quantum-mechanical size effect in silicon nanocrystals [3]. Proceeding from the Raman spectra data (see Fig. 1) on the average sizes and shapes of nanocrystals and using the data of [12], we find the following band gap changes: 0.4–1.0 and 0.04–0.05 eV for *nanopor*-Si and *mesopor*-Si, respectively.

The PL efficiency of *mesopor*-Si is appreciably lower than that of its crystalline substrate (Fig. 2). This fact can be explained by the high rate of nonradiative recombination in *mesopor*-Si, which is caused by defects at its developed surface area (about 100 m²/cm³ [13]) and the rather easy access of free carriers to these defects. The latter is caused by the morphology of *mesopor*-Si. *Nanopor*-Si has an even larger interior surface area (about 600 m²/cm³ [13]). However, due to the localization of carriers in silicon nanocrystals, access to defects is limited, which decreases the probability of nonradiative recombination and enhances the PL intensity of *nanopor*-Si in comparison with its crystalline substrate (see Fig. 2). An additional factor enhancing the PL intensity in *nanopor*-Si may be an increase in the probability of radiative transitions in silicon nanocrystals with small diameters [2, 3].

We now turn to a discussion of the dependence of the PL intensity in the studied samples on the excitation power. Crystalline Si with the resistivity $\rho = 0.015$ Ω cm ($p_0 = 5 \times 10^{18}$ cm^{-3}) has a linear dependence of the PL intensity on the pump power (Fig. 3). This dependence is explained on the basis of the model formulated above [see (1)]. Actually, the linear dependence of the PL corresponds to the condition $n = g\tau \ll p_0$ [see formula (5a)], which, taking into account the short PL lifetimes and the used excitation intensities, is certainly met.

A quadratic dependence of the PL intensity on the excitation power is observed in *mesopor*-Si (Fig. 3). According to the suggested model of recombination in the system of connected nanocrystals, this corresponds to the condition $n = g\tau \gg p_0$ [see (5b)], which can be met when lifetimes are long (10^{-2} s) or when there is a strong decrease of the equilibrium hole concentration. According to our measurements of the PL lifetimes, the latter explanation is valid, assuming a decrease by at least four orders of magnitude in p_0 in *mesopor*-Si. The p_0 decrease is probably caused by the fact that most of the equilibrium holes are captured at dangling Si bonds. As is known, a great number of defects, i.e., dangling Si bonds, arise at the silicon surface in the initial oxidation stage, when a "good" oxide has not yet had time to form [14].

The signal from dangling bonds is pronounced in the ESP spectra of *nanopor*-Si [15, 16]. Our measurements detected no dangling bonds in *mesopor*-Si within the ESR spectrometer sensitivity. According to our estimates, the dangling bond concentration is lower than 10^{15} cm^{-3}, which, being recalculated per unit of the interior surface of *mesopor*-Si, is less than 10^9 cm^{-2}. Such a low density of dangling bonds is inconsistent with low PL efficiency in *mesopor*-Si. Evidently, the nonradiative recombination in *mesopor*-Si probably proceeds via nonparamagnetic defects. Such centers can arise when a hole is captured by a neutral dangling Si bond at the nanocrystal surface. This leads to a decrease in the equilibrium hole concentration, which conforms to the observed quadratic dependence of the PL intensity in *mesopor*-Si on the excitation power.

As is evident from Fig. 4, the quadratic dependence of the PL intensity on the excitation power is observed for crystalline Si with the resistivity $\rho = 10$ Ω cm ($p_0 = 10^{15}$ cm^{-3}) within a range from 0.1 to 1 W/cm². Taking absorptivity into account, this excitation range corresponds to the generation rate $g = 2.5 \times 10^{20}$–5×10^{21} cm^{-3} s^{-1}. At higher intensities, the tendency to leveling off is observed, which may be caused by heating of the sample or by Auger recombination. Within the recombination model described by Eq. (1), the quadratic dependence of the PL intensity on the pump power corresponds to the condition $n \gg p_0$, from which the average lifetime of nonequilibrium carriers can be estimated. Using the smallest value of g, we obtain $\tau > 10^{-5}$ s. Our measurements yield $\tau = 2 \times 10^{-5}$ s, which conforms well to the conclusions of the model.

The PL intensity of *nanopor*-Si linearly grows with the excitation power (Fig. 4). Since the condition $n \ll p_0$ is not met at the PL times typical of *nanopor*-Si (about 10^{-5} s), the sole explanation of the linearity is the localization of photoexcited carrier pairs in nanoclusters separated from each other. The recombination of such carriers is described by set (6).

CONCLUSION

Based on the comparative study of PL in the *mesopor*-Si and *nanopor*-Si films, as well as in crystalline Si substrates, carrier recombination features in nanostructures with different morphologies were ascertained. For example, the quadratic dependence of *mesopor*-Si PL indicates that a significant fraction of equilibrium carriers are captured by surface dangling bonds. As this takes place, nonequilibrium charges can freely drift over the structure. The linear dependence of the *nanopor*-Si PL intensity can be explained by localization of photoexcited carrier pairs in nanoclusters separated from each other. Thus, based on the dependences of the interband PL intensities on the excitation power, one can assess the degree of carrier localization and the state of the surface in silicon nanostructures.

REFERENCES

1. T. Schmidt, K. Lischka, and W. Zulehner, Phys. Rev. B **45**, 8989 (1992).
2. D. Kovalev, H. Heckler, G. Polisski, and F. Koch, Phys. Status Solidi B **215**, 871 (1999).
3. A. G. Cullis, L. T. Canham, and P. D. J. Calcott, J. Appl. Phys. **82**, 909 (1997).
4. O. Bisi, S. Ossicini, and L. Pavesi, Surf. Sci. Rep. **38**, 1 (2000).
5. W. Theis, Surf. Sci. Rep. **29**, 91 (1997).
6. L. Pavesi, Riv. Nuovo Chimento **20**, 1 (1997).
7. L. Tsybeskov, K. L. Moore, D. G. Hall, and P. M. Fauchet, Phys. Rev. B **54**, R8361 (1996).
8. G. Mauckner, J. Hamann, W. Rebitzer, *et al.*, Mater. Res. Soc. Symp. Proc. **358**, 489 (1995).
9. P. K. Kashkarov, B. V. Kamenev, E. A. Konstantinova, *et al.*, Usp. Fiz. Nauk **168**, 577 (1998) [Phys. Usp. **41**, 511 (1998)].
10. I. H. Cambell and P. M. Fauchet, Solid State Commun. **58**, 739 (1986).
11. V. I. Gavrilenko, A. M. Grekhov, D. V. Korbutyak, and V. G. Litovchenko, *Optical Properties of Semiconductors* (Naukova Dumka, Kiev, 1987).
12. Y. M. Niquet, C. Delerue, A. Allan, and M. Lannoo, Phys. Rev. B **62**, 5109 (2000).
13. G. Bomchil, A. Halimaoi, and R. Herino, Appl. Surf. Sci. **41/42**, 604 (1989).
14. V. F. Kiselev and O. V. Krylov, *Electronic Processes in Adsorption and Catalysis on Semiconductors and Insulators* (Nauka, Moscow, 1979).
15. E. A. Konstantinova, P. K. Kashkarov, and V. Yu. Timoshenko, Phys. Low-Dimens. Struct. **12**, 127 (1996).
16. H. J. Bardeleben, D. Stievenard, A. Grosman, *et al.*, Phys. Rev. B **47**, 10899 (1993).

Translated by A. Kazantsev

<div align="center">

**AMORPHOUS, VITREOUS,
AND POROUS SEMICONDUCTORS**

</div>

Changes in Properties of a ⟨Porous Silicon⟩/Silicon System during Gradual Etching off of the Porous Silicon Layer

**E. F. Venger*, T. Ya. Gorbach, S. I. Kirillova,
V. E. Primachenko, and V. A. Chernobaĭ**

Institute of Semiconductor Physics, National Academy of Sciences of Ukraine, Kiev, 03028 Ukraine

* e-mail: mickle@semicond.kiev.ua

Submitted April 9, 2001; accepted for publication August 29, 2001

Abstract—Scanning electron microscopy has shown etching of a porous silicon layer in an HF solution to be irregular. The intensity of porous silicon photoluminescence significantly decreases during gradual etching off, and its peak initially shifts to shorter and then to longer wavelengths. Under red-light pulse excitation, photovoltage measurements have shown that the boundary potential φ_s of the p-Si substrate is positive, and φ_s grows with the etching time and as the temperature decreases from 300 to 200 K. At $T < 230$ K, the photomemory of φ_s caused by nonequilibrium electron capture by p-Si boundary traps is observed. The concentration of shallow traps and boundary electron states in p-Si increases as porous silicon is etched. At $T < 180$ K, the system of boundary electron states is rearranged. Photovoltage measurements with white-light pulses have revealed electron capture at oxide traps of aged porous silicon. © 2002 MAIK "Nauka/Interperiodica".

INTRODUCTION

Detection of porous silicon (*por*-Si) emission in the visible range of the spectrum (see [1]) stimulated extensive studies on its technical characteristics, as well as its structural, optical, electric, and photoelectric properties using various methods [2, 3]. Currently, it is generally believed that this emission is caused by silicon nanocrystals contained in *por*-Si, in which the band gap and the probability of radiative recombination of electron–hole pairs increase due to the quantum-mechanical size effect [2].

The small size of *por*-Si nanocrystals and the significant total area of their surface causes a high sensitivity of *por*-Si properties to the environment. In particular, the spectral dependence of the *por*-Si photoluminescence (PL) and the PL intensity vary when an environment is changed and in the course of *por*-Si aging in air [4–9]. During the latter process, the hydrogen coating (Si–H$_x$) of silicon nanocrystals in *por*-Si produced in HF solutions is changed to an oxide coating (Si–O$_y$) also containing hydroxyl groups, carbon compounds, as well as fluorine, chlorine, and nitrogen traces [4, 7, 10].

This study is devoted to an aged *por*-Si/*p*-Si system, as well as to changes of its properties in the course of gradual etching off of the *por*-Si layer in an HF solution. We measured spectral dependences of *por*-Si photoluminescence (PL), as well as the temperature dependences of the *por*-Si/*p*-Si photovoltage. The *por*-Si surface morphology in the course of etching was monitored using a scanning electron microscope.

Infrared transmission spectra of the *por*-Si/*p*-Si system, aged and treated in an HF solution for 20 s, were also studied. We note that etching of the aged *por*-Si/*p*-Si system in HF is interesting, because it provides new data on this system; this etching is also used to diminish the *por*-Si nanocrystal sizes [2, 8] and to achieve optimum current–voltage characteristics of the metal–*por*-Si–*p*-Si system with the aim of increasing its electroluminescence efficiency [11].

EXPERIMENTAL

The *por*-Si/*p*-Si structures were produced by anodic etching of *p*-Si samples ($\rho = 10\ \Omega$ cm) with the surface orientation (100) in a solution of HF (48%) : C$_2$H$_5$OH : H$_2$O = 1 : 2 : 1 at the current density of 20 mA/cm^2. The porous layer thickness was about 5 μm. At first, we studied the *por*-Si/*p*-Si structures aged in air for more than three years. Then, the studies were carried out after sequential etchings of the *por*-Si layer in an HF : H$_2$O = 1 : 1 solution within 5, 10, 15, 30, and 180 s. Thus, the total etching times, after which the measurements were carried out, were 5, 15, 30, 60, and 240 s. After each etching, the samples were rinsed in distilled water and dried in a desiccator at 50°C for 10 min. Then, the PL spectra and the temperature dependences of photovoltage were sequentially measured, after which the *por*-Si surface was examined using a scanning electron microscope (SEM). All the measurements after each etching were carried out within a day, after which the next etching was carried out.

The PL spectra were measured using conventional optical instrumentation with excitation by the light of an argon laser (514.5 nm) with a flux density of 25 mW/cm^2. To measure the photovoltage arising in the *por*-Si/*p*-Si

structure, a capacitor consisting of a semitransparent conducting SnO_2:Sb layer on mica and a *por*-Si/*p*-Si structure was constructed. The photovoltage signal was measured using a storage oscilloscope, with the capacitor being exposed to the light pulse of an ISSh-100 flash lamp for a duration of 10 μs and with an intensity of 10^{21} photon/cm^2 s^1. To determine the structure photovoltage V_{ph}, the signal measured by the oscilloscope was multiplied by the calibration coefficient of the measuring circuit, which was found using a calibration electric pulse. The photovoltage V_{ph} was measured in a cryostat in vacuum (10^{-4} Pa) as the temperature was lowered from 300 to 100 K. The dependences $V_{ph}(T)$ were measured with the *por*-Si/*p*-Si structure exposed to white and red-light pulses. In the latter case, we used a KS-19 optical filter transmitting light with wavelengths of 700–2700 nm, which excludes light absorption in the *por*-Si layer [12, 13].

At T < 230 K, the photovoltages V_{ph} measured at the first pulse of both white and red light differed from the V_{ph} measured at the second or any following pulse (the repetition frequency was 1 Hz). This is caused by nonequilibrium carrier capture by interfacial traps in the *por*-Si/*p*-Si structure during the first light pulse. The traps were already filled by carriers during the first pulse [14]. The time of captured charge retention in traps was significantly longer (to a few hours) at low temperatures. Therefore, the *por*-Si/*p*-Si structure was warmed after each measurement up to the temperature at which traps were freed from captured carriers and then it was cooled again in the dark to the temperature of the new measurements of the first and second values of V_{ph}.

RESULTS AND DISCUSSION

The *por*-Si visible PL band represents a superposition of emissions arising due to recombination of electron–hole pairs forming excitons [8]. These pairs are excited in nanocrystals of various sizes; therefore, the PL band is wide and its maximum can be at various wavelengths of the visible spectrum depending on the technical characteristics of *por*-Si and the environment [2–4].

Figure 1 shows the PL spectra of the initial aged *por*-Si/*p*-Si structure (curve *1*) and also after *por*-Si etching for 5, 15, 30, and 60 s (curves *2*, *3*, *4*, and *5*, respectively). After a 240-s etching, PL disappeared. One can see that the PL intensity significantly decreases as a result of gradual *por*-Si etching. The PL band peak initially shifts to shorter wavelengths and then to longer wavelengths. The PL band peak position for curves *1–5* corresponds to the quantum energies of 1.68, 1.75, 1.83, 1.80, and 1.72 eV with the FWHM remaining virtually unchanged (0.31 ± 0.01 eV).

The PL intensity decrease under treatments in HF : H_2O is caused by gradual etching of luminescent *por*-Si nanocrystals. The PL band-peak shift to shorter wave-
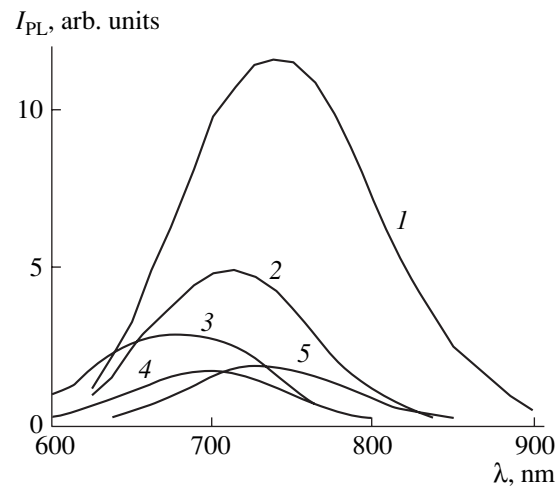

Fig. 1. Spectral distributions of the *por*-Si/*p*-Si PL intensity I_{PL} for (*1*) the initial aged structure and (*2–5*) the same structure after *por*-Si layer etching for 5, 15, 30, and 60 s, respectively. The values I_{PL} for curves *2–5* are increased by the factors 5, 50, 50, and 100, respectively.

lengths as a result of etching during 5 and 20 s is caused by changing the oxide coating of nanocrystals to a hydrogen coating Si–H_x [4, 8]. According to [4], such a coating in small nanocrystals (smaller than 3 nm) increases the energy of emitted light quanta due to the disappearance of Si–O bonds, which capture the electrons of excitons (or both electrons and holes of excitons as nanocrystal sizes decrease), thus lowering the emitted quanta energy. Actually, our study of infrared absorption showed strong absorption in the range of stretching and bending vibrations of Si-H_x bonds after a 20-s etching of the aged *por*-Si/*p*-Si structure, while absorption in the range of Si–O bonds significantly weakened. A small number of Si–O bonds probably arise within 10 min of the structure's exposure to air after etching before measurements [4].

The reverse shift of the PL band maximum to longer wavelengths after 30- and 60-s etchings may be attributed to a decrease in the number of small (smaller than 3 nm) nanocrystals in the *por*-Si layer at long etching times. Emission from these nanocrystals contributes to the short-wavelength component of the PL band. As is known [7], the etched first outer part of the *por*-Si layer has a higher porosity; i.e., it contains smaller nanocrystals in comparison with those arranged closer to the *por*-Si/*p*-Si interface.

Figure 2 displays the SEM micrographs of the initial surface of the aged *por*-Si/*p*-Si structure (a) and the surfaces after etching for 5 (b), 20 (c), and 240 s (d). One can see that the initial surface is not structured, is smooth or slightly spotty, and does not exhibit nanometer-scale morphology due to insufficient resolution of the SEM. After a 5-s etching, channels 1–2 μm wide arise, separating unstructured surface areas with widths and lengths varied within 2–15 μm (Fig. 2b). The areas
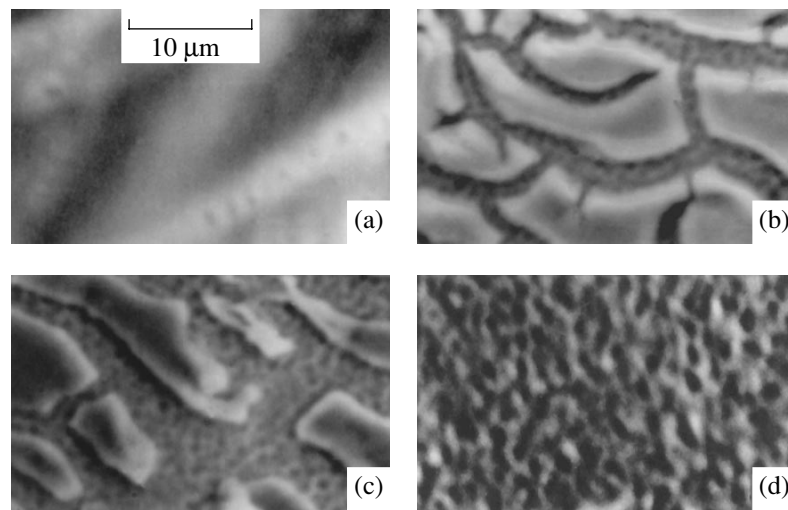
Fig. 2. SEM micrographs of the *por*-Si/*p*-Si structure: (a) the initial surface and (b–d) the surface after etching for 5, 15, and 240 s, respectively.

of extended channels and unstructured areas are almost equal in the micrograph after a 20-s etching (Fig. 2c), when the PL band peak is most shifted to shorter wavelengths. One can readily see that the channels consist of structural units the sizes of which are smaller than a micrometer. Finally, after a 240-s etching, when PL totally disappears, there are no unstructured *por*-Si areas, while the structured *p*-Si substrate surface is observed with structural units of size 0.5–2 μ (Fig. 2d).

Thus, it is evident from Fig. 2 that etching of the *por*-Si layer in an HF solution is nonuniform over the surface. There are areas where etching is faster, thus forming channels separated from *p*-Si even after a 5-s etching. These channels extend with increasing etching

duration, which indicates that etching can be both frontal (this confirms the PL band peak shift to longer wavelengths after 30-s etching) and lateral from the side of channels. Since the silicon etching rate in HF solutions is extremely low (4×10^{-8} nm/min [15]), the *por*-Si layer is etched due to dissolution of silicon oxide, which separates silicon nanocrystals. Therefore, nanocrystals responsible for PL gradually migrate to the HF solution or are washed off by water during subsequent rinsing. Etching of the entire *por*-Si layer indicates that it consists of nanocrystals or areas of silicon fibers of nanometer thickness, separated from the silicon substrate by an oxide layer. Certainly, silicon nanostructures are somewhat oxidized during measurements of the *por*-Si/*p*-Si system parameters within a 24-h interval between etching stages. However, this oxidation is insufficient [16] to separate the nanostructures from the *p*-Si substrate. Isolation of the silicon nanostructures is also confirmed by the photovoltage data.
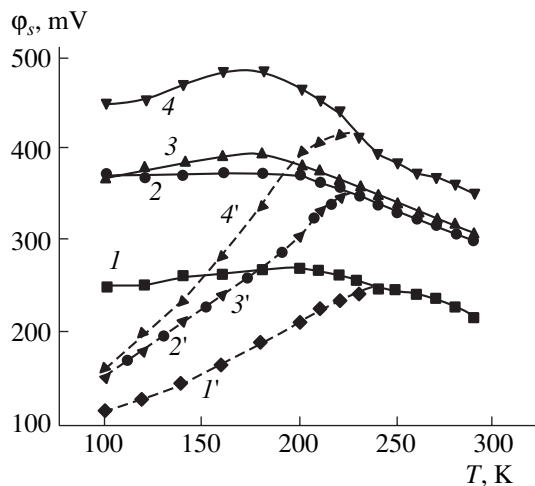
Figure 3 displays the temperature dependences of the interface potential φ_s of the *p*-Si substrate in the initial aged *por*-Si/*p*-Si structure (curves *1*, *1*') and after its etching for 5 (curves *2*, *2*'), 60 (*3* and *3*'), and 240 s (*4* and *4*'). Curves *1–4* and *1'–4*' correspond to exposure to the first and second (or any recurring) red-light pulses, respectively. The values of φ_s (always positive, which corresponds to a downward bending of energy bands) are equal (with an opposite sign) to the photovoltage V_{ph} measured when the *por*-Si/*p*-Si structure was exposed to red light. The high intensity of light absorbed only in *p*-Si allows one to flatten its energy bands at the interface and to determine the interfacial potential φ_s. We note that the Dember photovoltage contribution to V_{ph} is insignificant due to equalization of the diffusivities of electrons and holes due to mutual scattering of carriers at their high concentration [17].

Fig. 3. Temperature dependences of the *p*-Si interfacial potential φ_s of the initial aged *por*-Si/*p*-Si structure (curves *1* and *1*') and after its etching for 5 (curves *2*, *2*'), 60 (*3*, *3*'), and 240 s (*4*, *4*'). Curves *1–4* and *1'–4*' were plotted for the first and second red-light pulses, respectively.

One can see from Fig. 3 that the $\varphi_s(T)$ curves shift to the region of greater depletion of the subsurface region by p-Si holes as the layer is etched, which is caused by positive charging of the p-Si interfacial electron states (IESs) after treatments in HF [14]. At etching times of 15 and 30 s, the curves $\varphi_s(T)$ almost coincide with curves *2* and *3*; therefore, these curves are not shown in Fig. 3. The $\varphi_s(T)$ growth as the temperature decreases in curves *1–4* is related to the IESs filling with holes as the Fermi level shifts to the p-Si valence band. The φ_s decrease in curves *1–4* at $T \lesssim 180$ K is caused by rearrangement of the IES system due to reversible structural changes at the silicon–⟨surface film (por-Si or SiH$_x$O$_y$)⟩ interface as the temperature varies [18]. In the regions of φ_s growth as the temperature decreases (see curves *1–4*) and when the IES system is not rearranged, the BES density can be calculated in the p-Si band-gap region scanned by the Fermi level shift [19]. It turned out that the IES density near the midgap of the p-Si substrate is 7×10^{11} cm^{-2} eV^{-1} for the initial aged por-Si/p-Si structure, 8×10^{11} cm^{-2} eV^{-1} after etching for 5–60 s, and above 10^{12} cm^{-2} eV^{-1} after etching for 240 s. Thus, gradual etching off of the por-Si layer leads to a certain increase in the IES density.

Dependences *1–4* (Fig. 3) and *1'–4'* begin to differ at $T < 230$ K, which is caused by the capture of nonequilibrium electrons by p-Si interfacial traps filled with electrons even within exposure to the first light pulse. This maintains the photomemory of φ_s, defined as the difference between the values of φ_s for dependences *1–4* and *1'–4'* at a certain temperature.

Figure 4 displays the temperature dependences (calculated as in [20]) of the number $N(T)$ of electrons captured by interfacial traps for the initial aged por-Si/p-Si structure (curve *1*), as well as for the structures etched for 5 (curve *2*) and 240 s (curve *3*). Since the traps are filled with electrons even during the first light pulse, the dependences $N(T)$ also represent the temperature dependences of the trap concentrations. The N growth as the temperature decreases is related to participation of progressively shallower (arranged closer to the conduction band) traps in the capture and retention of electrons. One can see from Fig.4 that the concentration of shallow traps somewhat grows as the por-Si layer is etched off.

The temperature dependences of the photovoltage of por-Si/p-Si structure were also studied using white-light pulses. Previously [21], significantly differing results were obtained with white- and red-light pulses when studying the photovoltage of as-prepared and aged por-Si/p-Si structures, in which the por-Si layer was grown by chemical etching, rather than electrochemical etching. For white light also absorbed in the por-Si layer, the following special features were observed [21].

(i) Origination of the photovoltage in the por-Si layer (due to a built-in electric field), opposite in sign to
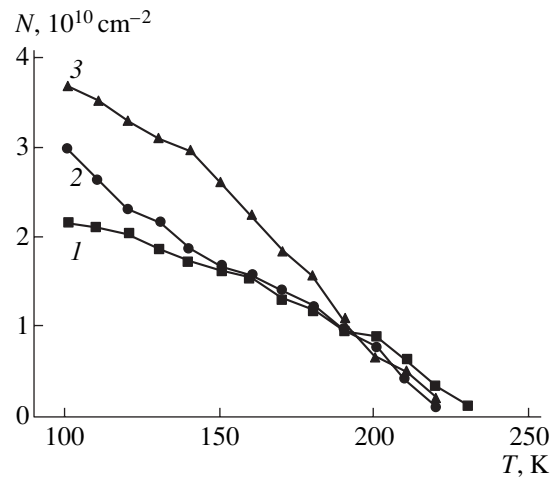

Fig. 4. Temperature dependences of the concentration N of electrons captured by traps of the por-Si/p-Si interface: (*1*) the initial structure and (*2*, *3*) after etching for 5 and 240 s, respectively.

the photovoltage induced in the subsurface depleted p-Si layer and comparable in magnitude.

(ii) Capture of nonequilibrium holes at the por-Si nanocrystal surface during exposure to the first pulse of white light.

(iii) Capture of nonequilibrium electrons by por-Si oxide traps, observed only with aged por-Si/p-Si structures exposed to a train of white-light pulses.

In this study, only the phenomenon described in (iii) was observed when the por-Si/p-Si structure was exposed to white light. When the initial aged structure was irradiated, the interfacial potential φ_s of the silicon substrate gradually decreased as the number of illuminating pulses grew (more than twofold after 300 pulses). We note that the value of φ_s was equal (with an opposite sign) to the photovoltage V_{ph}, which was identical for white and red light. The φ_s decrease is related to charging the por-Si oxide traps by electrons (the so-called optical charging of insulator traps IT$^-$ [22]). This charging IT$^-$ significantly reduced as the measurement temperature was lowered, and it was enhanced at 290 K on irradiation in air. The retention time of a captured electron charge in por-Si oxide traps was on the order of 10^4 s. Removal of a significant fraction of por-Si oxide by etching within 5 s eliminates the optical charging IT$^-$, and φ_s is unchanged with a train of white-light pulses. There was no difference between the photovoltages V_{ph} and their temperature dependences determined under exposure to the red- and white-light pulses after all other subsequent etchings of the por-Si layer.

The absence of differences between the measured photovoltages induced by white and red light in the por-Si/p-Si structure produced by anodic etching indicates that no appreciable signal of the photovoltage arises in the por-Si layer itself. There was also no signal with certain variations of the anodic etching and aging

conditions [23]. On the other hand (see above), a photovoltage signal was formed in the *por*-Si layer in the *por*-Si/*p*-Si structures produced by chemical etching, where hole capture at the silicon nanostructure surface was also observed [21]. We believe that the different properties of the *por*-Si layers produced by the two methods are caused by their structural features.

As the high-resolution transmission electron microscopy data [24] show, the *por*-Si layers produced by anodic etching consist of separated silicon nanocrystals. Most of them are randomly distributed in the *por*-Si layer; the others are incorporated into filamentary formations originating at the silicon substrate hillocks spaced 0.5 μm to a few micrometers from each other (these hillocks probably emerge after etching of the *por*-Si layer (see Fig. 2)). The photovoltage of electron–hole pairs in the *por*-Si layer, which would be comparable to the photovoltage in *por*-Si, cannot arise (even under a relatively weak electric field built in *por*-Si) in separated nanocrystals when excited by a short-wavelength component of the white-light pulse. The reason is that spatial separation of electrons and holes in the *por*-Si layer is hampered. For the same reason, we did not detect the capture of holes at the silicon nanocrystal surface.

The previously observed [21] significant photovoltage and hole capture in the *por*-Si layer produced by chemical etching are obviously caused by rather extended filamentary silicon formations in such *por*-Si structures, with these formations being connected to the substrate. Spatial separation of electron–hole pairs is possible in such filamentary structures, which leads to the origination of photovoltage and to hole capture effects.

CONCLUSION

(I) Gradual etching off (in an aqueous HF solution) of the *por*-Si layer of the aged *por*-Si/*p*-Si structure produced by anodic etching has shown that the PL band maximum initially shifts to shorter wavelengths and then to longer wavelengths with a significant decrease in the PL intensity. These shifts are caused, respectively, by the replacement of the oxide coating of silicon nanocrystals in *por*-Si with a hydrogen coating and by the etching of progressively shallower nanocrystals contained mostly in the upper *por*-Si layers away from the *p*-Si substrate.

(II) The SEM studies have shown the *por*-Si etching to be nonuniform. Aside from etch off of the upper layer, the *por*-Si layer in some places was etched down to the *p*-Si substrate even after the beginning of etching. This process formed characteristic channels that extended with time due to lateral etching off of the *por*-Si layer. Total etching off of the *por*-Si layer (which leads to the disappearance of PL) uncovers a substrate surface with a micrometer-scale relief.

(III) The photovoltage studies of the *por*-Si/*p*-Si structure exposed to red-light pulses has shown that the substrate interfacial potential φ_s is positive (hole depletion of the *p*-Si subsurface region) and the values of φ_s increase as the *por*-Si layer is gradually etched off. The values of φ_s also increase as the temperature decreases to 200 K due to the charging of the interfacial electron states (IESs) by holes. These values then level off and somewhat decrease due to rearrangement of the IES system. At T < 230 K, the φ_s photomemory arises, which is explained by capture of nonequilibrium electrons by interfacial traps. The calculations show that the shallow trap and IES concentrations near the *p*-Si midgap somewhat increase during the gradual etching off of the *por*-Si layer.

(IV) Exposure of the aged *por*-Si/*p*-Si structure to a train of white-light pulses causes capture of electrons by *por*-Si oxide traps. The time of retention of a captured electron charge is about 10^4 s. Even a 5-s etching of the *por*-Si/*p*-Si structure leads to the disappearance of the oxide traps, and the photovoltage signals under exposure to the white and red light are equal in the entire temperature range of 100–300 K. Since the photovoltage signals from white- and red-light pulses considerably differed for the *por*-Si/*p*-Si systems produced by chemical and electrochemical etching, it was concluded that these *por*-Si structures differed significantly.

REFERENCES

1. L. T. Canham, Appl. Phys. Lett. **57**, 1046 (1990).
2. M. S. Bresler and I. N. Yassievich, Fiz. Tekh. Poluprovodn. (St. Petersburg) **27**, 871 (1993) [Semiconductors **27**, 475 (1993)].
3. S. V. Svechnikov, A. V. Sachenko, G. A. Sukach, *et al.*, Optoélektron. Poluprovodn. Tekh., No. 27, 3 (1994).
4. M. V. Wolkin, J. Jorne, P. M. Fauchet, *et al.,* Phys. Rev. Lett. **82**, 197 (1999).
5. V. F. Agekyan, A. M. Aprelev, R. Laiho, and Yu. A. Stepanov, Fiz. Tverd. Tela (St. Petersburg) **42**, 1393 (2000) [Phys. Solid State **42**, 1431 (2000)].
6. N. E. Korsunskaya, T. V. Torchinskaya, B. R. Dzhumaev, *et al.*, Fiz. Tekh. Poluprovodn. (St. Petersburg) **31**, 908 (1997) [Semiconductors **31**, 773 (1997)].
7. L. A. Balagurov, V. F. Pavlov, E. A. Petrova, and G. P. Boronina, Fiz. Tekh. Poluprovodn. (St. Petersburg) **31**, 957 (1997) [Semiconductors **31**, 815 (1997)].
8. P. K. Kashkarov, B. V. Kamenev, E. A. Konstantinova, *et al.*, Usp. Fiz. Nauk **168**, 577 (1998) [Phys. Usp. **41**, 511 (1998)].
9. V. A. Karavanskiĭ, A. A. Lomov, E. V. Rakova, *et al.*, Poverkhnost, No. 12, 32 (1999).
10. P. V. Galiĭ, Ukr. Fiz. Zh. **45**, 985 (2000).
11. T. Ya. Gorbach, S. V. Svechnikov, P. S. Smertenko, *et al.*, Fiz. Tekh. Poluprovodn. (St. Petersburg) **31**, 1414 (1997) [Semiconductors **31**, 1221 (1997)].
12. F. P. Romstad and E. Veje, Phys. Rev. B **55**, 5220 (1997).

13. L. Burstein, Y. Shapira, J. Partee, *et al.*, Phys. Rev. B **55**, R1930 (1997).

14. V. E. Primachenko and O. V. Snitko, *Physics of Semiconductor Surface Doped with Metals* (Naukova Dumka, Kiev, 1988).

15. G. Wilieke and K. Kellermann, Semicond. Sci. Technol. **11**, 415 (1996).

16. H. Angermann, W. Henrion, M. Rebien, *et al.*, Thin Solid Films **313/314**, 552 (1998).

17. Z. S. Gribnikov and V. I. Mel'nikov, Fiz. Tekh. Poluprovodn. (Leningrad) **2**, 1352 (1968) [Sov. Phys. Semicond. **2**, 1133 (1969)].

18. S. I. Kirillova, V. E. Primachenko, V. A. Chernobaĭ, and O. V. Snitko, Poverkhnost, No. 11, 74 (1991).

19. E. F. Venger, S. I. Kirillova, V. E. Primachenko, and V. A. Chernobaĭ, Ukr. Fiz. Zh. **42**, 1333 (1997).

20. S. I. Kirillova, V. E. Primachenko, and V. A. Chernobaĭ, Optoélektron. Poluprovodn. Tekh., No. 21, 60 (1991).

21. E. F. Venger, É. B. Kaganovich, S. I. Kirillova, *et al.*, Fiz. Tekh. Poluprovodn. (St. Petersburg) **33**, 1330 (1999) [Semiconductors **33**, 1202 (1999)].

22. V. F. Kiselev, S. N. Kozlov, and A. V. Zoteev, *Foundations of the Solid Surface Physics* (Mosk. Gos. Univ., Moscow, 1999).

23. B. M. Bulakh, E. F. Venger, É. B. Kaganovich, *et al.*, Ukr. Fiz. Zh. **45**, 1083 (2000).

24. A. Nakajima, Y. Ohsima, T. Itakura, and Y. Goto, Appl. Phys. Lett. **62**, 2631 (1993).

Translated by A. Kazantsev

Carrier Transport in Porous Silicon

N. S. Averkiev, L. P. Kazakova*, and N. N. Smirnova

Ioffe Physicotechnical Institute, Russian Academy of Sciences, St. Petersburg, 194021 Russia
* e-mail: kazakova@pop.ioffe.rssi.ru
Submitted August 2, 2001; accepted for publication August 29, 2001

Abstract—Carrier transport in porous silicon layers has been studied by the time-of-flight method in the strong injection mode at temperatures $T = 290–350$ K and electric field strengths $F = (1.5–7) \times 10^4$ V cm^{-1}. The electron and hole drift mobilities $\mu_e \approx 2 \times 10^{-3}$ cm^2 V^{-1} s^{-1} and $\mu_h \approx 6 \times 10^{-4}$ cm^2 V^{-1} s^{-1} were obtained at $T = 292$ K and $F = 4 \times 10^4$ V cm^{-1}. An exponential temperature dependence of drift mobility with activation energy of ~0.38 and ~0.41 eV for, respectively, electrons and holes was established. It is shown that the type of time dependences of the photocurrent associated with carrier drift and the superlinear dependence of the transit time on the reciprocal of the voltage applied to a sample allow use of the concept of space-charge-limited currents under the conditions of anomalous dispersive transport. The experimental data are accounted for in terms of the model of transport controlled by carrier trapping into localized states with energy distribution near the conduction and valence band edges described by an exponential function with a characteristic energy of ~0.03 eV. © 2002 MAIK "Nauka/Interperiodica".

Porous silicon (PS) attracts the attention of numerous researchers owing to the possibility of developing on its basis a wide variety of devices, including those for optoelectronics. Photoresistors, solar cells, and light-emitting diodes have already been created [1–3]. Despite the numerous successful technological studies aimed at improving the quality of the PS material [4–6], a sufficiently high quantum efficiency of electroluminescence has not be obtained as yet (the presently achieved value is ~0.1% [2, 3, 6]). To find ways to raise the quantum efficiency of electroluminescence, knowledge of the fundamental aspects of carrier motion in an electric field is required. A PS used to create optoelectronic devices is prepared from both *p*- and *n*-type silicon [3, 6]. However, until recently, most attention has been given to investigations of carrier transport in PS obtained from *p*-type silicon [7–9]. In this connection, the present study is concerned with carrier transport in PS prepared from *n*-type silicon at electric field strengths $F = (1.5–7) \times 10^4$ cm^2 V^{-1} s^{-1} and temperatures $T = 290–350$ K.

SAMPLE FABRICATION TECHNOLOGY AND MEASUREMENT TECHNIQUE

Porous silicon layers were obtained electrochemically on an *n*-type material with the resistivity $\rho = 1$ Ω cm and the (111) orientation. Preliminarily, the surface of the starting material was mechanically polished. Prior to anodizing, samples were thoroughly degreased and then washed with deionized water. The current density during anodizing was 8 mA cm^{-2}, and the process duration, 25 min. The electrolyte was composed of hydrofluoric acid and isopropanol taken in 1 : 1 ratio. The illumination was done with a 60-W incandescent lamp.

The experimental samples had sandwich configuration. As the top electrode, a semitransparent aluminum layer, with the area $S = 2.3 \times 10^{-2}$ cm^2 and deposited by vacuum evaporation was used. Crystalline silicon served as the bottom contact. The drift mobility was studied by the time-of-flight technique [10]. An excess carrier concentration was created in a sample near the top electrode by means of a light pulse from an ILGI-503 laser (wavelength 0.337 nm, pulse duration 8 ns). A pulsed voltage was applied to the samples, with pulse duration of ~1 ms and a time delay of ~100 μs with respect to the leading edge of the light pulse. The measurements were done in the strong-injection mode, with space-charge-limited current (SCLC) flowing in the sample.

EXPERIMENTAL RESULTS AND DISCUSSION

The investigation demonstrated that the time dependences $I(t)$ of both hole and electron photocurrents have the form of a prolonged structureless current decay (Fig. 1). The current exhibited a quadratic dependence on the voltage U applied to a sample and was independent of the intensity of injecting illumination, indicating the attainment of the SCLC mode [11]. However, the shape of the photocurrent curves was in disagreement with the ideal SCLC behavior characterized by the presence of a peak in the $I(t)$ dependence. In the case of ideal SCLC, the position of the current peak is used to determine the time t_T of carrier transit across the sample, related to the transit time t_0 under conditions of small charge drift in a sample by

$$t_T \approx 0.8 t_0. \tag{1}$$

Since the expression for t_0 has the form

$$t_0 = L^2/\mu U, \qquad (2)$$

where L is the sample thickness and μ is the drift mobility, expression (1) gives the following formula for the drift mobility:

$$\mu = 0.8 L^2/t_T U. \qquad (3)$$

In the present study, t_T was found from $I(t)$ curves plotted in the log–log scale from the instant of time when the quasi-stationary behavior of the current gives way to a steeper decay (Fig. 1). The transit times are shown in Fig. 1 by arrows. For convenience of examining the $I(t)$ dependences, the currents in curves 1, 3, and 4 are multiplied by, respectively, 0.25, 1.5, and 5.

It was shown in [12] that such a shape of transient SCLS without a peak is observable in anomalous dispersive transport [13, 14] occurring under conditions of unattained equilibrium between free carriers and those trapped by localized states. In this case, a strongly spatially spread packet of carriers, which is characterized by mobility dependent on time and, consequently, also on L and U, drifts in a sample. In [12], a model of transport controlled by carrier capture into localized states with energy distribution $g(E)$ described by an exponential function was considered. To simplify the calculation, it was assumed that $g(E) = g_c$ up to a certain energy $E_1 > E > E_c$, beginning with which (at $E > E_1$) the distribution $g(E)$ obeys the exponential law: $g(E) = g_c \exp(-(E - E_1)/kT_0)$, where E is reckoned from the conduction band edge E_c, and kT_0 is the characteristic energy of the exponential distribution. As a result, it was found that the expression for the transit time takes the form

$$t_T^* = t_0(0.78)^{1/\alpha}, \qquad (4)$$

where

$$\alpha = kT/kT_0. \qquad (5)$$

The parameter α varying between 0 and 1 characterizes the degree of transport dispersion. The smaller the value of α, the higher the dispersion (the stronger the spreading of the carrier packet).

Figure 2 presents t_T^* values for electrons and holes in relation to the reciprocal of the applied voltage, obtained from the experimental curves. As seen from the figure, the carrier transit time decreases with increasing U. The dependences obtained can be described by the power function $t_T^* \propto \left(\dfrac{1}{U}\right)^n$. The exponent is ~1.2 for both electrons and holes at $T = 292$ K and decreases to ~1 at $T = 352$ K.

Since $t_0 \propto \left(\dfrac{L}{F}\right)^{1/\alpha}$ under conditions of anomalous dispersive transport [13, 14], then, in accordance with
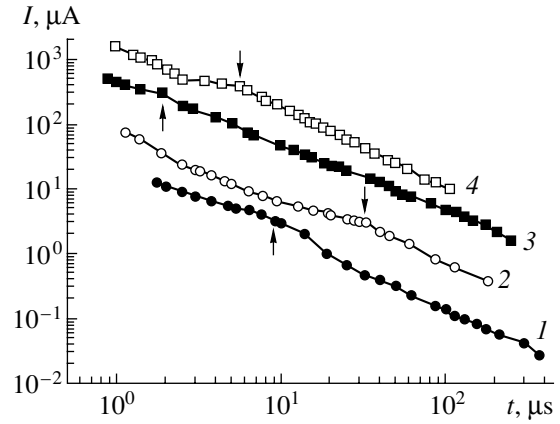

Fig. 1. (1, 3) Electron and (2, 4) hole photocurrents vs. time in a 10-μm-thick PS layer at different temperatures T: (1, 2) 292 and (3, 4) 335 K. Values of the current are multiplied by 0.25, 1.5, and 5 for, respectively, curves 1, 3, and 4.
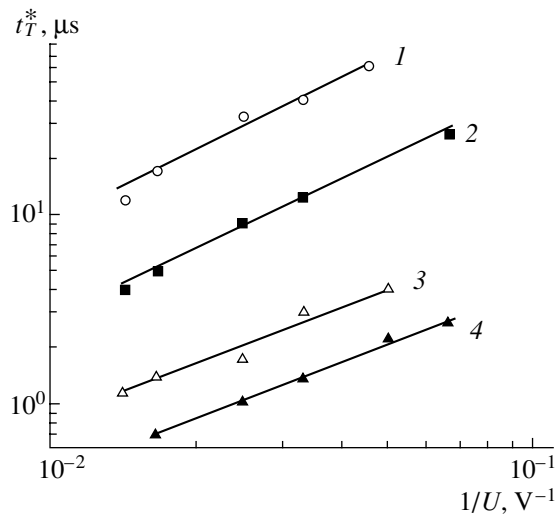

Fig. 2. Transit time for (1, 2) holes and (3, 4) electrons in PS vs. the reciprocal of the applied voltage at different temperatures T: (1, 2) 292 and (3, 4) 352 K. $L = 10\ \mu$m.

(4), $t_T^* \propto \left(\dfrac{1}{U}\right)^{1/\alpha}$. Consequently, $n = 1/\alpha$ and $\alpha \simeq 0.8$ for room temperature and $\alpha \simeq 1$ at $T = 352$ K.

Thus, the result obtained indicates that the dispersion parameter α depends on temperature, in agreement with formula (5), and allows use of the SCLC concept under conditions of anomalous dispersive transport in experimental data analysis. The established room temperature value $\alpha \simeq 0.8$ assumes, in accordance with the transport model in question, an exponential distribution $g(E)$ with characteristic energy $kT_0 \simeq 0.03$ eV, as follows from (5).

It is noteworthy that, at the exponential energy distribution of localized states controlling the transport, the time dependence of the current at $t > t_T^*$ can be
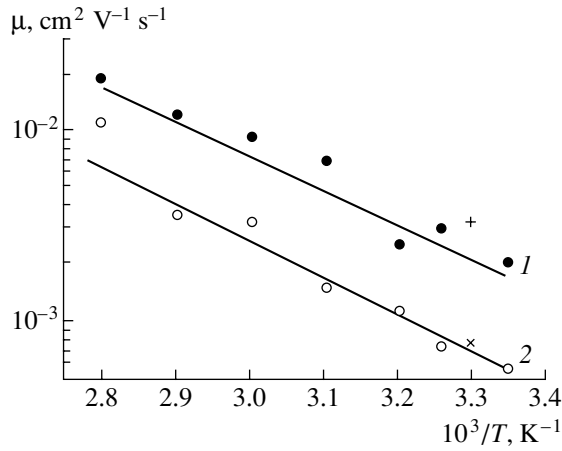
μ, cm^2 V^{-1} s^{-1}

Fig. 3. Drift mobilities of (*1*) electrons and (*2*) holes vs. the reciprocal of temperature in PS. $F = 4 \times 10^4$ V cm^{-1}, $L = 10$ μm. The crosses correspond to mobilities obtained upon the reverse run of the temperature.

described, according to the model under consideration, by the power function

$$I(t) \sim t^{-(1+\alpha_f)},$$

and the parameter α_f must be equal to α, i.e., $\alpha_f = 0.8$ at room temperature, and, consequently, $I(t)|_{t > t_T^*} \propto t^{-1.8}$. However, analysis of experimental data yields values $\alpha_f = 0.1$–0.3, which points to a much higher degree of dispersion than that indicated by the parameter α. To account for such a discrepancy, it is presumably necessary to assume the existence of an additional spreading of the drifting packet, which results from the mobility distribution of carriers, caused by structural heterogeneities in the PS layer [15].

The $I(t)$ dependences with a quasi-plateau portion at $t \leq t_T^*$ are in satisfactory agreement with $I(t)$ calculated in terms of the model under consideration [12]. The reason for the initial fast decay of $I(t)$ remains unclear. It should be noted that the SCLC curves of this kind have been observed in *a*-Si:H [16, 17].

The carrier drift mobility μ was found using formula (4), which differs only slightly from (3) at $\alpha = 0.8$, having 0.73 as the coefficient instead of 0.8. As a result, at room temperature and $F = 4 \times 10^4$ V/cm, the electron mobility $\mu_e \approx 2 \times 10^{-3}$ cm^2 V^{-1} s^{-1} and the hole mobility $\mu_h \approx 6 \times 10^{-4}$ cm^2 V^{-1} s^{-1}.

As is known, the μ value in the SCLC mode can also be determined from the initial current I_0 and the peak current I_m at an instant of time $t = t_T$ [11], which exceeds I_0 by a factor of 2.7 in the case of an ideal SCLC. An analysis [12] of SCLC under conditions of anomalous dispersive transport demonstrated that the peak is virtually indiscernible on the background of the $I(t)$ decay at $\alpha \leq 0.8$, and $I(t_T^*) \leq I_0$ at $\alpha = 0.8$, with the $I_m \approx I_0$ value only insignificantly differing from the corresponding

value for the ideal SCLC. In this connection, the following expression for I_0 was used to evaluate the mobility [11]:

$$I_0/S = \mu\kappa U^2/2.25 \times 10^{13}L^3, \quad \text{A/cm}^2, \qquad (6)$$

where κ is the relative permittivity.

As a rule, it is rather difficult to determine I_0, since its value is masked by the initial peak related to the establishment of an electric field, back diffusion of carriers, and motion of carriers of opposite polarity in the carrier generation region toward the injecting electrode [17]. Therefore, with account taken of the fact that $I(t_T^*) \approx I_0$ at $\alpha = 0.8$, the current at instant of time t_T^* is substituted in formula (6). In doing so, it was assumed that $\kappa = 5$ in accordance with the data of [18]. This gives the values $\mu_e \approx 1.5 \times 10^{-3}$ cm^2 V^{-1} s^{-1} and $\mu_h \approx 3.8 \times 10^{-4}$ cm^2 V^{-1} s^{-1}, which are close to those found from t_T^*. It is noteworthy that the μ_e values obtained here are four times lower, and the μ_h values, an order of magnitude lower, than those found for PS in our previous studies [9, 18]. The established difference in the mobilities can be accounted for by the fact that, in the present study, the samples were subjected to prolonged storage in air, whereas previous measurements were done with freshly prepared samples. It is known that freshly prepared PS contains a large amount of hydrogen, which is displaced from PS, in the course of storage, by atmospheric oxygen [19].

The temperature dependence of the drift mobility was measured by heating samples in a vacuum at a residual pressure of 10^{-2} Torr. Figure 3 presents carrier drift mobilities obtained in the temperature range 292–352 K at $F = 4 \times 10^4$ V/cm.

It follows from the data obtained that the temperature dependence of the electron and hole mobility in PS is of the Arrhenius type. The activation energy of mobility is $\Delta E_e = (0.38 \pm 0.05)$ eV for electrons and $\Delta E_h = (0.41 \pm 0.05)$ eV for holes. It is noteworthy that, in contrast to [9], where the same activation energy was established for μ_h in PS prepared from *p*-type silicon, the measurements in the present study were done with stabilized samples.

The mobilities obtained upon a reverse run of temperature, denoted by crosses in the figure, virtually coincided with the initial values.

In accordance with the model of transport controlled by capture into localized states with energy distribution described by an exponential function, considered here, and in agreement with [13, 20], the expression for the activation energy of mobility can be written as

$$\Delta E = E_1 + kT_0 \ln\left(\frac{L}{\sqrt{2}\mu_0\tau_0 F}\right), \qquad (7)$$

where μ_0 is the mobility of carriers in the allowed band, and τ_0 is their lifetime. Substituting the known values of kT_0, L, and F into (7) and assuming $E_1 = 0.03$ eV, we

obtain ΔE_e and ΔE_h close to the experimentally established values at $\mu_0\tau_0 = 10^{-9}$ cm^2 V^{-1}.

It should be noted that a $\mu_0\tau_0$ value of the same order is characteristic of semiconductors with disordered structure. For example, $\mu_0\tau_0 = 4 \times 10^{-10}$ cm^2 V^{-1} for glassy As$_2$Se$_3$ [14, 21]. This fact suggests a similarity of carrier transport mechanisms in PS and disordered semiconductors. Analysis of the data obtained in the present study admits the existence of allowed band "tails" in the energy gap of PS. A similar conclusion was made in studying photoluminescence in PS [19].

CONCLUSION

Thus, it is shown that the time dependences of transient photocurrent associated with carrier drift in PS can be described in terms of space-charge-limited current under conditions of anomalous dispersive transport.

The carrier drift mobilities and their activation energies are found for electrons and holes: $\mu_e \approx 2 \times 10^{-3}$ cm^2 V^{-1} s^{-1} and $\mu_h \approx 6 \times 10^{-4}$ cm^2 V^{-1} s^{-1} at $T = 292$ K and $F = 4 \times 10^4$ V cm^{-1} and $\Delta E_e = (0.38 \pm 0.05)$ eV and $\Delta E_h = (0.41 \pm 0.05)$ eV at $F = 4 \times 10^{-10}$ V cm^{-1}.

It is shown that the data obtained can be accounted for in terms of the model of transport controlled by carrier capture into localized states whose energy distribution near the valence and conduction band edges is described by an exponential function with a characteristic energy of ~0.03 eV.

REFERENCES

1. L. A. Balagurov, S. C. Bayliss, A. F. Orlov, *et al.*, in *Abstracts of the International Conference "Porous Semiconductors—Science and Technology", Madrid, 2000*, p. 53.

2. A. G. Cullis, L. T. Canham, and P. D. J. Calcott, J. Appl. Phys. **82**, 909 (1997).

3. B. Das and S. P. McGinnis, Semicond. Sci. Technol. **14**, 998 (1999).

4. J. A. Roger, M. G. Blanchin, B. Canut, *et al.*, Semicond. Sci. Technol. **14**, L29 (1999).

5. M. Stewart, E. G. Robins, T. W. Geders, *et al.*, in *Abstracts of the International Conference "Porous Semiconductors—Science and Technology", Madrid, 2000*, p. 31.

6. M. Balucani, V. Bondarenko, G. Lamedica, *et al.*, Appl. Phys. Lett. **74**, 1960 (1999).

7. É. A. Lebedev, G. Polisski, and V. Petrova-Kokh, Fiz. Tekh. Poluprovodn. (St. Petersburg) **30**, 1468 (1996) [Semiconductors **30**, 772 (1996)].

8. E. A. Lebedev, E. A. Smorgonskaya, and G. Polisski, Phys. Rev. B **57**, 14607 (1998).

9. N. S. Averkiev, L. P. Kazakova, É. A. Lebedev, and N. N. Smirnova, Fiz. Tekh. Poluprovodn. (St. Petersburg) **35**, 609 (2001) [Semiconductors **35**, 588 (2001)].

10. W. E. Spear, J. Non-Cryst. Solids **1**, 197 (1969).

11. M. A. Lampert and P. Mark, *Current Injection in Solids* (Academic, New York, 1970; Mir, Moscow, 1973).

12. M. Silver, E. Snow, D. Wesson, and K. Okamoto, J. Non-Cryst. Solids **66**, 237 (1984).

13. A. F. Rudenko and V. I. Arkhipov, Philos. Mag. B **45**, 189 (1982).

14. *Electron Phenomena in Chalcogenide Vitreous Semiconductors*, Ed. by K. D. Tséndin (Nauka, St. Petersburg, 1996).

15. V. I. Arkhipov, É. A. Lebedev, and A. I. Rudenko, Fiz. Tekh. Poluprovodn. (Leningrad) **15**, 712 (1981) [Sov. Phys. Semicond. **15**, 405 (1981)].

16. C. E. Nebel and R. A. Street, Philos. Mag. B **67**, 721 (1993).

17. J. Kočka, O. Klima, E. Šipek, *et al.*, Phys. Rev. B **45**, 6593 (1992).

18. L. P. Kazakova, A. A. Lebedev, and É. A. Lebedev, Fiz. Tekh. Poluprovodn. (St. Petersburg) **31**, 609 (1997) [Semiconductors **31**, 517 (1997)].

19. S. Komuro, T. Kato, T. Morikana, *et al.*, J. Appl. Phys. **80**, 1749 (1996).

20. V. I. Arkhipov, M. S. Iovu, A. I. Rudenko, and S. D. Shutov, Phys. Status Solidi A **54**, 67 (1979).

21. V. I. Arkhipov, L. P. Kazakova, É. A. Lebedev, and A. I. Rudenko, Fiz. Tekh. Poluprovodn. (Leningrad) **21**, 724 (1987) [Sov. Phys. Semicond. **21**, 442 (1987)].

Translated by M. Tagirdzhanov

PHYSICS
OF SEMICONDUCTOR DEVICES

Solar Cells Based on $CuIn_{1-x}Ga_xSe_2$ Films Obtained by Pulsed Laser Evaporation

V. F. Gremenok*, I. V. Bodnar'*, V. Yu. Rud'**, Yu. V. Rud'***, and H.-W. Schock****

* Institute of Solid-State and Semiconductor Physics, Belarussian Academy of Sciences,
ul. Brovki 17, Minsk, 220072 Belarus
** St. Petersburg State Technical University, ul. Politekhnicheskaya 29, St. Petersburg, 195251 Russia
e-mail: rudvas@uniys.hop.stu.neva.ru
*** Ioffe Physicotechnical Institute, Russian Academy of Sciences,
Politekhnicheskaya ul. 26, St. Petersburg, 194021 Russia
**** Institut für Physikalische Elektronik, Universität Stuttgart, D-70569 Stuttgart, Germany
Received May 11, 2001; accepted for publication May 25, 2001

Abstract—Solar cells based on polycrystalline films of $CuIn_{1-x}Ga_xSe_2$ solid solutions were produced for the first time by the pulsed laser evaporation of source targets. The current–voltage characteristics of the cells were investigated, and the main photoelectrical parameters were ascertained. The optimal concentration of gallium ensuring maximal conversion efficiency of the thin-film solar cells and the films of the solid solutions with a chalcopyrite structure were determined. © 2002 MAIK "Nauka/Interperiodica".

INTRODUCTION

In modern engineering of photoconvertors, special attention is being paid to the development of inexpensive and highly efficient thin-film solar cells (TFSCs), which, in the future, are intended to replace single-crystal silicon cells [1–5]. A program aimed at the investigation of TFSCs has already been in progress in the USA and Western Europe for nearly 25 years.

The long-term aim of this program is the development of highly stable TFSCs that feature efficiency higher than 15% and do not require expensive techniques for their manufacturing. It is supposed that modules with an efficiency of 10% and a cost of less than 1 US dollar per watt will provide cost-effective photoelectric power installations that will be appropriate for wide-scale use in public electric utilities. Taking into account the cost of auxiliary equipment and service charges, as well as the overhead, the cost of electric power provided by TFSCs is estimated at 0.13 US dollars per kilowatt hour.

The ternary compounds based on copper, specifically, $CuInSe_2$ and the Cu(In, Ga)Se$_2$ solid solutions, seem to be most promising for the design of highly efficient photocells. These materials are of particular interest in view of the following features [1, 2]: (a) the band gaps fall in the range that is optimal for conversion of solar radiation (E_g = 1.04–1.7 eV); (b) these are the direct gap semiconductors, a fact which in itself allows one to obtain conductivity of either type and, hence, to design photocells of various types; and (c) high optical absorption coefficients within the solar spectral range (up to 3×10^5–6×10^6 cm^{-1}) provide for the complete absorption of radiation in the thin films produced from these materials.

Apart from the fundamental characteristics suitable for the conversion of solar energy, another advantage of the semiconductors mentioned above is that they allow for the manufacture of highly stable devices. Thus, after the continuous operation for 7×10^4 h at a temperature of 60°C under imitator illumination, none of the parameters of the unsealed TFSCs degraded [2], whereas, for the other semiconductor materials, similar life tests have failed. Moreover, the radiation resistance of the devices based on Cu(In, Ga)Se$_2$ is ~50 times as high as that for the Si- or GaAs-based devices [2–4]. It has also been established that the radiation damage produced in TFSCs based on Cu(In, Ga)Se$_2$ can be removed during annealing for 10–15 minutes at temperatures of 200–250°C.

In this paper, we present data on the research and development of solar cells based on films produced by the pulsed laser evaporation of $CuIn_{1-x}Ga_xSe_2$ solid solutions.

EXPERIMENTAL

The targets which were evaporated for the deposition of the films were crystalline $CuIn_{1-x}Ga_xSe_2$ ($0.0 \le x \le 1.0$) solid solutions synthesized and subjected to planar crystallization in a vertical one-zone furnace. Stoichiometrically rationed amounts of highly pure initial components (copper, indium, gallium of V3 grade, and selenium of V5 grade) were loaded into quartz cells, pumped down to the pressure of 10^{-4} Pa, sealed up, and placed into a furnace. During synthesis, the

temperature in the furnace was raised up to 923–973 K at a rate of 50 K/h; then, for homogenization purposes, the melt was subjected to mechanical vibrations for ~2 h. After that, the temperature increased at the same rate up to 1270–1370 K (depending on composition of the solid solution) and the substance was held for ~2 h at the above temperatures. After the holding, the temperature was lowered to 1080–1220 K at a rate of 100 K/h with the vibration switched on and the crystals were homogenized by annealing for 600 h. The resulting ingots were 40 mm long and 14 mm in diameter and had a large-block structure.

Chemical analysis of the composition of the solid solutions showed satisfactory agreement between the experimental and predicted concentrations of elements [6]. The homogeneity of $CuIn_{1-x}Ga_xSe_2$ solid solution ingots grown in this way was established by the X-ray diffraction technique (copper radiation). A chalcopyrite structure was found for the crystallized solid solutions. The parameters of the unit cell vary with the atomic composition of the solid solutions in accordance with Vegard's law.

The system of pulsed laser deposition included a commercial laser of the GOS-1001 type in the free running mode ($\lambda = 1.06$ μm, $\tau_p = 10^{-3}$ s). A glass lens with a focal length of 500 mm focused the beam to the target surface. Laser pulses with an energy of 150–180 J were generated with a repetition rate of 3×10^2 Hz. The deposition of films was performed in a vacuum chamber with a residual pressure of 2×10^{-5} Pa, with the condensation rate amounting to $(2–4) \times 10^5$ Å/s. Chemically cleaned 2.5×4.0-cm glasses of the Corning 7059 type (pure or with the preliminary deposition of a molybdenum layer with a thickness of 1.0–1.2 μm) were used as substrates. The substrate temperature was maintained nearly constant in the range from 790 to 810 K. The resultant $CuIn_{1-x}Ga_xSe_2$ films were between 0.6 and 1.5 μm thick, depending on the conditions of condensation.

Using the laser-deposited films, thin-film polycrystalline solar cells with a glass/Mo/Cu(In, Ga)Se$_2$/CdS/ZnO:Al/Al–Ni structure were constructed according to the scheme shown in Fig. 1. The TFSC manufacturing process involved the following stages [5]: (a) chemical deposition (lasting for ~4 min at a temperature of ~60°C) of up to 50-nm-thick CdS films from the mixture of ammonia NH$_3$ (1 M), cadmium salts CdJ$_2$ or CdSO$_4$ ($1.4 \times 10^{-3}M$), and thiourea NH$_2$CSNH$_2$ ($0.14M$); (b) magnetron sputtering that resulted in the production of an ~1000-nm-thick ZnO:Al film; (c) electrodeposition of the upper Al–Ni collector; and (d) dicing of separate elements with an area up to 0.3 cm^2.

The current–voltage (I–V) characteristics of the TFSCs obtained were measured on exposure to AM-1.5 (100 mW/cm^2) at a temperature of ~25°C in accordance with European standards for testing photoconverters.
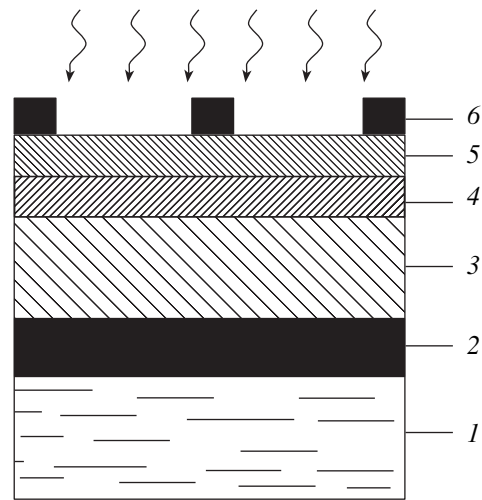

Fig. 1. Schematic representation of the cross section of TFSC based on $CuIn_{1-x}Ga_xSe_2$: (1) glass, (2) molybdenum, (3) $CuIn_{1-x}Ga_xSe_2$, (4) CdS, (5) ZnO:Al, and (6) Al–Ni.
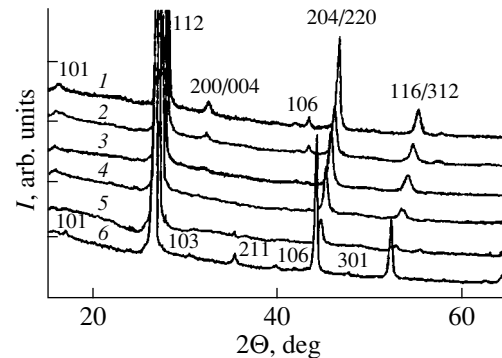

Fig. 2. X-ray diffractogram of the laser-deposited $CuIn_{1-x}Ga_xSe_2$ films ($T = 300$ K). Numbers at the curves stand for the reflection indices.

RESULTS AND DISCUSSION

The X-ray diffractograms of the films from the $CuIn_{1-x}Ga_xSe_2$ solid solutions display a set of lines typical of structures of the chalcopyrite type (Fig. 2) [6–8]. The preferred orientation of the films' texture lies in the (112) plane. The parameters of a unit cell correlate well with those of the crystal target and are linear in x, thus giving more evidence for the identical composition of the source target and the film obtained after target evaporation.

The elemental composition of the films was determined by the X-ray energy dispersion (EDX) method with the use of a JEOL-6400 scanning electron microscope (accuracy of measurements was about ±5%). Typical results are listed in Table 1. A close correlation between the atomic composition of the films and the targets can be seen. It should be specially mentioned that pulsed laser evaporation does not actually affect the content of selenium. This circumstance eliminated
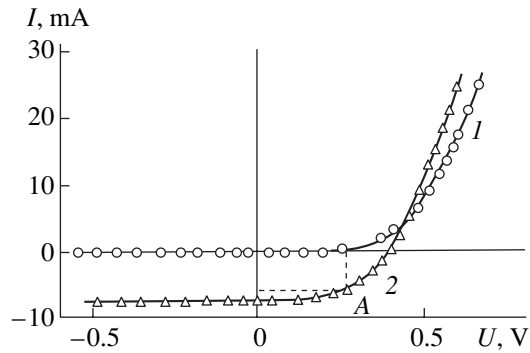
Fig. 3. The I–V characteristics measured (*1*) in the dark and (*2*) under illumination for TFSC based on ZnO/CdS/CuIn$_{1-x}$Ga$_x$Se$_2$. Sample no. 7, $x = 0.16$, cell no. 7–5, AM-1.5 illumination from the side of ZnO, area $S = 0.3$ cm^2, illuminance $L = 100$ mW/cm^2, positive polarity of the external bias corresponds to the CuIn$_{1-x}$Ga$_x$Se$_2$ film, point *A* indicates the mode of the TFSC peak power output.

the need for the thermal treatment of films in selenium vapor—a stage which is commonly used in alternative technologies. Therefore, this study is the first to demonstrate the potential of employing pulsed laser evaporation for the production of homogeneous chalcogenide films based on triple and quadruple semiconductor materials.

All of the TFSC samples obtained were found to feature distinct rectifying properties. For any *x*, the conducting direction corresponds to the positive polarity of the external bias on the *p*-type CuIn$_{1-x}$Ga$_x$Se$_2$ films, which is in accordance with the approximate energy-band diagram for this type of structure. On illumination of a TFSC, the films of the solid solutions become positive, and this is in agreement with the direction of rectification. A typical I–V characteristic is plotted in Fig. 3. It can be seen that illumination of the TFSC sample leads to a downward shift of its I–V characteristic along the current axis and gives rise to crossing of the forward portions of the I–V characteristics measured in the dark and under illumination. This feature may be caused by a decrease in the series resistance of the structure due to the separation of photoinduced nonequilibrium carriers in the electric field of the barrier. However, photoinduced majority carriers also vary the conditions for their own separation in the active region of a TFSC, which may also result in the intersection of the forward I–V characteristics observed for all of the TFSC samples under study.

By way of example, the main parameters measured for the seven cells comprising TFSCs are listed in Table 2. As can be seen from the data presented, the open-circuit voltage U_{oc}, the density of the short-circuit photocurrent j_{sc}, and the filling factor of a load I–V characteristic β are close for different TFSC cells. First and foremost, this is an indication of high local homogeneity of the CuIn$_{1-x}$Ga$_x$Se$_2$ films, which was ensured by the pulse laser evaporation of selenides even of such a complicated atomic composition. This homogeneity turned out to be typical of TFSCs with differing atomic compositions varying in the range of $0 < x < 1$.

The results of testing TFSC produced on the basis of solid solutions with different *x* are listed in Table 3.

Table 1. Composition of CuIn$_{1-x}$Ga$_x$Se$_2$ films

Target	Sample no.	Composition (at. %)			
		Cu	In	Ga	Se
CuInSe$_2$	2	24.98	26.04	0	49.98
CuIn$_{0.8}$Ga$_{0.2}$Se$_2$	7	25.21	21.00	3.89	49.91
CuIn$_{0.8}$Ga$_{0.2}$Se$_2$	8	27.28	20.78	3.79	48.51
CuIn$_{0.6}$Ga$_{0.4}$Se$_2$	5	22.80	15.16	11.06	50.95
CuIn$_{0.6}$Ga$_{0.4}$Se$_2$	6	21.83	15.68	11.50	50.99

Table 2. Parameters of TFSCs based on ZnO/CdS/CdS/CuIn$_{1-x}$Ga$_x$Se$_2$

Cell no.	U_{oc}, mV	I_{sc}, mA/cm^2	β, %	η, %
7–1	435.51	–22.34	53.19	5.17
7–2	433.89	–22.57	55.13	6.40
7–3	419.84	–23.32	51.99	5.09
7–4	409.84	–24.52	51.58	5.18
7–5	409.39	–24.95	53.45	5.48
7–6	406.22	–24.40	54.06	5.36
7–7	404.81	–24.86	51.98	5.23

Table 3. Parameters of TFSCs based on the laser-deposited CuIn$_{1-x}$Ga$_x$Se$_2$ films

Sample no.	x, at. %	U_{oc}, mV	I_{sc}, mA/cm^2	β, %	η, %
2	0	395.5	−23.9	52.5	4.9
7	3.89	409.4	−25.0	53.5	5.5
8	3.79	385.1	−24.2	52.1	4.2
5	11.06	46.3	−5.5	25.4	0.1
6	11.50	168.9	−6.5	29.3	0.3

These data suggest a distinct dependence of the main photoelectric parameters of a TFSC on the content of gallium in a CuIn$_{1-x}$Ga$_x$Se$_2$ solid solution. Peak efficiency of the power conversion η is achieved in TFSCs based on films with $x \approx 4\%$; a further increase in x leads to a noticeable decrease in η.

Thus, the pulsed laser evaporation of crystalline CuIn$_{1-x}$Ga$_x$Se$_2$ solid solutions proved to be a promising technique for the production of highly efficient polycrystalline thin-film solar cells. By choosing the right atomic composition of the solid solution, the TFSC efficiency may be noticeably enhanced.

REFERENCES

1. J. L. Shay and J. H. Wernick, *Ternary Chalcopyrite Semiconductors: Growth, Electronic Properties and Applications* (Pergamon, New York, 1975).
2. *Current Topics in Photovoltaics*, Ed. by T. Coutts and J. Meakin (Academic, London, 1985; Mir, Moscow, 1988).
3. U. Rau and H. W. Schock, Appl. Phys. A **A69**, 131 (1999).
4. L. Kazmerski, Renewable and Sustainable Energy Reviews **1**, 71 (1997).
5. H. W. Schock, Appl. Surf. Sci. **92**, 606 (1996).
6. V. F. Gremenok, E. P. Zaretskaya, I. V. Bodnar, and I. A. Victorov, Cryst. Res. Technol. **31**, 485 (1996).
7. Yu. V. Rud', V. Yu. Rud', I. V. Bodnar, and V. F. Gremenok, Fiz. Tekh. Poluprovodn. (St. Petersburg) **32**, 385 (1998) [Semiconductors **32**, 343 (1998)].
8. Yu. V. Rud', V. Yu. Rud', V. F. Gremenok, *et al.*, Solid State Phenom. **67–68**, 415 (1999).

Translated by A. Sidorova-Biryukova

Analysis of Threshold Current Density and Optical Gain in InGaAsP Quantum Well Lasers

N. A. Pikhtin, S. O. Sliptchenko, Z. N. Sokolova, and I. S. Tarasov

Ioffe Physicotechnical Institute, Russian Academy of Sciences, St. Petersburg, 194021 Russia

Submitted August 2, 2001; accepted for publication August 29, 2001

Abstract—Single-mode and multimode quantum well (QW) laser diodes with emission wavelengths $\lambda = 1.0$ and 1.58 μm, based on MOCVD-grown separate-confinement heterostructures, have been studied. An analysis of the threshold current density and optical gain is made on the basis of experimental dependences of the threshold current and differential quantum efficiency on the cavity length. The threshold current is decomposed into principal components in terms of model approximations taking into account the Auger recombination, ejection of electrons from QWs into waveguide layers, and lateral current spreading to passive regions of a mesa-stripe laser. © 2002 MAIK "Nauka/Interperiodica".

1. INTRODUCTION

The threshold current density and the gain are the most important characteristics of semiconductor lasers which define the possibility of their practical use and affect all the basic parameters. First studies analyzing the threshold current density and the gain of semiconductor lasers date back to the 1960s–70s [1–3]. The appearance of quantum well (QW) heterolasers required that the existing models be developed and further studies performed. In [4–6], specific features of the threshold current density in separate-confinement heterostructure lasers were studied theoretically and experimentally. Further, the gain of semiconductor lasers with QW active regions was analyzed in detail in [7–12]. An analysis of the threshold current density of long-wavelength (1.3–2.0 μm) lasers is complicated by the presence of nonradiative Auger recombination channels [13–16]. An elaborate theoretical model taking into account the current of nonradiative Auger recombination and the diffusion leak currents in single-mode lasers operating at $\lambda = 1.3$ μm was presented in [17]. The appearance of laser heterostructures with an active region comprising an array of quantum dots, and the development of lasers based on these structures, required that the gain and threshold current density of these lasers be analyzed [18].

The creation of new types of devices or essential improvement of parameters of the already known devices demands revision and development of the existing physical models. Recent technological findings and the deeper insight gained into the physical processes occurring in separate-confinement lasers with low internal optical losses enabled us to achieve nearly record-breaking optical emission power, threshold current density, and stimulated internal quantum efficiency [19–24]. In the present work, an attempt is made to analyze threshold current density and gain in multi- and single-mode InGaP/GaAs/InGaAs and InP/InGaAsP/InGaAs separate-confinement heterostructure lasers on the basis of a vast body of experimental data.

2. EXPERIMENTAL SAMPLES

MOCVD-grown InGaP/GaAs/InGaAs and InP/InGaAsP separate-confinement heterostructures were used in experiments. The details of the technological installation and heterolaser fabrication methods have been described elsewhere [19–24]. Mesa-stripe laser diodes (Fig. 1) were fabricated on the basis of these heterostructures.

Laser heterostructures on the GaAs substrate had $In_xGa_{1-x}P$ emitter layers (see Fig. 2). Epitaxial GaAs layers were used as the waveguide layer (0.4–05 μm thick). The active region of the laser heterostructure was comprised of a single strained ~90-Å-thick $In_xGa_{1-x}As$
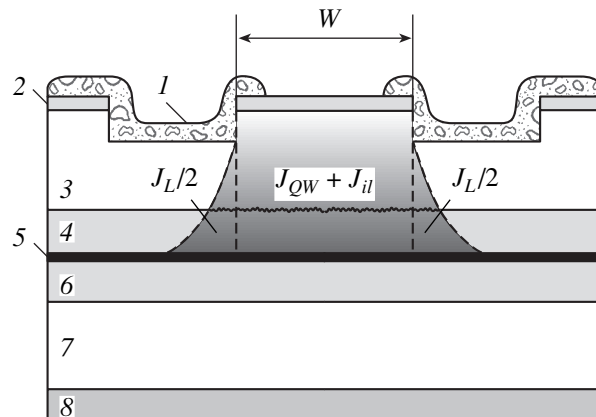

Fig. 1. Schematic representation of a laser diode and components of its threshold current. *W* mesa-stripe contact width; (*1*) SiO$_2$ insulating layer, (*2*) contact layer, (*3, 7*) emitters, (*4, 6*) waveguide, (*5*) active region, and (*8*) substrate.
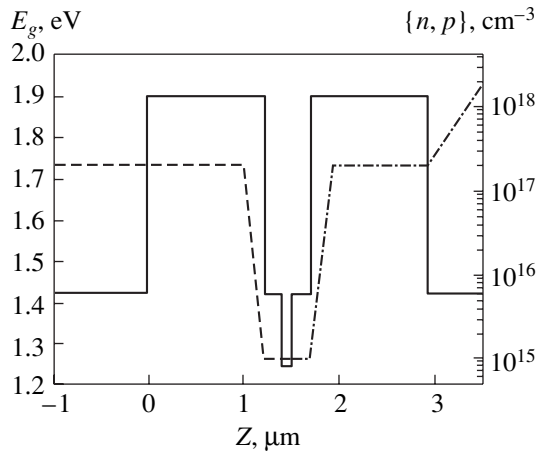
Fig. 2. Band diagram of InGaP/GaAs/InGaAs separate-confinement heterostructure (solid line); calculated doping profiles: (dashed line) Si donor, (dot-dashed line) Mg acceptor. Z—structure growth coordinate.
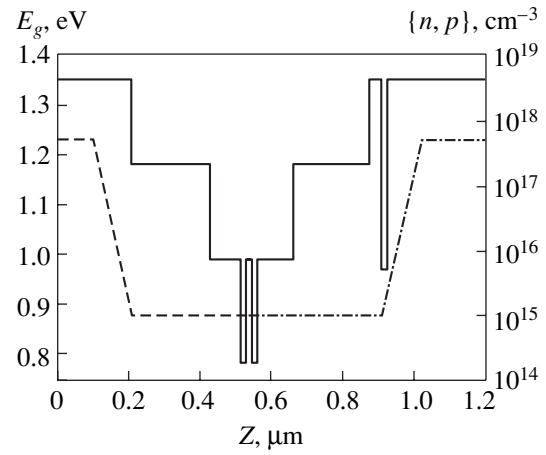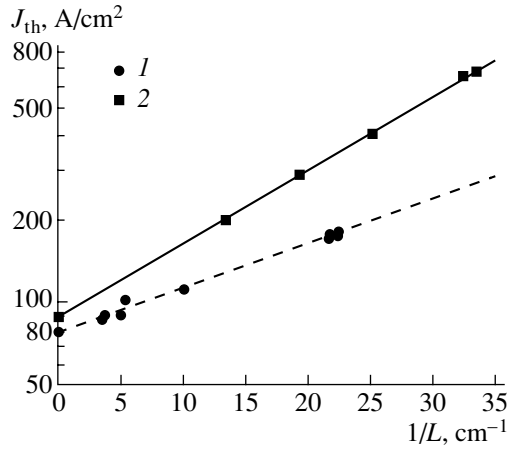

Fig. 3. Band diagram of InP/InGaAsP separate-confinement heterostructure (solid line); calculated doping profiles: (dashed line) Si donor, (dot-dashed line) Zn acceptor. Z—structure growth coordinate.

Fig. 4. Experimental threshold current densities J_{th} vs. inverse cavity length $1/L$ for InGaP/GaAs/InGaAs laser diodes ($\lambda = 1$ μm). Stripe width W: (1) 100 and (2) 5 μm; the same in Figs. 5, 6, and 7.
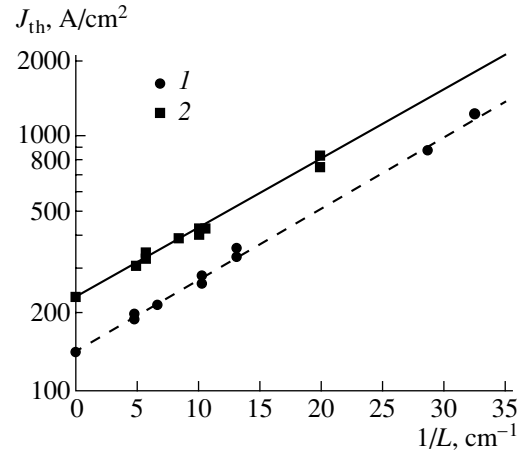
Fig. 5. Experimental threshold current densities J_{th} vs. inverse cavity length $1/L$ for InP/InGaAsP laser diodes ($\lambda = 1.58$ μm).

QW ($x \approx 20\%$ with an emission wavelength of ~1 μm). Mg served as the acceptor dopant, and Si served as the donor impurity.

Laser heterostructures on the InP substrate (Fig. 3) had InP emitter layers and two 60-Å-thick strained QWs of $In_{1-x}Ga_xAs_{1-y}P_y$ solid solution with an emission wavelength of ~1.58 μm. The barrier spacer between the wells was 200 Å thick. A step waveguide was used to raise the internal quantum efficiency [21]. Zn served as the acceptor dopant, and Si, as the donor impurity. The estimated doping level (n, p) of the wide-gap emitters and waveguide layers is shown in Figs. 2 and 3 for both heterostructures by dashed and dot-dashed lines, respectively.

The two types of fabricated heterostructures differed in their waveguide properties, carrier ejection into

barrier layers [25–27], and Auger recombination coefficients [28], whose values for the $IIn_{1-x}Ga_xAs_{1-y}P_y$ solid solution were taken from experiments [29–31].

Single-mode and multimode mesa-stripe laser diodes were fabricated on the basis of the two types of heterostructures [19–24]. For these diodes, the dependences of the threshold current density (J_{th}) on the inverse cavity length of a diode (L^{-1}) (Figs. 4, 5) and of the inverse differential quantum efficiency (η_d^{-1}) on the cavity length (Figs. 6, 7) were obtained and light–current characteristics were studied. Heterostructures of both types demonstrated threshold current densities close to minimal values for laser diodes with an infinitely long cavity, low internal optical loss α_i, and high stimulated internal quantum efficiency of radiation η_i.
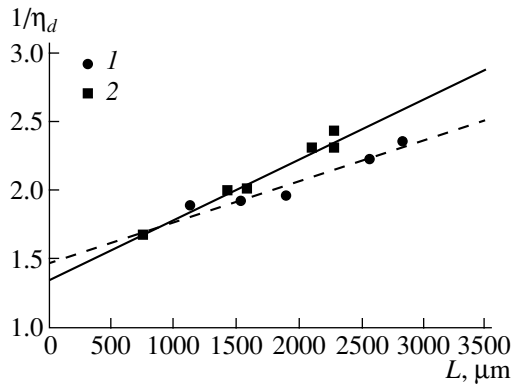
Fig. 6. Experimental values of the inverse of external differential quantum efficiency $1/\eta_d$ vs. cavity length L for InGaP/GaAs/InGaAs laser diodes ($\lambda = 1$ μm).
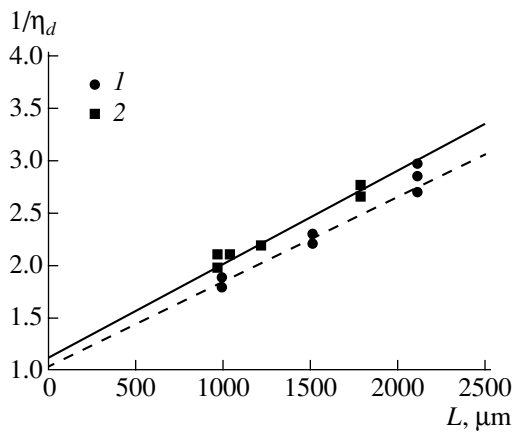

Fig. 7. Experimental threshold current densities J_{th} vs. inverse cavity length $1/L$ for InP/ InGaAsP laser diodes ($\lambda = 1.58$ μm).

3. COMPONENTS OF THRESHOLD CURRENT DENSITY

The threshold current density in semiconductor lasers can be determined experimentally in several ways, all of which are reduced to determining the current corresponding to the onset of stabilization of the rise in the carrier density in the active region of a laser. In this study, we define the threshold current as the current at the beginning of the linear portion of the light–current characteristic. In this case, the density of injected carriers in the active region is stabilized, the contribution of spontaneous emission to the modes is negligible, and the internal quantum efficiency of radiation is governed by the stimulated quantum efficiency.

The experimental threshold current density can be represented as a sum of current components characterizing separate physical processes:

$$J_{th} = J_{th}^* + J_L. \tag{1}$$

Their physical meaning is as follows: J_{th}^* is the component of the threshold current density that characterizes the properties of a laser heterostructure; J_L is the spreading current related to the specific design of the laser diode with a narrow current region. The current components in a laser diode are shown schematically in Fig. 1.

The J_{th}^* component can be represented as the sum

$$J_{th}^* = J_{QW} + J_{il}, \tag{2}$$

where J_{QW} is the recombination current in the active region of a diode, and J_{il} is the component related to leakage currents inside the laser heterostructure, which are due to deviation of the stimulated internal quantum efficiency (η_i) from 100% at the generation threshold.

The current in the active region J_{QW} consists of two components:

$$J_{QW} = J_R + J_A, \tag{3}$$

where J_R is the current component related to radiative recombination, and J_A is associated with nonradiative Auger recombination.

The J_{QW} component can be determined at the generation threshold using the experimental value of the stimulated internal quantum efficiency η_i, which indicates what part of the carriers in the flowing current participates in the recombination in the active region. In what follows, we assume that η_i is independent of the driving current above the generation threshold. We assume also that above the generation threshold the J_L component is independent of the driving current or that its increase can be neglected and, therefore, does not affect the internal quantum efficiency. The experimental values of η_i are determined from Figs. 6, 7 using the expression for the differential quantum efficiency:

$$\eta_d = \eta_i \alpha_{ext}/(\alpha_i + \alpha_{ext}), \tag{4}$$

where α_i is the internal optical loss, $\alpha_{ext} = (1/L)\ln(1/R)$ is the output optical loss, and $R = 0.3$ is the reflectivity of the laser diode cavity mirrors.

The component of current, flowing through the active region, is expressed as

$$J_{QW} = \eta_i J_{th}^*, \tag{5}$$

where J_{th}^* is the threshold current flowing through the heterostructure on the condition that the spreading current component J_L is negligible.

At the threshold, in accordance with the lasing condition

$$g\Gamma = \alpha_i + a_{ext}, \tag{6}$$

when the gain of the waveguide mode ($g\Gamma$) equals the sum of the internal α_i and output α_{ext} optical losses (Γ is the optical confinement factor of the waveguide

Table 1. Experimental parameters of structures

Structure no. (λ, μm)	Stripe width W, μm	η_i, %	α_i, cm^{-1}	Γ, %	B, cm^3 s^{-1}	R, cm^6 s^{-1}
X2585 (1 μm)	100	68	2.5	1.5 [32]	1.2×10^{-10} [28, 32, 33]	1×10^{-31} [28]
	5	73	3.7			
KP-1168 (1.58 μm)	100	96	9	1.2 [23]	1.1×10^{-10} [28, 33]	3.5×10^{-29}–5×10^{-30} [29–31]
	5	95	12			

mode, and g is the material gain), the current of radiative recombination can be represented as

$$J_R = J_0 + J_i + J_{\text{ext}}, \qquad (7)$$

where J_0 is the transparency current, J_i is the current required to compensate for the internal optical losses, and J_{ext} is the component compensating for the useful losses related to the emission output from the cavity.

Thus, representing the threshold current density as a sum of components characterizing different physical processes yields the following expression:

$$J_{\text{th}} = J_0 + J_i + J_{\text{ext}} + J_A + J_{il} + J_L. \qquad (8)$$

4. ANALYSIS OF EXPERIMENTAL DATA

The methods applied to determine the components of the threshold current density for the "short-wavelength" ($\lambda \approx 1$ μm) and "long-wavelength" ($\lambda \approx 1.58$ μm) lasers are different. This is due to the fact that we disregard the Auger recombination current component for the former and take it into account for the latter. This assumption is based on the use of experimental Auger recombination coefficients differing by a factor of 10–100 for the short- and long-wavelength lasers. Table 1 presents the η_i and α_i values determined from the experimental curves (Figs. 6, 7), along with published values of the coefficients of radiative recombination (B), Auger recombination (R), and the optical confinement factor (Γ) used in further calculations, with references given.

It is noteworthy that the stimulated quantum efficiencies for the lasers differing in mesa-stripe width coincide within the experimental error and are determined by the properties of a heterostructure. In this study, we assume that the coefficients of radiative recombination B are independent of carrier density in the strained QWs of the active region. This can be explained as follows. In the materials constituting the active region, the electron and hole masses in the bulk differ by a factor of ~10, which leads to a decrease in B in the degenerate material of the active region with increasing density of injected carriers. In compressed-strained QWs, the heavy hole mass decreases with increasing strain, thus making the overlapping integral between the conduction and valence bands larger and suppressing its dependence on carrier density. Therefore, the assumption that B is independent of the threshold carrier density is justified.

4.1. InGaAsP/GaAs/InGaAs Heterolasers

Let us now determine the above-defined components of the threshold current density for short-wavelength laser diodes with a wide mesa-stripe contact. For these lasers, the current spreading to passive regions (J_L) and the nonradiative Auger recombination current (J_A) in (8) can be neglected. Then, according to (3), relation (5) takes the form

$$J_R = \eta_i J_{\text{th}}^*. \qquad (9)$$

In the first stage, using the known expression (6) for the material gain, along with relation (9) for the radiative recombination current, the η_i values from Fig. 6, and the dependence of the threshold current density on inverse cavity length (Fig. 4), we can obtain the gain as a function of the radiative component of the threshold current density (Fig. 8). This dependence can be approximated, with reasonable accuracy, by the expression

$$g = g_0 \ln(J_R/J_0). \qquad (10)$$

Using this approximation and the dependence presented in Fig. 8, we determined the gain g_0 and the transparency current J_0. These parameters are heterostructure characteristics which depend on the material properties and the parameters of the QWs in the active region of a heterolaser. In short-wavelength lasers, $g_0 =$
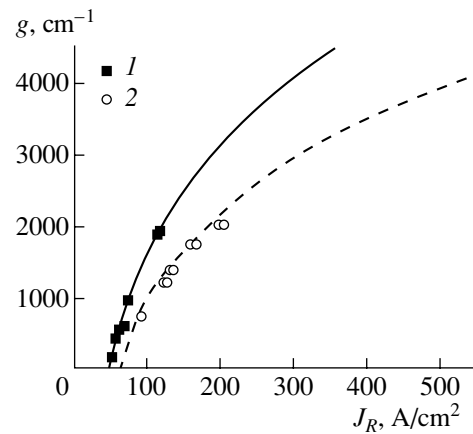

Fig. 8. Material gain g vs. the radiative component of the threshold current density, J_R, for (*1*, solid line) InGaP/GaAs/InGaAs and (*2*, dashed line) InP/InGaAsP laser diodes.
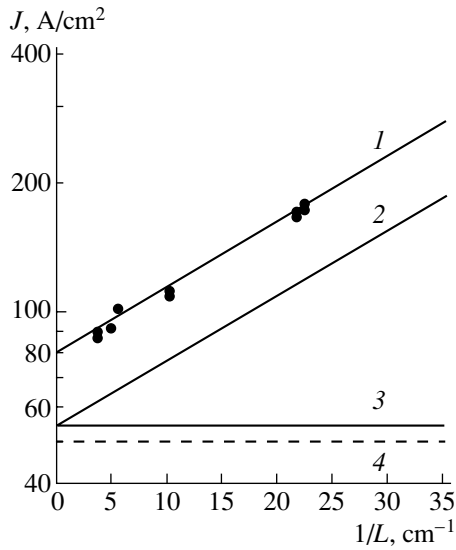
J, A/cm^2

Fig. 9. Components J of the threshold current density vs. the inverse cavity length $1/L$ for InGaP/GaAs/InGaAs ($\lambda = 1$ μm) multimode laser diodes with stripe width $W = 100$ μm: (*1*) threshold current density J_{th}: (points) experiment and (solid line) calculated, (*2*) radiative component J_R, (*3*) $J_i + J_0$ components, and (4) transparency current J_0.

2300 cm^{-1}. The transparency current, at which the population inversion ensuring equal rates of electron transitions from the conduction to the valence band and in the opposite direction is achieved in the active medium of a laser diode, is 50 A/cm^2. It is noteworthy that, in contrast to the commonly accepted dependence of the gain on the threshold current [9, 10], the gain is related in (10) only to the radiative component of the current, rather than to the overall threshold current.

Using (2) and (9), we can find the J_{il} component

$$J_{il} = J_{th}^*(1 - \eta_i). \qquad (11)$$

Now the component of the radiative current increment, which is required to compensate for the internal optical losses for scattering on free carriers and inhomogeneities, can be found for laser diodes with infinite cavity length ($J_{ext} \approx 0$) from (8) with the use of (1) and (11):

$$J_i = J_{th}^*(L \longrightarrow \infty)\eta_i - J_0. \qquad (12)$$

We assume that the component J_i is independent of the cavity length of a diode, because the internal optical loss α_i is a specific parameter of a laser heterostructure, which is independent of the threshold carrier density in the active region. To verify this approximation, we represent α_i as the sum

$$\alpha_i = \alpha_{CL}\Gamma_{CL} + \alpha_W\Gamma_W + \alpha_{QW}\Gamma_{QW}, \qquad (13)$$

where α_{CL}, α_W, and α_{QW} are the optical losses; and Γ_{CL}, Γ_W, and Γ_{QW} are the optical confinement factors of a light wave in the emitter, waveguide, and QW, respectively. In our case, $\Gamma_{QW} \approx 1\%$ (Table 1), and, therefore, the rise in the internal optical loss α_i with increasing threshold concentration is insignificant and can be neglected as compared with the contribution of optical loss in the emitter layers at $\Gamma_{QW} \approx 40\%$.

For lasers with a finite cavity length, the threshold current component related to compensation of useful output losses is found from expressions (7) and (9):

$$J_{ext} = J_{th}^*\eta_i - J_0 - J_i. \qquad (14)$$

Thus, using the experimental dependences in Figs. 4 and 6, we determined all the threshold current density components for short-wavelength lasers with a wide mesa-stripe contact. Figure 9 shows these current components as functions of the inverse cavity length. The numerical values of the current components are presented in Table 2 for laser diodes with selected cavity lengths.

Table 2. Current components for laser diodes

	$\lambda = 1.0$ μm						$\lambda = 1.58$ μm					
	$W = 100$ μm			$W = 5$ μm			$W = 100$ μm			$W = 5$ μm		
L, μm	$\longrightarrow \infty$	1500	500	$\longrightarrow \infty$	1500	500	$\longrightarrow \infty$	1500	500	$\longrightarrow \infty$	1500	500
J_{th}, A/cm^2	80	100	159	90	133	299	143	218	519	230	331	768
J_0, A/cm^2	50						63					
J_i, A/cm^2	4.4			5.7			31			43.6		
J_{ext}, A/cm^2	0	13	54	0	15	56	0	41	183	0	60	223
J_R, A/cm^2	54	68	108	56	70	112	94	134	277	107	154	317
J_A, A/cm^2	–	–	–	–	–	–	43	75	221	53	91	270
J_{il}, A/cm^2	25	32	51	21	26	41	6	9	21	7	10	25
J_L, A/cm^2	–	–	–	14	37	146	–	–	–	63	75	156
g_0, cm^{-1}	2300						1900					
g_{0n}, cm^{-1}	4780						3700					
g_{0p}, cm^{-1}	4780						3700					
n_0, cm^{-3}	1.625×10^{18}						1.291×10^{18}					
p_0, cm^{-3}	1.625×10^{18}						2.52×10^{18}					

For single-mode short-wavelength lasers with a narrow mesa-stripe contact, the current spreading into passive regions cannot be disregarded and the component J_L of the threshold current density should be taken into account. In further considerations, we assume that J_0 and g_0 are characteristic parameters of the given heterostructure. Then, the values obtained for wide-contact diodes can also be used for diodes with a narrow contact.

First, we find from the dependence in Fig. 8, obtained for short-wavelength wide-contact lasers, the radiative current $J_R(J_{QW} = J_R)$ for a laser diode of a given length, using relation (6) and α_i values from Table 1. It is necessary to note that the internal optical losses in narrow-contact lasers exceed those in wide-contact laser diodes. This is due to the increased contribution of losses associated with light wave scattering on the edges of the transverse waveguide to the total internal optical losses.

The threshold current density J_{th}^* is found from (9); the experimental values of η_i are taken from Table 1. The current compensating for the internal, J_i, and external optical losses, J_{ext}, is determined from (12) and (14), respectively. The current loss in a heterostructure, J_{il}, is found from (11), and the leakage J_L, associated with current spreading to the passive regions in a mesa-stripe laser diode, is found from (1). Figure 10 presents the components of the threshold current density as functions of the inverse cavity length for laser diodes with a narrow-stripe ($W = 5\ \mu m$) contact. The numerical values of the current components for laser diodes with selected cavity lengths are given in Table 2.

We considered in detail the algorithm for determining the components of the threshold current density for short-wavelength laser diodes with wide and narrow mesa stripes. For the short-wavelength lasers, in which the Auger processes are negligible, all the components of the threshold current density can be found from the experimental dependences (Figs. 4, 6, and 8) and relations (1), (9), (11), (12), and (14).

4.2 InGaAsP/InP Heterolasers

Now we proceed to the case of long-wavelength laser diodes ($\lambda = 1.58\ \mu m$), in which the nonradiative Auger recombination current component J_A cannot be neglected in (3) and where the algorithm for component selection is strongly complicated.

We first consider wide mesa-stripe long-wavelength laser diodes, in which current spreading to passive regions J_L can be disregarded. In this case, the radiative J_R and nonradiative J_A current components can only be defined in terms of the coefficients of radiative (B) and nonradiative (R) Auger recombination:

$$J_R = ed_{QW}NBn_{QW}p_{QW}, \qquad (15)$$

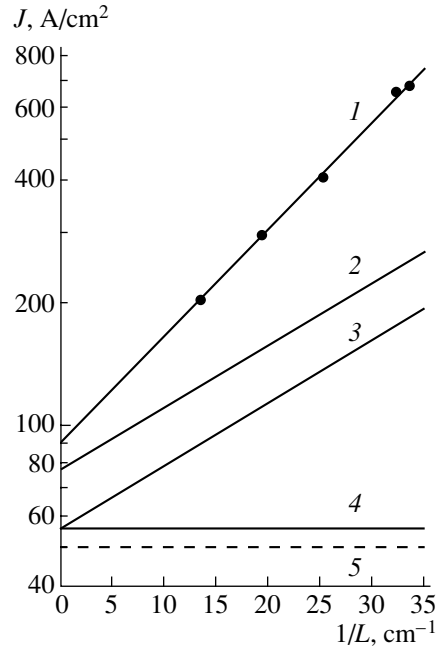$$J_A = ed_{QW}NRn_{QW}(p_{QW})^2, \qquad (16)$$

Fig. 10. Components J of the threshold current density vs. the inverse cavity length $1/L$ for InGaP/GaAs/InGaAs single-mode laser diodes ($\lambda = 1\ \mu m$) with stripe width $W = 5\ \mu m$: (*1*) threshold current density J_{th}: (points) experiment and (solid line) calculated, (*2*) $J_{il} + J_R$ components, (*3*) radiative component J_R, (*4*) $J_i + J_0$ components, and (*5*) transparency current J_0.

where d_{QW} is the QW thickness; N is the number of QWs; e is the elementary charge; and n_{QW} and p_{QW} are the bulk densities of electrons and holes in a QW. In (15) and (16), it is assumed that all the QWs are equally filled with carriers. Relation (16) accounts for the fact that, in the structures under study, the fastest of the Auger recombination channels is the zero-phonon Auger process with excitation of a heavy hole into a band split off due to the spin–orbit interaction [28]. We used experimental values of the Auger coefficient, which show a wide scatter [29–31] indicated in Table 1. The radiative recombination coefficient B has been found with reasonable accuracy [28, 33]. We believe that the coefficient R, as well as B, is independent of the threshold carrier density in a QW.

Further, the depth of a strained QW in separate-confinement long-wavelength laser diodes does not exceed 50 meV for electrons in the active region, and, therefore, electrons can be ejected from a QW into waveguide layers. This was shown in our experiments [24, 26]. To determine the relation between the density of carriers ejected into the barrier layers and the carrier density in the strained QW, we use the calculational model from [17]. According to the electrical neutrality principle, the density of holes in a QW equals the sum of electron densities in the QW (n_{QW}) and in the barrier (n_{bar}):
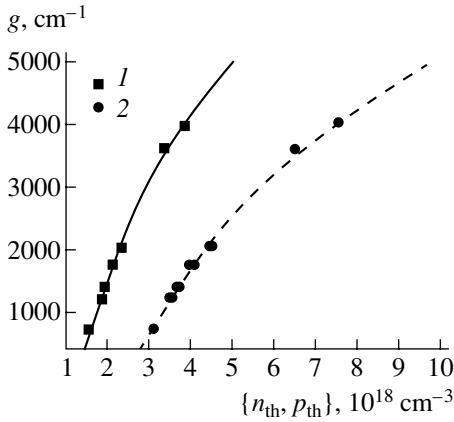
$$p_{QW} = n_{QW} + n_{bar}. \qquad (17)$$

Fig. 11. Material gain g vs. (*1*) electron density n_{th} and (*2*) hole density p_{th} in the QW for InP/InGaAsP laser diodes ($\lambda = 1.58$ μm).
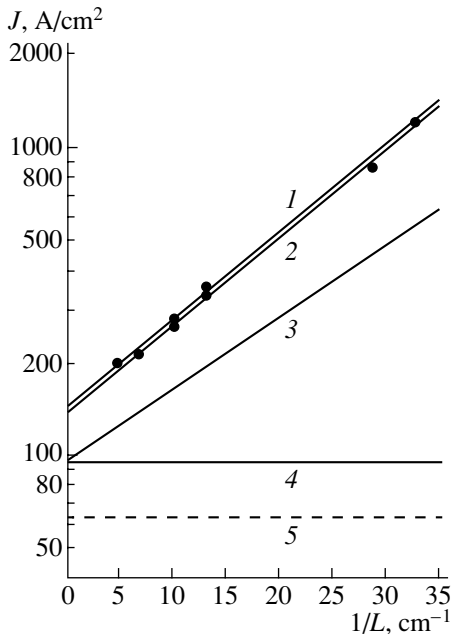

Fig. 12. Components J of the threshold current density vs. the inverse cavity length $1/L$ for multimode InP/InGaAsP ($\lambda = 1.58$ μm) laser diodes with stripe width $W = 100$ μm: (*1*) threshold current density J_{th}: (points) experiment and (solid line) calculated, (*2*) $J_A + J_R$ components, (*3*) radiative component J_R, (*4*) $J_i + J_0$ components, and (*5*) transparency current J_0.

In its turn, the electron density in the barrier is a function of the electron density in a QW. With account taken of relations (3), (5), and (15)–(17), the threshold current density can be written as follows:

$$J_{th}^* = ed_{QW}N_{QW}n_{QW}(n_{QW} + n_{bar}) \tag{18}$$
$$\times [B + R(n_{QW} + n_{bar})]/\eta_i.$$

Using the experimental dependence of the threshold current density on L (Fig. 5) and relations (1) and (18),

we can determine the threshold electron and hole densities in a QW and the electron density in the barrier. The η_i and B values are taken from Table 1; $R = 1.5 \times 10^{-29}$ cm^6/s.

Further, we can construct the dependences of the gain in the long-wavelength lasers on the densities of electrons and holes in a QW on the basis of relation (6) and the experimental dependence in Fig. 5. The obtained dependences of the gain on the electron and hole densities, presented in Fig. 11, can be approximated with reasonable accuracy by functions of the type [11]

$$g = g_{0n}\ln(n_{QW}/n_0), \tag{19}$$

$$g = g_{0p}\ln(p_{QW}/p_0), \tag{20}$$

where g_{0n} and g_{0p} are the gain coefficients, and n_0, p_0 are the transparency densities for electrons and holes.

In the case of short-wavelength ($\lambda = 1$ μ) laser diodes, the threshold electron and hole densities in a QW can also be calculated from (15) if the radiative component of the threshold current density is known and the threshold densities of electrons and holes in the QW are equal. The parameters g_0 and n_0, characterizing this case, are presented in Table 2.

For long-wavelength lasers, we determine the radiative component of the threshold current density, J_R, from (15) and then find the dependence of the gain on J_R (Fig. 8), which is well described by relation (10) with the gain coefficient $g_0 = 1900$ cm^{-1} and transparency current $J_0 = 63$ A/cm^2.

The J_A component is found from (16), and J_{il}, from (11). Then, by analogy with the short-wavelength lasers, we find the current component J_i from (12) and J_{ext} from (14). Figure 12 shows the components of the threshold current density for long-wavelength ($\lambda = 1.58$ μm) laser diodes with a wide mesa stripe, and the numerical values of components for laser diodes with selected cavity lengths are presented in Table 2.

For long-wavelength single-mode lasers with a narrow mesa-stripe contact, current spreading to the passive regions cannot be disregarded. The order in which the threshold current density components are calculated is the same as in the case of single-mode short-wavelength lasers, but the components J_R and J_A are found from (15) and (16).

Figure 13 presents the determined threshold current density components for single-mode long-wavelength laser diodes, and the numerical values of components for selected cavity lengths are presented in Table 2.

5. DISCUSSION OF THE RESULTS

We analyzed the components of the threshold current density and demonstrated that, in heterostructures with stimulated internal quantum efficiency η_i differing from unity, it is necessary to take into account current loss J_{il}, which can significantly raise the threshold cur-

rent density (Figs. 9, 10). As seen in Table 1, η_i is virtually unaffected by the leakage current J_L. Therefore, η_i characterizes only a heterostructure, rather than a diode as a whole. In calculating the threshold current density, the J_{il} component of the current is commonly disregarded, because η_i is frequently taken to be unity when the stimulated generation is achieved. The η_i value defines the fraction of carriers participating in the recombination in the active region. At the generation threshold, the Auger recombination does not affect the η_i value (Figs. 12 and 13, Table 2). The contribution of the Auger recombination to the threshold current is taken into account as a separate component, J_A, which strongly affects the threshold current density of the long-wavelength lasers and is equal to 50–400 A/cm^{-2}, depending on the cavity length (Table 2). There are three principal ways to diminish the J_A component: to reduce the threshold carrier density [13–16], to make the number of QWs in the active region of a heterostructure smaller [34], and to make the compressive strain in QWs higher [35].

The radiative component of the threshold current, J_R, contains three contributions: J_0, J_i, and J_{ext} (7). J_0 is the transparency current at which $g = 0$; i.e., the medium neither amplifies, nor absorbs. We determined the transparency current from the dependence of the material gain in the active region on the radiative component of the threshold current (Fig. 8). In short- and long-wavelength lasers with a 1500-μm-long cavity, the transparency current makes a major contribution to the threshold current. The J_0 value is ~50 A/cm^2 for both types of laser diodes. The transparency current is defined by the position of the quantum levels and the band structure parameters of the strained material in the active region. It is inexpedient to reduce the transparency current component by making the QW thinner because of the strong decrease in the optical confinement factor [22, 31] and the resulting rise in the threshold current density. Theoretically, the share of the transparency current in the threshold current density can be reduced by using QWs with a δ-function density-of-states in the active region of a laser heterostructure; this will be possible in the future with technological progress ensuring uniform geometrical dimensions of QWs [18].

The next component of the threshold current density, J_i, which compensates for the waveguide mode scattering on free carriers and macro- and microheterogeneities of a laser heterostructure, becomes significant at internal optical losses $\alpha_i > 10$ cm^{-1}. The modern level of epitaxial technology, both MOCVD and MBE, ensures $\alpha_i < 2$ cm^{-1} [19–23] through the use of low-doped waveguide layers and the fabrication of highly uniform heterojunctions in a laser structure. J_i depends on the stripe width. The internal optical losses α_i are somewhat different in laser diodes fabricated on the basis of the same heterostructure but with stripes of different widths. This is due to an increase in the relative contribution of losses associated with light-wave scat-
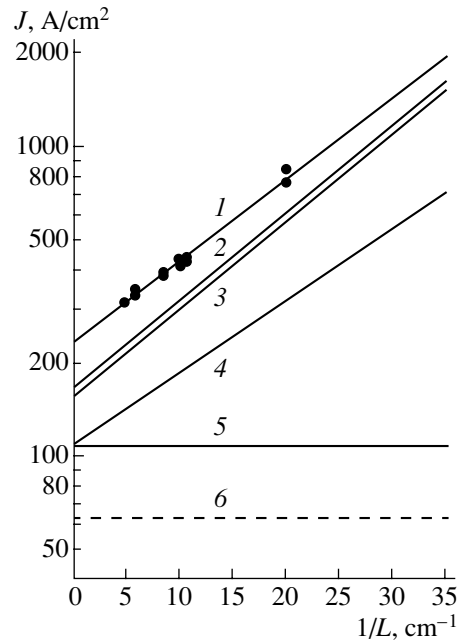

Fig. 13. Components J of the threshold current density vs. the inverse cavity length $1/L$ for single-mode InP/InGaAsP ($\lambda = 1.58$ μm) laser diodes with stripe width $W = 5$ μm: (*1*) threshold current density J_{th}: (points) experiment and (solid line) calculated; (*2*) $J_{il} + J_A + J_R$ components; (*3*) $J_A + J_R$ components; (*4*) radiative component J_R; (*5*) $J_i + J_0$ components; and (*6*) transparency current J_0.

tering at the boundaries of the longitudinal waveguide to the threshold current density. The J_i component does not contribute significantly to the threshold current density. This behavior is especially pronounced in separate-confinement laser heterostructures with an expanded waveguide, in which this component decreases to 1−3 A/cm^2. However, α_i affects the optical power of a heterolaser.

The current compensation of the output optical losses, J_{ext}, also causes a rise in the threshold carrier density in the active region of a laser structure. The output losses decrease with increasing cavity length, and at $L > 1500$ μm the contribution of J_{ext} to the overall threshold current becomes negligible (Figs. 9, 10, 12, 13).

The three above-discussed components of the threshold current density make up the radiative component J_R. In short-wavelength lasers with a stimulated output quantum efficiency close to 100%, this quantity virtually coincides with the threshold current density J_{th}, provided that the J_L component can be neglected (wide-stripe lasers).

The spreading current J_L is defined by the specific design of a single-mode laser diode. This component grows with decreasing mesa-stripe width, which is, therefore, commonly made as narrow as possible. However, the principal requirement for the design of a narrow-mesa-stripe laser diode is its single-mode operation. In multimode lasers, the leakage current J_L is vir-

tually absent [34] and, therefore, J_L can be determined to a first approximation from the difference between the threshold current densities of single- and multimode lasers (Figs. 4, 5, and 12, 13). The leakage current J_L constitutes nearly half of the threshold current in short-wavelength single-mode lasers with a small cavity length, $L \leq 500$ μm (Fig. 10, Table 2), and about one third in long-wavelength lasers with the same L (Fig. 13, Table 2). With increasing L, the contribution of J_L grows.

The dependence of the gain on the driving current is no less important a parameter of a semiconductor laser than the threshold current density. Figure 8 presents the gain as a function of the radiative component of the threshold current density, J_R, obtained from the experimental curves in (Figs. 4–7) and relation (6); the latter is well approximated by logarithmic dependence (10). It is worth noting that the right-hand side of (6) includes optical losses compensated for only by the radiative component of the threshold current, J_R (7). It was found that the gain coefficients g_0 virtually coincide for the long- and short-wavelength lasers, being equal to ~2000 cm^{-1}. Commonly, the dependence of the maximum gain on the total threshold current J_{th} is plotted, which nearly coincides with the $g(J_R)$ dependence for high-efficiency multimode short-wavelength lasers. However, in high-efficiency multimode long-wavelength lasers, the dependences of the gain on J_{th} and J_R differ significantly, because the threshold current includes a major nonradiative contribution related to the Auger recombination current. In addition, the actual density of electrons in the active region is several times lower than the hole density owing to ejection of electrons into the barrier layers. The gain necessary for the threshold conditions to be satisfied is obtained when the threshold electron density is achieved, with the hole density being several times higher.

6. CONCLUSION

Short- and long-wavelength single-mode and multimode laser diodes were studied. It is shown that, using a simplified calculational model, the experimental threshold current densities can be represented as the sum of current components. In heterostructures with a stimulated internal quantum efficiency of emission other than unity, the current losses J_{il}, which can markedly raise the threshold current density, should be taken into account. In high-efficiency short-wavelength laser diodes, the principal constituent of the threshold current density is the radiative component J_R. In long-wavelength laser diodes, electron ejection from QWs and the nonradiative component J_A should be taken into account in analyzing the threshold current density. In mesa-stripe single-mode short- and long-wavelength laser diodes, the spreading current component J_L should be taken into account. It is shown that the gain can be approximated accurately enough by a logarithmic function of the radiative component of the thresh-

old current and of the electron and hole densities in the QW active region.

Ways of reducing the threshold carrier density in short- and long-wavelength lasers were discussed. We have shown [5] that making the cavity longer in laser diodes is an effective method for reducing the threshold current density. However, when the cavity is longer than 1500 μm, the main contribution to the threshold current comes from the transparency current J_0, equal to ~50 A/cm^2 for both short- and long-wavelength lasers. The design of a laser heterostructure with an expanded step-like waveguide, proposed in our previous work [21], ensures high stimulated quantum efficiency, low internal optical losses, and, as a consequence, minimum values of the current components J_{il} and J_i. The above requirements are in agreement with the concept of power semiconductor lasers.

REFERENCES

1. R. F. Kazarinov, O. V. Konstantinov, V. I. Perel', and A. L. Éfros, Fiz. Tverd. Tela (Leningrad) **7**, 1506 (1965) [Sov. Phys. Solid State **7**, 1210 (1965)].

2. Zh. I. Alferov, V. M. Andreev, D. Z. Garbuzov, *et al.*, Fiz. Tekh. Poluprovodn. (Leningrad) **4**, 1826 (1970) [Sov. Phys. Semicond. **4**, 1573 (1970)].

3. F. Stern, IEEE J. Quantum Electron. **QE-9**, 290 (1973).

4. D. Z. Garbuzov, V. P. Evtikhiev, S. Yu. Karpov, *et al.*, Fiz. Tekh. Poluprovodn. (Leningrad) **19**, 449 (1985) [Sov. Phys. Semicond. **19**, 279 (1985)].

5. V. P. Evtikhiev, D. Z. Garbuzov, Z. N. Sokolova, *et al.*, Fiz. Tekh. Poluprovodn. (Leningrad) **19**, 1420 (1985) [Sov. Phys. Semicond. **19**, 873 (1985)].

6. I. S. Tarasov, D. Z. Garbuzov, V. P. Evtikhiev, *et al.*, Fiz. Tekh. Poluprovodn. (Leningrad) **19**, 1496 (1985) [Sov. Phys. Semicond. **19**, 920 (1985)].

7. D. Z. Garbuzov, A. V. Tikunov, S. N. Zhigulin, *et al.*, Fiz. Tekh. Poluprovodn. (Leningrad) **22**, 1035 (1988) [Sov. Phys. Semicond. **22**, 653 (1988)].

8. P. W. A. McIlroy, A. Kurobe, and Y. Uematsu, IEEE J. Quantum Electron. **QE-21**, 1958 (1985).

9. J. Z. Wilcox, G. L. Peterson, S. Ou, *et al.*, J. Appl. Phys. **64**, 6564 (1988).

10. S. Y. Hu, S. W. Corzine, K. K. Law, *et al.*, J. Appl. Phys. **76**, 4479 (1994).

11. T. Makino, IEEE J. Quantum Electron. **QE-32**, 493 (1996).

12. J. E. A. Whiteaway, G. H. B. Thompson, P. D. Green, and R. W. Glew, Electron. Lett. **27**, 340 (1991).

13. B. L. Gel'mont, Z. N. Sokolova, and I. N. Yassievich, Fiz. Tekh. Poluprovodn. (Leningrad) **16**, 592 (1982) [Sov. Phys. Semicond. **16**, 382 (1982)].

14. B. L. Gel'mont and Z. N. Sokolova, Fiz. Tekh. Poluprovodn. (Leningrad) **16**, 1670 (1982) [Sov. Phys. Semicond. **16**, 1067 (1982)].

15. G. G. Zegrya and V. A. Kharchenko, Zh. Éksp. Teor. Fiz. **101**, 327 (1992) [Sov. Phys. JETP **74**, 173 (1992)].

16. M. I. Dyakonov and V. V. Kocharovskii, Phys. Rev. B **49**, 17130 (1994).

17. L. V. Asryan, N. A. Gunko, A. S. Polkovnikov, *et al.*, Semicond. Sci. Technol. **15**, 1131 (2000).

18. A. R. Kovsh, A. E. Zhukov, A. Yu. Egorov, *et al.*, Fiz. Tekh. Poluprovodn. (St. Petersburg) **33**, 215 (1999) [Semiconductors **33**, 184 (1999)].

19. D. A. Livshits, I. V. Kochnev, V. M. Lantratov, *et al.*, Electron. Lett. **36**, 1848 (2000).

20. D. A. Livshits, A. Yu. Egorov, I. V. Kochnev, *et al.*, Fiz. Tekh. Poluprovodn. (St. Petersburg) **35**, 380 (2001) [Semiconductors **35**, 365 (2001)].

21. E. G. Golikova, V. A. Kureshov, A. Yu. Leshko, *et al.*, Pis'ma Zh. Tekh. Fiz. **26** (20), 40 (2000) [Tech. Phys. Lett. **26**, 913 (2000)].

22. E. G. Golikova, V. A. Gorbylev, Yu. V. Il'in, *et al.*, Pis'ma Zh. Tekh. Fiz. **26** (7), 57 (2000) [Tech. Phys. Lett. **26**, 295 (2000)].

23. E. G. Golikova, V. A. Kureshov, A. Yu. Leshko, *et al.*, Fiz. Tekh. Poluprovodn. (St. Petersburg) **34**, 886 (2000) [Semiconductors **34**, 853 (2000)].

24. A. Yu. Leshko, A. V. Lyutetskiĭ, N. A. Pikhtin, *et al.*, Fiz. Tekh. Poluprovodn. (St. Petersburg) **34**, 1457 (2000) [Semiconductors **34**, 1397 (2000)].

25. S. Adachi, *Physical Properties of III–V Semiconductor Compounds* (Wiley, New York, 1992).

26. D. Z. Garbuzov, A. V. Ovchinnikov, N. A. Pikhtin, *et al.*, Fiz. Tekh. Poluprovodn. (Leningrad) **25**, 929 (1991) [Sov. Phys. Semicond. **25**, 560 (1991)].

27. B. Broberg and S. Lingren, J. Appl. Phys. **55**, 3376 (1984).

28. D. Z. Garbuzov, V. V. Agaev, Z. N. Sokolova, *et al.*, Fiz. Tekh. Poluprovodn. (Leningrad) **18**, 1069 (1984) [Sov. Phys. Semicond. **18**, 665 (1984)].

29. M. C. Wang, K. Kash, C. E. Zah, *et al.*, Appl. Phys. Lett. **62**, 166 (1993).

30. Y. Zou, J. S. Osinski, P. Grodzinski, *et al.*, Appl. Phys. Lett. **62**, 175 (1993).

31. L. Davis, Y. Lam, D. Nichols, *et al.,* IEEE Photonics Technol. Lett. **5**, 120 (1993).

32. M. R. Gokhale, J. C. Dries, P. V. Studenkov, *et al.*, IEEE J. Quantum Electron. **QE-33**, 2266 (1997).

33. Z. N. Sokolova and V. B. Khalfin, Fiz. Tekh. Poluprovodn. (Leningrad) **23**, 1806 (1989) [Sov. Phys. Semicond. **23**, 1117 (1989)].

34. G. G. Zegrya, N. A. Pikhtin, G. V. Skrynnikov, *et al.*, Fiz. Tekh. Poluprovodn. (St. Petersburg) **35**, 1001 (2001) [Semiconductors **35**, 962 (2001)].

35. P. J. A. Thijs, L. F. Tiemeijer, J. J. M. Binsma, and T. van Dongen, IEEE J. Quantum Electron. **30**, 477 (1994).

Translated by D. Mashovets

PHYSICS
OF SEMICONDUCTOR DEVICES

The Use of SiC Triode Structures as Detectors of Nuclear Particles

N. B. Strokan, A. M. Ivanov, N. S. Savkina, D. V. Davydov,
E. V. Bogdanova, and A. A. Lebedev

Ioffe Physicotechnical Institute, Russian Academy of Sciences,
Politekhnicheskaya ul. 26, St. Petersburg, 194021 Russia
Submitted August 2, 2001; accepted for publication August 29, 2001

Abstract—The possibility of the internal amplification of the signal by a factor of approximately 100 for SiC-based detectors of short-range ions was demonstrated. The detectors were fabricated from the growth of p-epilayers on 6H-SiC n^+-substrates. The film thickness was approximately 10 μm, and the doping level was 2.8×10^{15} cm^{-3}. The Schottky barriers were formed on the films by magnetron sputtering of Ni. The structure of the detectors was $n–p–n^+$, and their parameters were investigated in the floating-base mode. The α particles from ^{244}Cm with an energy of 5.8 MeV were used, and the increase in the signal (E) with a rise in applied voltage (U) was investigated. The structures irradiated are equivalent to the phototriodes. The superlinear rise of E was observed with a considerable (by a factor of tens) amplification of the nonequilibrium charge introduced by the α particle. © 2002 MAIK "Nauka/Interperiodica".

1. INTRODUCTION

At present, considerable progress in obtaining pure SiC films is being seen. The content of electrically active impurities in films is on the level of 10^{15} cm^{-3} with electron and hole lifetimes of ~1 μs for both n-type and p-type conduction. The characteristics mentioned permit testing the applicability of SiC for the detection and spectrometry of nuclear radiation.

In the first case, specifically, in the radiation detection mode, release of the total energy of the nuclear particle (quantum) in the detector is desirable but not necessary. However, for the mode of the exact determination of energy, the complete deceleration of the particle in the active zone of the detector is a necessary condition. For this reason, in order to analyze the detectors based on SiC films, the α particles of natural decay are used, whose range is no longer than ~30 μm. Note that typical detector construction is based on the $p–n$ junction. Thus, recent results on the use of SiC films in detectors [1–3] have been obtained for diode structures. In this study, the characteristics of the triode structure of the $n^+–p–n^+$ type are investigated. The conditions in which the nonequilibrium charge introduced by the α particle is considerably (by a factor of tens) amplified are clarified.

EXPERIMENTAL

The 6H-SiC films of p-type conduction, which were grown on n^+ substrates by the vacuum sublimation technique [4], were the starting material for the base region of the structure. The net concentration of impurities ionized at room temperature was 2.8×10^{15} cm^{-3}

for the film thickness of ~10 μm. The second electrode was the Schottky barrier obtained by the evaporation of Ni.

The structures were investigated in a switching-on mode with the floating base. The irradiation of the structures was carried out from the Schottky barrier side. The α particles from the ^{244}Cm source with an energy of 5.8 MeV and a range in SiC of 20 μm were used. The latter quantity exceeded the film thickness. Since the incidence angle of particles was close to the normal, the nonequilibrium charge emerging in the base corresponded to the absorption of approximately one-third of the above-mentioned energy, with allowance made for the Bragg curve for ionization losses. The structures were connected to the circuit in series with the load resistance and the bias source. The signals from α particles were recorded using a preamplifier which was sensitive to the charge flowing in the circuit. Subsequently, the shape of the signal spectrum and the average amplitude were measured as a function of the applied voltage using the standard technique of amplitude analysis. All measurements were carried out at room temperature in the conditions of a forevacuum.

The capacitance measurements demonstrated that the $p–n^+$ junctions of the structure, as should be expected, are not identical. The Schottky barrier corresponds to an abrupt junction, whereas the transition to the p-type conduction at the n^+ substrate is smooth. For this reason, two polarities of switching were compared. Either the $p–n$ junction of the substrate or the Schottky barrier served as the collector.
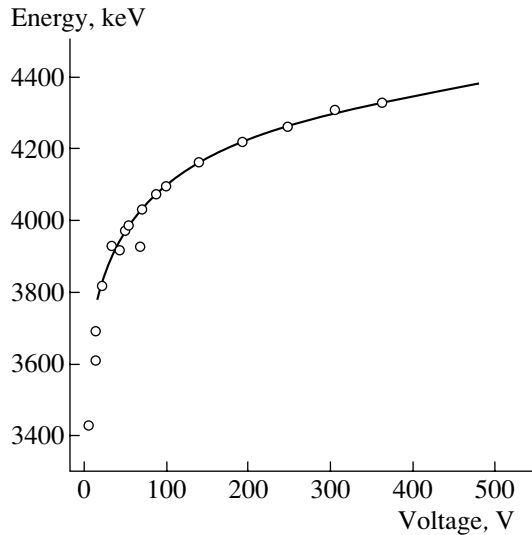
Fig. 1. Dependence of the signal from the α particle, which is expressed in energy units, on the voltage across the triode structure. The p–n^+ junction of the substrate plays the role of the collector.

RESULTS OF MEASUREMENTS

1. Figure 1 demonstrates the signal (E) as a function of voltage (U) across the structure for the case in which the p–n^+ junction of the substrate served as the collector. It can be seen that a sharp increase in the signal, which is observed for $U \leq 50$ V, gives way to a sublinear dependence with a pronounced tendency to leveling off. It is important that the signal exceeds the energy which is released by the α particle in the base. However, the excess is only by a factor of 2; i.e., no substantial amplification is observed. It is our opinion that such behavior of the signal is explained by the manifestation of two factors. These are the weak injection ability of the emitter (Schottky barrier) and the low charge-carrier lifetime at the barrier.

The spectral line shape was Gaussian (Fig. 2). The ratio of the spectrum width to the average amplitude as a function of U increases only slightly (Fig. 3). The value of ~9%, which was obtained for the spread of amplitudes, is partially associated with the fluctuations of ionization losses by single α particles during transit through the base. However, even with the above-mentioned fluctuations disregarded, values of ~10% are indicative of a rather high uniformity of charge transport conditions in the film.

2. For the mode in which the collector is the Schottky barrier, the dependence $E(U)$ becomes superlinear. The signal corresponds to a magnitude of about 100 MeV, whereas the initial value of energy released by the α particle is close to 2 MeV. The spectrum, similarly to the first case, is Gaussian-shaped. It is significant that the considerable spread of amplitudes (Fig. 4), which was observed for low voltages ($U \leq 15$ V), tended further to the constant value of ~9%, which was actually
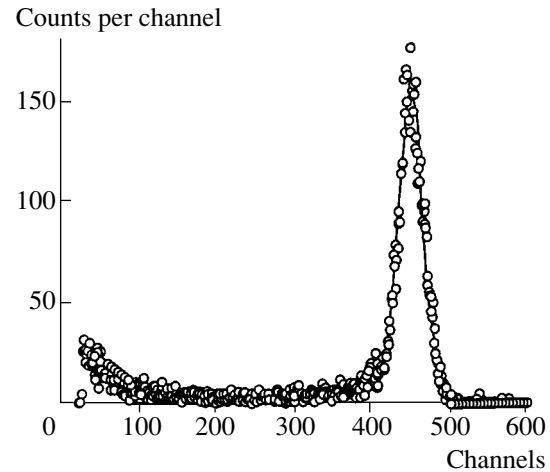
Fig. 2. Spectral line shape for the voltage of 305 V. The solid line is the approximation of the spectrum by a Gaussian function.

equal to the above-obtained one. It should also be noted that the constancy of the ratio between the spectrum width and its average amplitude points to the linear character of amplification for both large and small portions of the initially introduced charge.

DISCUSSION OF RESULTS

Since the structure under investigation is equivalent to the phototriode, the amplification observed should be qualitatively described in the context of the following model (see, for example, [5]). Minority carriers (electrons in our case), which are formed in the base during the deceleration of the α particle, diffuse to the emitter and collector junctions, where they are involved in the drift by existing fields. Nonequilibrium holes reside in
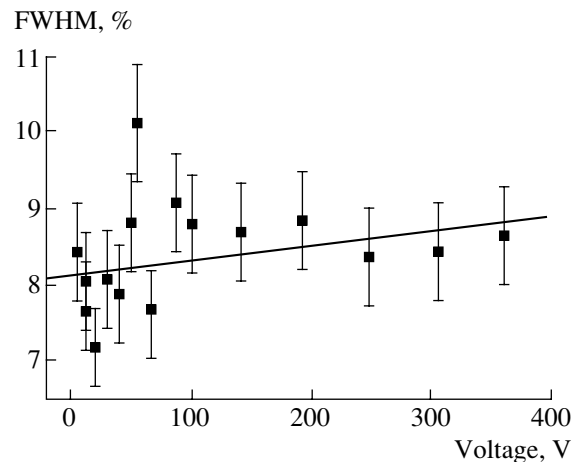

Fig. 3. Ratio of the full width at the half-maximum of the spectral line to the average amplitude of the spectrum as a function of the voltage across the triode structure. The p–n^+ junction of the substrate plays the role of the collector.
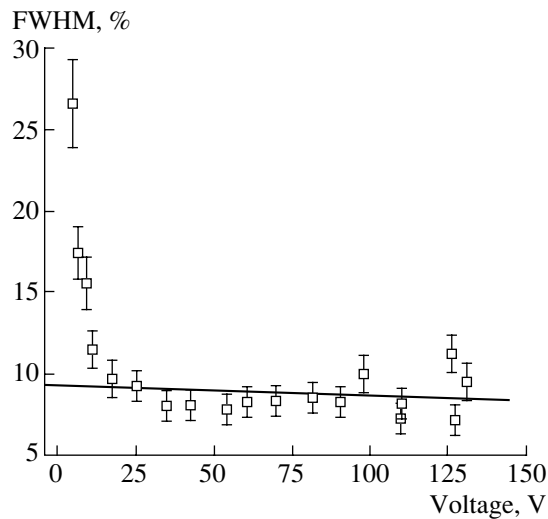
FWHM, %

Fig. 4. Ratio of the full width at half-maximum of the spectral line to the average amplitude of the spectrum as a function of the voltage across the triode structure. The Schottky barrier plays the role of the collector.

Energy, MeV

Fig. 5. Dependence of the signal from an α particle, which is expressed in energy units, on the space-charge region width at the collector junction (the Schottky barrier). Points correspond to the experiment, and the solid lines represent the approximation by formula (1) with the values of fitting parameters: $L_D = 8.85$ and 5.85 μm, and the film thickness $d = 10.75$ and 8.53 μm for samples 1 and 2, respectively.

the quantum well and charge it positively relative to the emitter. The variation in the difference of the emitter–base potentials increases the electron current, which is injected by the emitter.

In order to describe the effect quantitatively, let us first take into account that the primary current of the phototriode is amplified by a factor of $(1 - \alpha_T)^{-1}$. Here, α_T is the coefficient of electron transport in the base. This representation is valid on the assumption that the emitter efficiency is equal to unity. Let us base the expression for α_T according to [6] on transport of the charge entering the base during the δ pulse of the voltage at the emitter–base junction. Thus, for our case, α_T can be written as $[(d - w)/L_D]/\sinh[(d - w)/L_D]$. Here, d, w, and L_D are the film thickness, the width of the space-charge region of the collector junction, and the diffusion length for electrons, respectively.

When considering the initially formed charge, let us only make allowance for the carriers that enter into the collector. Assume that the nonequilibrium electron charge, which is generated by the α particle in the ω region, is completely transported into the collector by the drift. In order to describe the contribution of electron diffusion to the boundary of the region of the electric field, w, it is possible to write $(d - w)\exp(-(d - w)/L_D)$. In this case, for the signal in energy units, we derive

$$E = 0.2[w + (d - w)\exp(-(d - w)/L_D)]/[1 - ((d - w)/L_D)/\sinh((d - w)/L_D)]. \tag{1}$$

Here, the coefficient 0.2 keV/μm describes the specific energy losses of the α particle for the ionization in the beginning of deceleration in SiC.
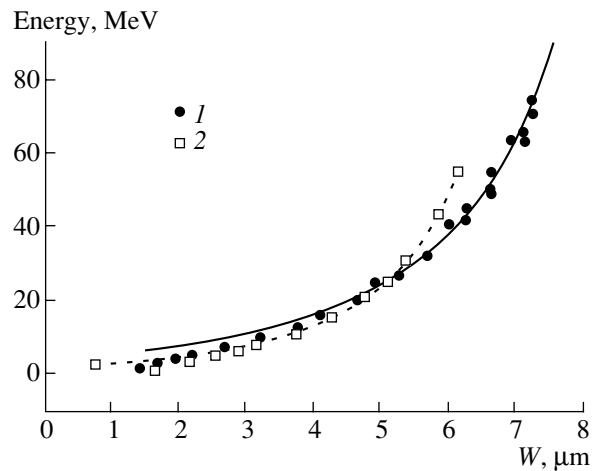
Formula (1) represents the behavior of the signal as a function of the width of the region w. Using the d and L_D quantities as the parameters, formula (1) is convenient for an approximation of the experimental data. Since the $E(U)$ dependences were directly recorded experimentally, the U values were converted to w values. Here, the impurity concentration of 2.8×10^{15} cm^{-3}, which was known to us, and an abrupt character of behavior of the junction at the Schottky barrier were used. The result of fitting the data obtained to dependence (1) for two samples is shown in Fig. 5. It is noteworthy that the diffusion lengths of electrons are considerable ($L_D = 8.85$ and 5.85 μm) and practically coincide with actual values of film thicknesses.

The fitting accuracy is characterized by the values $d = 8.53 \pm 0.09$ μm and $1/L_D = 0.171 \pm 0.005$ 1/μm, which are obtained for sample 2.

For monitoring the L_D values, the results of the EBIC (Electron Beam Induced Current) technique were also used. They yielded values (from 2.6 to 4.1 μm) which are in satisfactory agreement with the above-mentioned data, since charge transport in the EBIC method occurs over the surface.

CONCLUSION

It is demonstrated that internal signal amplification on the order of about a hundred may be realized in detectors of short-range particles based on pure SiC films. This is achievable for relatively simply fabricated structures in which the Schottky barrier is used as the collector. The results are quantitatively described according to the phototriode model.

It is our opinion that similar structures that take the high radiation [7] and chemical stability of SiC into account should be of interest for practical applications. For example, these structures may be used for the detection of neutrons by their reactions with light elements, which are accompanied by the emission of α particles of the type $^{10}B(n, \alpha)^7Li$.

From the point of view of material science, the experiments with particle detection allowed us to determine the diffusion lengths for electrons, which are high for SiC. It is also found that the nonuniformity of parameters of the diffusion–drift carrier transport in the films is no more than 10%.

ACKNOWLEDGMENTS

REFERENCES

1. A. A. Lebedev, N. S. Savkina, A. M. Ivanov, *et al.*, Fiz. Tekh. Poluprovodn. (St. Petersburg) **34**, 249 (2000) [Semiconductors **34**, 243 (2000)].

2. F. Nava, P. Vanni, G. Verzellesi, *et al.,* Mater. Sci. Forum **353–356**, 757 (2001).

3. G. Violina, P. Shkreby, E. Kalinina, *et al.*, in *Abstracts of the III International Seminar on Silicon Carbide and Related Materials, Novgorod, Russia, 2000*, p. 125.

4. N. S. Savkina, A. A. Lebedev, D. V. Davydov, *et al.,* Mater. Sci. Eng. B **B61–62**, 165 (1999).

5. S. M. Ryvkin, *Photoelectric Effects in Semiconductors* (Fizmatgiz, Leningrad, 1963; Consultants Bureau, New York, 1964).

6. A. A. Grinberg, Fiz. Tverd. Tela (Leningrad) **1**, 31 (1959) [Sov. Phys. Solid State **1**, 29 (1959)].

7. A. A. Lebedev, N. B. Strokan, A. M. Ivanov, *et al.*, Mater. Sci. Forum **353–356**, 763 (2001).

Translated by N. Korovin

Electrical Properties of Silicon Layers Implanted with Erbium and Oxygen Ions in a Wide Dose Range and Thermally Treated in Different Temperature Conditions

O. V. Aleksandrov*, A. O. Zakhar'in*, N. A. Sobolev**, and Yu. A. Nikolaev**

* St. Petersburg Electrotechnical University, St. Petersburg, 197376 Russia

** Ioffe Physicotechnical Institute, Russian Academy of Sciences, St. Petersburg, 194021 Russia

Abstract—The electrical properties of silicon implanted with Er and O ions in a wide dose range have been studied. The dependence of electron mobility on the concentration of electrically active centers is determined for Si:Er layers with Er concentrations in the range of 9×10^{15}–8×10^{16} cm^{-3}. Sharp bends related to specific features of Er segregation in solid-phase epitaxial recrystallization are observed in the concentration profiles of electrically active centers, $n(x)$, and Er atoms, $C(x)$, at Er ion implantation doses exceeding the amorphization threshold. The $n(x)$ and $C(x)$ profiles virtually coincide near the surface. A linear rise in the maximum concentration of electrically active centers at approximately constant effective coefficient of their activation, k, is observed at Er implantation doses exceeding the amorphization threshold. At an Er concentration higher than 7×10^{19} cm^{-3}, the concentration of electrically active centers levels off and k decreases. © 2002 MAIK "Nauka/Interperiodica".

1. INTRODUCTION

The properties of silicon doped with rare-earth elements (Er, in particular) and Si:Er structures are attracting considerable interest owing to their possible application in silicon-based optoelectronics (see reviews [1, 2]). To fabricate Si:Er light-emitting devices, it is necessary to raise the concentration of optically active centers, which correlates with that of electrically active centers [3, 4]. One of the ways to increase the concentrations of electrically and optically active centers is to increase the Er ion implantation dose. However, the concentrations of electrically and optically active centers decrease at doses exceeding the Si amorphization threshold [5]. This effect can be attributed to the formation of Er precipitates [6]. The threshold Er concentration, at which the onset of precipitation occurs, is 1.3×10^{18} cm^{-3} for the annealing temperature of 900°C [6]. To raise the concentration of active centers, Er and O ions are commonly implanted simultaneously. The activation behavior of electrically and optically active centers during implantation of Er and O was studied in [3, 7], with the amorphization threshold not being exceeded because of the use of either low implantation doses [7] or substrate heating [3]. As shown in [8], simultaneous implantation of Er and O ions allows one to raise the concentration of electrically active centers even if the amorphization threshold is exceeded.

In the present study, the electrical properties of Si layers implanted simultaneously with Er and O ions, with doses below and above the amorphization threshold, have been investigated in order to reveal the specific features associated with amorphization.

2. EXPERIMENTAL PROCEDURE

Erbium ions with energies of 0.5 or 1 MeV and, respectively, 70 or 135 keV oxygen ions were coimplanted at room temperature into boron-doped (100) silicon wafers with a resistivity of 7.5–20 Ω cm. The Er ion implantation dose Q(Er) was varied in the range from 1×10^{13} to 3.2×10^{15} cm^{-2}, with the O dose being an order of magnitude higher. Nonamorphized implanted Si layers (Q(Er) $< 5 \times 10^{13}$ cm^{-2}) were annealed in a single stage in the temperature range of 700–900°C in a chlorine-containing atmosphere. Amorphized Si layers (Q(Er) $\geq 5 \times 10^{13}$ cm^{-2}) were annealed in two stages: at 620°C (1 h) to recrystallize the amorphized layer and at 900°C (0.5 h) to form donor centers. The Er impurity distribution across the sample thickness was determined by secondary-ion mass spectrometry (SIMS) using a Cameca IMS 4f system. The density and mobility of charge carriers were measured at room temperature by means of the differential Hall effect, with successive removal of thin (~0.02 μm) silicon layers. The donor center concentration profiles across the sample thickness were determined using the differential conductivity method. The effective coefficient of activation of electrically active centers, k, was calculated as the ratio of the number of donor centers in the layer, found by integrating the $n(x)$ profile, to the total implanted dose of Er ions.

3. EXPERIMENTAL RESULTS

As a result of annealing, donor centers are formed in the silicon layers coimplanted with Er$^+$ and O$^+$ ions.

The distributions of electrically active centers and electron mobility across the sample thickness, $n(x)$ and $\mu(x)$, were determined by means of the differential Hall effect. Figure 1 shows dependences of the electron mobility on the concentration of electrically active centers, found from comparison of the $n(x)$ and $\mu(x)$ profiles. The least-squares technique was applied to find the concentration dependence of the electron mobility $\mu_{Er}(n)$ (Fig. 1, dashed line) describing the experimental values with an rms deviation of $\pm 10\%$:

$$\mu(n) = \mu_{min} + \frac{\mu_{max} - \mu_{min}}{1 + \left(\dfrac{n}{N_{ref}}\right)^{\alpha}}.$$

The table presents the obtained parameters μ_{max}, μ_{min}, N_{ref}, and α of the $\mu_{Er}(n)$ dependence, together with the parameters of the $\mu_{Yb}(n)$ dependence for the Yb impurity [9] and $\mu_{don}(n)$ for main donor impurities (P, As, Sb) [10]. As seen from Fig. 1 and the table, the obtained $\mu_{Er}(n)$ dependence virtually coincides with the known empirical dependences $\mu_{Yb}(n)$ (dot-dashed line) and $\mu_{don}(n)$ (solid line). As shown in [11, 12], varying the O ion implantation dose and the annealing temperature leads to changes in the spectrum of electrically active centers in Si layers implanted with Er ions. Comparison of the experimental data obtained in the present study and in [11, 12] shows that the electron mobility in Si:Er layers is virtually independent of the energy spectrum of electrically active centers.

Figure 2 shows the concentration profiles of Er atoms, $C(x)$, and electrically active centers, $n(x)$, after the annealing of layers implanted with Er ions with doses of 1×10^{13} (curves *1*, *3*) and 4×10^{14} cm^{-2} (curves *2*, *4*) together with O ions. For doses below the amorphization threshold, the concentration of electrically active centers is lower than that of implanted Er ions across the entire thickness of the implanted layer. If the amorphization threshold is exceeded ($Q(\text{Er}) \geq 4 \times 10^{14}$ cm^{-2}), the concentration of electrically active centers at depths exceeding 0.15 μm is also lower than the concentration of implanted Er ions. In addition, two features are observed: the $C(x)$ and $n(x)$ profiles show sharp bends at a depth corresponding to the initial boundary between the amorphized and single-crystal Si (curves *2*, *4* in Fig. 2) and virtually coincide near the surface.

Figure 3 shows the concentrations of electrically active centers at peaks of the corresponding profiles and the effective coefficient of their activation as functions of the concentration of implanted O ions. With increasing Er and O implantation doses, the peak concentration of electrically active centers n_{max} grows approximately linearly up to $\sim 1.4 \times 10^{19}$ cm^{-3} at Er ion implantation energies of 0.5 and 1 MeV (Fig. 3, curves *1* and *2*, respectively). With rising n_{max}, the effective coefficient of activation of electrically active centers remains virtually unchanged, being $k \approx 0.25$ and ≈ 0.17 for Er
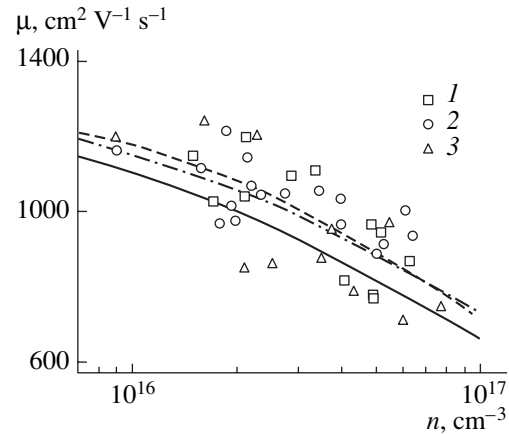

Fig. 1. Electron mobility vs. concentration of electrically active centers in Si layers implanted with 1 MeV Er and 0.135 MeV O ions. Er ion dose 10^{13} cm^{-2}, O doses: (*1*) 10^{13} and (*2*, *3*) 5×10^{13} cm^{-2}. Annealing temperature: (*1*, *2*) 800 and (*3*) 900°C. Dashed line: $\mu_{Er}(n)$, this study; dot-dashed line: $\mu_{Yb}(n)$ [9]; solid line: $\mu_{don}(n)$ [10].
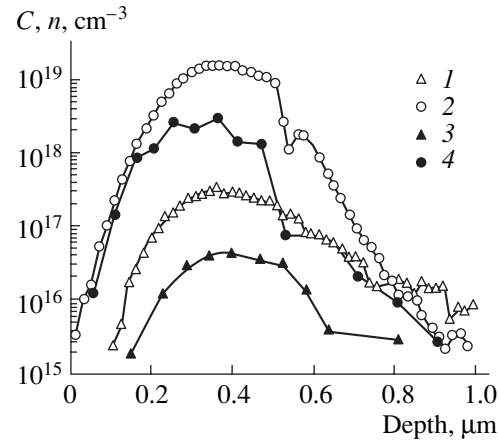

Fig. 2. Concentration profiles of (*1*, *2*) Er atoms and (*3*, *4*) electrically active centers upon implantation of 1 MeV Er and 0.135 MeV O ions. Er ion doses: (*1*, *3*) 10^{13} and (*2*, *4*) 4×10^{14} cm^{-2}; oxygen doses: (*1*, *3*) 10^{14} and (*2*, *4*) 4×10^{15} cm^{-2}.

implantation energies of 0.5 and 1 MeV, respectively (Fig. 3, curves *4*, *5*). At a peak concentration of O, $C_{O\,max}$, exceeding 6×10^{20} cm^{-3} and a corresponding Er peak concentration, $C_{Er\,max}$, higher than 7×10^{19} cm^{-3},

Parameters of the concentration dependence of electron mobility

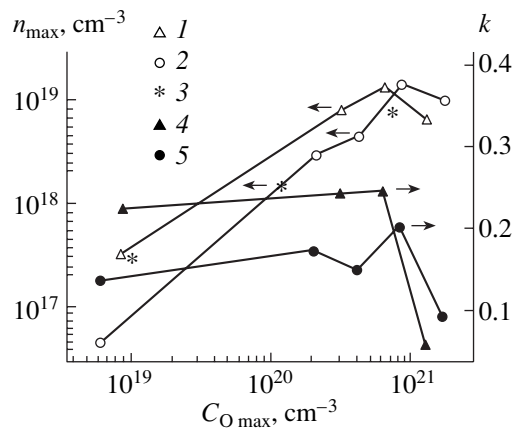| Parameter	Si : Er	Si : Yb [9]	Main donor impurities in Si [10]
μ_{min}	65	60	65
μ_{max}	1320	1350	1330
N_{ref}	1.06×10^{17}	1.1×10^{17}	8.5×10^{16}
α	0.87	0.72	0.72

Fig. 3. (*1–3*) Maximum concentration of electrically active centers, and (*4, 5*) effective coefficient of their activation vs. concentration of implanted oxygen at the concentration profile peak. Erbium ion energy: (*1, 4*) 0.5, (*2, 5*) 1, and (*3*) 5 MeV; (*3* data of [3]).

n_{max} values level off and the activation coefficient sharply decreases.

4. DISCUSSION

The dependences of the electron mobility on the concentration of electrically active centers coincide within the experimental error for Si layers doped with Er, Yb, and the main donor impurities (see Fig. 1). This can be presumably accounted for by the identical mechanisms of electron scattering, by ionized centers and acoustic phonons, in such layers [13].

The sharp bend in the $C(x)$ and $n(x)$ profiles at Er implantation doses exceeding the amorphization threshold arises from the specificity of Er impurity segregation at the interface between amorphous and single-crystal silicon, with Er accumulated in the initial stage of solid-phase epitaxial recrystallization in the transition layer moving toward the surface [14]. The same process leads to an increase in the activation coefficient of electrically active centers in the surface layer (to the $C(x)$ and $n(x)$ profiles approaching each other; see Fig. 2, curves *2, 4*). Presumably, intrinsic point defects incorporated into donor centers (supposedly, silicon self-interstitials [15]) are gradually accumulated in the transition layer while it moves to the surface. The influence of the spatial separation of vacancies and self-interstitials during ion implantation is also possible. According to calculations in [16], in the case of implantation of heavy ions, vacancies are mainly located near the surface, whereas self-interstitials are predominantly located in the bulk near the peak of the impurity profile. Accumulation of intrinsic point defects at the moving phase boundary accounts for the high (up to 0.8) coefficient of activation of electrically active centers, observed in [8] during the crystallization of thick (~2.3 μm) amorphized Si layers obtained using a set of

O and Er energies and doses at a 10 : 1 ratio of their concentrations.

The rise in the concentration of electrically active centers with an increase in the dose of introduced Er and O ions is due to the formation of several donor centers incorporating Er and O [7, 11, 12]. A linear increase in n_{max} with a growing dose of introduced O, with its subsequent leveling-off, has been observed earlier in nonamorphized silicon [3]. The n_{max} values obtained in [3] for [O]/[Si] concentration ratios of 5–10 (Fig. 3, points *3*) are close to the corresponding n_{max} values obtained in the present study at a similar concentration ratio (7–8). As seen in Fig. 3 (curves *1, 2*), the linear increase persists above the amorphization threshold, up to a concentration of electrically active centers of ~1.4×10^{19} cm^{-3} with an O concentration in the profile peak of ~5×10^{20} cm^{-3} and a corresponding Er peak concentration of 7×10^{19} cm^{-3}. A somewhat higher concentration of electrically active centers, ~2×10^{19} cm^{-3}, was achieved at a higher [O]/[Si] concentration ratio (~40) [3]. The decrease in n_{max} with the further increase in the O concentration (Fig. 3) can be attributed to the onset of precipitation of the O impurity, whose concentration exceeds the equilibrium solubility by approximately three orders of magnitude and whose diffusion coefficient is fairly high ($D(O) \approx 2 \times 10^{-12}$ cm^2 s^{-1} at 900°C [17]).

5. CONCLUSION

It is established that the concentration dependence of electron mobility in Si layers implanted with Er and O ions virtually coincides with similar dependences for Si doped with Yb rare-earth and main donor impurities, with the mobility independent of the energy spectrum of electrically active centers. When Er and O implantation doses exceed the amorphization threshold, sharp bends are observed in the concentration profiles of donor centers and Er, $n(x)$ and $C(x)$; these bends are associated with Er segregation at the ⟨amorphized Si⟩–⟨single-crystal Si⟩ interface during solid-phase epitaxial recrystallization. Near the surface, the $n(x)$ and $C(x)$ profiles virtually coincide. With Er and O implantation doses raised above the amorphization threshold, the donor center concentration at the profile peak increases linearly up to 1.5×10^{19} cm^{-3}, with the activation coefficient of electrically active centers remaining nearly constant; i.e., $k \approx 0.25$ and ≈ 0.17 for Er ion implantation energies of, respectively, 0.5 and 1 MeV. At O concentrations exceeding 6×10^{20} cm^{-3} and Er concentrations higher than 7×10^{19} cm^{-3}, the peak concentration of donor centers levels off and the activation coefficient decreases.

REFERENCES

1. N. A. Sobolev, Fiz. Tekh. Poluprovodn. (St. Petersburg) **29**, 1153 (1995) [Semiconductors **29**, 595 (1995)].

2. J. Michel, L. V. C. Assali, M. T. Morse, and L. C. Kimerling, in *Semiconductors and Semimetals* (Academic, San Diego, 1998), Vol. 49, p. 111.

3. F. Priolo, S. Coffa, G. Franzo, *et al.*, J. Appl. Phys. **74**, 4936 (1993).

4. J. Michel, J. Palm, X. Duan, *et al.*, Mater. Sci. Forum **258–263**, 1485 (1997).

5. J. L. Benton, J. Michel, L. C. Kimerling, *et al.*, J. Appl. Phys. **70**, 2667 (1991).

6. D. J. Eaglesham, J. Michel, E. A. Fitzgerald, *et al.*, Appl. Phys. Lett. **58**, 2797 (1991).

7. O. V. Aleksandrov, A. O. Zakhar'in, N. A. Sobolev, and E. I. Shek, Izv. Gos. Élektrotekh. Univ. **516**, 48 (1998).

8. S. Coffa, F. Priolo, G. Franzo, *et al.*, Phys. Rev. B **48**, 11782 (1993).

9. O. V. Aleksandrov, A. O. Zakhar'in, and N. A. Sobolev, Fiz. Tekh. Poluprovodn. (St. Petersburg) **36**, 134 (2002) [Semiconductors **36**, 126 (2002)].

10. D. M. Caughey and R. E. Thomas, Proc. IEEE **55**, 2192 (1967).

11. V. V. Emtsev, V. V. Emtsev, Jr., D. S. Poloskin, *et al.*, Fiz. Tekh. Poluprovodn. (St. Petersburg) **33**, 649 (1999) [Semiconductors **33**, 603 (1999)].

12. V. V. Emtsev, V. V. Emtsev, Jr., D. S. Poloskin, *et al.*, Fiz. Tekh. Poluprovodn. (St. Petersburg) **33**, 1192 (1999) [Semiconductors **33**, 1084 (1999)].

13. G. Kaiblinger-Grujin, H. Kosina, and S. Selberherr, J. Appl. Phys. **83**, 3096 (1998).

14. O. V. Aleksandrov, Yu. A. Nikolaev, and N. A. Sobolev, Fiz. Tekh. Poluprovodn. (St. Petersburg) **33**, 114 (1999) [Semiconductors **33**, 101 (1999)].

15. O. V. Aleksandrov, N. A. Sobolev, E. I. Shek, and A. V. Merkulov, Fiz. Tekh. Poluprovodn. (St. Petersburg) **30**, 876 (1996) [Semiconductors **30**, 468 (1996)].

16. L. Pelaz, G. H. Gilmer, M. Jaraiz, *et al.*, Appl. Phys. Lett. **73**, 1421 (1998).

17. R. A. Devine, D. Mathiot, W. L. Warren, and B. Asper, J. Appl. Phys. **79**, 2302 (1996).

Translated by D. Mashovets

===== **PERSONALIA** =====

Igor' Georgievich Neizvestnyĭ (on his 70th birthday)
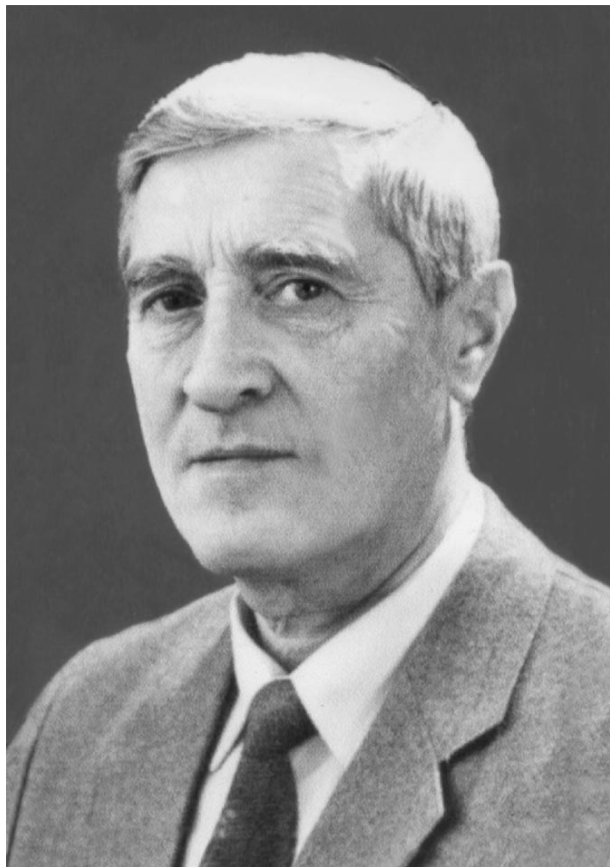
On November 26, 2001, Igor' Georgievich Neizvestnyĭ celebrated his 70th birthday. Igor' Georgievich is a well-known scientist active in the fields of semiconductor physics and semiconductor science and technology, as well as the deputy director of the Institute of Semiconductor Physics, Siberian Division, Russian Academy of Sciences, and a corresponding member of the Russian Academy of Sciences.

After graduating from the Moscow Power Institute (having majored in the physics of semiconductors and insulators), Neizvestnyĭ worked for seven years as a member of a team headed by A.V. Rzhanov at the laboratory of semiconductor physics of the Lebedev Physical Institute, USSR Academy of Sciences.

In 1962, Doctor Rzhanov asked Neizvestnyĭ to be the deputy scientific director of the just-founded Institute of Semiconductor Physics in Novosibirsk; Neizvestnyĭ still works at this institute.

It is difficult to overestimate the role which Neizvesnyĭ played (and still plays) in the development of the Institute of Semiconductor Physics. His exceptional abilities as a scientist, a manager, and a teacher manifested themselves in the directions of the activities of the Institute, in the expansion of the Institute, in equipping the laboratories and auxiliary departments with new facilities, and in the selection and training of personnel. Neizvestnyĭ was awarded the Order of the Red Banner in 1970 for his outstanding personal contribution to the erection of a unique thermostatically controlled building at the Institute.

Neizvestnyĭ is the author and co-author of more than 130 scientific publications. His studies in the field of the physics of semiconductor surfaces and interfaces in multilayer heterostructures are well known to the scientific community.

In 1995, Neizvestnyĭ and his colleagues were awarded the State Prize of the Russian Federation in the field of science and technology for the discovery and experimental and theoretical studies of a new class of photosensitive semiconductors.

Neizvestnyĭ is an active member of the editorial boards of several scientific journals and sits on several academic and specialized councils. He directs the studies supported by the Russian Foundation for Basic Research and the Ministry of Industry, Science, and Technology and heads the department "Microelectronics and Semiconductor Devices" of the Novosibirsk State Technical University at the Institute of Semiconductor Physics, where, for many years, he has been giving a lecture course on the fundamentals of high-speed microelectronics and nanoelectronics. Neizvestnyĭ, in cooperation with his colleagues from the department he presently heads, conducts studies in simulating molecular-beam epitaxy, producing and investigating quantum dots, and developing the physical foundations for the component base of a quantum-mechanical computer.

Friends and colleagues of Neizvesnyĭ wish him a happy birthday and also wish him further creative activity and every success in the realization of his numerous scientific ideas and plans.

Colleagues, friends, and the editorial board of this journal

Translated by A. Spitsyn